Dynamics of marine zooplankton: social behavior, ecological interactions, and physically-induced variability

by

Ariane Verdy

B.Ing. Ecole Polytechnique de Montréal, 2001
S.M. Massachusetts Institute of Technology & Woods Hole Oceanographic Institution, 2006

Submitted in partial fulfillment of the requirements for the degree of

Doctor of Philosophy

at the

MASSACHUSETTS INSTITUTE OF TECHNOLOGY

and the

WOODS HOLE OCEANOGRAPHIC INSTITUTION

February 2008

Author ....
Joint Program in Physical Oceanography
Massachusetts Institute of Technology
and Woods Hole Oceanographic Institution
November 2007

Certified by ....
Glenn R. Flierl
Professor of Oceanography
Thesis Supervisor

Accepted by ....
Raffaele Ferrari
Chair, Joint Committee for Physical Oceanography
Massachusetts Institute of Technology

Dynamics of marine zooplankton: social behavior, ecological interactions, and physically-induced variability

by

Ariane Verdy

Submitted to the Joint Program in Oceanography at the Massachusetts Institute of Technology and the Woods Hole Oceanographic Institution, in partial fulfillment of the requirements for the degree of Doctor of Philosophy

November 2, 2007

Abstract

Marine ecosystems reflect the physical structure of their environment and the biological processes they carry out. This leads to spatial heterogeneity and temporal variability, some of which is imposed externally and some of which emerges from the ecological mechanisms themselves. The main focus of this thesis is on the formation of spatial patterns in the distribution of zooplankton arising from social interactions between individuals. In the Southern Ocean, krill often assemble in swarms and schools, the dynamics of which have important ecological consequences. Mathematical and numerical models are employed to study the interplay of biological and physical processes that contribute to the observed patchiness.

The evolution of social behavior is simulated in a theoretical framework that includes zooplankton population dynamics, swimming behavior, and some aspects of the variability inherent to fluid environments. First, I formulate a model of resource utilization by a stage-structured predator population with density-dependent reproduction. Second, I incorporate the predator-prey dynamics into a spatially-explicit model, in which aggregations develop spontaneously as a result of linear instability of the uniform distribution. In this idealized ecosystem, benefits related to the local abundance of mates are offset by the cost of having to share resources with other group members. Third, I derive a weakly nonlinear approximation for the steady-state distributions of predator and prey biomass that captures the spatial patterns driven by social tendencies. Fourth, I simulate the schooling behavior of zooplankton in a variable environment; when turbulent flows generate patchiness in the resource field, schools can forage more efficiently than individuals. Taken together, these chapters demonstrate that aggregation/ schooling can indeed be the favored behavior when (i) reproduction (or other survival measures) increases with density in part of the range and (ii) mixing of prey into patches is rapid enough to offset the depletion. In the final two chapters, I consider sources of temporal variability in marine ecosystems. External perturbations amplified by nonlinear ecological interactions induce transient excursions away from equilibrium; in predator-prey dynamics the amplitude and duration of these transients are controlled by biological processes such as growth and mortality. In the Southern Ocean, large-scale winds associated with ENSO and the Southern Annular Mode cause convective mixing, which in turn drives air-sea fluxes of carbon dioxide and oxygen. Whether driven by stochastic fluctuations or by climatic phenomena, variability of the biogeochemical/physical environment has implications for ecosystem dynamics.

Thesis Supervisor: Glenn R. Flierl
Title: Professor of Oceanography

Acknowledgments

First and foremost, I thank my advisor, Glenn Flierl. I thank Mike Neubert, Hal Caswell, and the students and postdocs in the Mathematical Ecology Lab at WHOI for their hospitality and many stimulating discussions. Thanks to Mick Follows, Dan Rothman, and Bob Beardsley for helpful advice throughout the realization of this thesis. I am grateful for the mentorship provided by John Marshall and Sonya Legg. Thanks to my classmates and officemates for fun times. To my family, for unconditional support.

Funding was provided by the Academic Programs Office of the MIT-WHOI Joint Program, an Ocean Ventures Fund Award, an Anonymous Ys Endowed Science Fellowship, and by NSF grants OCE-0221369 and OCE-336839.

Contents

Introduction **11**

1 Predator-prey dynamics with density-dependent mating success **19**
- 1.1 Introduction: Allee effects 20
- 1.2 Stage-structured model 22
  - 1.2.1 Density-dependent reproduction 23
  - 1.2.2 Full model and adimensionalization 25
- 1.3 Asymptotic dynamics 27
  - 1.3.1 Stability boundaries 29
  - 1.3.2 Imposing structure in the population 31
- 1.4 One-stage limit 33
  - 1.4.1 Bifurcations and multiple equilibria 36
  - 1.4.2 Destabilization due to Allee effect 39
  - 1.4.3 On the Allee effect term in the prey equation 39
- 1.5 A continuous-weight model with power laws for birth and growth 42
- 1.6 Summary 46
- 1.7 Appendix: Fixed points and stability 48

2 Evolution and social behavior in krill **57**
- 2.1 Introduction 58
- 2.2 Model formulation 60
  - 2.2.1 Genetic model 61
  - 2.2.2 Ecological dynamics 61
  - 2.2.3 Turbulent stirring 64
- 2.3 Development of patches 66
  - 2.3.1 Non-dimensional system of equations 66
  - 2.3.2 Numerical simulations 70
- 2.4 Conditions for success of the grouping strategy 74
  - 2.4.1 Grouping parameter and invasions 74

2.4.2 Mixing and stirring effects . . . 77
2.4.3 Threshold values of flow and grouping parameter . . . 79
2.5 Adding complexity: life history . . . 81
2.6 Conclusions . . . 83
2.7 Appendix A: Genotype frequencies in the two-allele model . . . 86
2.8 Appendix B: Linear stability of the ecological model . . . 87

3 Spatial instability driven by social behavior in predator-prey dynamics 91
3.1 Introduction . . . 92
3.2 Motion in a one-dimensional space . . . 93
3.2.1 The model . . . 93
3.2.2 Linear growth of patches . . . 94
3.3 Analytical solution for fully-developed patches . . . 95
3.3.1 Weakly nonlinear equations . . . 97
3.3.2 Steady-state solutions . . . 100
3.4 Ecosystem dynamics . . . 102
3.4.1 Fast diffusion ($\nu \gg 1$) . . . 103
3.4.2 Slow diffusion ($\nu \ll 1$) . . . 104
3.5 Swarming as a strategy for survival . . . 107
3.5.1 Competition model . . . 107
3.5.2 Optimal strategies . . . 109
3.6 Summary . . . 112
3.7 Appendix: Weakly nonlinear stability analysis . . . 114

4 Collective motion in a variable environment: Does schooling behavior improve foraging success? 119
4.1 Introduction . . . 120
4.2 Individual-based modeling approach . . . 121
4.2.1 Movement algorithm . . . 121
4.2.2 Simulated groups . . . 125
4.3 Variability of the flow . . . 128
4.4 Foraging on patchy resources . . . 134
4.4.1 Hybrid model and foraging algorithm . . . 134
4.4.2 Optimal strategy . . . 135
4.5 Phase transitions in the density-distribution of Antarctic krill . . . 138
4.5.1 Observed patterns . . . 139
4.5.2 Emergent properties of simulated schools . . . 141
4.5.3 Behavior switching as a mechanism for observed phase transitions . 143
4.6 Conclusions . . . 145

5 Sensitivity analysis of reactive ecological dynamics 147
- 5.1 Introduction 148
  - 5.1.1 Characterizing transient dynamics 149
  - 5.1.2 The sensitivity problem 152
- 5.2 Equilibria, linearizations, and their sensitivities 154
  - 5.2.1 The linearization 154
  - 5.2.2 Sensitivity of equilibria 155
  - 5.2.3 Sensitivity of the linearization 155
- 5.3 Sensitivity of transient indices 156
  - 5.3.1 Sensitivity of reactivity 157
  - 5.3.2 Sensitivity of the amplification envelope 157
  - 5.3.3 Sensitivity of the optimal perturbation 158
  - 5.3.4 Anisotropic measures of transient amplification 159
- 5.4 Applications to consumer-resource dynamics 161
  - 5.4.1 Predator-prey interactions 162
  - 5.4.2 Multiple food chains 174
- 5.5 Discussion 179
- 5.6 Appendix A: The sensitivity problem in index notation 180
- 5.7 Appendix B: Derivatives of equilibria and indices of transient dynamics, with an example 182

6 Carbon dioxide and oxygen fluxes in the Southern Ocean: mechanisms of interannual variability 193
- 6.1 Introduction 194
- 6.2 Air-sea fluxes of carbon and oxygen in a global ocean model 195
  - 6.2.1 Model description 195
  - 6.2.2 Simulated variability 197
- 6.3 Modes of air-sea flux variability, ENSO and SAM 201
- 6.4 Mechanisms 204
  - 6.4.1 Diagnostic Framework 204
  - 6.4.2 Lagrangian model 207
  - 6.4.3 Further simplifications to the diagnostic framework 210
- 6.5 Conclusions 211

7 Concluding remarks 215

References 221

Introduction

This thesis is about the structure and dynamics of marine ecosystems. Photosynthesis in the ocean provides energy to sustain a diverse and abundant fauna, which is assembled into communities of multiple species interacting with each other and with their environment. The interplay of ecological and physical processes has important consequences for the evolution of communities. Some of these processes, such as individual behavior and predator-prey interactions, can be best expressed as mathematical equations. Theoretical frameworks can thus be used to represent idealized marine ecosystems. The main advantage of this approach is that it offers the possibility to perform quantitative analyses and to strip out most of the system's complexity in order to focus on key mechanisms.

Zooplankton patchiness

Zooplankton occupy an important position in oceanic food webs. By filling the size gap between the phytoplankton and animals that are too large to prey directly on microscopic algae, they provide a crucial link for energy transfer toward higher trophic levels. The spatial distribution of zooplankton is observed to be highly variable (e.g. Mackas and Boyd, 1979); the patchiness is produced in part by the environmental variability and in part by the ecological dynamics (Levin, 1992). Because of their small size, planktonic organisms have a limited ability to swim against currents, allowing their distribution to be strongly influenced by ocean circulation patterns. At small scales and mesoscales, turbulent motions generate patchiness (e.g. Flierl and McGillicuddy, 2002; Abraham, 1998). Clustering can also result from the actions and interactions of individuals (Levin, 1994; Young et al., 2001). In particular, social behavior is responsible for the formation of dense aggregations in swimming organisms. These spatial patterns have significant effects on the structure and function of ecosystems (Steele, 1974; Hobson, 1989; Bracco et al., 2000; Brentnall et al., 2003; Martin et al., 2002; Martin, 2003).

Social behavior refers to the tendency of individuals to move toward their conspecifics, which results in the formation of social groups. The behavior is observed in many kinds of animals, including larger species of zooplankton such as euphausiids (Mauchline, 1980; Folt and Burns, 1999; Hamner and Hamner, 2000). Also known as “krill”, euphausiids are shrimp-like crustaceans found in pelagic waters throughout the world’s oceans. Antarctic krill (*Euphausia superba*) is a notable example of zooplankton with social behavior. Social aggregations of krill (called *swarms* or *schools*) can be very dense, with up to $10,000$ individuals per cubic meter, and extend horizontally for several kilometers (e.g. Miller and Hampton, 1989; Hewitt and Demer, 1993). As a source of food for whales, seals, penguins, and other large predators, krill plays a central role in the Southern Ocean food web. Its ecological relevance has motivated numerous studies, both in situ and in laboratory settings, of the ecology and physiology of Antarctic krill. While these studies have contributed significantly to understanding the species as well as the local ecosystem, the question remains: why has social behavior evolved so strongly in krill?

Distribution and behavior of Antarctic krill

Observations of the density distribution of krill in the Southern Ocean consistently show high levels of variability at a wide range of spatial scales. Non-random aggregations, which result not by chance but from biological and/or physical processes, occur throughout the year and over the whole geographical range of Antarctic krill. Hydroacoustic measurements have proven particularly useful for estimating the morphology, internal structure, and vertical position of such aggregations (Lawson, 2006). The smallest swarms have typical lengths of tens of meters and densities often exceeding 100 g/m^3 (Kalinowski and Witek, 1985; Miller and Hampton, 1989). Aggregations tend to be larger, denser and deeper during daytime than during the night (Lawson, 2006); swarms can reach densities of 1000 g/m^3 and horizontal scales of a few kilometers (Hamner et al., 1983; Kalinowski and Witek, 1985; Miller and Hampton, 1989).

Variance spectra reveal that there is significantly more fine-scale structure in krill density than in temperature or phytoplankton in the Southern Ocean (Figure 0-1). At scales of approximately 100 km, all spectra have the same slope, which suggests that ocean circulation controls the large-scale distribution of the three tracers. At small scales, however, the spectrum of krill is flatter than the others; this implies that environmental variability is not the only factor generating patchiness in the density-distribution of krill, and that a different mechanism must explain the small-scale patterns (Levin, 1992). The scale at which the transition occurs is consistent with the observed length of krill swarms ($<$ 10 km). The interpretation of these data is that social behavior is the main driver of small-scale variability in the density-distribution of krill.

The processes involved in the generation and maintenance of swarms can be investigated using a combination of data and models. Existing models of social aggregation in krill are either formulated as reaction-advection-diffusion equations (e.g. Flierl et al., 1999) or they are individual-based models (e.g. Flierl et al., 1999; Hofmann et al., 2004). Observational and experimental data is used to constrain the parameter values in these models. Theory predicts that the size of social aggregations in zooplankton depends primarily on the swimming speed, the distance at which individuals can sense their neighbors, and the rate at which they are diffused (Flierl et al., 1999). Some of these parameters can be measured directly (the swimming velocity) or indirectly (the sensing radius), while others are poorly constrained (the diffusivity).

Despite their relatively small size, Antarctic krill are strong swimmers: adults can maintain cruising speeds of 0.08 – 0.15 m/s (Kils, 1982), which corresponds to roughly two body lengths per second. It is believed that individuals use visual methods to detect each other (Strand and Hamner, 1990). The distance at which individuals can respond to neighbors is difficult to measure, but can be estimated from the distance at which they avoid nets

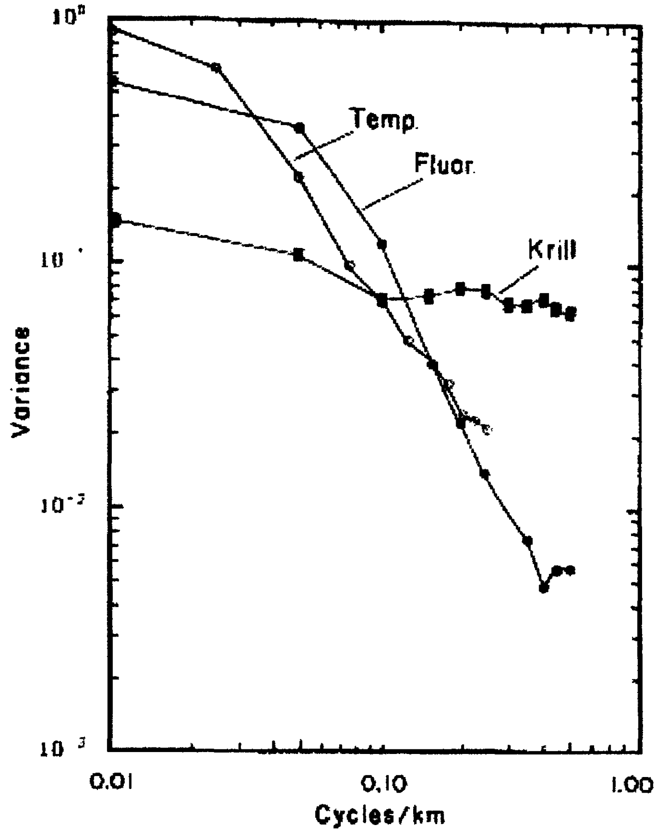

Figure 0-1: Fourier spectra of the spatial distributions of temperature, fluorescence, and krill biomass in the Southern Ocean. Spatial scale increases from the right to the left. Temperature is an indicator of water movements; fluorescence is a proxy for phytoplankton activity. From Weber (1986), reproduced in Levin (1992).

or divers, from the morphology of their eye compound, or from model sensitivities. These methods yield maximum sensing distances of 0.2 m (Hofmann et al., 2004) to about 1 m (Lawson, 2006).

The tendency to swim toward neighbors that are within sensing range is, however, counterbalanced by the homogenizing effect of diffusion. Zooplankton individuals tend to disperse as a result of randomness in the swimming movements and of the turbulent mixing resulting from small-scale ocean circulation patterns. Social aggregations can only form if the attraction tendency is greater than the effective diffusion (e.g. Okubo, 1986). Diffusivity, especially the movement-related component, is difficult to measure; this parameter is often adjusted in models so that self-organized aggregations can develop. When realistic values for krill behavior are used, simulated social aggregations have spatial scales of 10 m or less (Hofmann et al., 2004). These correspond to the smallest of observed swarms. The mechanisms though which swarms assemble into larger scale patterns are not known, but perhaps involve using the variability of the flow at different scales.

Why is social behavior a successful strategy?

Several hypotheses have been proposed to explain why social behavior has evolved in euphausiids. Benefits gained by aggregating include a higher probability of mating, improved foraging success, and reduced predation risk. Some of these ideas are supported by observational evidence. In the species *Nyctiphanes australis*, swarming is seasonal and linked to breeding (Blackburn, 1980; O'Brien, 1988), suggesting that organisms aggregate in order to find mates. In the Southern Ocean, schools of Antarctic krill are observed to disperse rapidly when approached by underwater vehicles (Hamner et al., 1983; O'Brien, 1987), which is thought to be a strategy for escaping predator attacks by confusing the predator. Ritz (2000) has speculated that the hydrodynamics in schools might optimize the capture rate of suspended prey. Modeling studies also suggest that collective motions can improve ability to forage in a noisy resource field (Grünbaum, 1998; Wood and Ackland, 2006).

There are also negative effects associated with the social behavior. An obvious cost is that available resources are shared with other group members. When in aggregations, krill are also more vulnerable to large predators that have evolved efficient strategies to detect and exploit groups (Nicol and O'Dor, 1985; Ritz, 1994): in the St-Laurent estuary, for example, mammals are attracted by aggregations of krill (Sourisseau et al.; de Lafontaine et al., 1991; Kingsley and Reeves, 1998) which might be induced by tidal currents (Cotté and Simard, 2005); krill densities are generally high and patchy in regions where whales are observed (Simard and Lavoie, 1999). In addition, dense aggregations favor the spread of infectious diseases which can lead to mass mortality in krill (Gómez-Gutiérrez et al., 2003).

These ideas can be put into mathematical form to quantify the costs and benefits of social behavior and relatedly to address the question of why it has evolved so strongly in krill. Numerical simulations provide powerful tools for studying spatial ecosystems involving multiple interacting species with their distribution constantly changing in time.

Overview of thesis

To investigate the mechanisms and consequences of zooplankton patchiness, I develop and use numerical models that include swimming behavior, population dynamics, and some aspects of environmental variability. First, I examine the density-dependence of reproductive success as a driver for the evolution of social behavior. The benefit associated with the proximity of mates trades off with the cost of intra-specific competition for resources. In **Chapter 1**, I formulate a model that accounts for these two effects. The stage-structured consumer-resource model includes a mating probability for the consumer, which is assumed to be a saturating function of the local density of mature conspecifics. In Chapters 2 and 3, I consider a spatial version of that ecosystem model to simulate the formation of social groups. The model is written as a set of reaction-advection-diffusion equations for the density of phytoplankton and krill. The advection term represents swimming behavior of the predator; a simple behavior rule produces aggregations. **Chapter 2** addresses the success of the grouping strategy under different environmental conditions. The spatial distribution of zooplankton influences their ability to eat and to reproduce; whether aggregation behavior is overall a successful strategy depends on the balance of the costs and benefits. **Chapter 3** focuses on the asymptotic dynamics of the patchy ecosystem in the absence of environmental variability. The steady-state density-distribution is solved numerically and compared to the solution obtained analytically from the weakly-nonlinear approximation to the model. In **Chapter 4**, I investigate the foraging success of a schooling population. To this end, I construct an individual-based model for krill coupled to a continuous-field physical-ecological model that simulates the variability, in time and space, of the resource. The next chapters examine other external mechanisms that induce spatial and temporal variability in marine ecosystems. In **Chapter 5**, I analyze the transient response of consumer-resource models to external perturbations. In **Chapter 6**, I describe the biogeochemical variability in the Southern Ocean induced by large-scale climatic patterns. The main findings of each chapter are summarized in **Chapter 7**.

Chapter 1

Predator-prey dynamics with density-dependent mating success

Abstract

An Allee effect arising from density-dependent mating success is incorporated into mathematical models of predator-prey interactions. When the predator's life cycle is formulated as a two-stage model and coupled to a logistically-growing resource, reproduction and recruitment can be expressed as a transfer of biomass from the prey to the predator. The mating probability modulates the rate at which offsprings are produced, thus effectively reducing the predation rate in the model. The implications of nonlinearity in the mating function for predator-prey dynamics are investigated. Examination of the fixed points and bifurcations in the model reveals that enhancing the Allee effect can destabilize a locally stable equilibrium, stabilize oscillating dynamics, or cause catastrophic extinction of the predator population. The stage-structured model is compared to a model with a continuous weight distribution; if the birth and growth rates are assumed to have a power-law dependence on weight, the continuous model reduces to a set of ordinary differential equations that behaves similarly to the discrete-stage predator-prey model with Allee effect.

1.1 Introduction: Allee effects

When individual fitness is positively correlated with the density of conspecifics, the population growth rate increases with population size. This correlation is referred to as the "Allee effect" (after ecologist W.C. Allee) and is often cited as a possible cause of animal extinctions. In sexually-reproducing species, Allee effects arise from density-dependence of the mating success, the probability of encounters between potential mates being proportional to the local number of individuals (Dennis, 1989; McCarthy, 1997; Courchamp et al., 1999). Behaviors that induce local density enhancement, such as the formation of social groups, might have evolved because of their positive impact on the per capita reproduction rate (Stephens and Sutherland, 1999).

Allee effects can be incorporated into single-species population models by simply multiplying the reproduction function by the probability of successful mating (Boukal and Berec, 2002). The density-dependence affects the population dynamics (e.g. Scheuring, 1999; Schreiber, 2003). Multi-species and spatial models with Allee effects also reveal significant implications for predatory interactions (Kent et al., 2003; Webb, 2003; Zhou et al., 2005) and biological invasions (e.g. Lewis and Kareiva, 1993; Taylor and Hastings, 2005).

Here I investigate the effects of density-dependent reproduction on the dynamics of predator-prey models. A classical formulation for predator-prey interaction is the Rosenzweig and MacArthur (1963) model,

$$\frac{dP}{dt} = rP\left(1-\frac{P}{K}\right) - G(P)Z \tag{1.1}$$

$$\frac{dZ}{dt} = \epsilon G(P)Z - dZ \tag{1.2}$$

where P is the prey population and Z the predator population. It can be employed to describe the dynamics of planktonic ecosystems, in which case the prey represents a primary producer (phytoplankton) and the predator is an herbivore (zooplankton).

The functional response, which reflects the saturation of predation rate when resources are abundant, is expressed as a Holling-Type II function, $G(P) = g\frac{P}{P+P_h}$, where g is the maximum predation rate and P_h is the half-saturation prey density; ϵ is the assimilation efficiency, and d is the mortality rate. The model assumes logistic growth for the prey, with r the maximum growth rate and K the carrying capacity. Dynamics of systems of the form (1.1-1.2) have been thoroughly investigated (e.g. May, 1972; Gilpin, 1972; Myerscough et al., 1996; Kot, 2001). The basic structure of the model has also been adapted to take into account spatial heterogeneity, higher-order trophic levels, etc. To include Allee effects in the predator population, Bazykin (1998; reproduced in Webb, 2003) and Zhou et al. (2005) multiply the predator growth term in (1.2) by the density-dependent probability of reproducing (see Section 1.4.3).

A different approach is adopted here for constructing predator-prey models with non-linear life cycle processes. In a structured population model, reproduction and growth can be viewed as processes generating biomass. This view is emphasized by associating developmental stages with individual weight, so that organisms changing stage experience changes in their weight. Both discrete and continuous formulations are considered for the population structure. The simplest model has two discrete stages, corresponding to juvenile and adult organisms, which are born and recruited in continuous time. Knowing how much mass is gained by the predator population in a given time interval, it is possible to infer how much resources must have been consumed to produce it; that information is then used to formulate an equation for the population dynamics of the prey. This contrasts with the more conventional approach, which decouples developmental activities and inter-specific interactions (see e.g. Gurney and Nisbet, 1998); it provides a new way of constructing multi-species ecological models.

The chapter begins with a description of the discrete-stage predator-prey model in Section 1.2. Stability of the model equilibria is examined in Section 1.3. In Section 1.4, an equivalent standard predator-prey model is derived by reformulating the structured model in terms of a single-stage predator population; differences with other published models that include the Allee effect only in the equation for the predator are highlighted. In Section 1.5, it is shown that consistent results are obtained when a continuous-weight model is used to describe the dynamics of the predator population. Results are briefly discussed in Section 1.6.

1.2 Stage-structured model

Consider a stage-structured population for the predator, with a life cycle consisting of juvenile and adult stages. The life cycle is represented schematically in Figure 1-1: birth of new individuals supplies the juvenile stage, during which organisms develop; if they survive, they are recruited into the adult stage, where they reproduce and eventually die. Reproduction and maturation are assumed to be food-dependent processes, so that birth and recruitment rates are limited by the availability of resources. The birth rate can also be a function of adult density; the mortality rate is assumed to be constant.

Mathematically, this is expressed as

$$\frac{dN_j}{dt} = B(P, N_a)N_a - Q(P)N_j - d_jN_j \tag{1.3}$$

$$\frac{dN_a}{dt} = Q(P)N_j - d_aN_a \tag{1.4}$$

where N is the number of individuals, with subscripts j and a referring to the juvenile and adult stages, respectively; P is the prey density, B is the birth rate, Q the recruitment rate, and d the mortality rate.

When thinking about resource consumption, it is useful to convert the number of individuals into predator biomass. If individuals in the juvenile and adult stages have an average weight of w_j and w_a, respectively, with the total biomass given by $Z = wN$, we write

$$\frac{dZ_j}{dt} = \frac{w_j}{w_a}B(P,Z_a)Z_a - Q(P)Z_j - d_jZ_j \tag{1.5}$$

$$\frac{dZ_a}{dt} = \frac{w_a}{w_j}Q(P)Z_j - d_aZ_a \tag{1.6}$$

From the equations above it is evident that the increase of adult biomass through recruitment exceeds the amount of biomass removed from the juvenile stage, the ratio w_a/w_j being greater than 1: in the discrete-stage formulation, recruitment implies a sudden weight gain. Similarly, newborn individuals acquire a finite mass. Assuming that this new biomass is taken out of the prey population, as illustrated in Figure 1-1, and that the transfer has efficiency ϵ, the equation for the resource is

$$\frac{dP}{dt} = rP\left(1-\frac{P}{K}\right) - \frac{1}{\epsilon}\left[\frac{w_j}{w_a}B(P,Z_a)Z_a + \left(\frac{w_a}{w_j}-1\right)Q(P)Z_j\right] \tag{1.7}$$

where r is the maximum growth rate and K is the carrying capacity.

1.2.1 Density-dependent reproduction

To account for intraspecific density-dependence, the effect of adult population size is included in the birth function. The maximum birth rate is multiplied by the probability of mating, Π, which we write as a rectangular hyperbolic function (Boukal and Berec, 2002):

$$\Pi(Z_a) = \frac{Z_a}{Z_a + c} \tag{1.8}$$

where c, referred to as the “Allee effect constant”, is the density at which the probability of mating is $1/2$. The magnitude of this parameter is a measure of the intensity of the Allee effect.

The mating success function (1.8) can be inferred from the probability for a female to encounter at least one mate during the reproductive period, assuming that the area searched

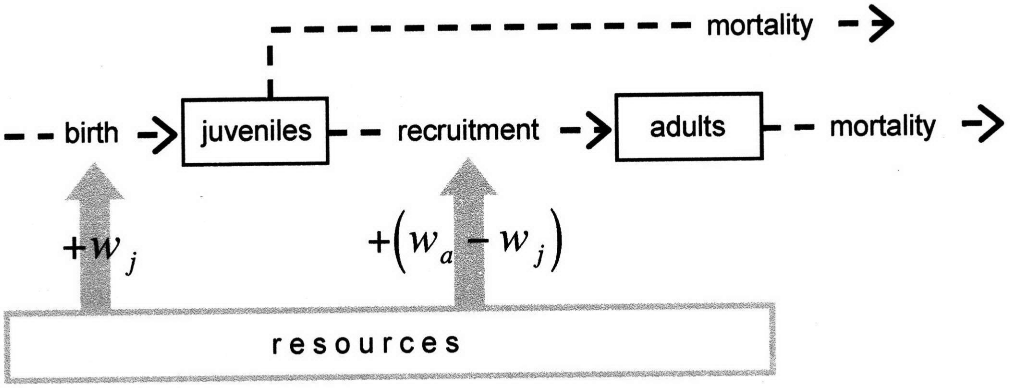

Figure 1-1: Life cycle of the 2-stage predator population. Juveniles and adults have an average weight of w_j and w_a, respectively. Generation of new biomass through birth and recruitment is taken out of the resource.

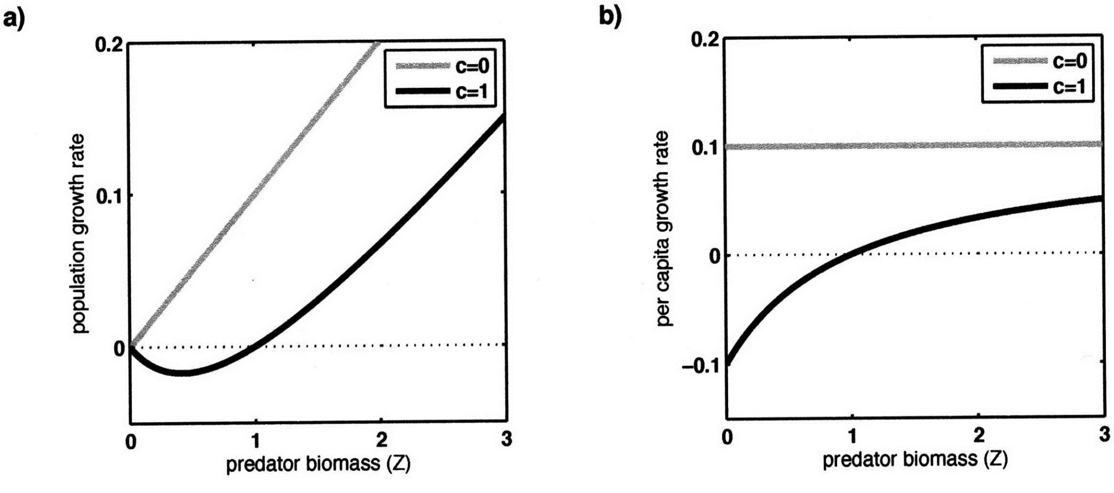

Figure 1-2: Growth rate versus population size in a single-stage population with density-dependent mating success ($c > 0$, black curves) or constant mating success ($c = 0$, gray curves) and linear mortality. a) population growth rate, b) per capita growth rate. Negative feedbacks that would slow down growth at high density are not taken into account.

by females, A, is an exponentially distributed random variable (Dennis, 1989). Following Dennis (1989), we write the probability of encountering no mates as $e^{-m\rho A Z_a}$, where ρ is the ratio of males to females and m is a constant with units of m·kg^{-1}.

Define $S \equiv m\rho A$, with probability density function $f(S)$. Assuming that a single encounter is sufficient for the full reproductive potential to be realized and that ρ is constant, the probability of successful mating is obtained by integrating the probability of meeting at least one mate over all possible values of S:

$$1 - \int_0^\infty e^{-SZ_a} f(S) \mathrm{d}S \tag{1.9}$$

The integral in (1.9) is the Laplace transform of $f(S)$; it corresponds to the probability of not mating. If the probability density function of S is an exponential distribution,

$$f(S) = \frac{1}{<S>} e^{-S/<S>} \tag{1.10}$$

where $<S>$ is the mean value for the effective search area. Substituting (1.10) into (1.9) yields the function (1.8), with $c = <S>^{-1}$.

An alternative derivation of (1.8) can be obtained by considering "a 1 : 1 sex ratio and a monogamous mating system in which females compete for males" (Boukal and Berec, 2002); in that case the constant is inversely proportional to A, which is assumed to be the same for all individuals (McCarthy, 1997). The density-dependent effect on per capita and population growth rates is illustrated in Figure 1-2.

1.2.2 Full model and adimensionalization

For the dependence of the birth and recruitment rates on resource availability, a Holling Type II functional form is assumed. While this function is formally derived from considerations of prey handling time and predator attack rate, it is used here in a looser interpretation to describe variations in biomass production rate, from linear increase at low prey density to saturation at high prey density. Using the mating probability described above, we write

$$B = b\frac{P}{P+P_h}\frac{Z_a}{Z_a+c}$$

and

$$Q = q\frac{P}{P+P_h}$$

where b and q are maximum rates, and P_h is the half-saturation prey density. It is implied that the maximum recruitment rate, q, is a function of the ratio of weights w_a/w_j: the larger the ratio, the more time must be spent in the juvenile stage in order to gain enough weight to become an adult.

The ecosystem dynamics are given by the following three coupled differential equations:

$$\frac{dZ_j}{dt} = \frac{w_j}{w_a}b\frac{P}{P+P_h}Z_a\Pi - q\frac{P}{P+P_h}Z_j - d_jZ_j \tag{1.11}$$

$$\frac{dZ_a}{dt} = \frac{w_a}{w_j}q\frac{P}{P+P_h}Z_j - d_aZ_a \tag{1.12}$$

$$\frac{dP}{dt} = rP\left(1-\frac{P}{K}\right) - \frac{1}{\epsilon}\left[\frac{w_j}{w_a}b\frac{P}{P+P_h}Z_a\Pi + \left(\frac{w_a}{w_j}-1\right)q\frac{P}{P+P_h}Z_j\right] \tag{1.13}$$

The structured predator-prey model is similar in some ways to the one proposed by Wang and Chen (1997) when there are no time delays (equation 3.1 in their paper). These authors also consider a two-stage structure for the predator, and assume that resource depletion is proportional to the rate at which juveniles are generated. Their model, however, does not include an Allee effect, not does it take into account uptake of resources by the juvenile class (included here in the recruitment term).

In (1.11-1.13), the Allee effect term appears in the equation for the prey; the number of new juveniles depends on the mating success, hence so does the amount of resources required to produce this new biomass. Previous models have included the density-dependence only in the predator equation (Bazykin, 1998; Zhou et al., 2005); these are discussed in Section 1.4.3. Omitting the mating probability (Π) in the prey equation (1.13), however, implies that there is an unidentified sink for resources, a fraction of which leave the ecosystem without going through the predator population. This is different from the fraction $1-\epsilon$ of resources that are ingested but not converted to juvenile biomass (these resources leave the ecosystem as a result of predator respiration or excretion).

The system can be adimensionalized to facilitate the analysis. Prey biomass is scaled by P_h, juvenile and adult predator biomass are respectively scaled by $\epsilon r P_h/q$ and $\epsilon r P_h w_a/b w_j$; time is scaled by r^{-1}. Lower-case letters indicate scaled variables. Dimensionless parameters are introduced:

$$\eta \equiv w_a/w_j \quad \beta \equiv b/r \quad \theta \equiv q/r \quad \delta \equiv d/r \quad \chi \equiv K/P_h$$

as well as λ, which is simply the Allee effect constant c redefined. After substituting the expression for Π, the non-dimensional system of equations is

$$\frac{dz_j}{d\tau} = \theta\frac{p}{p+1}\left[\frac{z_a^2}{z_a+\lambda} - z_j\right] - \delta_j z_j \tag{1.14}$$

$$\frac{dz_a}{d\tau} = \beta\frac{p}{p+1}z_j - \delta_a z_a \tag{1.15}$$

$$\frac{dp}{d\tau} = p\left(1-\frac{p}{\chi}\right) - \frac{p}{p+1}\left[\frac{z_a^2}{z_a+\lambda} + (\eta-1)\,z_j\right] \tag{1.16}$$

The dynamics of this system are analyzed next. Stability of the fixed points will be examined in parameter space, focusing on the Allee effect parameter, λ, the birth and recruitment parameters, β and θ, and what we refer to as the "enrichment parameter", χ.

1.3 Asymptotic dynamics

The 3-compartment model has three fixed points: trivial extinction ($p^* = z_j^* = z_a^* = 0$), extinction of the predator ($p^* = \chi$, $z_j^* = z_a^* = 0$), and coexistence. The first is always

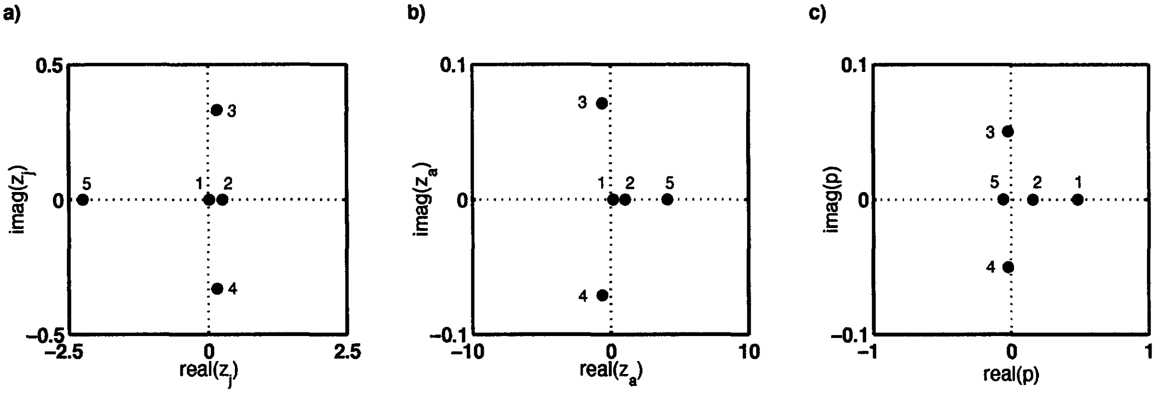

Figure 1-3: Solutions to the equation for the coexistence equilibrium, in the complex plane; a) juvenile predator density, b) adult predator density, c) prey density. Solutions labeled 1 and 2 are real and positive; 3 and 4 are complex conjugates; 5 has both positive and negative real parts. Parameters are $\beta = 3$, $\theta = 1$, $\delta_j = 0.15$, $\delta_a = 0.1$, $\chi = 0.5$, $\eta = 2$, $\lambda = 1$.

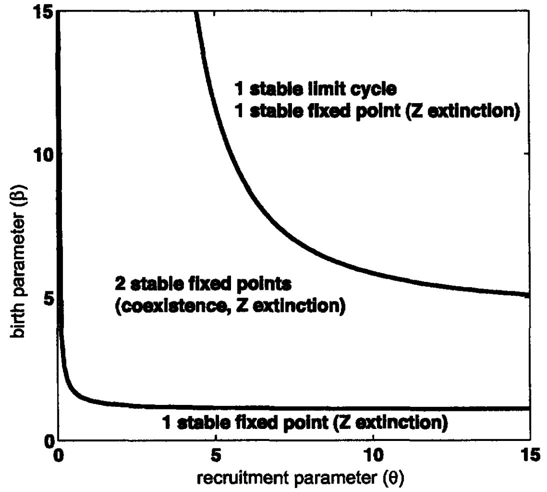

Figure 1-4: Regions of stability in the stage-structured predator-prey model, in function of the birth parameter (β) and the recruitment parameter (θ). Other parameters as in Figure 1-3. Thick lines indicate bifurcations.

unstable, while the second is always stable for $\lambda > 0$, a well-known consequence of the Allee effect.

The coexistence equilibria and their stability are examined numerically; details of the calculations are presented in Appendix 1.7.1. Equilibrium values are shown in Figure 1-3 for specific values of the model parameters. The system has five coexistence equilibria; at most two are real and positive, one is strictly negative, and the others come in pairs of complex conjugate. Solutions that are negative or imaginary are not biologically possible and will not be considered further. Stability depends on the parameters. We find that of the two possible coexistence equilibria, only the one corresponding to higher predator biomass can be stable; thus there can be a single coexistence attractor. Transitions from stability to instability are examined next.

1.3.1 Stability boundaries

The region of stable coexistence is shown in Figure 1-4, when all parameters are fixed but β and θ. There are minimum values of the birth parameter and the recruitment parameter below which coexistence is not possible, and above which it is asymptotically stable. As these parameters are increased, the coexistence fixed point loses its stability and a stable limit cycle is created instead, thus allowing for oscillatory asymptotic dynamics.

Because of the structure in the predator population, stability of the coexistence equilibrium is not highly sensitive to variations in β or θ when they are not varied simultaneously. Multiple stable equilibria (Figure 1-4) are a consequence of the Allee effect; for some parameter values, initial conditions determine whether the system will reach asymptotic coexistence or extinction of the predator.

The various dynamical regimes are illustrated in Figure 1-5; asymptotic solutions are shown together with example of trajectories in phase space. For small values of β and θ, the extinction equilibrium is globally stable; there are no real and positive coexistence equilibria. All initial conditions lead to extinction of the predator, while the prey density settles at the carrying capacity (Figure 1-5a). When the parameters are increased, two equilib-

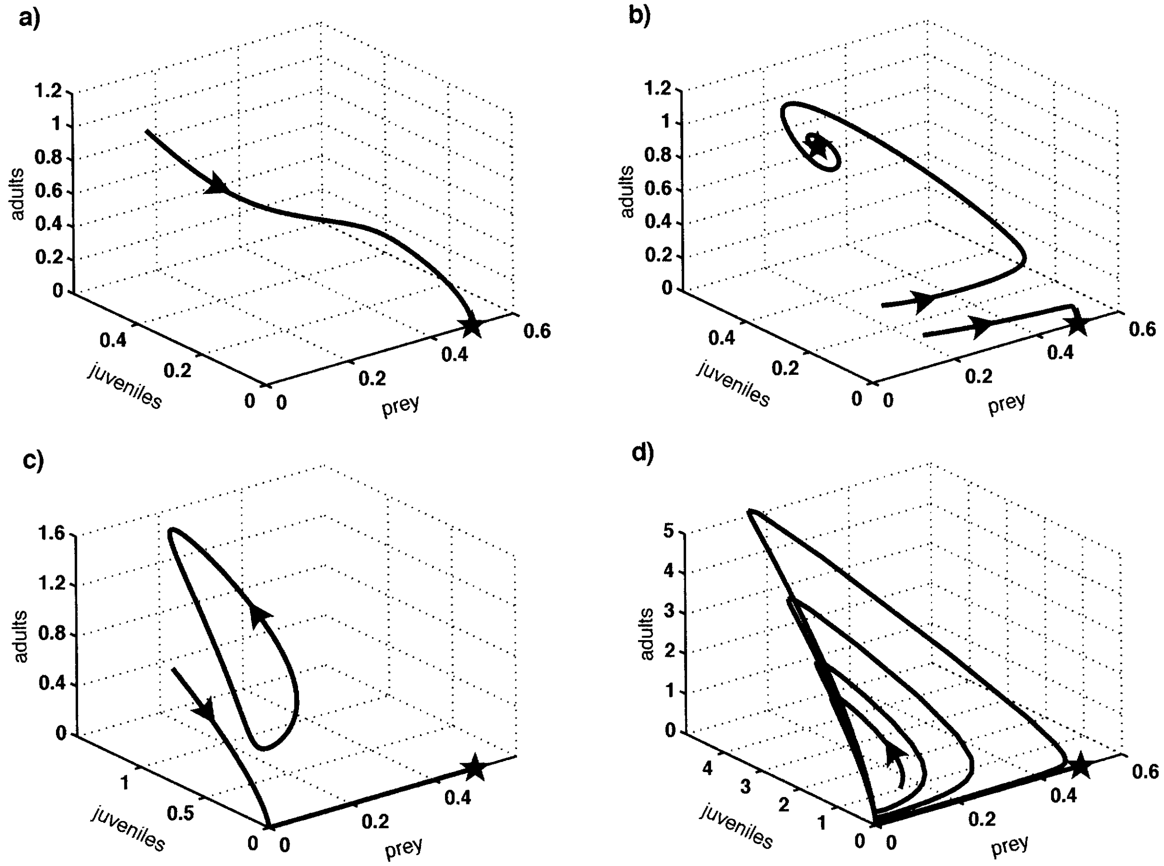

Figure 1-5: Phase portraits illustrating the dynamical regimes in the stage-structured predator-prey model; star symbol indicates steady state. a) $\beta = \theta = 1$, all initial conditions lead to extinction of the predator (there is no possible coexistence equilibrium). b) $\beta = \theta = 2.5$, the system reaches one of two possible equilibria, stable coexistence or extinction of the predator. c) $\beta = \theta = 10$, the system either exhibits a limit cycle, or extinction of the predator occurs. d) $\beta = \theta = 30$, all initial conditions lead to extinction of the predator after transient oscillations (both coexistence equilibria are unstable). Other parameters as in Figure 1-3.

ria appear as the result of a saddle-node bifurcation; one of them, the one associated with the highest predator biomass, is stable. Figure 1-5b shows two steady-states, one corresponding to stable coexistence and the other to extinction of the predator. The coexistence attractor becomes unstable when the values of β and θ are large. The transition from stability to instability occurs via a supercritical Hopf bifurcation; oscillatory dynamics appear as the system is attracted to a stable limit cycle, shown in Figure 1-5c. When the parameters are further increased, the stable oscillator disappears and the extinction equilibrium becomes globally stable again. This results from a homoclinic bifurcation: the limit cycle merges with the low-density coexistence equilibrium and vanishes; all initial conditions then lead to extinction of the prey, as illustrated in Figure 1-5d. For most initial conditions, large transient oscillations are seen before the extinction equilibrium is reached. Unlike in the slow birth and recruitment scenario (Figure 1-5a), the system has two coexistence equilibria, but they are not stable.

1.3.2 Imposing structure in the population

Can the structured model be simplified by assuming that the proportion of adults and juveniles in the population is constant? In (1.14-1.16), the ratio of juvenile to adult biomass, $R \equiv z_j/z_a$, evolves according to

$$\begin{aligned} \frac{\partial R}{\partial \tau} &= \frac{1}{z_a}\frac{\partial z_j}{\partial \tau} + \frac{z_j}{z_a^2}\frac{\partial z_a}{\partial \tau} \\ &= -\beta\frac{p}{p+1}R^2\theta\frac{p}{p+1}\left(\frac{z_a}{z_a+\lambda} - R\right) + (\delta_a - \delta_j)R \qquad (1.17) \end{aligned}$$

In steady-state, the ratio is

$$R^* = -\frac{\theta}{2\beta} - (\delta_j - \delta_a)\frac{p+1}{2\beta p} \pm \sqrt{\left(\frac{\theta}{2\beta} + (\delta_j - \delta_a)\frac{p+1}{2\beta p}\right)^2 + \frac{\theta}{\beta}\left(\frac{z_a}{z_a+\lambda}\right)} \qquad (1.18)$$

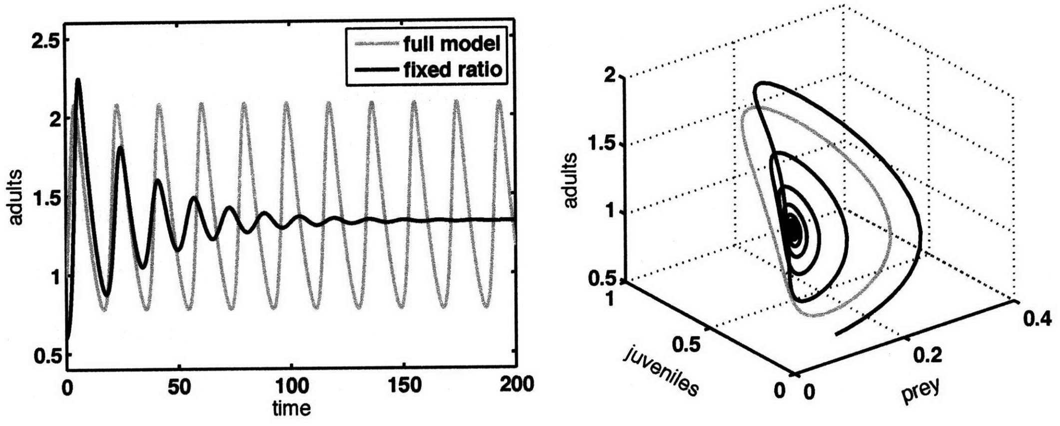

Figure 1-6: Left: time series of adult biomass. Sustained oscillations in the 3-compartment model (gray curve) disappear when the population structure is assumed to be fixed (black curve, from equations 1.19-1.20). Parameters are $\beta = 10$, $\theta = 2$, $\eta = 2$, $\chi = 0.8$, $\delta_j = 0.3$, $\delta_a = \lambda = 1$. Right: the corresponding trajectories in phase plane, showing a limit cycle and an attractor.

By substituting this in equations (1.15-1.16), we can derive an equivalent standard predator-prey model, in which the population structure is fixed:

$$\frac{dz_a}{d\tau} = \beta\theta \frac{p}{p+1} R^* z_a - \delta_a z_a \tag{1.19}$$

$$\frac{dp}{d\tau} = p\left(1 - \frac{p}{\chi}\right) - \frac{p}{p+1}\left[\frac{z_a^2}{z_a + \lambda} + (\eta - 1) R^* z_a\right] \tag{1.20}$$

The coexistence equilibria are the same as in the full, structured model; however the stability properties are different, as shown in Figure 1-6. Parameters that lead to stable oscillatory behavior in the structure model lead to a stable equilibrium in the constant ratio version (1.19-1.20). This indicates that imposing structure in the population affects the predator-prey dynamics. A different approach for formulating a two-dimensional model is examined in the next section.

1.4 One-stage limit

Most predator-prey models do not distinguish between the different stages of predator development (but see e.g. Persson et al., 1998; de Roos et al., 2003), and to investigate the dynamical consequences of the Allee effect it is useful to formulate an unstructured version of the model which can be directly compared to popular models of interacting species. In this section, the population structure is "deconstructed" by projecting the predator equations onto a single-stage population model.

Let's assume that juvenile and adult organisms differ only by their body mass, ignoring all other characteristics such as the ability to reproduce or to capture prey. The maturation process then implies nothing else than a weight gain, and the rate of recruitment is inversely proportional to the weight difference between stages. By assuming that juveniles and adults have the same weight, we then effectively remove all information on the population structure. To investigate this, it is convenient to return to the dimensional equations (1.11-1.13).

In the limit $w_a/w_j = 1$, recruitment occurs very rapidly, so that $q \to \infty$. This leads to $q\frac{P}{P+P_h} \gg d$, so that the last term in (1.11) can be neglected. Then, in steady-state,

$$Z_j = \frac{b}{q}\frac{Z_a^2}{Z_a + c} \tag{1.21}$$

Substituting in (1.12) and (1.13) yields

$$\begin{aligned} \frac{dP}{dt} &= rP\left(1 - \frac{P}{K}\right) - \frac{b}{\epsilon}\frac{P}{P + P_h}\frac{Z_a^2}{Z_a + c} && (1.22) \\ \frac{dZ_a}{dt} &= b\frac{P}{P + P_h}\frac{Z_a^2}{Z_a + c} - dZ_a && (1.23) \end{aligned}$$

This system of equations is analogous to (1.1-1.2), with the function $G(P)$ replaced by

$$G(P, Z_a) = \frac{b}{\epsilon}\frac{P}{P + P_h}\frac{Z_a}{Z_a + c} \tag{1.24}$$

Table 1.1: Equilibrium densities in the 2-stage model and the equivalent standard (unstructured) model. Parameters: $w_j = w_a = 1$, $\epsilon = 0.5$, $b = 2$, $d = 0.1$, $r = 1$, $K = 1.5$, $P_h = 3$, $c = 1$. The coexistence equilibrium is stable for all values of q.

	structured model			standard pred/prey model
	$q = 2$	$q = 20$	$q = 200$	
P^*	0.88	0.58	0.54	0.53
Z_j^*	0.75	0.12	0.01	-
Z_a^*	1.71	1.93	1.96	1.96

that is, the predation function is multiplied by the probability of mating. Note that the probability function appears in the equation for the prey as well as in the equation for the predator. In this case $G(P, Z_a)$ is interpreted as production of biomass through reproduction (adults are giving birth to new adults), and the newly generated biomass is taken out of the resource.

Numerical simulations confirm the agreement between the stage-structured model (1.11-1.13) with $w_a = w_j$, and the equivalent standard predator-prey model (1.22-1.23), when the recruitment rate is large (Table 1.1). The equilibrium predator biomass (juvenile + adults) is underestimated in the unstructured model.

The system (1.22-1.23) is asimensionalized as in Section 5.4.1.2. Dropping the subscripts, we get

$$\frac{dp}{d\tau} = p\left(1 - \frac{p}{\chi}\right) - \frac{p}{p+1}\frac{z^2}{z+\lambda} \tag{1.25}$$

$$\frac{dz}{d\tau} = \beta\frac{p}{p+1}\frac{z^2}{z+\lambda} - \delta z \tag{1.26}$$

I will refer to this system of equations as the "modified Rosenzweig-MacArthur model"; the standard version of the model is retrieved when $\lambda = 0$, i.e. when density-dependence of the mating success is suppressed.

In addition to the trivial equilibrium and predator extinction equilibrium, the system

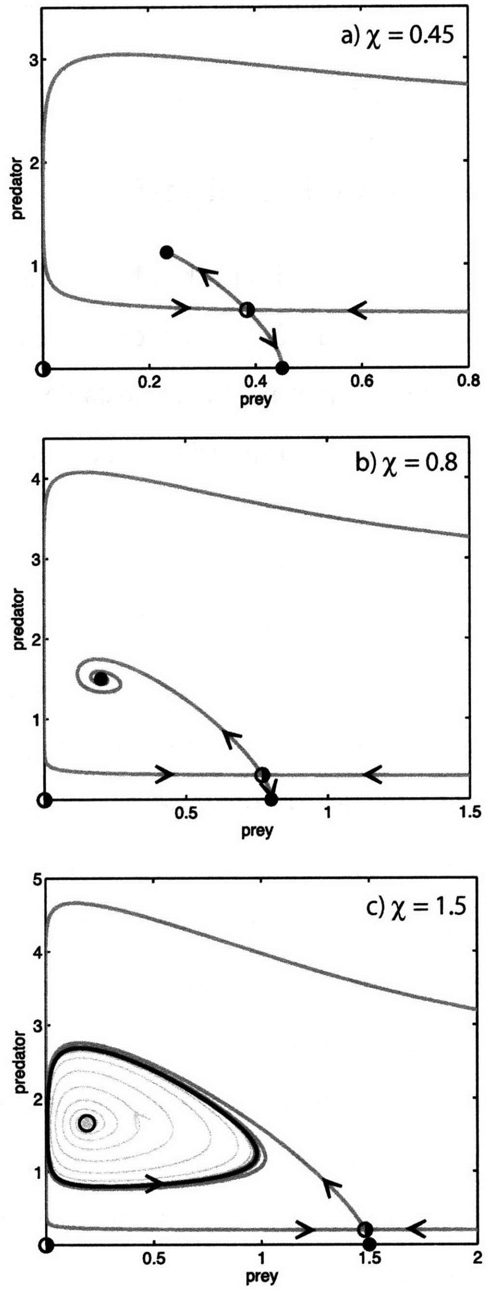

Figure 1-7: Basin of attraction for the coexistence equilibrium, for different values of the enrichment parameter; from top to bottom: $\chi = 0.45$, $\chi = 0.8$, $\chi = 1.5$. Thick lines show the saddle's manifolds; black dots indicate attractors; half-filled circles, saddle points; an empty circle, a repellor. Thin line in bottom plot shows a trajectory with initial condition near the unstable equilibrium, being attracted to the limit cycle. All initial conditions within the area delimited by the stable manifold lead to coexistence. Other parameters are $\beta = \lambda = 1$, $\delta = 0.1$.

allows three coexistence equilibria; calculation of the fixed points and their stability is in Appendix 1.7.2.

1.4.1 Bifurcations and multiple equilibria

Although the number of coexistence equilibria has been reduced from five to three, the dynamics of the predator-prey system (1.25-1.26) are qualitatively the same as for the stage-structured model. The trivial equilibrium is always unstable; extinction of the predator is always stable. Of the three coexistence equilibria, at most two are real and positive, and of those two, only the corresponding to high predator density can be stable (and if it is not stable, a stable limit cycle may exist). The low-density equilibrium is a saddle-point: it attracts trajectories along its stable manifold, and repels them along the unstable manifold.

When there are multiple possible asymptotic behaviors, the initial conditions determine the outcome of the predator-prey interactions. In the 1-stage model, the saddle-point's stable manifold delimitates the basins of attraction for coexistence and extinction. The stable manifold, drawn by integrating the model backwards in time with initial conditions close to the saddle point, is shown in Figure 1-7 for various values of χ. The enrichment parameter affects the value of the fixed points, as well as the stability of the high-density coexistence equilibrium. Although increasing χ leads to destabilization of the coexistence attractor (the so-called paradox of enrichment), it also enlarges the basin of attraction of the coexistence asymptotic state. By reducing the region of phase space in which trajectories are attracted to the extinction fixed point, enrichment thus contributes to sustaining predator populations that are subject to an Allee effect.

The bifurcations resulting from varying the parameter χ in the model with Allee effect are shown in Figure 1-8, bottom panel. It is compared with the bifurcation diagram of the equivalent Rosenzweig-MacArthur model obtained by setting $\lambda = 0$, shown in the top panel. Coexistence is the only possible asymptotic behavior for most values of the enrichment parameter in the model without Allee effect. For large values of χ, there is a stable limit cycle; the amplitude of the cycle decreases with the parameter, until it collapses to a

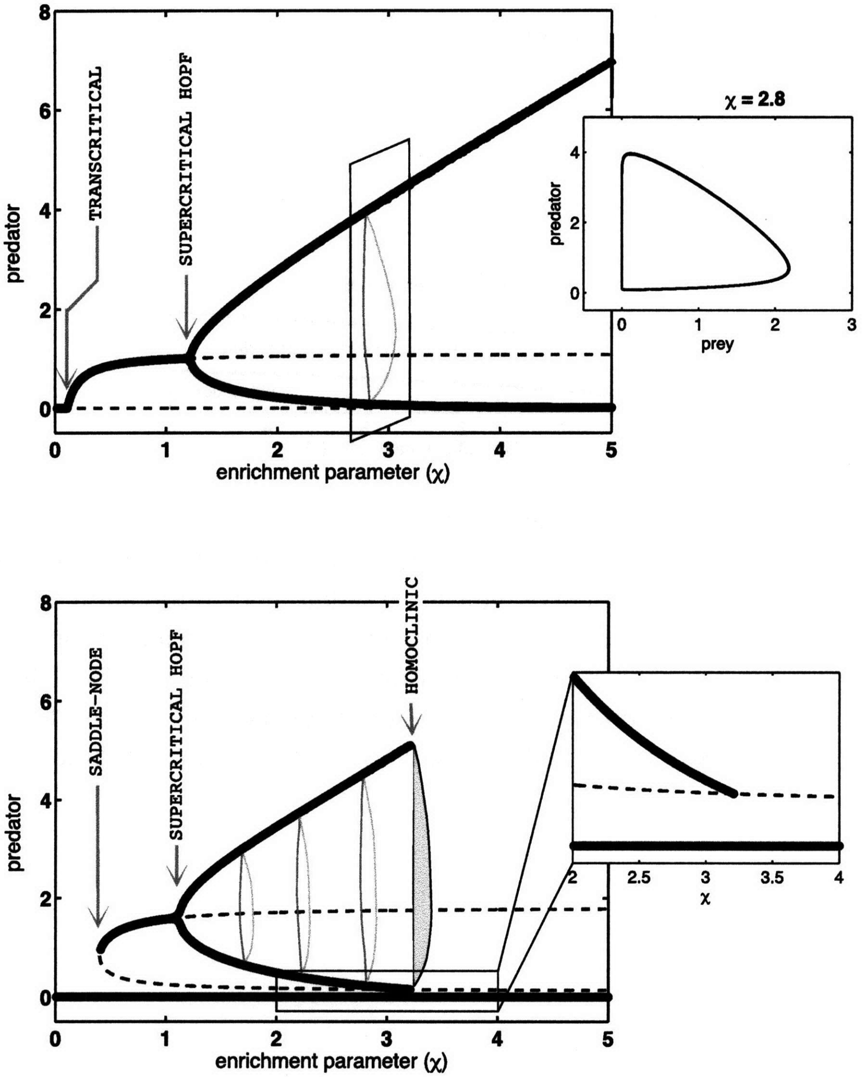

Figure 1-8: Bifurcations in predator-prey models with and without Allee effect; the enrichment parameter is varied. Dashed lines indicate unstable equilibria; solid lines are obtained from numerical integration of the model. Top: $\lambda = 0$; the extinction equilibrium loses its stability as the coexistence equilibrium becomes stable, via a transcritical bifurcation. A limit cycle appears for sufficiently large values of χ as a result of a supercritical Hopf bifurcation; the oscillatory dynamics are represented in the Figure as two thick black lines, showing the minimum and maximum values of the predator population in the simulation, after transients have died out. A cross-section of the diagram shows the limit cycle (inset). Bottom: $\lambda = 1$; two coexistence equilibria appear through a saddle-node bifurcation. A limit cycle results from a supercritical Hopf bifurcation, but disappears for large values of χ. Inset shows in more details the collision of the limit cycle with the low-density coexistence equilibrium in a homoclinic bifurcation.

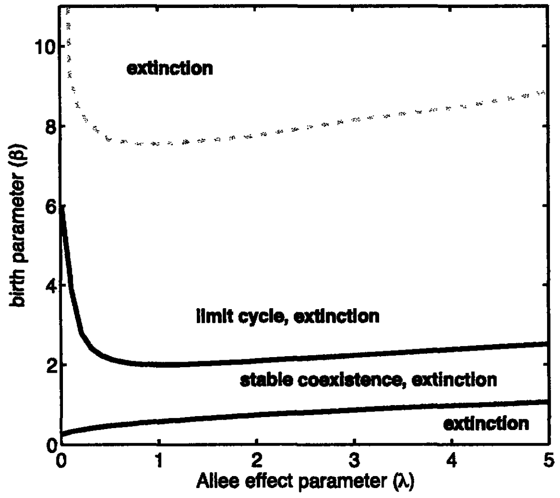

Figure 1-9: Dynamical regimes of the model for different values of the Allee effect parameter (λ) and the birth parameter (β). Solid black lines bound the region of stability of the coexistence equilibrium. Lower curve indicates a saddle-node bifurcation; below it, extinction of the predator is the only attractor. Higher black curve indicates a super-critical Hopf bifurcation; above it, the coexistence equilibrium exists but is unstable. The dashed gray line represents a homoclinic bifurcation, and delimitates the region of existence of a stable limit cycle; the curve is drawn based on results from numerical experiments. Parameters are $\chi = 0.8$, $\delta = 0.1$.

stable equilibrium in a supercritical Hopf bifurcation. As χ decreases more, the equilibrium predator density decreases until it meets the extinction equilibrium, to which it loses its stability in a transcritical bifurcation.

In the model with Allee effect, the transcritical bifurcation is replaced by a saddle-node bifurcation, and the coexistence attractor disappears suddenly when χ decreases, leading to catastrophic extinction of the predator population. A homoclinic bifurcation occurs for larger values of χ, when the stable limit cycle collides with the saddle point and disappears; the oscillating predator-prey system then experiences sudden extinction of the predator.

1.4.2 Destabilization due to Allee effect

The bifurcations discussed above are shown in a two-dimensional parameter space (Figure 1-9). The position of the saddle-node and Hopf bifurcations is found analytically: because they are associated with loss of stability of the coexistence equilibrium, they take place when the leading eigenvalue of that equilibrium's jacobian goes through zero. The homoclinic bifurcation is found numerically.

As evidenced in Figure 1-9, adding an Allee effect can have a significant impact on the stability of the ecosystem, compared to the standard case without density-dependent reproduction. For very small values of the parameter β, the stable coexistence equilibrium, which is stable when $\lambda = 0$, disappears when an Allee effect is introduced, leading the predator population to extinction. Similarly, increasing the value of λ from 0 can destabilize a limit cycle, for large values of β, with the same catastrophic result for the predator. For intermediate values of β, Allee effects can destabilize the stable coexistence and induce oscillatory dynamics. This is in agreement with previous study arguing that Allee effects are destabilizing for predator-prey interactions (Zhou et al., 2005). On the other hand, in a system with weak density-dependence ($\lambda < 1$), increasing the Allee effect parameter can actually stabilize the coexistence equilibria, or even allow survival of a predator population otherwise doomed to be extinct.

1.4.3 On the Allee effect term in the prey equation

The dynamics of our single-stage model are qualitatively similar to the dynamics of the models of Bazykin (1998) and Zhou et al. (2005). These authors also formulate predator-prey models with Allee effect for the predator, but do not include the Allee effect term in the prey equation. To compare the two formulations, let's write

$$\frac{dp}{d\tau} = p\left(1-\frac{p}{\chi}\right) - \frac{p}{p+1}z\mathcal{F} \tag{1.27}$$

$$\frac{dz}{d\tau} = \beta\frac{p}{p+1}\frac{z^2}{z+\lambda} - \delta z \tag{1.28}$$

with

$$\mathcal{F} = \frac{z}{z+\lambda} \qquad \text{model A} \tag{1.29}$$

$$\mathcal{F} = 1 \qquad \text{model B} \tag{1.30}$$

Model A is the modified Rosenzweig-MacArthur model (1.25-1.26). Model B has two coexistence fixed points (see Appendix 1.7.B). Although model A has one more fixed point, that equilibrium is always negative; thus there are no major differences in qualitative behavior between the two models, i.e. they exhibit the same bifurcations in parameter space. However, there are significant quantitative differences; bifurcations occur for different values of the model parameters (Figure 1-10), and the equilibrium values of predator and prey biomass differ (Figure 1-11).

From Figure 1-10, it is clear that including the Allee effect in the prey equation affects the asymptotic behavior of the model. For example, with $\lambda = 5$, $\gamma = 2$, this version of the model supports a stable limit cycle, but when the Allee effect term is omitted in the prey equation, extinction of the predator is the only possible steady-state. Also, the extinction boundary (saddle-node bifurcation) is less sensitive to the Allee effect parameter in model A; compared to model B, larger variations in λ are required for catastrophic extinction of the predator.

The equilibrium zooplankton biomass can be significantly higher in our model, as shown in Figure 1-11. Another interesting difference is that increasing λ always results in a decrease in predator biomass in model B, whereas it can have the opposite effect in model A. Although it is counter-intuitive that the biomass increases when reproduction rate is reduced, a similar effect arises in the standard predator-prey model (1.1-1.2) when the predation rate is increased: slowing down predation allows for higher prey density at equilibrium which, depending on parameter values, may enhance the per capita growth rate of the predator population. This is unlike reducing the assimilation efficiency, which always causes the equilibrium predator population to decrease (see Appendix 1.7.3).

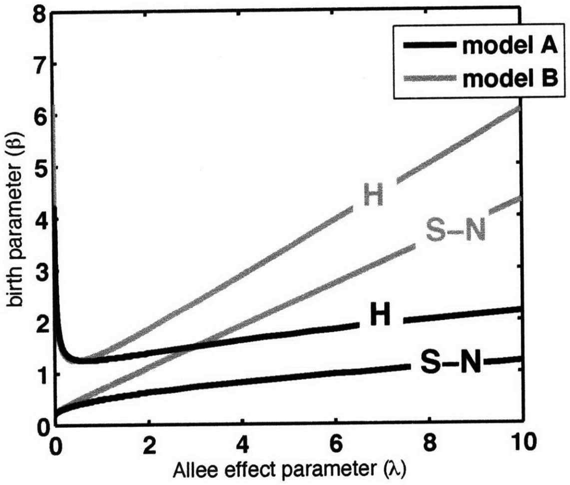

Figure 1-10: Regions of stability for the coexistence equilibrium. Black: this model. Gray: Allee effect term is not in the prey equation. Lower curve is saddle-node bifurcation (S-N); higher curve is supercritical Hopf bifurcation (H). Stable coexistence of the prey and predator is possible between the two curves. Parameters are $\chi = 1$, $\delta = 0.1$.

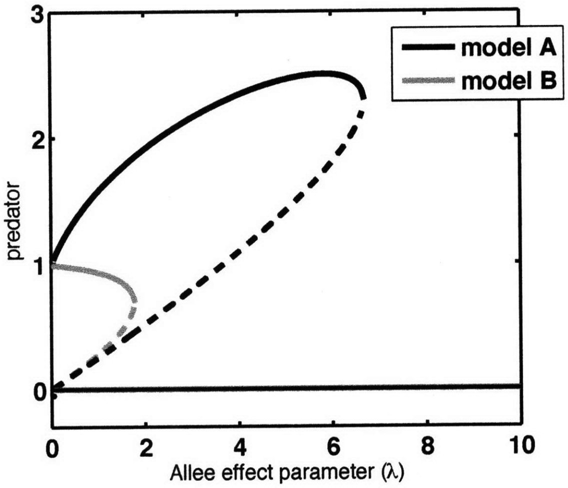

Figure 1-11: Equilibrium predator density; stable (solid lines) and unstable (dashed) equilibria. Limit cycles are not shown. Black: this model. Gray: Allee effect term is not in the prey equation. Predator extinction is always stable in both models. Parameters: $\beta = \lambda = \chi = 1$, $\delta = 0.1$.

In model B, the derivative $\partial Z^*/\partial\lambda$, calculated in Appendix 1.7.3, is strictly negative; thus increasing the strength of the Allee effect is qualitatively equivalent to reducing the assimilation efficiency. In contrast, because it appears in both equations in model A, the Allee effect term effectively decreases the predation rate. The derivative $\partial Z^*/\partial\lambda$ is positive for small values of λ, and can change sign when the Allee effect parameter is increased; this is analogous to the effect of varying the predation parameter β in the model without Allee effect, as discussed in Appendix 1.7.3.

Thus we can think of an effective predation rate, inversely proportional to the Allee effect parameter,

$$\beta_{\text{eff}} = \beta\frac{z}{z+\lambda}$$

and the sensitivity of the predator equilibrium biomass to λ is qualitatively similar to the sensitivity to β_{eff}. When the effective predation rate is low (strong density-dependence in mating success), the population size increases with β_{eff}; however because enhanced predation causes a decline in the standing prey density, the equilibrium predation population decreases when β_{eff} increases when the the effective predation rate is large. This is illustrated in Figure 1-11.

1.5 A continuous-weight model with power laws for birth and growth

In the single-stage projection of the predator-prey model, an Allee effect arising from nonlinear mating success translates into density-dependent predation, with important consequences for the dynamics of the two interacting populations. In deconstructing the population structure, however, we have lost all information on the uptake of resources by growing organisms. A different approach consists of formulating a model for the integrated biomass in a population with a continuous distribution in weight space; this is examined here. For specific forms of the growth and reproduction function, the continuous-weight model reduces exactly to a standard form of predator-prey model, analogous to the one obtained in the previous section.

The McKendrick-von Foerster equation is adapted to describe the dynamics of a weight-structured population. With $n = n(w,t)$ the number density per unit weight, we have

$$\frac{\partial n}{\partial t} + \frac{\partial}{\partial w} G(w,P)\, n = -dn \tag{1.31}$$

with boundary condition

$$G(w_B, P)\, n(w_B, t) = \int B(w,P)\, \Pi\, n(w,t)\, \mathrm{d}w \tag{1.32}$$

representing the birth process; w_B is the weight at birth; G is the growth rate, d the mortality rate, B the birth function, and Π the mating probability.

Growth and birth are separated into a weight-dependent part and a resource-dependent part. We assume that limitation by the availability of resources can be expressed as a Holling type II function;

$$\begin{aligned} G(w,P) &= g(w)\frac{P}{P+P_h} && (1.33)\\ B(w,P) &= b(w)\frac{P}{P+P_h} && (1.34) \end{aligned}$$

The mating probability can be written as a rectangular hyperbolic function of an arbitrary moment of N. For simplicity, we assume that is is related to the α_2 moment

$$\Pi = \frac{N_{\alpha_2}}{N_{\alpha_2} + c} \tag{1.35}$$

For the weight-dependence, we assume power laws. Let

$$\begin{aligned} g(w) &= g_0\, w^{\alpha_1} && (1.36)\\ b(w) &= b_0\, w^{\alpha_2} && (1.37) \end{aligned}$$

where α_1 and α_2 are non-negative integers. The boundary condition (1.32) then becomes

$$g_0 \, {w_B}^{\alpha_1} \, n(w_B, t) = \int b_0 \, w^{\alpha_2} \, \Pi \, n(w, t) \, \mathrm{d}w \tag{1.38}$$

Now, make use of the definition of central moments

$$N_m \equiv \int w^m n \, \mathrm{d}w \tag{1.39}$$

N_m is the m^{th} raw moment of the number distribution. N_0 is the total number of individuals; the first moment, N_1, gives the total biomass. The ratio N_1/N_0 is the mean weight of individuals in the population. Similarly, higher moments (N_2/N_0, N_3/N_0, and N_4/N_0) can be related to the variance, skewness and kurtosis of the distribution, respectively.

Multiplying (1.31) by w^m and integrating by parts yields

$$\frac{dN_m}{dt} = b_0 \frac{P}{P + P_h} {w_B}^m \, \Pi \, N_{\alpha_2} + m \, g_0 \frac{P}{P + P_h} N_{m-1+\alpha_1} - d N_m \tag{1.40}$$

assuming d to be constant. The partial differential equation has been transformed into a set of ordinary differential equations.

From the equation for the first moment, we can infer the amount of predator biomass generated; it is given by the sum of the birth and growth terms:

$$\Delta P_{uptake} \equiv \frac{P}{P + P_h} \left(b_0 \, w_B \, \Pi \, N_{\alpha_2} + g_0 \, N_{\alpha_1} \right) \tag{1.41}$$

As before, it is assumed that this new biomass comes from ingestion of resources. We can then write an equation for the prey, which is assumed to grow logistically in the absence of predators;

$$\frac{dP}{dt} = rP \left(1 - \frac{P}{K} \right) - \frac{1}{\epsilon} \left(\Delta P_{uptake} \right) \tag{1.42}$$

Closed set of equations can be obtained for $\alpha_1 = 0$ and $\alpha_1 = 1$. When the growth rate is independent of weight ($\alpha_1 = 0$), then (1.40) yields a recursive relation between $\alpha_2 + 1$

equations.

When the growth rate is a linear function of weight ($\alpha_1 = 1$), we get a system of at most 3 ordinary differential equations:

$$\frac{dN_1}{dt} = b_0 \frac{P}{P+P_h} w_B \, \Pi \, N_{\alpha_2} + g_0 \frac{P}{P+P_h} N_1 - dN_1 \tag{1.43}$$

$$\frac{dN_{\alpha_2}}{dt} = b_0 \frac{P}{P+P_h} {w_B}^{\alpha_2} \, \Pi \, N_{\alpha_2} + \alpha_2 \, g_0 \frac{P}{P+P_h} N_{\alpha_2} - dN_{\alpha_2} \tag{1.44}$$

$$\frac{dP}{dt} = rP\left(1 - \frac{P}{K}\right) - \frac{1}{\epsilon}\frac{P}{P+P_h}\left({w_B}^{\alpha_2} \, b_0 \, \Pi \, N_{\alpha_2} + g_0 \, N_1\right) \tag{1.45}$$

This three-dimensional system bears some similarities with equations (1.11-1.13), especially if the value of α_2 is greater than 1 because then more mature (heavier) individuals have a larger birth rate than young ones. The bifurcations structure of these equations is not discussed here, but could be addressed in a future study.

In the special case $\alpha_2 = \alpha_1 = 1$, the model (1.43-1.45) reduces to a two-dimensional system of equations. These can be adimentionalized as in Section 5.4.1; we define $\beta \equiv b_0/r$, $\gamma \equiv g_0/r$, and use z for the scaled predator biomass; weight is scaled by w_B. This yields

$$\begin{aligned} \frac{dz}{d\tau} &= \beta \frac{p}{p+1} \frac{z^2}{z+\lambda} + \gamma \frac{p}{p+1} z - \delta z && (1.46) \\ \frac{dp}{d\tau} &= p\left(1 - \frac{p}{\chi}\right) - \frac{p}{p+1}\left(\frac{z^2}{z+\lambda} + \frac{\gamma}{\beta} z\right) && (1.47) \end{aligned}$$

These equations are similar to the one-stage model (1.26-1.25) but with an extra term involving γ, and exhibit the same dynamical behavior. We can also rearrange these equations to get

$$\begin{aligned} \frac{dz}{d\tau} &= \beta \frac{p}{p+1} z \Sigma - \delta z && (1.48) \\ \frac{dp}{d\tau} &= p\left(1 - \frac{p}{\chi}\right) - \frac{p}{p+1} z \Sigma && (1.49) \end{aligned}$$

where

$$\Sigma \equiv \left(1+\frac{\gamma}{\beta}\right)\frac{z}{z+\lambda}+\frac{\gamma}{\beta}\frac{\lambda}{z+\lambda} \tag{1.50}$$

The terms involving $\frac{\lambda}{z+\lambda}$ can be neglected when $\lambda \ll z$. In that case, the predator-prey model has the same form as the modified Rosenzweig-MacArthur model analyzed in Section 1.4.

1.6 Summary

This chapter describes the construction of a model for the coupled interactions between a two-stage predator population with density-dependent mating success and a logistically-growing prey population. Analysis of the model reveals that stable coexistence and sustained oscillations are both possible asymptotic states. In addition, because of the density-dependence in reproduction which gives rise to an Allee effect, extinction of the predator is always a stable solution. Changes in the parameters describing biological rates thus threaten the viability of the predator population; catastrophic extinction can occur through saddle-node or homoclinic bifurcations. The behavior of the 3-compartment model is qualitatively similar to that of other models with Allee effects, implying that we have added structure in the predator population without significantly altering the predator-prey dynamics.

The main result is the model (1.22-1.23), obtained by projecting the stage-structured predator population onto a single stage. In the proposed modified version of the Rosenzweig-MacArthur model, the Allee effect term appears in both the equation for the predator and the equation for the prey: the probability of mating modulates the rate at which offsprings are produced. This leads to significant disagreement with other published models that include the term only in the equation for the predator (Bazykin, 1998; Zhou et al., 2005) regarding the equilibrium values for predator and prey density, as well as the asymptotic behavior of the system.

Allee effects and predator-prey interactions also influence the dynamics of a predator population with a continuous weight structure. Assuming power-law relationships for the weight-dependence of the growth and birth rates, a two-dimensional set of equations is derived for the evolution of predator and prey biomass. The equivalent predator-prey model is remarkably similar to the single-stage model with Allee effect; both exhibit qualitatively similar dynamics. The agreement is due in part to the form of the birth function, which assumes a non-zero reproduction rate for young (low weight) individuals. If instead one assumes a critical weight below which predators cannot reproduce, the dynamics of the continuous-weight model become more complex. Population models with explicit maturation delays can be described by delay-differential equations (see Gurney and Nisbet, 1998) which can exhibit chaotic dynamics when coupled to a prey population.

1.7 Appendix: Fixed points and stability

1.7.1 Three-compartment model

Equilibria in the stage-structured predator-prey model (1.14-1.16) are found by equating the time derivatives to 0. The trivial solution is $\{p^* = z_j^* = z_a^* = 0\}$; another corresponds to extinction of the predator: $\{p^* = \chi, \quad z_j^* = z_a^* = 0\}$. There are five coexistence equilibria, for which the juvenile and adult densities are

$$\begin{aligned} z_j^* &= \frac{\lambda\left(\theta\frac{p^*}{p^*+1} + \delta_j\right)}{\frac{\beta^2}{\delta_a^2}\theta\frac{(p^*)^3}{(p^*+1)^3} - \left(\theta\frac{p^*}{p^*+1} + \delta_j\right)\frac{\beta}{\delta_a}\frac{p^*}{p^*+1}} && (1.51) \\ z_a^* &= \frac{\beta}{\delta_a}\frac{p^*}{p^* + 1}z_j^* && (1.52) \end{aligned}$$

(except in the special case $\lambda = 0$), and the equilibrium prey density is given by the solution to the polynomial equation:

$$a_1p^5 + a_2p^4 + a_3p^3 + a_4p^2 + a_5p + a_6 = 0 \qquad (1.53)$$

with

$$\begin{aligned} a_1 &= -\frac{\theta\beta^2}{\chi} + \frac{\beta\delta_a}{\chi}(\theta + \delta_j) \\ a_2 &= \theta\beta^2 - \beta\delta_a(\theta + \delta_j) + \frac{\beta\delta_a}{\chi}(\theta + 2\delta_j) \\ a_3 &= -\beta\delta_a(\theta + 2\delta_j) + \frac{\beta\delta_j\delta_a}{\chi} - \frac{\lambda\delta_a^2\delta_j}{\theta}(\theta + \delta_j) - \eta\lambda\delta_a^2(\theta + \delta_j) \\ a_4 &= -\beta\delta_j\delta_a - \frac{\lambda\delta_a^2\delta_j}{\theta}(2\theta + 3\delta_j) - \eta\lambda\delta_a^2(\theta + 2\delta_j) \\ a_5 &= -\frac{\lambda\delta_a^2\delta_j}{\theta}(\theta + 3\delta_j) - \eta\lambda\delta_a^2\delta_j \\ a_6 &= -\frac{\lambda\delta_a^2\delta_j^2}{\theta} \end{aligned}$$

The roots of (1.53) can be found numerically, but examination of the characteristic equation provides some information about the nature of the solutions. From Descartes' rule of signs, we know that the number of real positive roots in a n^{th} order polynomial equation is no greater than, and of the same parity as, the number of changes in sign in the sequence of coefficients $a_1, a_2, \ldots, a_n$.

In (1.53), the three last coefficients, a_4 – a_6, are all negative; a_3 is negative unless the enrichment parameter χ is small. If a_3 is positive, the inequality $\frac{\beta\delta_a\delta_j}{\chi} > \beta\delta_a(\theta + 2\delta_j)$ is necessarily satisfied. Thus, a_2 must be positive as well; the total number of changes in sign cannot exceed 2, implying that there is a maximum of two positive equilibria. We cannot say more unless we make some assumptions about the parameter values. When solving (1.53), we observe that $\beta < \delta_a$ yields solutions $p^* > \chi$, which is not biologically possible, and for which the corresponding predator equilibrium biomasses are negative.

Thus we impose $\beta > \delta_a$. When this condition is satisfied, then $a_1 < 0$ and $a_2 > 0$. Consequently, the ecosystem possesses either 2 or 0 real positive equilibria. Since all coefficients are real, the three remaining solutions must be real (and negative) or come in complex conjugate pairs, so there is always at least one real negative solution. Numerical experiments reveal that there is never more than one.

The jacobian of the ecosytem model is

$$\begin{bmatrix} -\theta\frac{p}{p+1} - \delta_j & \theta\frac{p}{p+1}\frac{z_a^2+2\lambda z_a}{(z_a+\lambda)^2} & \frac{\theta}{(p+1)^2}\left(\frac{z_a^2}{z_a+\lambda} - z_j\right) \\ \beta\frac{p}{p+1} & -\delta_a & \frac{\beta}{(p+1)^2}z_j \\ -(\eta-1)\frac{p}{p+1} & -\frac{p}{p+1}\frac{z_a^2+2\lambda z_a}{(z_a+\lambda)^2} & 1 - \frac{2p}{\chi} - \frac{1}{(p+1)^2}\left(\frac{z_a^2}{z_a+\lambda} - (\eta-1)z_j\right) \end{bmatrix} \tag{1.54}$$

The trivial equilibrium is always unstable, since the jacobian evaluated at that point

$$\begin{bmatrix} -\delta_j & 0 & 0 \\ 0 & -\delta_a & 0 \\ 0 & 0 & 1 \end{bmatrix} \tag{1.55}$$

has a positive eigenvalue, 1, in addition to two negative eigenvalues, $-\delta_j$ and $-\delta_a$.

Predator extinction is always a stable equilibrium; the jacobian becomes

$$\begin{bmatrix} -\theta\frac{\chi}{\chi+1}-\delta_j & 0 & 0 \\ \beta\frac{\chi}{\chi+1} & -\delta_a & 0 \\ -(\eta-1)\frac{\chi}{\chi+1} & 0 & -1 \end{bmatrix} \tag{1.56}$$

which has eigenvalues $-\theta\frac{\chi}{\chi+1}-\delta_j$, $-\delta_a$ and -1, all negative.

For coexistence equilibria, the jacobian is evaluated numerically.

1.7.2 One-stage model

Here we repeat the calculations of Appendix 1.7.1, for the case of an unstructured population. To avoid unnecessary repetition, some steps have been slightly abbreviated; refer to previous section for more details. The one-stage predator-prey model (1.25-1.26), also "Model A" version of equations (1.27-1.28), has a trival equilibrium, $\{p^* = z^* = 0\}$, an equilibrium in which the predator population is extinct, $\{p^* = \chi, \quad z^* = 0\}$, and three coexistence equilibria, for which the predator density is

$$z^* = \frac{\lambda\delta(p^*+1)}{\beta p^* - \delta(p^*+1)} \tag{1.57}$$

and the equilibrium prey density is a solution to

$$a_1p^3 + a_2p^2 + a_3p + a_4 = 0 \tag{1.58}$$

with

$$\begin{aligned} a_1 &= -\frac{\beta^2}{\chi}+\frac{\beta\delta}{\chi} \\ a_2 &= \beta^2-\beta\delta+\frac{\beta\delta}{\chi} \\ a_3 &= -\beta\delta-\delta^2\lambda \\ a_4 &= -\delta^2\lambda \end{aligned} \tag{1.59}$$

Here again we shall examine the changes of sign in the sequence of coefficients to the characteristic equation. Assuming $\beta > \delta$ based on the same argument as for the structured population case, we find that $a_2 > 0$ and all other coefficients are negative. We then know that either 2 or 0 equilibria are real and positive; one must be real and negative, since there can be only one or two pairs of complex conjugates.

The jacobian is

$$\begin{bmatrix} \beta\frac{p}{p+1}\frac{z^2+2\lambda z}{(z+\lambda)^2} - \delta & \frac{\beta}{(p+1)^2}\frac{z^2}{z+\lambda} \\ -\frac{p}{p+1}\frac{z^2+2\lambda z}{(z+\lambda)^2} & 1 - \frac{2p}{\chi} - \frac{1}{(p+1)^2}\frac{z^2}{z+\lambda} \end{bmatrix} \tag{1.60}$$

It is easy to see that the trivial equilibrium is unstable, and that extinction of the predator is a stable equilibrium. Stability of coexistence equilibria is examined numerically.

In the "Model B" version of (1.27-1.28), the Allee effect term does not appear in the prey equation. In addition to the unstable trivial equilibrium and the stable predator extinction equilibrium, the model has two coexistence fixed points:

$$p^* = \frac{\delta(z^* + \lambda)}{\beta z^* - \delta(z^* + \lambda)} \tag{1.61}$$

$$\begin{aligned} z^* &= \frac{-\beta\delta + \chi(\beta - \delta)(\beta + 2\delta\lambda)}{2\chi(\beta - \delta)^2} \\ &\quad \pm \frac{\beta}{2\chi(\beta - \delta)^2}\sqrt{(\delta - \chi(\beta - \delta))^2 - 4\delta\chi\lambda(\beta - \delta)} \end{aligned} \tag{1.62}$$

where we note that the expression (1.61) is equivalent to (1.57). If one of the coexistence equilibria is stable, it will always be the one corresponding to high predator biomass (positive root in 1.62). Existence of the equilibrium requires $\beta > \delta$.

In the special case $\lambda = 0$, the equations take the form of the standard Rosenzweig-MacArthur model. Multiple equilibria are not possible; the only coexistence fixed point is

$$p^* = \frac{\delta}{\beta - \delta} \tag{1.63}$$

$$z^* = \frac{\beta}{\beta - \delta} - \frac{\beta\delta}{\chi(\beta - \delta)^2} \tag{1.64}$$

Without getting into the details of the stability analysis (which can be found in a mathematical ecology textbook, for example Kot, 2001), I will simply state that stability of the coexistence equilibrium (and thus instability of the predator extinction equilibrium) requires

$$\frac{\beta}{\delta} < \frac{1+\chi}{1-\chi} \tag{1.65}$$

When $\chi < 1$, the inequality is always satisfied, so oscillatory asymptotic solutions are not possible.

1.7.3 Derivatives of the coexistence equilibria

The sensitivity of the coexistence equilibrium to the predation rate and the assimilation efficiency is examined in the modified Rosenzweig-MacArthur model. First, consider the case without Allee effect, $\lambda = 0$, with equilibrium predator and prey densities given by (1.63-1.64).

For the sensitivity to the assimilation efficiency, recall that the predator biomass is scaled by $\epsilon r P_h / B$ (Section 5.4.1); hence

$$\frac{\partial Z^*}{\partial \epsilon} = \frac{\partial}{\partial \epsilon}\frac{\epsilon r P_h z^*}{g} = \frac{P_h z^*}{\beta} \tag{1.66}$$

is always positive. As one would expect, the population size increases with efficiency.

The equilibrium prey biomass is independent of ϵ, but it is sensitive to changes in the predation rate, β:

$$\frac{\partial p^*}{\partial \beta} = \frac{-\delta}{(\beta - \delta)^2} \tag{1.67}$$

This expression is negative, which means that increasing β always results in a decrease of prey density. (The dimensional biomass is proportional to the non-dimensional value.)

For the predator population, the sensitivity is

$$\begin{aligned}\frac{\partial Z^*}{\partial \beta} &= \epsilon P_h \frac{\partial}{\partial \beta}\left(\frac{z^*}{\beta}\right)\\ &= \frac{\epsilon P_h}{\beta}\frac{\partial z^*}{\beta} - \frac{\epsilon P_h}{\beta^2} z^*\\ &= \frac{\delta}{\chi(\beta-\delta)^3}[\delta(\chi+1) - \beta(\chi-1)] - \frac{\epsilon P_h}{\beta^2} z^* \qquad (1.68)\end{aligned}$$

The first term on the right hand side is positive for stable equilibria [see condition (1.65)]; the second term is always positive, so that the difference depends on the parameter values. We find that predator density increases with β when

$$\frac{\beta}{\delta} < \frac{\chi+2}{\chi} \qquad (1.69)$$

that is, when the predator birth rate is small compared to the mortality rate. At equilibrium, the per capita growth rate is $\beta\frac{p^*}{p^*+1}$; when β is sufficiently large, the enhanced grazing is not sufficient to compensate for the reduction in available prey. Dependence of the equilibrium predator biomass on β is illustrated in Figure 1-12. Numerical simulations reveals that the same dependence holds for the model with Allee effect.

In the one-stage model with Allee effect, we are interested in the sensitivity of the stable coexistence equilibrium to the parameter λ. The equilibrium prey density can be expressed, for both models A and B, as

$$p^* = \frac{\delta}{\beta\frac{z^*}{z^*+\lambda} - \delta} \qquad (1.70)$$

Since the ratio $\frac{z^*}{z^*+\lambda}$ is not greater than 1, the equilibrium density is always larger when an Allee effect is present than when the mating success is constant. This implies that at least for small values of λ, the derivative $\partial p^*/\partial\lambda$ is positive.

In model A, we differentiate the expression for the equilibrium predator density, (1.57);

$$\frac{\partial z^*}{\partial \lambda} = \frac{\delta(p^*+1) + \lambda\delta\frac{\partial p^*}{\partial \lambda}}{\beta p^* - \delta(p^*+1)} - \frac{\lambda\delta(p^*+1)\frac{\partial p^*}{\partial \lambda}(\beta-\delta)}{\left[\beta p^* - \delta(p^*+1)\right]^2} \tag{1.71}$$

For small values of λ, we have shown that $\frac{\partial p^*}{\partial \lambda} > 0$. Since existence of the equilibrium requires $\beta > \delta$, both terms are positive, and the value of the derivative depends on their difference. When $\lambda \rightarrow 0$, the derivative is positive, so that enhancing the density-dependence in mating success yields an increase in predator biomass; further increasing the strength of the Allee effect might (or not) cause the equilibrium density to decrease.

In model B, we differentiate the positive root in (1.62),

$$\frac{\partial z^*}{\partial \lambda} = \frac{\delta}{\beta-\delta} - \frac{\beta\delta}{(\beta-\delta)\sqrt{\xi}} \tag{1.72}$$

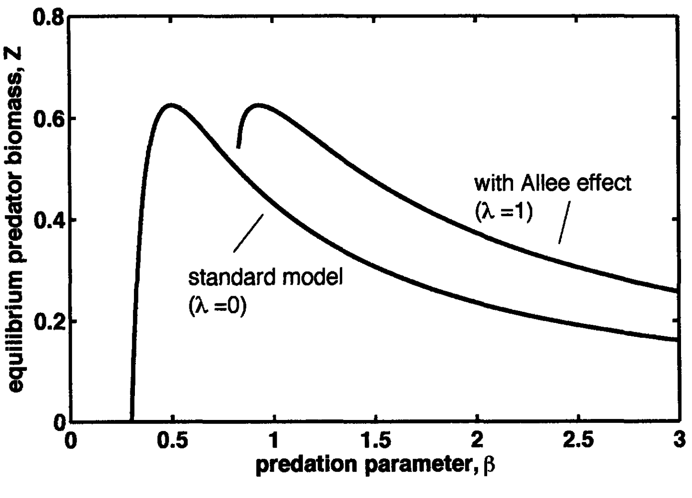

Figure 1-12: Equilibrium predator biomass Z^* (dimensional units) vs grazing parameter. Only real positive coexistence equilibrium is shown (for $\lambda = 1$, the equilibrium corresponding to higher predator density is plotted). Parameters: $\epsilon = 0.5$, $P_h = 1$, $\delta = 0.1$, $\chi = 0.5$.

where

$$\xi \equiv [\delta - \chi(\beta - \delta)]^2 - 4\delta\chi\lambda(\beta - \delta)$$

It can be shown that the derivative is always negative for stable equilibria. For the expression to be positive, it would be required that $\beta < \sqrt{\xi}$. Since increasing λ reduces the value of ξ, if this condition is satisfied for $\lambda = 0$ it will hold for $\lambda > 0$ as well. With $\lambda = 0$, the derivative (1.72) is positive when

$$\beta < |\delta - \chi(\beta - \delta)| \tag{1.73}$$

It is easy to see that this contradicts the condition for stability (1.65).

Chapter 2

Evolution and social behavior in krill

Adapted from the manuscript by A. Verdy and G.R. Flierl (2007)
To be published in *Deep-Sea Research II*

Abstract

We simulate the formation of social aggregations in a turbulent fluid environment. The theoretical framework is employed to investigate the ecological consequences of spatial patchiness in the density-distribution of krill, which often assemble in swarms or schools. In the first part of the paper, we describe the formation of aggregations resulting from the interplay of social forces and population dynamics. We consider an idealized ecosystem model of zooplankton with social behavior who feed on phytoplankton; this is solved analytically for the initial growth of patches and numerically for the steady-state distributions of predator and prey biomass. Environmental variability changes the linear instability criterion for spontaneous aggregation. The second part of the paper addresses the evolution of social behavior in a population with density-dependent mating success. The model simulates the transmission of a gene controlling social behavior; natural selection determines whether the grouping or non-grouping type becomes dominant. It is found that the behavior can evolve when mixing occurs rapidly enough for resources to remain available to the clustered organisms. Turbulent advection prevents the grouping type from becoming dominant if the shear of the flow is strong enough to disrupt the patches; otherwise the aggregated zooplankton benefit from enhanced diffusion of resources by the turbulent flow.

2.1 Introduction

Zooplankton aggregation occurs as the result of both biological and physical processes. In the ocean, the density distribution of plankton is influenced by circulation patterns such as mesoscale vortices (Abraham, 1998; Flierl and McGillicuddy, 2002; Pasquero, 2005) and fronts (Epstein and Beardsley, 2001; Franks, 1992; Genin et al., 2005). The behavior of individuals responding to their environment also plays a significant role in the generation of dense, quasi-horizontal patches of zooplankton commonly called swarms (Folt and Burns, 1999). Physical and chemical cues can trigger collective movements in a population, or the cue can be the density of conspecifics, in which case the tendency to form groups is referred to as *social behavior.*

A variety of mathematical models have been employed to describe the mechanisms responsible for the development of swarms in populations of organisms with social behavior. Forces of attraction towards others can balance the diffusive tendencies, leading to the formation of cohesive groups (e.g. Okubo, 1986; Flierl et al., 1999). Even in the absence of environmental variability, groups can form spontaneously when swimming velocities are, on average, directed up the gradient of population density and are strong enough to overcome dispersion resulting from the flow and from the randomness of individual motion. Schools develop when organisms also tend to align their orientation with close-by neighbors (Grünbaum, 1994, 1998; Flierl et al., 1999).

From an evolutionary point of view, the reasons for self-organized patchiness are not well known. The dynamics of groups have important ecological consequences (Levin, 1994; Parrish and Edelstein-Keshet, 1999); however the nonlinear nature of predator-prey and competitive interactions makes it hard to predict exactly how grouping affects individual fitness. In many cases, aggregation is thought to be an anti-predator strategy (e.g. Hamilton, 1971; Pulliam, 1973; see Bednekoff and Lima, 1998, for a review); but aggregations are also more vulnerable to predators that attack large numbers of prey (Hamner, 1984; Ritz, 1994; Connell, 2000). Other advantages include improvement of the foraging success and higher mating probability; these benefits are traded-off with the costs of competition for resources between group members (Clark and Mangel, 1986; Ritz, 1994; Parrish and Edelstein-Keshet, 1999).

Most likely, all of the above-mentioned effects have played a role in the evolution of social behavior in zooplankton. The balance between costs and benefits, which depends on the species and their environment, determines whether the behavior is favored or not. Predation has both positive and negative consequences on the fitness of aggregated zooplankton; in this paper, we we do not address these effects but consider a constant mortality risk. Similarly, we get rid of the group effects in foraging success by assuming a uniform environment for phytoplankton growth. We consider only two density-dependent effects: the correlation between mating success and population size, which gives rise to an Allee effect, and the competition for resources between group members. These are put in mathematical form, in order to quantify their impact on the fitness of zooplankton in an idealized environment; we modify the model of Flierl et al. (1999) to incorporate population dynamics, and couple the single-species model with an equation for the prey.

The theoretical framework allows us to simulate the competition between a population with grouping behavior and a hypothetical non-grouping population. The model simulates transmission of a gene controlling aggregation behavior; natural selection determines whether the grouping or non-grouping type becomes dominant. The success of the aggregation strategy will depend on the environmental conditions. Turbulent stirring and mixing affect ecosystem dynamics, thus impacting the competitive abilities of organisms with social behavior; turbulent flows are associated with horizontal and vertical transport of resources in the euphotic zone and also cause merging and splitting of plankton aggregations (Flierl et al., 1999). We investigate under what flow conditions does social behavior represent a favorable adaptation and therefore can evolve in the population.

Our work is motivated by observations of Antarctic krill (*Euphausia superba*), which are a central part of the Southern Ocean ecosystem. These animals clearly exhibit aggregative and schooling behavior (e.g. Miller and Hampton, 1989) and respond to large- and meso-scale circulations (Hofmann and Murphy, 2004). The observed variance spectrum of krill in the Southern Ocean is significantly flatter than that of phytoplankton or temperature in the same region, indicating the presence of fine-scale structure in the density distribution of krill (Weber et al., 1986); smaller zooplankton have variance spectra that lie between those of krill and phytoplankton (Mackas and Boyd, 1979). Swarms, which are thought to be the basic unit of organization in krill, often assemble to form large-scale patches and schools. The modeling study of Hofmann et al. (2004) examines the role of social attraction, foraging, and predation in the formation of swarms. The work of Zhou and Dorland (2004) addresses the effect of horizontal shear flows on the maintenance of aggregations. Results from our numerical model will be discussed in light of these previous studies.

The paper begins with a description of the model (Section 2.2), which is constructed by coupling reaction-advection-diffusion equations for ecosystem dynamics to a discrete-time model of an idealized turbulent flow. Numerical simulations of the growth of patches are presented in Section 2.3. In Section 2.4, we simulate the interactions between grouping and non-grouping populations competing for resources and examine how environmental conditions influence the success of the grouping invader. Conclusions are presented in Section 2.6.

2.2 Model formulation

The biological dynamics and motion of a single species of zooplankton are simulated in a 2-dimensional periodic horizontal plane representing the oceanic mixed layer. A continuum approach is used, where modeled fields are biomass densities rather than discrete organisms. In order to capture the effects of resource limitation, the dynamics of phytoplankton are also simulated. Density-dependence of the zooplankton reproduction is taken into account, but predation by higher trophic levels is parameterized as independent of the zooplankton density.

2.2.1 Genetic model

We adopt a one-locus, two-allele model to simulate the transmission of a gene controlling social behavior. Although it is a highly simplified representation of the real genetic mechanism, it provides us with a quantitative framework to study the evolution of a phenotypic trait in a sexually-reproducing population, for which the density-dependent probability of mate encounters is an important driver of ecological and evolutionary dynamics.

Let the two alleles be 0 and 1. Of the three possible genotypes 00, 01 and 11, only the last one exhibits social behavior. Mendelian inheritance is assumed (Appendix 2.7). The relative abundance of types in a population depends on their relative fitness and on allele mutations. In the simple case where genetic differences do not influence survival and both alleles have the same mutation rate, the population equilibrates to a 1:2:1 ratio of types. Expression of the social trait, however, affects the ecological dynamics and thereby might change the fitness of the grouping type; aggregated organisms benefit from enhanced reproductive success, but experience reduced availability of resources. Individual fitness, as measured by the per capita growth rate, results from the balance between these two effects. In our model, fitness is not explicitly specified: the relative success of the grouping and non-grouping types is determined through numerical simulations.

2.2.2 Ecological dynamics

The equations describing the movements of organisms in the continuum approximation are derived in Flierl et al. (1999). Zooplankton motion driven by attractive forces is expressed as an advection term, representing average swimming velocities, and a diffusion term representing randomness of individual displacements. The average swimming velocity of zooplankton at a given location results from social behavior; for non-grouping organisms (genotypes 00 and 01), the movements are random and vanish on average ($\mathbf{u} = 0$), but social behavior (in genotype 11) translates into a mean advective velocity that depends on the local density gradient:

$$\mathbf{u} = \nabla\phi \tag{2.1}$$

$$\phi = W_0 \iint W(\mathbf{x}')\, Z(\mathbf{x}+\mathbf{x}')\, \mathrm{d}\mathbf{x}' \tag{2.2}$$

where Z is the local density of zooplankton, vertically integrated, with units kg m^{-2}.

The function $\phi(\mathbf{x})$ represents the desirability of being at location $\mathbf{x}$; it is a weighted average of the density of zooplankton within the sensing radius of an individual. The weighting function $W(\mathbf{x})$ is a dimensionless function that has a characteristic horizontal scale L, and a magnitude proportional to the swimming speed; it is normalized so that $\iint W = 1$. To make ϕ of units m^2 s^{-1}, the weighting is multiplied by a constant W_0 expressed in units m^2 s^{-1} kg^{-1}. We choose a radially-symmetric function that is negative for small distance x and positive for larger values, has a maximum at $x = L$ and tends to 0 as $x \longrightarrow \infty$; this geometry accounts for the finite area of attraction and the repulsion at short distances (Figure 2-1).

Here we also consider the population dynamics, thus allowing for changes in the mean biomass. A simple predator-prey model is adapted to take into account the nonlinear reproductive success, and the advection and diffusion terms described above. We obtain a system of coupled differential equations describing the interactions between zooplankton and their food resource, phytoplankton (P):

$$\frac{\partial Z}{\partial t} = \epsilon g \frac{P}{P+P_h} Z\Pi(Z) - dZ - \nabla\cdot(\mathbf{u}Z - \kappa\nabla Z) \tag{2.3}$$

$$\frac{\partial P}{\partial t} = rP\left(1-\frac{P}{K}\right) - g\frac{P}{P+P_h} Z\Pi(Z) + \nabla\cdot\kappa\nabla P \tag{2.4}$$

where ϵ is the assimilation efficiency, g the maximum grazing rate, P_h the half-saturation prey density, d the mortality rate, r the prey growth rate, and K the carrying capacity; κ is

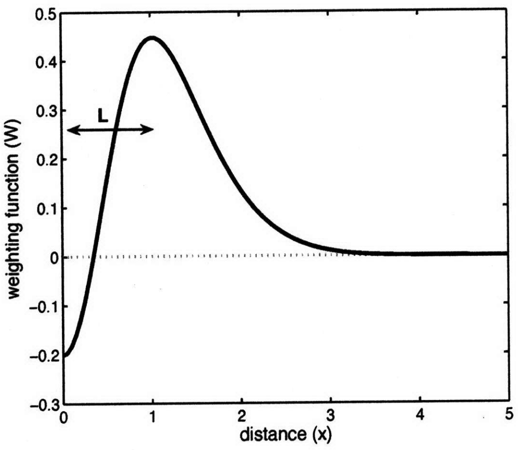

Figure 2-1: Weighting of neighboring organisms as a function of their distance from zooplankton located at $x = 0$ which adjust their velocity to move up the gradient of neighbors density: $W(x) = \exp(-x^2/2) - \exp(-2x^2)$. Distances are expressed in units of L, the characteristic perception length scale. The sensing radius has an approximate value of $2L$; individuals within the sensing radius are perceived by zooplankton with social behavior. Positive weighting indicates attraction to neighbors. Repulsion at short distance prevents over-crowding.

the diffusivity. Predator growth is a function of the density-dependent mating probability:

$$\Pi(Z) = \frac{Z}{Z + c} \tag{2.5}$$

where c is a positive constant.

Zooplankton growth is also limited by the prey density; we assume a Holling type II functional response, $g\frac{P}{P+P_h}$, which reflects saturation of krill ingestion rates when resources are abundant (Boyd et al., 1984) and is often used to describe zooplankton growth. The linear mortality rate represents both natural mortality and predation. The assimilation efficiency accounts for depletion of resources due to metabolic activities. We assume logistic growth for the prey. The mating probability Π appears in the equation for the prey as a consequence of biomass conservation; we adopt the view that resources are depleted at a rate proportional to the generation of predator biomass [the formulation of the predator-prey model is discussed in more details in Chapter 1.

There is a positive correlation between the mating probability and the zooplankton population size. For sparse populations, the zooplankton growth term $Z\Pi(Z)$ behaves like a quadratic function; for large populations the growth term becomes a nearly-linear function of Z. Thus as the population decreases, its growth slows down, further decreasing the population density. This positive feedback, known as the Allee effect, can induce stochastic extinction in small populations (Boukal and Berec, 2002). It also provides an advantage for the grouping organisms. In the case of Antarctic krill, mating involves direct contact between male and female organisms, thus it is likely that the process is density-dependent. The rectangular hyperbolic form of Π that we choose emerges from considerations of probabilities of encounters during the reproductive period, competition for mates, or fecundity that depends on the mating frequency (Boukal and Berec, 2002). The constant c is a measure of the strength of the Allee effect.

Mixing occurring on small scales that are not resolved by the model is also parameterized as diffusion, and affects both the phyto- and zoo-plankton fields. For simplicity we consider a unique value for the diffusivities of both species; this is equivalent to making the assumption that the random component of zooplankton motion is small.

The predator equation (2.3) is solved for each of the zooplankton genotypes, with interactions between types described by Mendelian inheritance and allele mutations (Appendix 2.7). It should be noted that advection and diffusion act only on the type considered, but the density in (2.2) refers to the total zooplankton population, as organisms with social behavior are attracted not only to their type but to all conspecifics. The system described above is solved numerically using a finite-differences scheme.

2.2.3 Turbulent stirring

To represent turbulent advection, we use a formalism akin to Pierrehumbert (2000). The grid underlying the numerical model is viewed as a lattice, with grid size Δx, whose elements are displaced by a non-divergent flow (u, v). The "lattice mixing algorithm" (Pierrehumbert, 2000) is formulated in discrete time. The position of fluid particles is iterated at every time step according to the map

$$x(t+\Delta t) = x(t) + \left[\frac{u(t)}{\Delta x}\Delta t\right]\Delta x \qquad (2.6)$$

$$y(t+\Delta t) = y(t) + \left[\frac{v(t)}{\Delta x}\Delta t\right]\Delta x \qquad (2.7)$$

where [.] rounds to the nearest integer: displacements are constrained to be multiples of the grid size to ensure preservation of the lattice area.

We consider a unidirectional shear flow whose direction changes in a time-periodic manner. The flow is the x-direction during the first half of the period (*T*), and in the y-direction during the second half. The velocity fields have a sinusoidal pattern with randomly-varying phase. Alternating sinusoidal shear flows are often considered as a simple example of chaotic flow, including in studies of mixing in biological or chemical systems (e.g. Károlyi et al., 2005; Benczik, 2005).

Setting $\Delta t = T/2$, we have

$$\left.\begin{aligned} u(t) &= V\sin\left[\tfrac{2\pi}{D}y + \theta_u(t)\right] \\ v(t) &= 0 \end{aligned}\right\} \quad \mathrm{mod}(t,T) = 0 \qquad (2.8)$$

for the first half period, and

$$\left.\begin{aligned} u(t) &= 0 \\ v(t) &= V\sin\left[\tfrac{2\pi}{D}x + \theta_v(t)\right] \end{aligned}\right\} \quad \mathrm{mod}(t,T) = T/2 \qquad (2.9)$$

for the second half. *V* gives the magnitude of the flow, *D* is the width of the square domain, and the phases are

$$\theta_u(t+T) = \theta_u(t) + \mathcal{R}_u$$

$$\theta_v(t+T) = \theta_v(t) + \mathcal{R}_v$$

where $\mathcal{R}_u$ and $\mathcal{R}_v$ are independent random numbers sampled from a uniform distribution.

Although the algorithm does not explicitly include mixing of tracers between adjacent lattice sites, the stirring creates gradients in the density fields, thus enhancing diffusion at small scales which is included in the differential equations (2.3-2.4). It should be noted that Δt does not have to be the same as the time step used for solving the ecosystem model. The stirring calculated in (2.6-2.9) is applied to the biomass fields simply by permutating the elements of $P(\mathbf{x}, t)$, $Z(\mathbf{x}, t)$ which are solutions to (2.3-2.4).

2.3 Development of patches

In this section we examine the conditions leading to the formation of zooplankton patches. First, we adimensionalize the model equations and analyze the initial growth of patches. We then proceed to numerical simulations.

2.3.1 Non-dimensional system of equations

Following Flierl et al. (1999), we scale time by by L^2/κ, velocities by κ/L, lengths by L, and ϕ by κ. Phytoplankton and zooplankton biomass are scaled by P_h and $P_h r/g$, respectively. Some non-dimensional parameters are introduced to replace the variables describing the reaction terms: $\gamma = \epsilon g/r$, $\delta = d/r$, $\chi = K/P_h$; the non-dimensional Allee effect parameter is $\lambda = cg/rP_h$. Lower-case p and z denote scaled biomass; asterisks are used to differentiate non-dimensional variables from their dimensional counterpart. This yields

$$\frac{\partial z}{\partial t^*} = \tau\left[\gamma\frac{p}{p+1}\frac{z^2}{z+\lambda} - \delta z\right] - \nabla\cdot(\mathbf{u}^* z - \nabla z) \qquad (2.10)$$

$$\frac{\partial p}{\partial t^*} = \tau\left[p\left(1-\frac{p}{\chi}\right) - \frac{p}{p+1}\frac{z^2}{z+\lambda}\right] + \nabla\cdot\nabla p \qquad (2.11)$$

and, for individuals with social behavior,

$$\mathbf{u}^* = \nabla \phi^* \tag{2.12}$$

$$\phi^* = \mathcal{S} \iint W^*(\mathbf{x}')\, z(\mathbf{x}^* + \mathbf{x}')\, \mathrm{d}\mathbf{x}' \tag{2.13}$$

Two important non-dimensional parameters appear. The first one is $\mathcal{S}$, the Peclet number, comparing advective and diffusive rates (Flierl et al., 1999). Defining the characteristic swimming speed $U_{bio} = P_h r W_0 L/g$, we have

$$\mathcal{S} = U_{bio} L/\kappa$$

This parameter is a measure of the strength of social behavior. The second parameter is τ, the ratio of the timescale of diffusion over distance L relative to the phytoplankton growth timescale:

$$\tau = L^2 r/\kappa$$

Given that in our analysis we refer exclusively to dimensionless variables and parameters, we drop the asterisks in the remainder of the paper.

In the absence of motion, plankton would be uniformly distributed; the densities at equilibrium are then found by equating the terms in square brackets in (2.10) and (2.11) to 0. Here we will restrict our analysis to cases where the coexistence equilibrium is stable and steady. We set $\gamma = \lambda = 1$, $\chi = 0.5$ and $\delta = 0.1$; for these parameter values, the non-dimensional equilibrium biomasses are

$$\bar{p} = 0.22\,,\ \bar{z} = 1.23 \tag{2.14}$$

Spatial patterns appear in the zooplankton distribution when the tendency to swim up the gradient of neighbor density is sufficient to compensate dispersion resulting from the

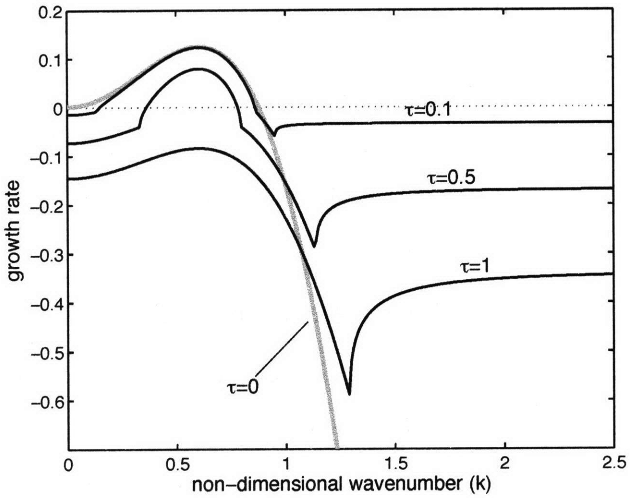

Figure 2-2: Linear growth rate of small perturbations around the equilibrium biomass versus the wavenumber of the perturbations, for $\mathcal{S} = 1.4$, and for different values of τ. In a uniform distribution of zooplankton, random variations will spontaneously lead to the formation of patches, if there is positive growth somewhere along the wavenumber spectrum. The gray line shows the case where zooplankton motion is decoupled from biological activities, as calculated in Flierl et al. (1999). When the diffusion rate is fast compared to phytoplankton growth ($\tau \ll 1$), population dynamics has a negligible impact on the linear growth rate of perturbations in the region of instability (positive growth). As biological processes become faster, their effect becomes more significant. In this example, predator-prey dynamics stabilize the equilibrium solution; the growth rate is negative for all wavenumbers when $\tau \approx 1$.

flow; this patchiness affects the mean densities. Spontaneous formation of patches requires the advection and diffusion terms in (2.10-2.11) to be destabilizing, so that small perturbations to the uniform distribution grow in time.

The linear stability problem is solved in Appendix 2.8. The growth rate of small perturbations around the uniform distribution is given by the leading eigenvalue of the jacobian of (2.10-2.11) evaluated at (2.14), and shown in Figure 5-1 for different values of τ. Perturbations are decomposed into Fourier modes, and for each mode (associated with a wavenumber **k**) we can calculate its linear growth rate; if growth is positive, perturbations are amplified in time and eventually form patches; when growth is negative, their amplitude decays exponentially in time. Thus, the uniform distribution is unstable if growth is

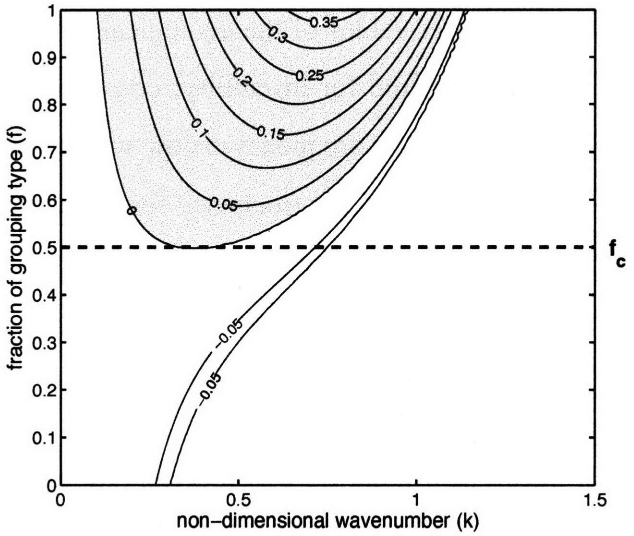

Figure 2-3: Linear growth rate in the ecosystem model as a function of the wavenumber of perturbations, and the frequency of the grouping type in the population. Parameters are $\mathcal{S} = 2$, $\tau = 0.04$. The shaded zone indicates positive growth of the perturbations, and thus instability which will lead to the formation of self-organized patches. A very small local minimum occurs near -0.05 for every wavenumber. There is a critical frequency (f_c) below which patchiness does not develop.

positive for at least one mode, leading to the spontaneous formation of patches. The spatial scale of growing patches is given by the wavelength of the mode associated with largest growth. Biological terms increase the stability (Figure 5-1), but for values of τ smaller than (roughly) 0.5 their effect is small: the growth rates for the cases with and without population dynamics are almost indistinguishable in the region of instability (positive growth).

When the population dynamics are slow compared to the motion, the condition for instability is $\mathcal{S} f_{11} \bar{z} \hat{W} \geq 1$, where $\bar{z}$ is the mean zooplankton density, $\hat{W}$ is the Fourier transform of the weighting function, and f_{11} is the frequency of the grouping type[1] (see

---

[1] In the linear stability problem, non-grouping organisms do not affect stability and can thus be ignored. In the full nonlinear model they do have an effect on stability, but only via higher order terms. These nonlinear effects are noticeable in the numerical simulations. To minimize discrepancies with our analytical predictions, we initialize the model with spatial perturbations in the 11-type zooplankton only, neutralizing the effects of non-grouping organisms on the initial development of patches by making them perfectly homogeneously distributed.

Appendix 2.8). For given parameter values of the ecological model, there is a minimum frequency of the grouping type required for instability; constraining $\bar{z}$ to its equilibrium value (2.14), we define f_c as the critical frequency below which there is no spontaneous formation of patches (Figure 2-3). This is the frequency for which the linear growth curve is tangent to 0 at its maximum.

2.3.2 Numerical simulations

After the initial period of linear growth during which perturbations gain amplitude, nonlinearities become increasingly important; eventually they contribute to stopping the growth mechanism. To obtain the final distribution of biomass, we solve the full nonlinear model numerically.

We begin by considering a population of grouping homozygotes. For $\mathcal{S} = 1.4$, $\tau = 0.1$ and $f = 1$, the condition for instability is satisfied so that patches are expected to form (Figure 5-1); indeed, numerical simulations show that small deviations from the equilibrium zooplankton biomass grow into well defined groups, as illustrated in Figure 2-4. Initially, the scale of patchiness is determined by the wavenumber that has the highest linear growth rate, but as they get denser patches tend to merge, so the patchiness shifts to larger scales.

In steady-state, the density of zooplankton results from a local balance between advection, diffusion, growth, and mortality. Swimming velocities are directed toward the center of the patch (Figure 2-5). This advection of biomass is balanced by down-gradient diffusion. The fully developed groups have peak densities of roughly 30 times the mean density and a diameter of $3 - 4\ L$. These characteristics vary slightly for different values of $\mathcal{S}$, larger values leading to the formation of denser, narrower patches. The spatial scale of the patches is in line with that of the simulated swarms of Hofmann et al. (2005), who find that the average swarm length varies between 0.2 m and 1.1 m for a sensing distance of 0.25 m.

The development of patches is also affected by environmental variability. When the zooplankton field is advected by a turbulent flow, the resulting streakiness enhances diffusion, which acts against the formation of social aggregations. Strong flows thus prevent

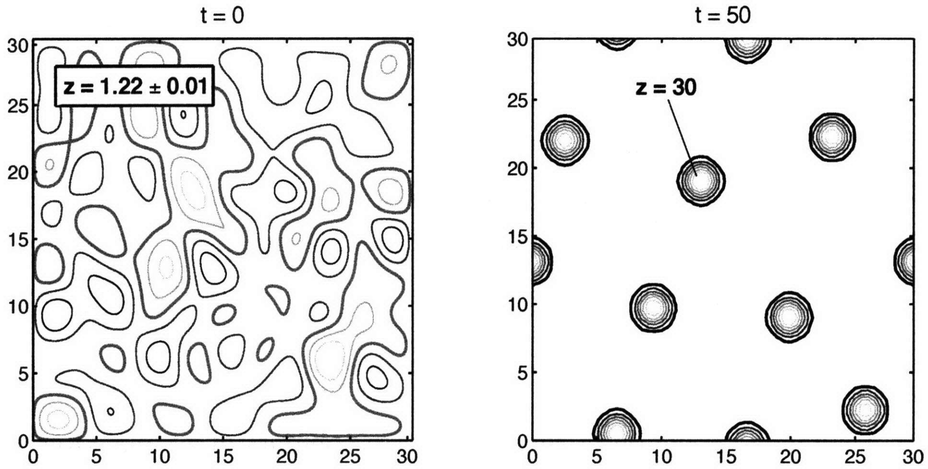

Figure 2-4: Zooplankton density in the horizontal plane. Biomass is initially uniformly distributed, with small perturbations (left); patches form spontaneously (right). The contour interval is 0.005 in the left panel, and 5 in the right panel; the equilibrium density $\bar{z} = 1.23$ is shown by a thicker contour. Patches have a horizontal scale proportional to the length L, which scales the spatial dimensions. All units are non-dimensional; parameters are $\mathcal{S} = 1.4, \tau = 0.1$.

groups from forming. Patchiness can develop if the currents are weak enough for zooplankton to overcome the dispersion resulting from the flow. We investigate numerically the response to different flows by varying the magnitude of the advective velocity, V (dimensionless). Alternatively, we could adjust the domain size to change the horizontal scale of the circulation patterns, which effectively increases the shear of the alternating flows.

Figure 2-6 illustrates the effect of weak and strong flows on the development of patches in a linearly unstable system. Although advection slows down their initial growth, perturbations evolve into fully-developed patches when $V = 2.5$ (Figure 2-6a). The turbulent flow causes collisions between patches, which then merge into a denser aggregation. Our model does not provide a mechanism for spontaneous fission of groups; once they have formed, patches are resistant to the shear of the flow (unless the shear is increased, but here we assume V to be constant). When turbulent advection is large ($V = 150$), patches do not develop, as shown in Figure 2-6b. In that case, the zooplankton field eventually be-

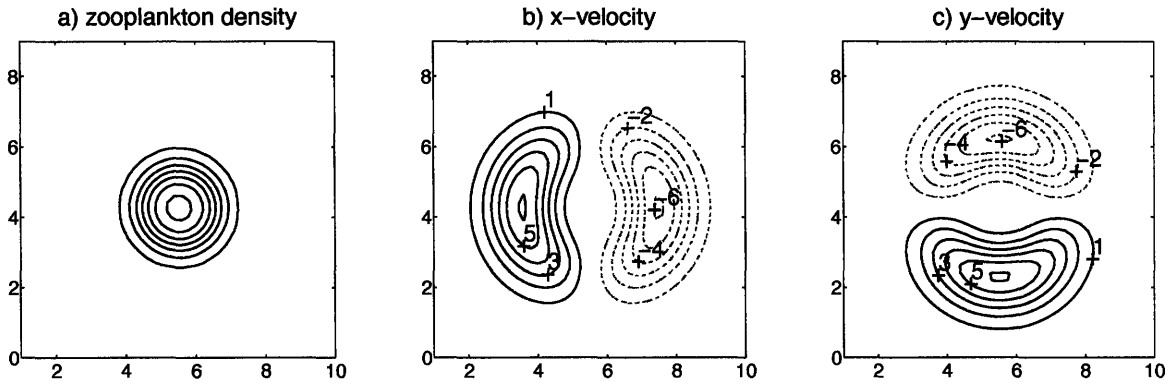

Figure 2-5: A single aggregation in steady-state. a) contours of zooplankton density; b) velocity in x-direction; c) velocity in y-direction. Dashed contours indicate negative velocities. Swimming is directed toward the center of the patch and balanced by down-gradient diffusion. Parameters are $\mathcal{S} = 1.4, \tau = 0.1$.

comes uniformly distributed in space, even though the uniform distribution is unstable in the absence of flow.

To quantify the patchiness, we define an index

$$[patchiness] = \frac{\iint \left(z(\mathrm{x}) \cdot \iint_{-1}^{1} z(\mathrm{x}+\mathrm{x}')d\mathrm{x}' \right) d\mathrm{x}}{4 \left(\iint z(\mathrm{x})d\mathrm{x} \right)^2 / D^{\,2}} - 1 \tag{2.15}$$

which compares the density of individuals within an area L^2 to the density expected if organisms were uniformly distributed.

Formation of patches is associated with a gradual increase in the patchiness index (Figure 2-6a). In the strongly-turbulent environment of Figure 2-6b, the patchiness index remains small throughout the simulation, but social behavior slows down the decay of perturbations. The zooplankton field tends to be spatially more intermittent than a passive scalar field under the same flow conditions, as indicated by comparison of their respective patchiness indices.

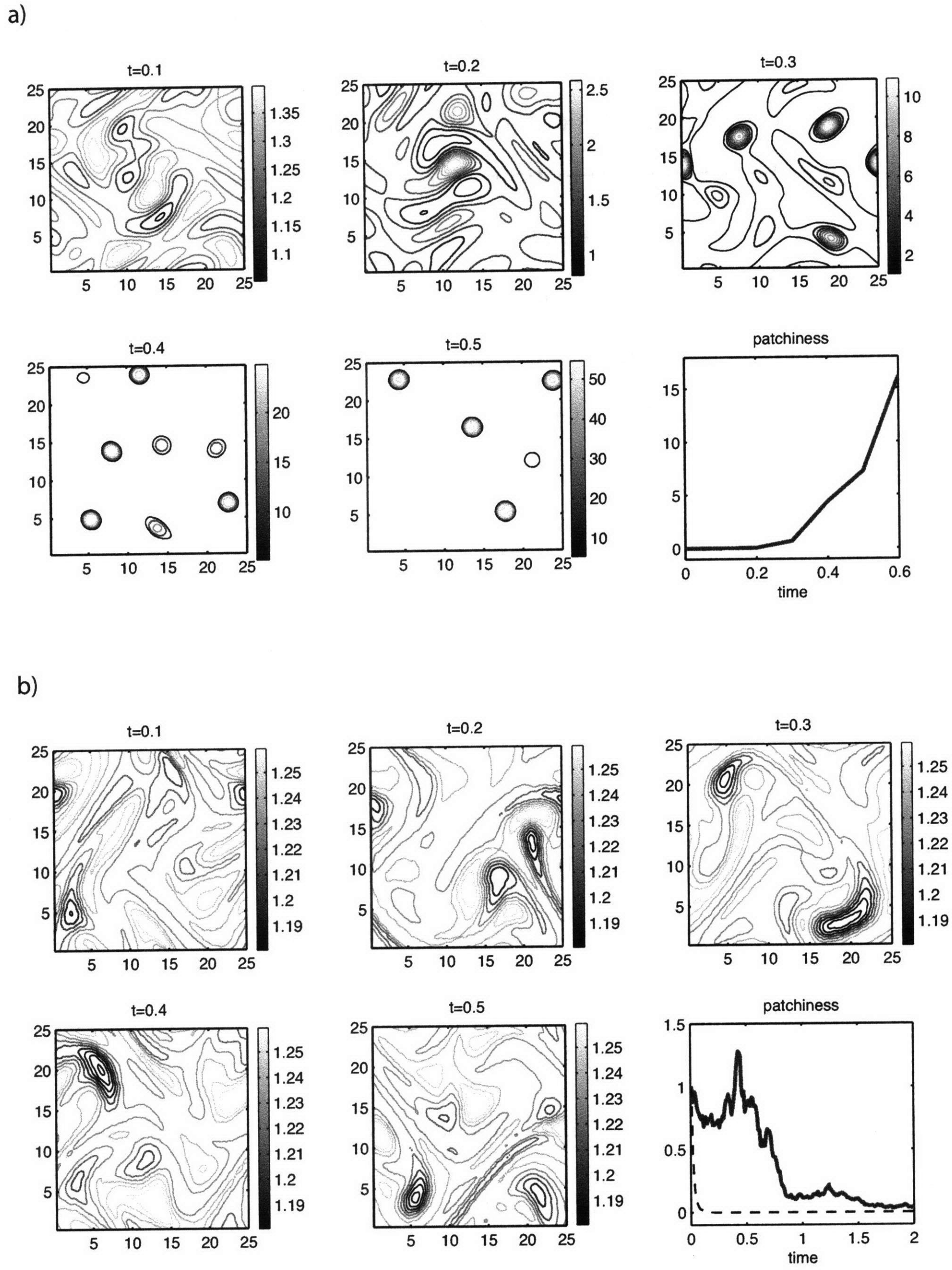

Figure 2-6: Effect of turbulent advection on the development of patches in a population of zooplankton with social behavior, $\mathcal{S} = 5$. a) weak flow, $V = 2.5$: groups form and merge. The last panel shows an index for patchiness as defined in (2.15), increasing in time. b) strong flow, $V = 150$: horizontal shear prevents the development of patches. Stirring and mixing homogenize the zooplankton distribution, which remains spatially more intermittent than a passive scalar field. The last panel shows the index for patchiness normalized by the value at $t = 0$; solid curve is for zooplankton with social behavior, dashed curve is for a passive tracer.

2.4 Conditions for success of the grouping strategy

In this section, we examine the conditions that determine whether the grouping or non-grouping type will be a better competitor. We proceed through numerical simulations, investigating successively the influence of the grouping parameter, rate of mixing, and turbulent stirring on the competitive ability of zooplankton with social behavior.

The evolutionary scenario that we consider is the following. In a population of non-grouping homozygote zooplankton (genotype 00), a grouping allele is introduced; mutations produce heterozygotes and grouping homozygotes (genotype 11). Initially the behavior is not expressed, the abundance of grouping organisms being below the critical frequency for the formation of aggregations, f_c; all types have the same fitness and neutral evolution controls the change in frequencies. Then, two things can happen: either the population equilibrates to a 1:2:1 ratio before the grouping type reaches f_c. Or, the grouping type becomes supercritical and aggregates, at which point its fate is determined by its fitness relative to that of the non-grouping type (mutations are assumed to occur very slowly compared to ecological interactions). We monitor the evolving ratio of types in the numerical simulations. If the grouping type becomes dominant, then social behavior represents a successful strategy in the idealized model.

2.4.1 Grouping parameter and invasions

The behavior of grouping zooplankton is determined by the non-dimensional parameter $\mathcal{S}$. The main effect of varying $\mathcal{S}$ in the model is to change to value of f_c, the minimum frequency of organisms with social behavior required for spontaneous formation of patches. For example, when $\mathcal{S} = 2$ and $\tau = 0.04$, the social invader does not reach $f_c \approx 0.5$ (simulation not shown, but see Figure 2-3). The behavior is never expressed, but neutral selection pressure allows the grouping allele to evolve (although it remains at lower density than the non-grouping types).

For larger values of the grouping parameter, the behavior can evolve if the invading

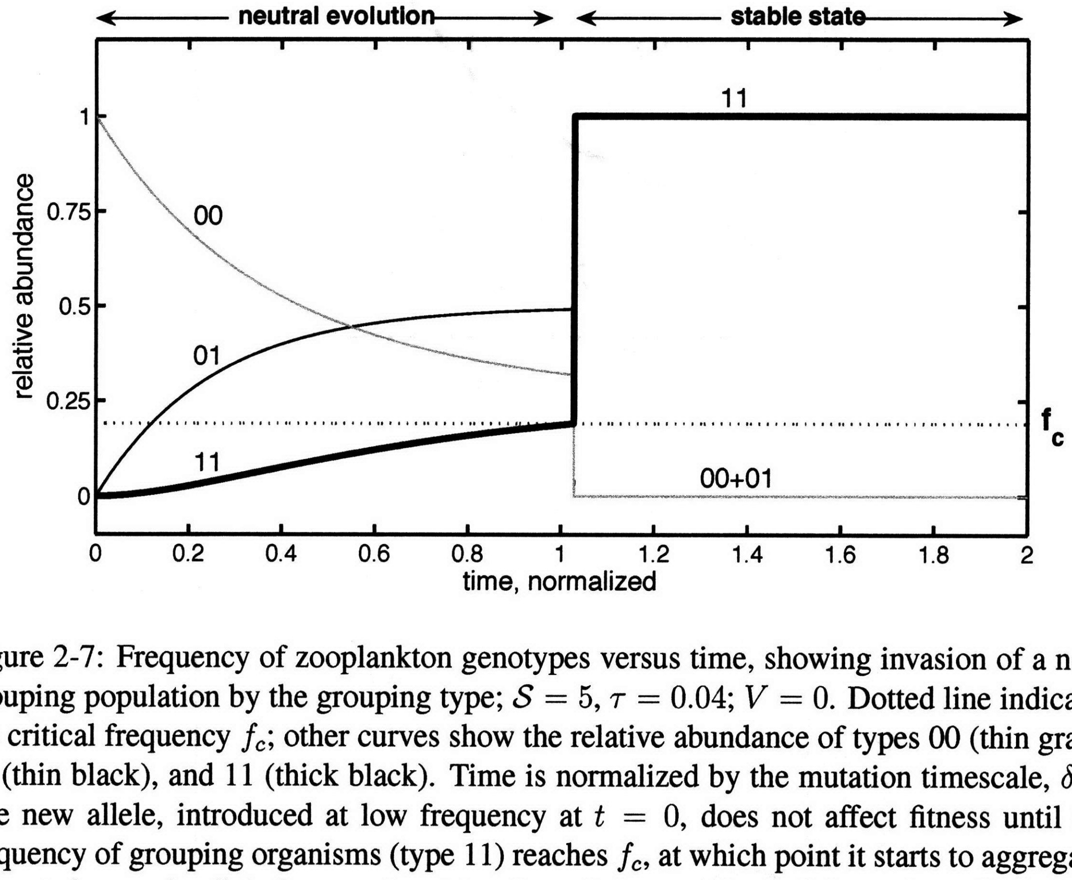

Figure 2-7: Frequency of zooplankton genotypes versus time, showing invasion of a non-grouping population by the grouping type; $\mathcal{S} = 5$, $\tau = 0.04$; $V = 0$. Dotted line indicates the critical frequency f_c; other curves show the relative abundance of types 00 (thin gray), 01 (thin black), and 11 (thick black). Time is normalized by the mutation timescale, δ^{-1}. The new allele, introduced at low frequency at $t = 0$, does not affect fitness until the frequency of grouping organisms (type 11) reaches f_c, at which point it starts to aggregate. Abrupt changes in allele frequencies at $t \approx 1$ result from ecological dynamics, which occur rapidly compared to the mutation timescale; details are shown in Figure 2-8. In this case, social behavior is a successful strategy: the grouping type wins the competition and the other types become extinct. The ecosystem is then stable with respect to mutations in the two-allele model.

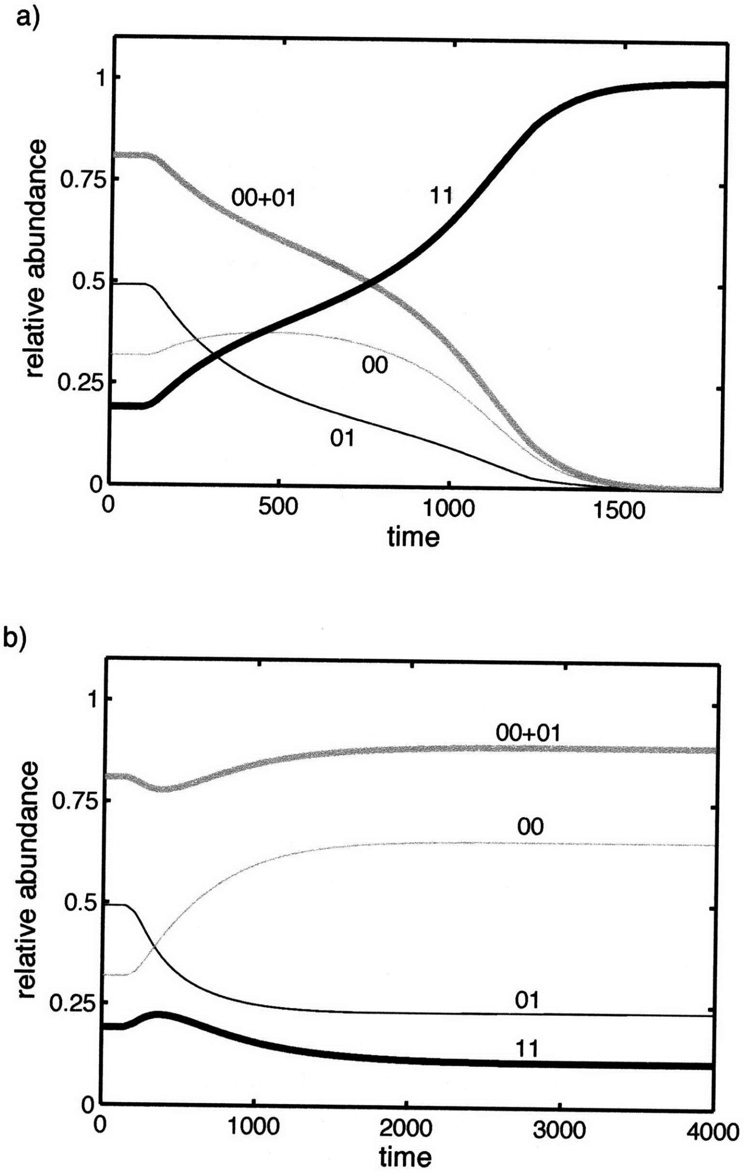

Figure 2-8: Frequency of zooplankton types versus time, for two different values of the parameter τ, with $\mathcal{S} = 5$. a) $\tau = 0.04$, the grouping type (11, thick black curve) outcompetes the resident population (00+01, thick gray curve). b) $\tau = 0.1$, the grouping type aggregates but does not invade the resident population. Decreasing τ has the effect of accelerating mixing relative to predation, thus effectively increasing resource supply to clustered zooplankton. Initially the grouping type represents a fraction f_c of the population.

type can breed with the resident population. Figure 2-7 shows an example of the grouping type ($S = 5$) outcompeting the non-grouping types, in the absence of turbulent advection. Initially set to $f_{00} = 1$, $f_{01} = f_{11} = 0$, the frequencies of genotypes change as a result of mutations. The number of grouping organisms increases slowly, until it crosses the threshold ($f_c = 0.19$) and aggregations suddenly form. In this simulation, social behavior is a successful strategy: the grouping type rapidly takes over, while the others disappear. Details of the competition, which occurs on a much faster timescale than the mutations, are shown in Figure 2-8a and discussed below. For these parameter values, the initial distribution $f_{00} = 1$ is an unstable state with respect to mutations.

The solution $f_{11} = 1$ is a stable state in the two-allele model, it cannot be invaded by the non-grouping types. However, introducing new alleles corresponding to different values of the grouping parameter might be destabilizing. The potential invasion of the (now resident) 11-type by a new type (say, 22) with $S' \neq S$ could be investigated using a framework similar to the one described here (Chapter 3).

2.4.2 Mixing and stirring effects

We find that the competitive ability of the grouping type is strongly affected by the rate of diffusivity, which in the model represents the effect of mixing by unresolved (sub-gridscale) turbulent processes. We vary the parameter τ, which effectively controls the rate at which resources are diffused into the zooplankton aggregations, by accelerating or slowing down the biological activities while keeping advection and diffusion rates constant. Reducing the rate of ingestion of resources partially relieves the resource limitation.

Figure 2-8 shows the changes in abundance of types resulting from ecological processes. At the beginning of the simulation, the frequency of the grouping type is exactly equal to the threshold for aggregations, f_c, and thus starts to aggregate. The fitness of the three genotypes then depends on their ability to eat and reproduce, which is strongly affected by their spatial distribution. Competitive interactions, described by the ecological model, drive changes in the relative abundance of types. Figure 2-8 illustrates the two possible outcomes of the competition. For the parameters of Figure 2-7, the grouping type invades the resident population (Figure 2-8a); but when $\tau = 1$, aggregation is not a successful strategy (Figure 2-8b). Changing the parameters of the model affects the balance between the costs and benefits of aggregating; in the first case, the positive effect resulting from the local abundance of mates drives the evolution of social behavior; in the second case, the negative effect of having to share resources with other group members is the dominant factor.

When the grouping type wins the competition, the types 00 and 01 are eliminated from the population; only the mutant allele remains in the gene pool. In cases where the non-grouping type dominates, however, the 11-type does not disappear from the population. Since the heterozygote does as well as the type 00, both alleles remain in the gene pool; grouping offsprings are produced from mating between heterozygotes. After a transient increase in the number of grouping zooplankton, their frequency decreases until they constitute only a small fraction of the total population; however, those remaining organisms are still found in aggregations. Simulations with different parameter values consistently show that there is a critical value of τ above which the grouping type outcompete the resident non-grouping population. These results highlight the importance of food availability for the survival of aggregated zooplankton.

Turbulent advection also affects the competition between the grouping and non-grouping types, by contributing to the supply of resources to clustered organisms. Zooplankton aggregations can form in turbulent flows when the social behavior is strong enough to overcome the shear of the flow. These aggregations are observed to conserve a circular geometry, even in the presence of the shear. The distribution of phytoplankton, however, is strongly affected by the shear of the flow; grazing creates regions of depleted resources, coinciding with the location of the zooplankton patches. In the model, phytoplankton is passively advected, thus depleted areas are subject to deformation by the flow. The resulting elongation enhances the gradient in phytoplankton density, which accelerates diffusion of resources toward aggregated zooplankton, as shown in Figure 2-9.

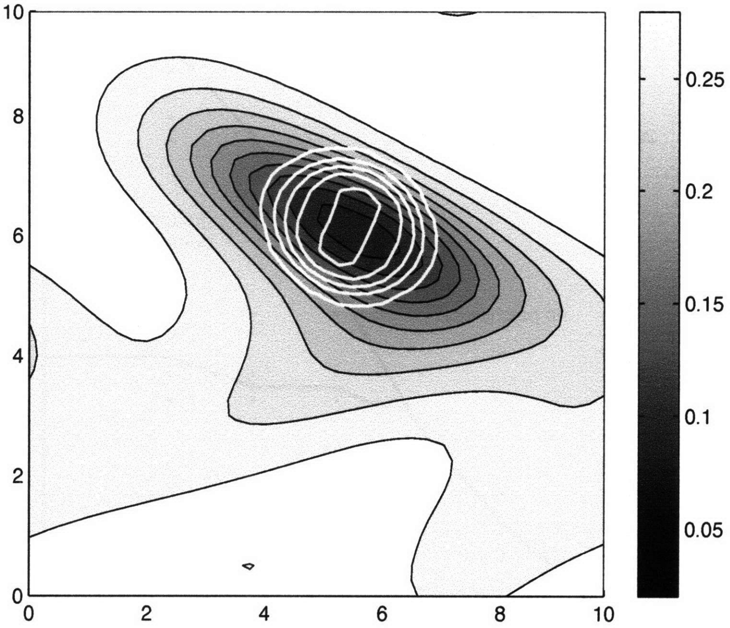

Figure 2-9: Contours of zooplankton biomass, white lines, superimposed on the phytoplankton field, gray shades. This shows stirring of resources by the turbulent field, for parameters $\mathcal{S} = 5$, $\tau = 0.1$, and $V = 5$.

2.4.3 Threshold values of flow and grouping parameter

The competition between grouping and non-grouping types is simulated in various flow conditions, in order to obtain a description of the ecosystem characteristics in parameter space. To avoid the merging of patches resulting from collisions in a turbulent environment, we limit the size of the domain such that a single group forms. The grouping type is introduced at the critical frequency.

Numerical simulations show that turbulent stirring and mixing can lead to dominance of the grouping type for parameters that would not have allowed for dominance in the absence of flow; this is illustrated by the diagram shown in Figure 2-10. For example, with $\mathcal{S} = 8$, $\tau = 0.1$ and $V = 0$ the non-grouping types win the competition, but when $V = 10$ the grouping type dominates. There is a threshold value of the turbulent stirring for which the ecosystem switches between being composed entirely of 11-type, and being

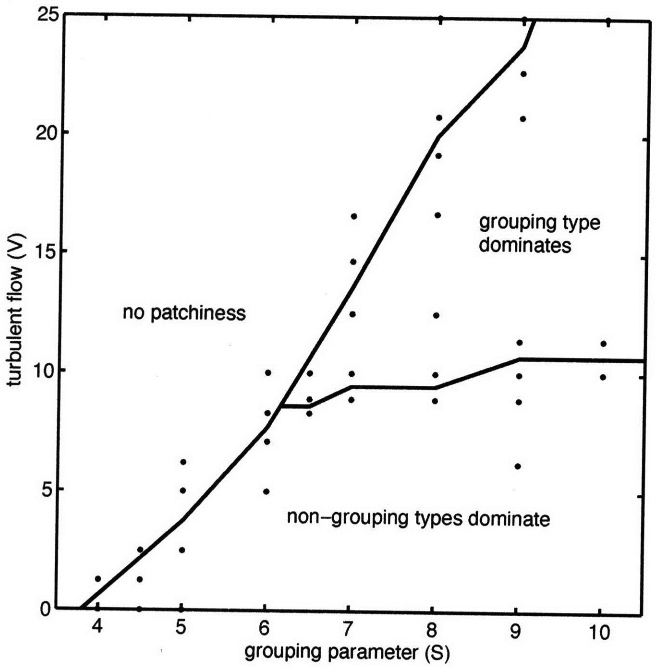

Figure 2-10: Outcome of the competition between grouping and non-grouping types, when the mutant allele is introduced at low density in a resident population of non-grouping organisms. The grouping parameter and strength of turbulent flow are varied; τ is kept constant ($\tau = 0.1$). The domain size is $D = 10$. Solid lines delimitate three distinct regions of parameter space. Except in the region labeled "no patchiness", zooplankton with social behavior spontaneously assemble in dense groups. Without turbulent advection ($V = 0$), they are outcompeted by the non-grouping types and remain a small fraction of the population. Weak flows do not affect the outcome of the competition, but under more turbulent flows the grouping type becomes a better competitor and replaces the non-grouping resident organisms. Black dots indicate parameter values for which numerical simulations were performed.

composed mostly of non-grouping zooplankton. This value is weakly dependent on the grouping parameter.

For small values of $\mathcal{S}$ or large values of the flow strength, f_c is larger than 1/4, the maximum fraction that can result from mutations; the ratio of genotypes thus equilibrates in a $1:2:1$ ratio and zooplankton remain randomly distributed in space. Figure 2-10 shows the range of values for which turbulent stirring and mixing has a positive impact on the success of the grouping type. For the parameters chosen, the grouping type does not dominate in the absence of turbulent advection, and weak flow does not change the outcome of the competition. As the strength of the flow is increased, grouping becomes an advantageous strategy.

In summary, we have found environmental conditions under which the grouping allele successfully invades a non-grouping population. Our results suggest that turbulent flows can promote the evolution of social behavior in a zooplankton population. It should be emphasized that the assumption of density-dependent mating success is critical; when the parameter λ in (2.5) is set to 0 such that reproduction is a linear function of the zooplankton biomass, we find that the grouping type is always outcompeted by the non-grouping types (not shown).

2.5 Adding complexity: life history

The ecosystem described in Section 2.2 is modified to include some aspects of the zooplankton life history. We consider a 2-stage model, which allows us to create a distinction between the behavior of juvenile and adult organisms, as well as separate density-dependent birth events from density-independent growth processes.

The stage-structured model is derived and analyzed in Chapter 1; here we merely add the motion terms. This yields

$$\begin{aligned}
\frac{\partial Z_j}{\partial t} &= \frac{1}{\eta}B(P,Z_a)Z_a - Q(P)Z_j - d_jZ_j + \kappa\nabla^2 Z_j & (2.16)\\
\frac{\partial Z_a}{\partial t} &= \eta Q(P)Z_j - d_aZ_a - \nabla\cdot[\mathbf{u}Z_a - \kappa\nabla Z_a] & (2.17)\\
\frac{\partial P}{\partial t} &= rP\left(1-\frac{P}{K}\right) - \left[\frac{1}{\eta}B(P,Z_a)Z_a + (\eta-1)Q(P)Z_j\right] + \kappa\nabla^2 P & (2.18)
\end{aligned}$$

where the subscripts j and a refer to juveniles and adults, respectively; η is the non-dimensional ratio of adult weight over juvenile weight, and $\mathbf{u}$ is the swimming velocity still given by (2.1). All species are diffusing, but only mature zooplankton exhibit social

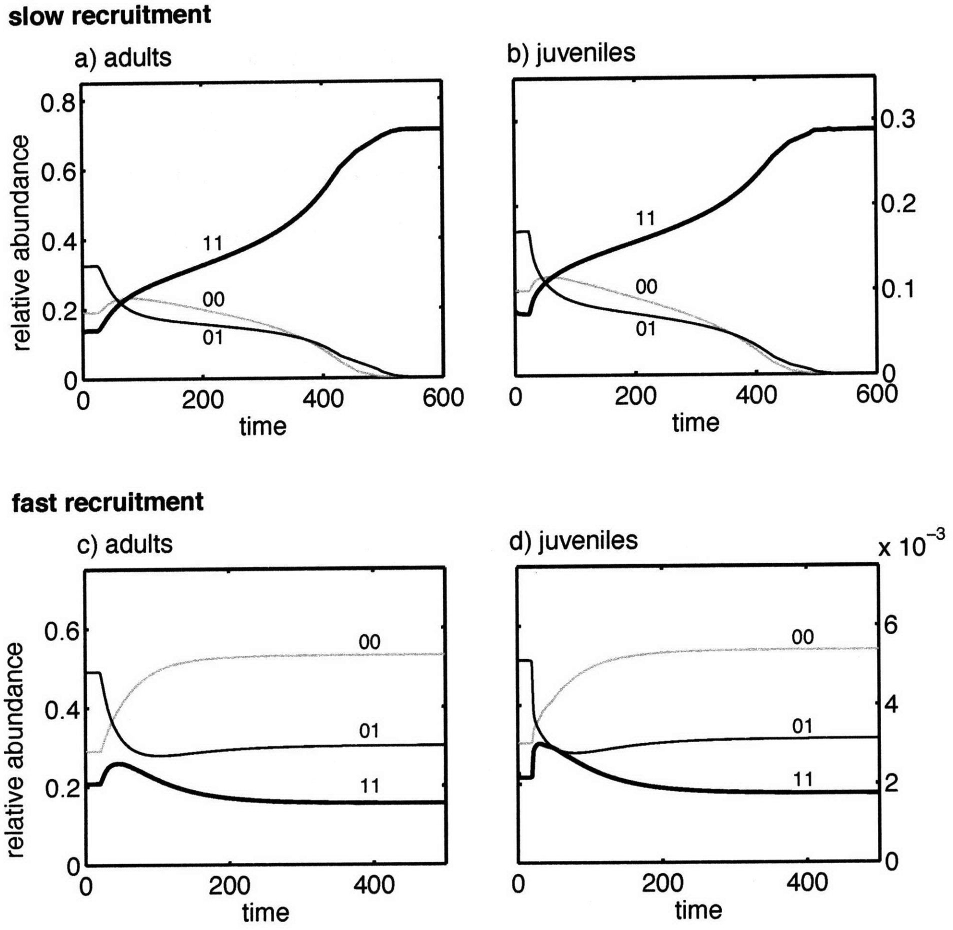

Figure 2-11: Relative abundance of zooplankton versus time in the structured model, for slow recruitment (top) and fast recruitment (bottom). a) and b) $q = 1$: the grouping type (11, thick black curve) outcompetes the resident population (00+01, thin curves); the frequency of the grouping allele increases monotonically in the juvenile and adult populations. c) and d) $q = 100$: the grouping type does not invade the resident population. When recruitment is fast, juveniles are a negligible fraction of the total population so that the model is equivalent to an unstructured predator-prey model.

behavior. Adults give birth to juvenile organisms, which are recruited in the adult class at a rate depending on their consumption of food; we have

$$B = \epsilon b \frac{P}{P + P_h} \Pi(Z_a) \tag{2.19}$$

$$Q = \epsilon q \frac{P}{P + P_h} \tag{2.20}$$

where b is the maximum birth rate, q is the maximum recruitment rate, and the mating probability is now a saturating function of the number of adults, $\Pi = \frac{Z_a}{Z_a + c}$.

We find that adding structure to the zooplankton population increases the success of the grouping strategy. To compare the structured model to the standard predator-prey model, we consider the limit $q \to \infty$, corresponding to instantaneous recruitment. Figure 2-11 shows an example where social behavior evolves in the 2-stage model when recruitment is slow ($q = 1$), but not in the unstructured model (as illustrated in a simulation with very fast recruitment, $q = 100$).

Because juveniles do not exhibit social behavior, they find abundant resources outside the patches; the costs associated with the grouping allele are thus reduced, while the benefits related to reproductive success are maintained. We can identify the flow conditions that favor the evolution of social behavior or that prevent the formation of patches, and obtain a bifurcation diagram qualitatively equivalent to the one presented in Figure 2-10. This leads us to conclude that the multi-stage model behaves qualitatively like the simpler model, and that the features observed in the simulations of Sections 2.3 and 2.4 still hold when more complex life histories are considered.

2.6 Conclusions

In aquatic environments, the spatial distribution of zooplankton is influenced by the behavior of individuals and by variability of the flow. Here we have studied how the interplay between behavior and physics affects the survival of organisms that form social aggregations. This issue is important for understanding the distribution of krill, which exhibit social behavior as well as response to large-scale and mesoscale circulations in the ocean.

We have examined under what environmental conditions grouping behavior represents an advantage for zooplankton, when the factors to balance are competition for resources and mating success. Our biological-physical model explicitly includes a phytoplankton population, in order to capture the effects of resource limitation on the competition between organisms with and without grouping behavior. It is found that the cost of sharing resources with other group members can be balanced by the benefit associated with the abundance of mates, making the grouping strategy a successful adaptation.

Turbulent environments are favorable to the evolution of social behavior, as stirring and mixing by the flow provide resources to the clustered zooplankton. Turbulent advection can also prevent patches from forming if the flow disperses zooplankton faster than they can aggregate, because of the diffusion induced by horizontal shears inherent to the turbulent flow. It should be noted that sheared mean flows do not break aggregations apart in our model; elongated patches tend to align with the mean flow and, because of the periodicity of the domain, become infinitely long. Variability in the direction of sheared flows is essential to disrupt social groups in our simulations. Zhou and Dorland (2004) have argued that horizontal shear controls the spatial scale of krill aggregations; in contrast, we find that the scale and geometry of social groups (if they can form) is independent of the turbulent flow.

Simulated patches in our model have a radius determined by the perception length and roughly equal to twice that distance. This is consistent with the results from the individual-based model of Hofmann et al. (2004). Even assuming that krill have good perception skills, the behavioral mechanism can only account for the formation of relatively small aggregations, of a few meters at most. Interactions between social groups, perhaps involving variability of the flow at different scales, might provide an additional mechanism for the formation of large swarms. Information transfer between group members could effectively increase the perception scale, again leading to wider groups. These effects would need to be large, however, to result in simulated swarms extending horizontally for many kilometers, as those observed in the Southern Ocean.

Many processes contributing to krill patchiness have not been considered in this study. Diurnal cycles of vertical migration keep organisms at a common depth and help maintaining coherent groups (e.g. Zhou and Dorland, 2004). Large-scale environmental gradients also influence the motion of zooplankton organisms searching for food; in the Southern Ocean, three-dimensional circulation patterns as well as sea-ice variability contribute to creating patchiness in the distribution of phytoplankton. Predation by penguins, seals, and other large animals is likely to be density-dependent; whales in particular are highly efficient at detecting aggregations of krill. In Hofmann et al. (2004), it is assumed that the predation risk increases with the local density of aggregations, since predators are attracted by groups. This effect needs to be considered simultaneously with the dilution of predation risk and predator-confusion effects that arise in aggregations. Predation risks in Antarctic krill also depend on the size of organisms and choice of habitat (Alonzo et al., 2003). All these effects, not considered in this study, certainly play a role in the evolution of social behavior in krill.

Perhaps there is seasonal variability in aggregation behavior related to the occurrence of the mating season; this could be incorporated in the model. An improved version of the model would also account for the tendency of individuals to align their orientation with their neighbors, a behavior responsible for the formation of schools, as opposed to "patches," in adult Antarctic krill.

2.7 Appendix A: Genotype frequencies in the two-allele model

Let the frequency of alleles 0 and 1 be q_0 and q_1, respectively. The rate of mutation, ν, is assumed to be the same for both alleles. In continuous-time, the rate of change of the frequencies is given by

$$\frac{\partial q_0}{\partial t} = \nu(q_1 - q_0) \tag{2.21}$$

$$\frac{\partial q_0}{\partial t} = \nu(q_0 - q_1) \tag{2.22}$$

Assuming random mating, the frequency of genotypes is

$$f_{00} = q_0^2 \tag{2.23}$$

$$f_{01} = 2\,q_0 q_1 \tag{2.24}$$

$$f_{11} = q_1^2 \tag{2.25}$$

and thus evolves according to

$$\frac{\partial f_{00}}{\partial t} = 2q_0\frac{\partial q_0}{\partial t} = -2\nu f_{00} + \nu f_{01} \tag{2.26}$$

$$\frac{\partial f_{01}}{\partial t} = 2q_0\frac{\partial q_0}{\partial t} = -2\nu f_{01} + 2\nu f_{00} + 2\nu f_{11} \tag{2.27}$$

$$\frac{\partial f_{11}}{\partial t} = 2q_0\frac{\partial q_0}{\partial t} = -2\nu f_{11} + \nu f_{01} \tag{2.28}$$

In steady-state, $f_{00} = f_{11} = 0.25$, and $f_{01} = 0.5$.

In the ecological model (2.3-2.4), the reproduction term involves multiplication of the zooplankton density by the mating probability; this is written

$$Z\Pi = \frac{Z^2}{Z+c} = \frac{(Z_{00} + Z_{01} + Z_{11})^2}{(Z_{00} + Z_{01} + Z_{11}) + c} \tag{2.29}$$

Table 2.1: Genotypes of offsprings in the one-locus two-allele model. Top row and left column indicate genotypes of the parents.

	00	01	11
00	00	$\frac{1}{2}$00+$\frac{1}{2}$01	01
01	$\frac{1}{2}$00+$\frac{1}{2}$01	$\frac{1}{4}$00+$\frac{1}{2}$01+$\frac{1}{4}$11	$\frac{1}{2}$01+$\frac{1}{2}$11
11	01	$\frac{1}{2}$01+$\frac{1}{2}$11	11

The distribution of offsprings is inferred from assuming Mendelian inheritance (Table 2.1). Equation (2.3) becomes, for each of the three genotypes:

$$\frac{\partial Z_{00}}{\partial t} = \epsilon g \frac{P}{P+P_h}\left({Z_{00}}^2 + Z_{00}Z_{01} + \frac{1}{4}{Z_{01}}^2\right)\frac{1}{Z+c} - dZ_{00} + \kappa\nabla^2 Z_{00} \tag{2.30}$$

$$\frac{\partial Z_{01}}{\partial t} = \epsilon g \frac{P}{P+P_h}\left(Z_{00}Z_{01} + 2\,Z_{00}Z_{11} + \frac{1}{2}{Z_{01}}^2 + Z_{01}Z_{11}\right)\frac{1}{Z+c} - dZ_{01} + \kappa\nabla^2 Z_{01} \tag{2.31}$$

$$\frac{\partial Z_{11}}{\partial t} = \epsilon g \frac{P}{P+P_h}\left({Z_{11}}^2 + Z_{01}Z_{11} + \frac{1}{4}{Z_{01}}^2\right)\frac{1}{Z+c} - dZ_{11} - \nabla\cdot\left(\mathbf{u}_{11}Z_{11} - \kappa\nabla Z_{11}\right) \tag{2.32}$$

assuming that κ is constant.

2.8 Appendix B: Linear stability of the ecological model

We examine the linear stability of the dynamical system (2.10-2.13) around the equilibrium biomass (2.14). Instability implies that groups will form spontaneously in a population of zooplankton that is initially uniformly distributed in space. Small perturbations in the density field will be damped if the system is stable, but will grow in time and become dense patches if it is unstable. Perturbations can be expressed as Fourier modes: $z' = z'\exp(i\mathbf{k}\cdot\mathbf{x})$ and $p' = p'\exp(i\mathbf{k}\cdot\mathbf{x})$, where $\mathbf{k}$ is the horizontal wavenumber (all variables are non-dimensional).

We begin with the assumption that the zooplankton population is composed entirely of individuals with social behavior. The jacobian of (2.10-2.11) evaluated at (2.14) is then

$$\mathbf{M} = \begin{bmatrix} \tau(\gamma G_z - \delta) - |\mathbf{k}|^2(\mathcal{S}\hat{W}\bar{z} - 1) & \tau\gamma G_p \\ -\tau G_z & \tau(1 - \frac{2\bar{p}}{\chi} - G_p) - |\mathbf{k}|^2 \end{bmatrix} \tag{2.33}$$

where we have defined

$$G_p \equiv \frac{1}{(\bar{p}+1)^2}\frac{\bar{z}^2}{\bar{z}+\lambda} \tag{2.34}$$

$$G_z \equiv \frac{\bar{p}}{\bar{p}+1}\frac{\bar{z}^2 + 2\lambda\bar{z}}{(\bar{z}+\lambda)^2} \tag{2.35}$$

and the Fourier transform of W is

$$\hat{W}(\mathbf{k}) \equiv \iint W e^{i\mathbf{k}\cdot\mathbf{x}'} d\mathbf{x}' \tag{2.36}$$

Eigenvalues of the jacobian matrix are interpreted as the linear growth rate of perturbations; if at least one eigenvalue is positive, the system is unstable.

In the limit $\tau \longrightarrow 0$, all non-diagonal terms in (2.33) vanish, implying that zooplankton and phytoplankton dynamics become decoupled. This corresponds to a case where motion is very fast compared to population growth. The expression for zooplankton density is reduced to a 1-dimensional equation, for which the stability criterion is derived in Flierl et al. (1999, section 4.4). Instability occurs for $\mathcal{S}\bar{z}\hat{W} \geq 1$, where $\bar{z}$ is the mean zooplankton concentration ($\bar{\rho}$ in Flierl et al., 1999). This implies that there are minimum values of the grouping parameter and of the density of organisms required for the formation of social aggregations.

Assuming now that only a fraction of the population exhibits social behavior, $\bar{z}$ can be replaced by $f_{11}\bar{z}$ in (2.33), with f_{11} the frequency of grouping type; the new stability criterion is found by solving the eigenvalue problem as above.

Chapter 3

Spatial instability driven by social behavior in predator-prey dynamics

Abstract

Spatial patterns resulting from social interactions between individuals are simulated in an idealized predator-prey model. When the homogeneous distribution of predator density is unstable to small perturbations, patches spontaneously develop; we analyze the growth and nonlinear stabilization of linearly unstable modes, and derive an analytical solution for the self-organized patchiness. Ecological dynamics of the patchy ecosystem are investigated through numerical simulations; oscillations in the predator-prey system can give rise to traveling waves or spatio-temporal chaos in the spatial model, but are damped when motion is fast compared to population dynamics. The implications of patchiness for the evolution of social behavior are addressed by quantifying the relative success of populations with different behaviors; in the model, grouping provides a reproductive advantage, which is traded-off with enhanced competition for resources. The per capita growth rate is linked to the geometry of groups; stronger grouping tendency results in narrower patches, hence high reproduction rate but low food availability. An optimal strategy is associated with intermediate patch sizes.

3.1 Introduction

Social aggregations result from attractive forces between individuals of the same species. The self-organized spatial patterns have significant consequences for ecosystem processes, such as predator-prey interactions. Aggregation of consumers stabilizes oscillatory dynamics in simple predator-prey models by providing a refuge for the prey (Scheffer and de Boer, 1995), although it can also be destabilizing when the prey adapt their behavior in response to changes in the environment (Abrams, 2007).

Grouping is usually thought to be an anti-predator strategy; benefits include dilution of the predation risk and increased collective vigilance (Pulliam, 1973; Foster and Treherne, 1981; see review in Bednekoff and Lima, 1998). On the other hand, groups can be vulnerable to attack by large predators – one might think of whales feeding on patches of krill – so that the success of the strategy likely depends on group size and predator behavior (Connell, 2001). Other advantages include navigational ability for migrating or foraging populations (Simons, 2004) and enhanced mating success in sexually-reproducing populations (McCarthy, 1997). In this paper, we investigate the ecological consequences of self-organized patchiness in a population with social behavior, moving in a homogeneous environment, when the growth rate is positively correlated with population size.

The model, written as a set of reaction-advection-diffusion equations, describes the population dynamics and motion of a predator population interacting with a prey (Section 3.2). It is based on the continuous-field model of Flierl et al. (1999). In Section 3.3, we obtain an approximate solution for the spatial distribution of predator and prey density in steady-state. Social behavior induces the formation of patterns in the density-distribution, which affects the dynamics of the predator-prey system; this is discussed in Section 3.4.

In Section 3.5, we examine how the spatial distribution of the predator population influences individual fitness. This extends the work of Chapter 2, where we simulated the competition between grouping and non-grouping organisms; here we allow for a continuous distribution of phenotypes, with social behavior as an evolvable trait. Optimal strategies are identified through numerical simulations. In the model, social behavior controls the shape of the predator patches; as a consequence of the trade-off between high reproductive success and enhanced intraspecific competition at high densities, the model selects for intermediate patch sizes.

3.2 Motion in a one-dimensional space

3.2.1 The model

We simulate the motion and population dynamics of two interacting species. The predator's movements are driven by social forces, and its reproduction rate increases with population size. The prey is passively diffusing; it grows logistically in a homogeneous environment. The one-dimensional domain is periodic. The dynamics of this system are captured by the following set of equations:

$$\frac{\partial P}{\partial t} = rP\left(1-\frac{P}{K}\right) - G(P,Z)Z + \kappa\nabla^2 P \tag{3.1}$$

$$\frac{\partial Z}{\partial t} = \epsilon G(P,Z)Z - dZ - \nabla(uZ) + \kappa\nabla^2 Z \tag{3.2}$$

where $P = P(x,t)$ and $Z = Z(x,t)$ are the densities of prey and predator, respectively; r is the growth rate of the prey, K is the carrying capacity, ϵ is the assimilation efficiency, d is the mortality rate, and G is the predation function; the diffusivity, κ, is assumed to be constant. We define a weighting function W with characteristic scale L, where L represents the distance at which organisms can sense their environment; W is dimensionless and normalized so that $\int\int W = 1$. The velocity u is given by

$$u = \nabla\phi \tag{3.3}$$

where

$$\phi(x) = W_0 \int W(x')Z(x+x')\,\mathrm{d}x' \tag{3.4}$$

The predation function, G, represents the transfer of biomass from the resource to the predator; a Holling Type II functional response is multiplied by a density-dependent probability function:

$$G(P, Z) = g\frac{P}{P+P_h}\frac{Z}{Z+c} \tag{3.5}$$

where g is the maximum predation rate, and P_h and c are half-saturation densities. The probability $\frac{Z}{Z+c}$ might represent the mating success in sexually-reproducing populations, where the probability of encountering mates is proportional to the population size, giving rise to an Allee effect (the per capita growth rate is positively correlated with density in small populations). In single species models, the mating probability multiplies the birth function (Boukal and Berec, 2002); conservation of biomass in unstructured predator-prey models requires the probability to multiply the resource depletion as well (cf. Chapter 1).

3.2.2 Linear growth of patches

We adimensionalize the model equations by scaling time by r^{-1}, prey biomass by P_h, predator biomass by $P_h r/g$, lengths by L, ϕ by κ, and velocities by κ/L. We introduce some dimensionless parameters: $\gamma = \epsilon g/r$, $\delta = d/r$, $\chi = K/P_h$; λ is the scaled Allee effect constant, and ν is the ratio of the movement timescale to the biological timescale. With lower-case p and z denoting scaled biomasses, we have

$$\frac{\partial p}{\partial t} = p\left(1-\frac{p}{\chi}\right) - \frac{p}{p+1}\frac{z^2}{z+\lambda} + \nu\nabla^2 p \tag{3.6}$$

$$\frac{\partial z}{\partial t} = \gamma\frac{p}{p+1}\frac{z^2}{z+\lambda} - \delta z - \nu\left[\nabla(uz) - \nabla^2 z\right] \tag{3.7}$$

and

$$u = \mathcal{S}\nabla\int W(x')z(x+x')\mathrm{d}x' \tag{3.8}$$

where now a single parameter controls social behavior: S, the ratio of advective timescale to diffusive timescale. The parameter ν is a measure of the diffusion rate of resources[1].

The dynamics of the ecological model without motion ($\nu = 0$) are discussed in Chapter 1. Because of the Allee effect, extinction of the predator is always a stable equilibrium; an additional asymptotic state may exist as a stable coexistence fixed point or a stable limit cycle.

The advection and diffusion terms in the predator equation can induce the formation of spatial patterns in the density field. Patchiness spontaneously appears if the uniform density distribution is unstable to small perturbations; the criterion for instability can be inferred from linear stability analysis (Flierl et al., 1999). In Chapter 2, the formation of patches in the predator-prey model (3.6-3.8) is examined under the assumption that the coexistence equilibrium is stable in the motionless system, in which case the stability problem is solved around steady-state densities. Linear growth of the most unstable mode is illustrated in Figure 3-1.

When the non-spatial model exhibits a limit cycle, the 1-dimensional ecosystem can support stable oscillations, steady-state solutions, traveling waves, and chaotic dynamics. If the motion is fast (small ν), patchiness tends to stabilize coexistence equilibria. The analytical solution for the patchy distribution of predator and prey densities presented in the next section applies to all cases where the ecosystem asymptotically reaches a steady-state.

3.3 Analytical solution for fully-developed patches

Linear theory describes the initial growth of self-organized patches, but nonlinearities become increasingly important as their amplitude becomes larger, breaking the symmetry around the mean density and eventually arresting the growth mechanism. We perform a weakly nonlinear stability analysis to identify stabilizing nonlinear modes, and then find

---

[1] Note that ν is the inverse of the dimensionless parameter τ in Chapter 2: $\nu \equiv \tau^{-1}$

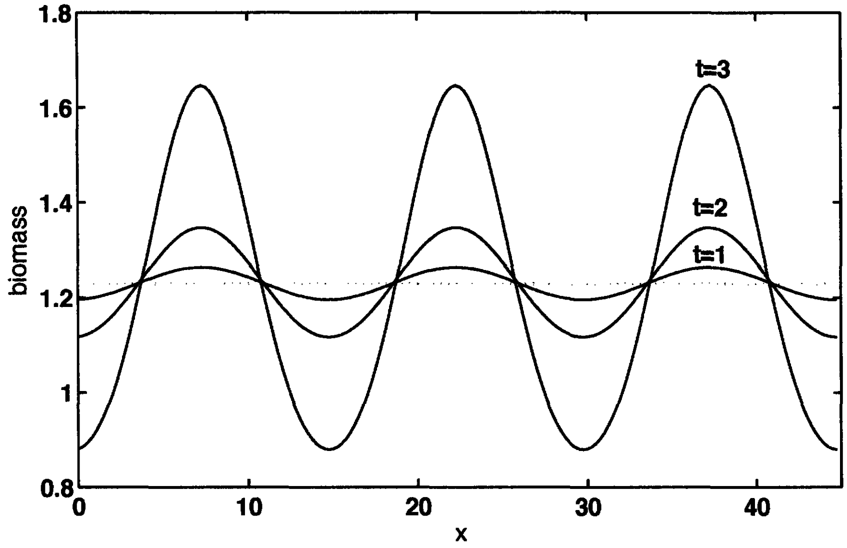

Figure 3-1: Initial growth of patches in the predator distribution. Parameters are $\mathcal{S} = 2$, $\nu = 10$, $\gamma = \lambda = 1$, $\chi = 0.5$, $\delta = 0.1$; the weighting function is $W = e^{-x^2/2} - 1.2e^{-x^2}$. The scale of patchiness is determined by the mode with the largest growth rate. Dotted line indicates mean biomass.

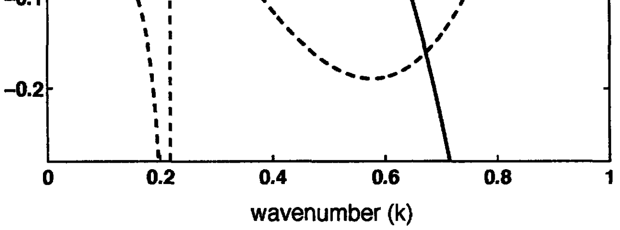

Figure 3-2: Linear growth rate (solid) and nonlinear coefficient (dashed). Population dynamics terms are neglected ($\nu \to \infty$); other parameters as in Figure 3-1. Nonlinearities are stabilizing in the wavenumber region where $\sigma_1 > 0$ and $N < 0$.

analytical solutions to the steady-state patchy distribution. This allows us to quantify the effects of patchiness on the mean densities of predator and prey.

3.3.1 Weakly nonlinear equations

To analyze the nonlinear behavior, we follow the procedure of Flierl et al. (1999), keeping only the terms of order 0, 1 and 2 in the Fourier-decomposition of the biomass:

$$p(\mathbf{x}) = \sum_{n=-2}^{2} p_n e^{in\mathbf{k}\cdot\mathbf{x}} \tag{3.9}$$

$$z(\mathbf{x}) = \sum_{n=-2}^{2} z_n e^{in\mathbf{k}\cdot\mathbf{x}} \tag{3.10}$$

where $\mathbf{k}$ is the wavenumber. These are substituted in the dimensionless equations (3.6-3.8) after making a Taylor expansion of the predation function around the mean biomass; see Appendix 3.7.1 for details of the calculation. Although here we consider a 1-dimensional model, the calculation applies to higher dimensional systems; thus we write $\mathbf{x}$ and $\mathbf{k}$ as vectors. Combining terms, we get a set of coupled equations for the mean, linear mode, and first harmonic:

$$\frac{\partial}{\partial t} z_0 = \gamma G_0 - \delta z_0 \tag{3.11}$$

$$\frac{\partial}{\partial t} z_1 = \gamma G_1 - \delta z_1 + \nu\,|\mathbf{k}|^2 \left[\mathcal{S}\hat{W}(\mathbf{k}) z_1 z_0 - \mathcal{S}\hat{W}(\mathbf{k}) z_1^* z_2 + 2\mathcal{S}\hat{W}(2\mathbf{k}) z_1^* z_2 - z_1\right] \tag{3.12}$$

$$\frac{\partial}{\partial t} z_2 = \gamma G_2 - \delta z_2 + \nu\, 2|\mathbf{k}|^2 \left[\mathcal{S}\hat{W}(\mathbf{k}) z_1^2 + 2\mathcal{S}\hat{W}(2\mathbf{k}) z_0 z_2 - 2z_2\right] \tag{3.13}$$

$$\frac{\partial}{\partial t} p_0 = p_0 - \frac{1}{\chi}(2p_2 p_2^* + 2p_1 p_1^* + p_0^2) - G_0 \tag{3.14}$$

$$\frac{\partial}{\partial t} p_1 = p_1 - \frac{1}{\chi}(2p_1^* p_2 + 2p_0 p_1) - G_1 - \nu\,|\mathbf{k}|^2 p_1 \tag{3.15}$$

$$\frac{\partial}{\partial t} p_2 = p_2 - \frac{1}{\chi}(2p_0 p_2 + p_1^2) - G_2 - \nu\, 4|\mathbf{k}|^2 p_2 \tag{3.16}$$

with

$$\begin{aligned}
G_0 &= \frac{p_0 z_0^2}{(p_0+1)(z_0+\lambda)} - \frac{z_0^2}{(p_0+1)^3(z_0+\lambda)}(2p_2p_2^* + 2p_1p_1^*) \\
&+ \frac{z_0^2 + 2\lambda z_0}{(p_0+1)^2(z_0+\lambda)^2}(p_2z_2^* + p_1z_1^* + p_1^*z_1 + p_2^*z_2) \\
&+ \frac{p_0\lambda^2}{(p_0+1)(z_0+\lambda)^3}(2z_2z_2^* + 2z_1z_1^*) \qquad (3.17) \\
G_1 &= \frac{z_0^2}{(p_0+1)^2(z_0+\lambda)}p_1 + \frac{p_0(z_0^2+2\lambda z_0)}{(p_0+1)(z_0+\lambda)^2}z_1 - \frac{z_0^2}{(p_0+1)^3(z_0+\lambda)}2p_1^*p_2 \\
&+ \frac{z_0^2 + 2\lambda z_0}{(p_0+1)^2(z_0+\lambda)^2}(p_1^*z_2 + p_2z_1^*) + \frac{p_0\lambda^2}{(p_0+1)(z_0+\lambda)^3}2z_1^*z_2 \qquad (3.18) \\
G_2 &= \frac{z_0^2}{(p_0+1)^2(z_0+\lambda)}p_2 + \frac{p_0(z_0^2+2\lambda z_0)}{(p_0+1)(z_0+\lambda)^2}z_2 - \frac{z_0^2}{(p_0+1)^3(z_0+\lambda)}p_1^2 \\
&+ \frac{z_0^2 + 2\lambda z_0}{(p_0+1)^2(z_0+\lambda)^2}p_1z_1 + \frac{p_0\lambda^2}{(p_0+1)(z_0+\lambda)^3}z_1^2 \qquad (3.19)
\end{aligned}$$

where $\hat{W}$ is the Fourier transform of the weighting function, and asterisks denote the complex conjugate. Mean densities are controlled by population dynamics only. Advective and diffusive effects appear in the equations for the first and second Fourier modes, and when ν is large, they are the dominant drivers of the spatial distribution.

Equations (3.11-3.16) are solved for a fixed value of the wavenumber, k. If the system is linearly stable at that wavenumber, then the solution is $z_0 = \bar{z}$, $p_0 = \bar{p}$, $z_1 = z_2 = p_1 = p_2 = 0$, where $\bar{z}$ and $\bar{p}$ are the equilibrium densities of the motionless model; infinitesimal perturbations decay in time and the asymptotic distribution is uniform. If however the system is linearly unstable, a steady-state solution requires that the nonlinear mode be stabilizing. In order to solve the nonlinear stability problem, we assume that motion is fast so that the population dynamics can be neglected in (3.12-3.13). The equation for the first-order perturbations then becomes (Flierl et al., 1999; see also Appendix 3.7.2)

$$\frac{\partial}{\partial t}z_1 = \left[\sigma_1 + N z_1^2\right] z_1 \qquad (3.20)$$

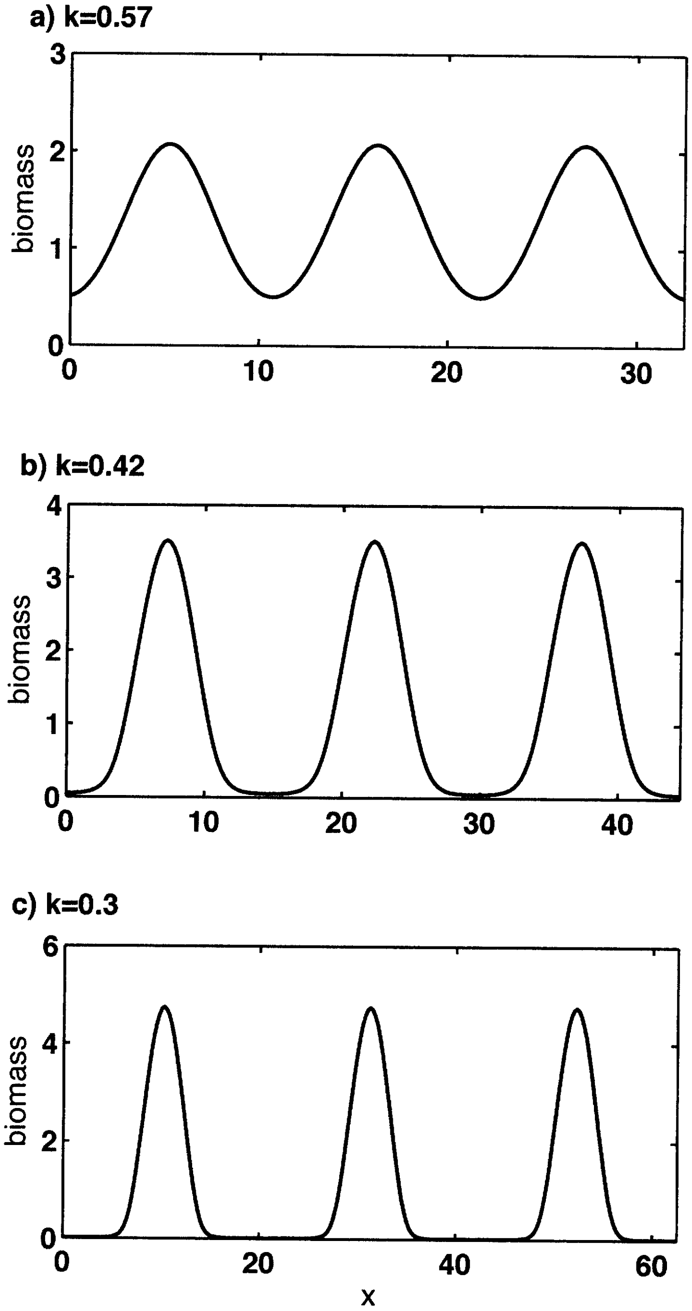

Figure 3-3: Steady-state distribution of predator density. a) $k = 0.57$: subcritical, b) $k = 0.42$: subcritical, but ratio σ_1/N is large, c): $k = 0.3$: supercritical. Parameters as in Figure 3-1.

with the n-th order growth rate defined as

$$\sigma_n = n^2|\mathbf{k}|^2[z_0 S\hat{W}(n\mathbf{k}) - 1] \tag{3.21}$$

and the nonlinear coefficient

$$N = \frac{2|\mathbf{k}|^4 S^2 \hat{W}(\mathbf{k})[2\hat{W}(2\mathbf{k}) - \hat{W}(\mathbf{k})]}{2\sigma_1 - \sigma_2} \tag{3.22}$$

The linear growth rate, σ_1, is shown with N in Figure 3-2. In the wavenumber region $0.3 < k < 0.5$, the system is linearly unstable ($\sigma_1 > 0$) but nonlinearities are stabilizing ($N < 0$); thus allowing (3.20) to reach a positive steady-state. This case is referred to as *subcritical*, as opposed to the *supercritical* case where $N > 0$. As in Flierl et al. (1999), we find that for smaller values of the grouping parameter S, growing waves are long and the nonlinearity is destabilizing around the fastest growing mode.

Numerical simulations help to illustrate the role of nonlinearities in the development of patches. Figure 3-3 shows steady-state distributions in the full model (3.6-3.8). Supercriticality leads to narrow, well-separated patches, whereas subcriticality leads to a smoother, sinusoidal-like pattern. A large ratio σ_1/N indicates that linearly-growing patches reach a larger amplitude before they are stabilized.

3.3.2 Steady-state solutions

The steady-state distribution of biomass can be estimated from the weakly nonlinear equations, which are solved numerically for values of k for which the system is linearly unstable and subcritical. In Figure 3-4a, analytical results are compared with the fully developed patches in the numerical model when a single wavenumber is allowed to grow. More nonlinear modes would be needed to capture the low-density regions between patches, but overall the agreement is very good.

Mean predator densities estimated from the weakly nonlinear equations and those simulated from the numerical model are compared in Table 3.1, for different values of the

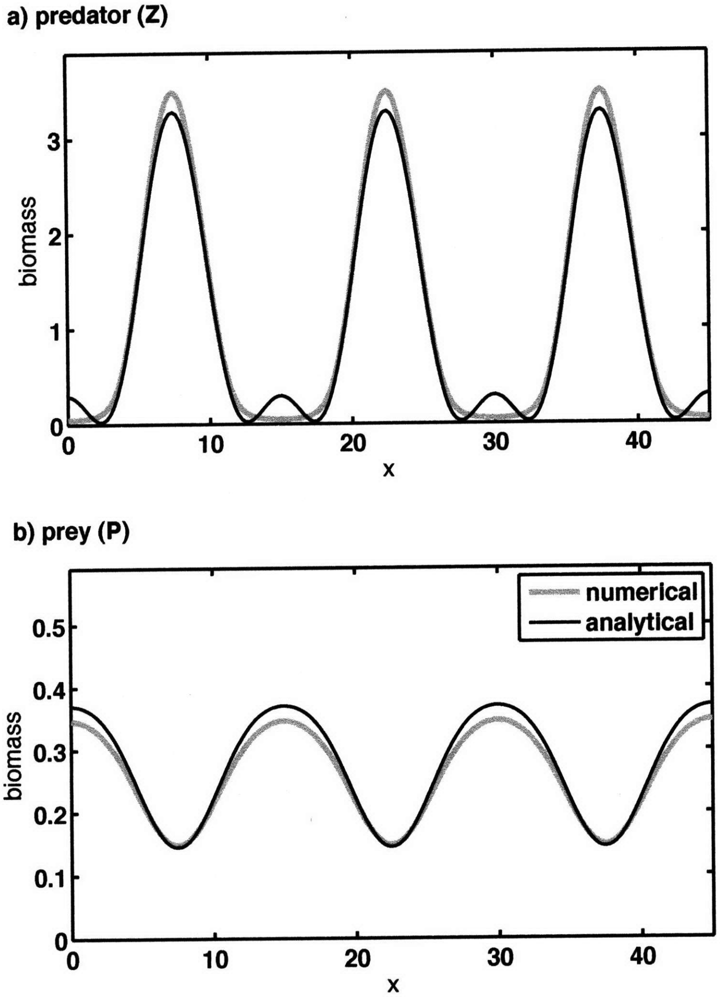

Figure 3-4: Steady-state solution to the weakly nonlinear equations (black line) and fully developed patches in the numerical model (gray line); the system is initially perturbed at a single wavenumber ($k = 0.42$). $\mathcal{S} = 2$; other parameters as in Figure 3-1.

Table 3.1: Predator biomass from numerical model and weakly nonlinear equations, and ratio of linear growth rate to nonlinear coefficient, for different values of the wavenumber. Linear growth rate is positive for all values of k in the table; weakly nonlinear solutions cannot be obtained for positive values of N. Parameters as in Figure 3-4.

	numerical	weakly nonlinear equations			
k	$\overline{Z}$	Z_0	Z_1	Z_2	σ_1/N
0.23	0.73	-	-	-	0.13
0.25	0.79	-	-	-	0.55
0.28	0.87	-	-	-	3.59
0.29	0.90	-	-	-	20.68
0.30	0.92	0.67	0.80	1.14	-7.80
0.35	1.04	0.76	0.75	0.76	-1.55
0.40	1.12	1.08	0.75	0.42	-1.04
0.42	1.14	1.11	0.74	0.34	-0.93
0.45	1.18	1.15	0.74	0.25	-0.78
0.50	1.20	1.20	0.68	0.14	-0.55
0.55	1.23	1.22	0.53	0.06	-0.30

wavenumber in the region of instability. We find that the agreement is best when the ratio σ_1/N is small, meaning that nonlinearities are strongly stabilizing; this is also associated with low values of Z_2. The steady-state density of prey is also captured well by the weakly nonlinear model (Figure 3-4b). Interactions between the two species determine the equilibrium biomass in the patchy ecosystem; clustered predators benefit from the abundance of mates but compete for resources, which grow to carrying capacity in regions where predators are absent. These effects are discussed in the next sections.

3.4 Ecosystem dynamics

Patchiness has significant implications for ecological processes; here we investigate how self-organized social aggregations affect predator-prey interactions in the model. The dynamics of the patchy ecosystem are dependent on the timescale ratio, ν, which compares

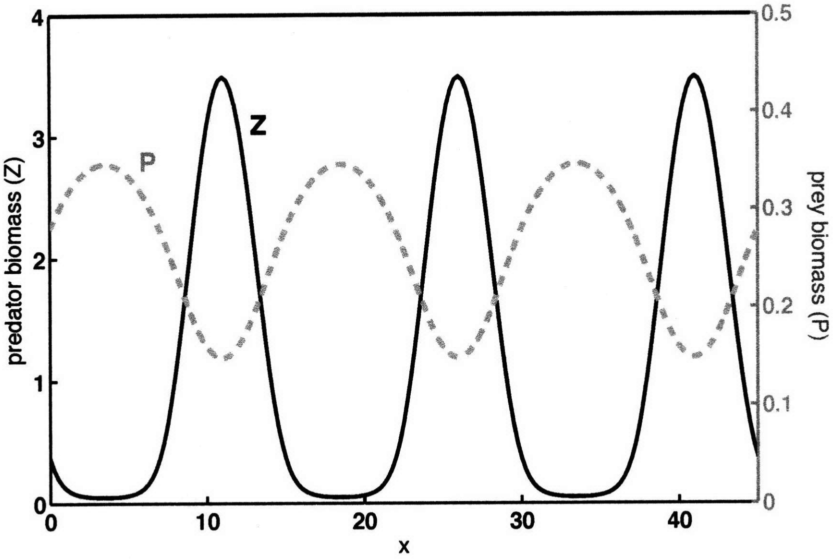

Figure 3-5: Steady-state distribution of prey (dashed gray line) and predator (solid black line) densities. Parameters as in Figure 3-4.

the rate of resource diffusion and resource growth. The cases of fast and slow diffusion are examined separately.

3.4.1 Fast diffusion ($\nu \gg 1$)

When motion is fast compared to population dynamics, aggregation is found to be strongly stabilizing. If patches grow, the average predator and prey densities reach a stable equilibrium and the final spatial distribution is a steady-state, even if the dynamics of the non-spatial model are oscillatory. Patchiness can also allow coexistence when, without motion, the only stable equilibrium is extinction of the predator. Figure 3-5 shows the patchy distributions of predator and prey in steady-state; the spatial patterns are anti-correlated, since the prey grows to high density in regions where the predator is absent but is depleted in predator aggregations. Because diffusions is fast and the distance between patches is relatively short, the maximum prey density is still well below carrying capacity ($\chi = 0.5$ in Figure 3-5).

The constant flux of resources from outside the patches stabilizes the predator-prey dynamics; this is the “refuge” mechanism described by Scheffer and de Boer (1995). The development of patches is controlled by the linear instability described in Section 2.2; then the size of the population adjusts to the amount of resources available, and reaches the steady-state predicted by the weakly nonlinear equations (Section 3.3). An example of the stabilizing effect of patchiness is illustrated in Figure 3-6a,b: without aggregation behavior, the predator-prey system exhibits a limit cycle; self-organized patches in predator biomass result in steady distributions of predator and prey. Parameters and initial conditions are the same in the two panels. Sustained oscillations in the homogeneous system are highlighted by the thick black curve, showing the local density at $x = 0$. In the patchy system, the curve becomes flat once patches are fully developed; the asymptotic density is determined by the spatial location since patches are stationary.

Whether the patchy ecosystem supports more or less biomass than the uniform distribution depends on the parameter values. When the carrying capacity is large, aggregation tends to result in an increase of predator biomass, due to higher efficiency of the refuge mechanism. At low carrying capacity, the Allee effect parameter is the dominant control on the direction of biomass change.

3.4.2 Slow diffusion ($\nu \ll 1$)

In contrast to the case described above, population dynamics play an important role in the development of patches when motion is slow. The predator-prey model can be highly reactive, meaning that it may experience significant transient growth when perturbed (Neubert and Caswell, 1997); spatial dynamics amplify this effect by allowing perturbations to propagate, and indeed long-lasting transients are observed in numerical simulations.

Steady-state distributions are still possible; they occur when social behavior is strong (S is large). The system supports other asymptotic states, however, when the non-spatial model exhibits a limit cycle. For weak social behavior, patch growth rates vary throughout the period of oscillation of the predator-prey model, gaining amplitude when predator den-

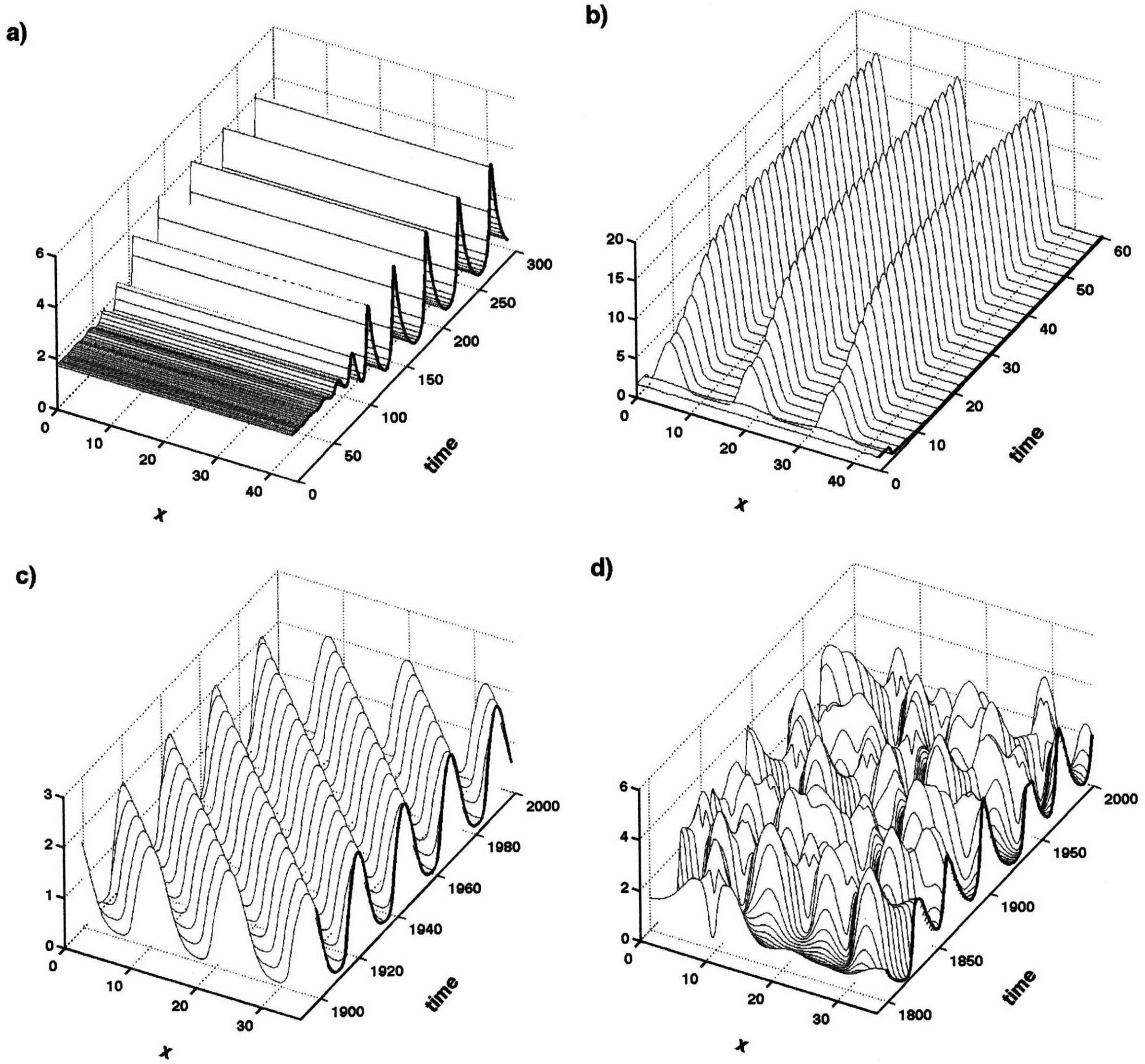

Figure 3-6: Predator biomass in time and space. Thin black contours show the instantaneous spatial distribution, at fixed intervals in time. Thick black curve shows the time series of biomass at a fixed location. a) Without aggregation behavior ($\mathcal{S} = 0$), the predator-prey system reaches a limit cycle after a period of transients; the simulation shown here is initialized near the unstable coexistence fixed point. b) With social behavior ($\mathcal{S} = 2$) and fast diffusion ($\nu = 10$), patches form spontaneously and the system loses its oscillatory behavior. c) With social behavior ($\mathcal{S} = 15$) and slow diffusion ($\nu = 0.05$), the system supports a regular wave traveling through the domain; transients are not shown. d) With social behavior ($\mathcal{S} = 5$) and slow diffusion ($\nu = 0.02$), the density field can appear chaotic. Parameters are, for a, b and d: $\gamma = \lambda = 1$, $\delta = 0.1$, $\chi = 2.5$; for c: $\gamma = 2$, $\lambda = 0.1$, $\delta = 0.2$, $\chi = 1$.

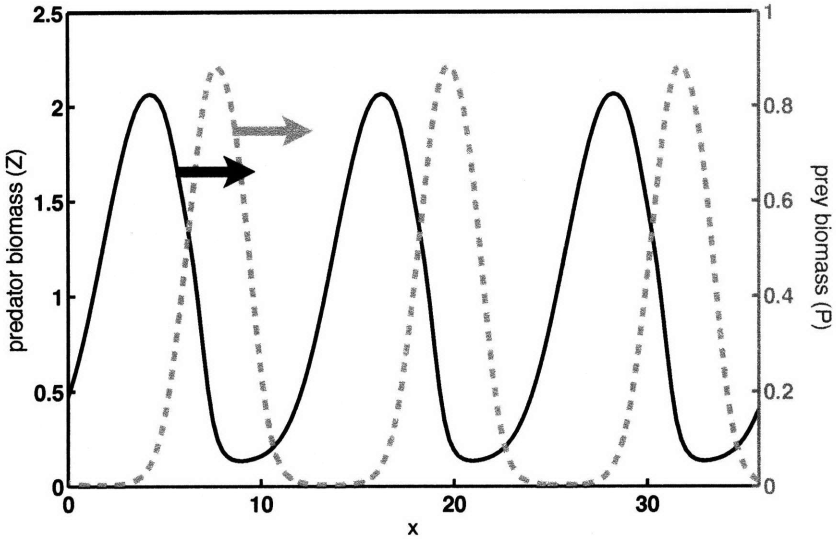

Figure 3-7: Snapshot of a traveling wave in the distribution of prey (dashed gray line) and predator (solid black line) densities. Parameters as in Figure 3-6c.

sities are high, but decaying when it is low; patchiness never fully develops and oscillations persist. For intermediate values of the behavior parameter, traveling waves may form after a period of transients; or the transients seem to never die out, and the dynamics of the spatial system appear chaotic. These two scenarios are illustrated in Figure 3-6c,d (the initial period of transients occurring while patches develop is not shown). During transients, and when the system exhibits spatio-temporal chaos, the mean densities of predator and prey fluctuate randomly in time. The density at a fixed spatial location is also chaotic, as hinted by the thick black line in Figure 3-6d. When a regular wave develops, the local density oscillates in time (thick black line in Figure 3-6c), but the spatial mean is constant.

Traveling waves of predator biomass are found to lag traveling waves of prey biomass; the two fields are not anti-correlated as in steady-state, instead they are slightly out of phase (Figure 3-7). The maximum of prey biomass is roughly aligned with the front of the predator wave. These propagating patterns are also observed when $\nu \approx 1$, whereas chaos only results from very small values of ν.

Although slowly diffusing systems present some interesting dynamics, in the remainder of this paper we will focus on cases where motion is fast compared to predator-prey dynamics, which might be more relevant for planktonic ecosystems.

3.5 Swarming as a strategy for survival

Social behavior clearly has important implications for the dynamics of predator-prey systems, but how does it affect survival of the grouping population? In our model, aggregated individuals experience a trade-off between enhanced reproductive success due to the abundance of conspecifics, and competition for resources between group members. We quantify these benefits and costs by simulating the competition for resources between populations of predator with different grouping behaviors, as determined by the parameter S. It is already known that an Allee effect is necessary for grouping to represent an advantageous adaptation (cf. Chapter 2), when the model does not account for higher-order predation or other positive density-dependent effects.

In this section we search for optimal values of the parameter controlling social behavior. The geometry of self-organized patches depends on S, larger values of the parameter being associated with narrower patches and higher peak densities (Figure 3-8a). We begin by describing the set-up for simulations, then present results suggesting that the optimal behavior corresponds to intermediate values of S when environmental conditions are mediocre, whereas in favorable conditions (when resources are plentiful and reproductive success is high even at low density), not aggregating is the best strategy.

3.5.1 Competition model

The model used to simulate competition is based on the one described in Section 2.2, but we now have two types of predators, z_a and z_b. It is assumed that organisms do not distinguish between types when they seek to reproduce or move toward their neighbors. It is also assumed that the type of offsprings is determined by the type of the parent – implying that the population is either reproducing asexually, or that a single sex is accounted for by the model equations and that both sexes are equally abundant. The dimensionless equations are

$$\begin{aligned} \frac{\partial z_a}{\partial t} &= \gamma \frac{p}{p+1} \Pi z_a - \delta z_a - \nu \left[\nabla (u_a z_a) - \nabla^2 z_a \right] && (3.23) \\ \frac{\partial z_b}{\partial t} &= \gamma \frac{p}{p+1} \Pi z_b - \delta z_b - \nu \left[\nabla (u_b z_b) - \nabla^2 z_b \right] && (3.24) \\ \frac{\partial p}{\partial t} &= p \left(1 - \frac{p}{\chi} \right) - \frac{p}{p+1} \Pi (z_a + z_b) + \nu \nabla^2 p && (3.25) \end{aligned}$$

where the density-dependent probability of reproducing is

$$\Pi \equiv \frac{z_a + z_b}{z_a + z_b + \lambda} \tag{3.26}$$

The advective velocity

$$u_{(a,b)} = S_{(a,b)} \nabla \int W(x') \left[z_a(x + x') + z_b(x + x') \right] \mathrm{d}x' \tag{3.27}$$

is directed up the gradient of the (weighted) total predator density, resulting in the formation of “mixed” patches in which both types coexist. We assume that there is no cost directly associated with social movements. Fitness of the two competing types is measured by their respective per capita growth rate, when competing for a common resource.

To first order, both types have the same fitness, determined by the spatial distribution of the total predator population. This is explained by the fact that both reproductive success and competition for resources depend on $z_a + z_b$. A population of two equally abundant types has a distribution that lies between that produced by each type independently (Figure 3-8a). However, organisms with strong social behavior are more abundant near the center of patches, and organisms with weak social behavior tend to occupy the edges (Figure 3-8b). This difference produces distinct values of fitness, and although the difference is small, it gives an advantage to one of the competitors.

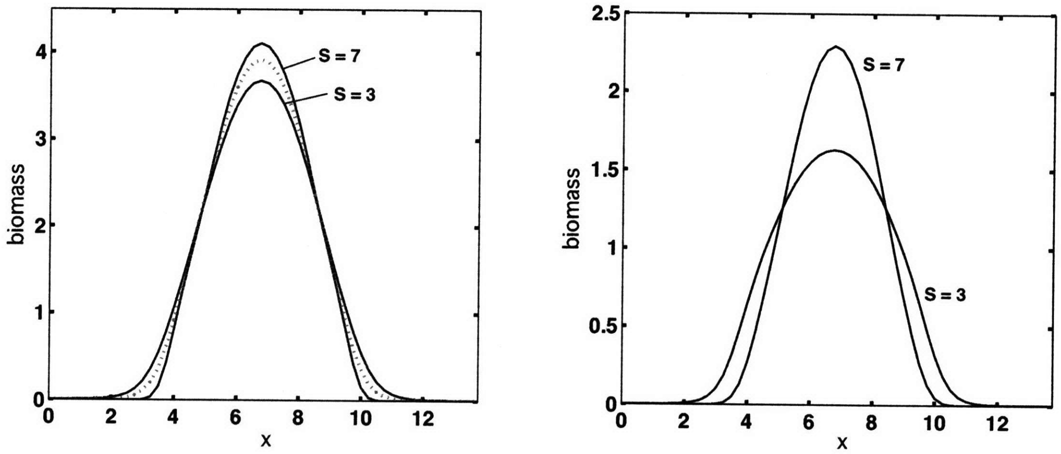

Figure 3-8: Steady-state distributions of predator density. Left: in the predator-prey model (3.6-3.8), the distributions for $\mathcal{S} = 3$ and $\mathcal{S} = 7$ (obtained from two different simulations) are compared. Dotted curve shows the distribution of a mixed population (the two types are interacting). Right: in the competition model, both types form a single patch; the type with stronger social behavior is the most abundant near the center of the patch, and the one with weaker social behavior is the most abundant type near the edges. The total predator biomass is given by the dotted curve in the left panel. Parameters are $\gamma = 1$, $\chi = \lambda = 0.5$, $\delta = 0.1$, $\nu = 10$, $k = 0.45$.

The relative abundance of a type within a patch also plays a role in its success as a competitor, since fitness is a nonlinear function of the local density. To avoid dealing with this frequency-dependence, we initialize the simulations with a 1:1 ratio of types. After a period of transients following the development of patches, the frequency of one of the types increases slowly but steadily. We identify the best competitor as the type with positive per capita growth rate.

3.5.2 Optimal strategies

When a continuous distribution of types is considered, competition between strategies can give some insight on the evolutionary dynamics of social behavior. Let's consider two

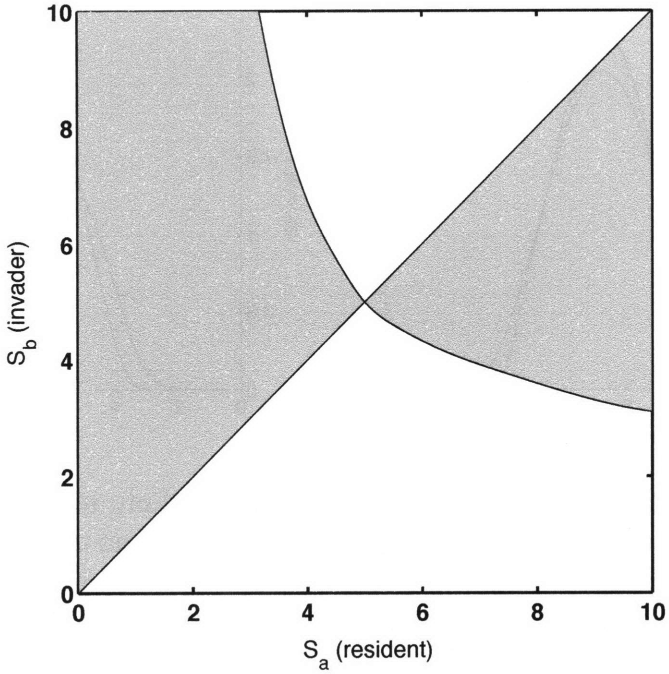

Figure 3-9: Pair-wise competition diagram; gray shading indicates that type b (y-axis) outcompetes type a (x-axis). $\mathcal{S} = 5$ is optimal. Parameters as in Figure 3-8.

types, $\mathcal{S}_a$ and $\mathcal{S}_b = \mathcal{S}_a + \Delta\mathcal{S}$, where $\Delta\mathcal{S}$ is small. These can be thought of as a resident population and a potential invader, or as a single population with adaptive behavior. If strategy b outcompetes strategy a, then eventually the whole population will be of type b; we can repeat the competition experiment to find out if it is in turn outcompeted by type c with $\mathcal{S}_c = \mathcal{S}_b + \Delta\mathcal{S}$. If b is a better competitor than both a and c, then it is the *optimal* strategy.

The pair-wise competition diagram of Figure 3-9 reveals that such an optimal exists in the predator-prey model with Allee effect. For the parameters considered, it corresponds to an intermediate value of the grouping parameter, $\mathcal{S} = 5$. Gray shading indicates that type a (x-axis) outcompetes type b (x-axis). The diagram is anti-symmetric along the diagonal

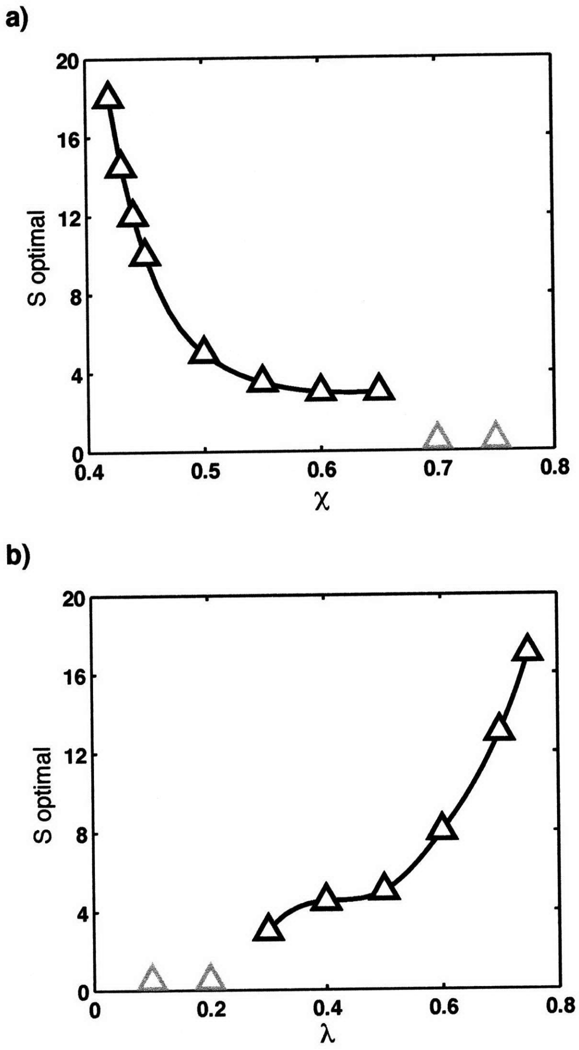

Figure 3-10: Optimal strategy vs a) the enrichment parameter, χ, and b) the Allee effect parameter, λ. Black symbols indicate optimal value of $\mathcal{S}$ from numerical simulations of the competition model, solid line is the spline interpolation. Gray symbols indicate that social behavior is not a successful strategy, in which case non-grouping types (which have $\mathcal{S}$ small enough for the uniform distribution to be stable) are the best competitors. Other parameters as in Figure 3-8.

$\mathcal{S}_a = \mathcal{S}_b$, because the two types were initialized at equal densities.

We've repeated the experiment for different values of the parameters describing environmental conditions: the enrichment parameter, χ, and the Allee effect parameter, λ (Figure 3-10). High values of χ and small values of λ imply that resources are abundant and reproductive success is high, thus indicating an environment in which the predator population thrives; such conditions favor the non-grouping types. In contrast, social behavior is a successful adaptation in environments where resources and/or mates are scarce.

Social organisms do well in the competition when reproduction is strongly density-dependent, which occurs when the equilibrium density $\bar{z}$ is small compared to the Allee effect parameter λ so that the mating probability $z/(z + \lambda)$ is nearly linear. However, denser aggregations (resulting from large values of $\mathcal{S}$) are not necessarily better, since the competition is intensified while the reproductive benefits saturate at high density. The optimal strategy is associated with intermediate values of $\mathcal{S}$, and thus intermediate patch sizes (Figure 3-10).

3.6 Summary

Social behavior drives the formation of animal aggregations. The tendency to move toward conspecifics can be expressed mathematically; a simple model that include this movement rule captures the spontaneous formation of social groups resulting from instability of the uniform distribution (Flierl et al., 1999; see also Chapter 2). In this paper, the model is adapted to include the dynamics of the social population and its interactions with a prey, which are strongly affected by the spatial distribution of biomass. A set of coupled partial differential equations is obtained, with reactions term describing the population dynamics, diffusion for both species, and an advection term for the predator; this advective component represents the movement driven by social behavior.

Asymptotic states supported by the model include stable coexistence, traveling waves of predator and prey density, and spatio-temporal chaos. However, when the population dynamics are slow compared to individual motion, aggregation tends to stabilize the predator-prey dynamics. In steady-state, the simulated predator population is organized into well-defined aggregations, in which the peak density is several times larger than the mean density. These overlay regions of low prey density, the result of many predators feeding in the same location. An approximate solution for the steady-state spatial patterns in predator and prey biomass can also be obtained by transforming the predator and prey equations into a set of ordinary differential equations. These can be solved much more easily than the original model, and the solution captures well the sharp gradients in predator density as well as the resource depletion within aggregations.

The model can also be used to address the ecological consequences of social behavior. Because reproduction is assumed to be both food-dependent and density-dependent, aggregation results in a trade-off between the benefit associated with the local abundance of mates and the cost of having to share resources with other group members. The balance between these positive and negative effects, which determines whether social behavior is a successful strategy, depends on the spatial distribution of organisms as well as the environmental conditions.

3.7 Appendix: Weakly nonlinear stability analysis

3.7.1 Full ecosystem

To do a nonlinear stability analysis, we consider solutions to the model equations of the form

$$
\begin{aligned}
p(\mathbf{x}) &= \sum_n p_n e^{in\mathbf{k}\cdot\mathbf{x}} && (3.28)\\
z(\mathbf{x}) &= \sum_n z_n e^{in\mathbf{k}\cdot\mathbf{x}} && (3.29)
\end{aligned}
$$

and truncate the solution, keeping only the mean and the first two Fourier modes. The model equations are separated into biological activities (reaction terms) and motion (advection and diffusion terms):

$$
\begin{aligned}
\frac{\partial p_n}{\partial t} &= \tau B_{p_n} + M_{p_n} && (3.30)\\
\frac{\partial z_n}{\partial t} &= \tau B_{z_n} + M_{z_n} && (3.31)
\end{aligned}
$$

We define a predation term: $G = \frac{pz}{(p+1)(z+\lambda)}$. Predator and prey densities are decomposed into mean and perturbations: $z = \overline{z} + z'$ and $p = \overline{p} + p'$; then we do a Taylor expansion around the mean:

$$
\begin{aligned}
G &\approx G(\overline{p},\overline{z}) + G_p p' + G_z z' + \frac{1}{2}G_{pp}(p')^2 + G_{pz}p'z' + \frac{1}{2}G_{zz}(z')^2 && (3.32)\\
&\approx \frac{\overline{pz}}{(\overline{p}+1)(\overline{z}+\lambda)} + \frac{\overline{z}^2}{(\overline{p}+1)^2(\overline{z}+\lambda)^2}p' + \frac{\overline{p}(\overline{z}^2+2\lambda\overline{z})}{(\overline{p}+1)(\overline{z}+\lambda)^2}z' - \frac{\overline{z}^2}{(\overline{p}+1)^3(\overline{z}+\lambda)}(p')^2\\
&\quad + \frac{\overline{z}^2+2\lambda\overline{z}}{(\overline{p}+1)^2(\overline{z}+\lambda)^2}p'z' + \frac{\lambda^2 p}{(\overline{p}+1)(\overline{z}+\lambda)^3}(z')^2 && (3.33)
\end{aligned}
$$

We substitute

$$p(\mathbf{x}) = p_{-2}e^{-2i\mathbf{k}\cdot\mathbf{x}} + p_{-1}e^{-i\mathbf{k}\cdot\mathbf{x}} + p_0 + p_1e^{i\mathbf{k}\cdot\mathbf{x}} + p_2e^{2i\mathbf{k}\cdot\mathbf{x}} \tag{3.34}$$

$$z(\mathbf{x}) = z_{-2}e^{-2i\mathbf{k}\cdot\mathbf{x}} + z_{-1}e^{-i\mathbf{k}\cdot\mathbf{x}} + z_0 + z_1e^{i\mathbf{k}\cdot\mathbf{x}} + z_2e^{2i\mathbf{k}\cdot\mathbf{x}} \tag{3.35}$$

into

$$\frac{dz}{dt} = \gamma G - \delta z \tag{3.36}$$

$$\frac{dp}{dt} = p\left(1 - \frac{p}{\chi}\right) - G \tag{3.37}$$

with $\overline{z} \equiv z_0$, $P' \equiv z_{-2}e^{-2i\mathbf{k}\cdot\mathbf{x}} + z_{-1}e^{-i\mathbf{k}\cdot\mathbf{x}} + z_1e^{i\mathbf{k}\cdot\mathbf{x}} + z_2e^{2i\mathbf{k}\cdot\mathbf{x}}$, and the same for p.

Grouping terms with similar exponents, we get

$$\begin{aligned} B_{z_0} = {} & \gamma\Big[\frac{p_0z_0^2}{(p_0+1)(z_0+\lambda)} - \frac{z_0^2}{(p_0+1)^3(z_0+\lambda)}(2p_2p_2^* + 2p_1p_1^*) \\ & + \frac{z_0^2+2\lambda z_0}{(p_0+1)^2(z_0+\lambda)^2}(p_2z_2^* + p_1z_1^* + p_1^*z_1 + p_2^*z_2) \\ & + \frac{p_0\lambda^2}{(p_0+1)(z_0+\lambda)^3}(2z_2z_2^* + 2z_1z_1^*)\Big] - \delta z_0 \end{aligned} \tag{3.38}$$

$$\begin{aligned} B_{z_1} = {} & \gamma\Big[\frac{z_0^2}{(p_0+1)^2(z_0+\lambda)}p_1 + \frac{p_0(z_0^2+2\lambda z_0)}{(p_0+1)(z_0+\lambda)^2}z_1 - \frac{z_0^2}{(p_0+1)^3(z_0+\lambda)}2p_1^*p_2 \\ & + \frac{z_0^2+2\lambda z_0}{(p_0+1)^2(z_0+\lambda)^2}(p_1^*z_2 + p_2z_1^*) + \frac{p_0\lambda^2}{(p_0+1)(z_0+\lambda)^3}2z_1^*z_2\Big] - \delta z_1 \end{aligned} \tag{3.39}$$

$$\begin{aligned} B_{z_2} = {} & \gamma\Big[\frac{z_0^2}{(p_0+1)^2(z_0+\lambda)}p_2 + \frac{p_0(z_0^2+2\lambda z_0)}{(p_0+1)(z_0+\lambda)^2}z_2 - \frac{z_0^2}{(p_0+1)^3(z_0+\lambda)}p_1^2 \\ & + \frac{z_0^2+2\lambda z_0}{(p_0+1)^2(z_0+\lambda)^2}p_1z_1 + \frac{p_0\lambda^2}{(p_0+1)(z_0+\lambda)^3}z_1^2\Big] - \delta z_2 \end{aligned} \tag{3.40}$$

$$\begin{aligned} B_{p_0} = {} & p_0 - \frac{1}{\chi}(2p_2p_2^* + 2p_1p_1^* + p_0^2) - \Big[\frac{p_0z_0^2}{(p_0+1)(z_0+\lambda)} - \frac{z_0^2}{(p_0+1)^3(z_0+\lambda)}(2p_2p_2^* + 2p_1p_1^*) \\ & + \frac{z_0^2+2\lambda z_0}{(p_0+1)^2(z_0+\lambda)^2}(p_2z_2^* + p_1z_1^* + p_1^*z_1 + p_2^*z_2\Big] \\ & + \frac{p_0\lambda^2}{(p_0+1)(z_0+\lambda)^3}(2z_2z_2^* + 2z_1z_1^*)) \end{aligned} \tag{3.41}$$

$$\begin{aligned}
B_{p_1} &= p_1 - \frac{1}{\chi}(2p_1^* p_2 + 2p_0 p_1) - \Big[\frac{z_0^2}{(p_0+1)^2(z_0+\lambda)} p_1 + \frac{p_0(z_0^2+2\lambda z_0)}{(p_0+1)(z_0+\lambda)^2} z_1 \\
&\quad - \frac{z_0^2}{(p_0+1)^3(z_0+\lambda)} 2p_1^* p_2 + \frac{z_0^2+2\lambda z_0}{(p_0+1)^2(z_0+\lambda)^2}(p_1^* z_2 + p_2 z_1^*) \\
&\quad + \frac{p_0\lambda^2}{(p_0+1)(z_0+\lambda)^3} 2z_1^* z_2\Big] && (3.42) \\
B_{p_2} &= p_2 - \frac{1}{\chi}(2p_0 p_2 + p_1^2) - \Big[\frac{z_0^2}{(p_0+1)^2(z_0+\lambda)} p_2 + \frac{p_0(z_0^2+2\lambda z_0)}{(p_0+1)(z_0+\lambda)^2} z_2 \\
&\quad - \frac{z_0^2}{(p_0+1)^3(z_0+\lambda)} p_1^2 + \frac{z_0^2+2\lambda z_0}{(p_0+1)^2(z_0+\lambda)^2} p_1 z_1 + \frac{p_0\lambda^2}{(p_0+1)(z_0+\lambda)^3} z_1^2\Big] && (3.43)
\end{aligned}$$

A similar procedure (without the Taylor expansion) applies for the motion terms, see Flierl et al. (1999);

$$\begin{aligned}
M_{z_0} &= 0 && (3.44) \\
M_{z_1} &= |\mathbf{k}|^2(\mathcal{S}\hat{W}(\mathbf{k}) z_0 z_1 + 2\mathcal{S}\hat{W}(2\mathbf{k}) z_1^* z_2 - \mathcal{S}\hat{W}(\mathbf{k}) z_1^* z_2 - z_1) && (3.45) \\
M_{z_2} &= 2|\mathbf{k}|^2(2\mathcal{S}\hat{W}(2\mathbf{k}) z_0 z_2 + \mathcal{S}\hat{W}(\mathbf{k}) z_1^2 - 2z_2) && (3.46) \\
M_{p_0} &= 0 && (3.47) \\
M_{p_1} &= -|\mathbf{k}|^2 p_1 && (3.48) \\
M_{p_2} &= -4|\mathbf{k}|^2 p_2 && (3.49)
\end{aligned}$$

The full weakly nonlinear equations are given by the sum of (3.38)-(3.43) and (3.44)-(3.49).

3.7.2 No population dynamics

We examine the motion-only equations by setting $\nu \longrightarrow \infty$, so that the predator equations reduce to $\frac{\partial z_n}{\partial t} = M_{z_n}$. The procedure of Flierl et al. (1999) is followed. (3.45) and (3.46) can be written

$$\frac{\partial}{\partial t} z_1 = \sigma_1 z_1 + |\mathbf{k}|^2 (2\mathcal{S}\hat{W}(2\mathbf{k}) - \mathcal{S}\hat{W}(\mathbf{k})) z_1^* z_2 \tag{3.50}$$

$$\frac{\partial}{\partial t} z_2 = \sigma_2 z_2 + 2|\mathbf{k}|^2 \mathcal{S}\hat{W}(\mathbf{k}) z_1^2 \tag{3.51}$$

with σ_n being the growth rate for perturbations of order n. For a steady-state solution to exist, it is required that $\sigma_2 < 0$, in which case a solution of the form $z_2 = R z_1^2$ is expected. Substituting this into (3.50) and (3.51) yields

$$\frac{\partial}{\partial t} z_1 = \sigma_1 z_1 + |\mathbf{k}|^2 (2\mathcal{S}\hat{W}(2\mathbf{k}) - \mathcal{S}\hat{W}(\mathbf{k})) R z_1^* z_1^2 \tag{3.52}$$

$$R \frac{\partial}{\partial t} z_1^2 = \sigma_2 R z_1^2 + 2|\mathbf{k}|^2 \mathcal{S}\hat{W}(\mathbf{k}) z_1^2 \tag{3.53}$$

This system of equations can be solved for R by substituting (3.52) into (3.53),

$$R = \frac{2|\mathbf{k}|^2 \mathcal{S}\hat{W}(\mathbf{k})}{2\sigma_1 - \sigma_2} z_1^2 + O(z_1^4) \tag{3.54}$$

so that, neglecting high order terms:

$$z_2 \approx \frac{2|\mathbf{k}|^2 \mathcal{S}\hat{W}(\mathbf{k})}{2\sigma_1 - \sigma_2} z_1^2 \tag{3.55}$$

and (3.52) becomes

$$\frac{\partial}{\partial t} z_1 = [\sigma_1 + N z_1^2] z_1 \tag{3.56}$$

where

$$N = \frac{2|\mathbf{k}|^4 \mathcal{S}^2 \hat{W}(\mathbf{k})[2\hat{W}(2\mathbf{k}) - \hat{W}(\mathbf{k})]}{2\sigma_1 - \sigma_2} \tag{3.57}$$

The growth rates σ_1 and σ_2 are given by (3.21).

Chapter 4

Collective motion in a variable environment: Does schooling behavior improve foraging success?

Abstract

Schooling is the large-scale expression of attraction and alignment forces acting at the level of individuals; the behavior has evolved in many species of fish and large zooplankton, such as Antarctic krill. I simulate schooling behavior in an individual-based model to investigate the ecological consequences of collective motion in krill. There are two parts to this chapter. The first deals with formulating a coupled biological-physical model of zooplankton foraging on a variable resource. The model simulates a two-dimensional turbulent flow as a source of environmental variability; the circulation patterns affect the distribution of phytoplankton by upwelling nutrients into the euphotic zone, where the algae can grow, and by stirring the density field. In the intermittent resource field, schooling can represent a successful foraging strategy. In the second part, I examine how the emergent properties of schools depend on the parameters describing individual motion. Phase transitions occur when the swimming speed is varied; the density and spatial scale of groups are found to be inversely proportional to speed. Modeled schools are compared to observed aggregations of Antarctic krill. I argue that acceleration patterns linked to the foraging behavior of krill might explain the observed qualitative changes in the depth and density of aggregations that occur over the diurnal cycle.

4.1 Introduction

Foraging animals adjust their behavior in response to environmental conditions, leading to the emergence of patterns in the spatial distribution of both the consumer and the resource. Taxis and kinesis types of strategies are used by individuals searching for prey, and translate into gradient-climbing motions of the predator at the population level (Grünbaum, 1998, 1999; Flierl et al., 1999). In addition, many animal species forage in groups, orienting their movements based on the decisions made by their conspecifics (e.g. Couzin et al., 2002; 2005). The social interactions involved in the formation of groups have been studied in natural populations as well as in theoretical models.

In aquatic environments, schools are formed when individuals tend to move toward their conspecifics and to align their velocity with that of their neighbors (Flierl et al., 1999), a behavior observed in Antarctic krill (*Euphausia superba*). Acoustic measurements reveal krill aggregations of various sizes in the Southern Ocean (Lawson, 2006), and visual observations confirm that the orientations of group members are highly correlated. It has been suggested that schooling can improve the ability to find resources, when the search strategy is a biased random walk in the direction of positive gradients in the resource concentration (Grünbaum, 1998); because alignment reduces the individual sampling errors, the orientation of the group is more accurate than that of individuals. This "many-wrongs principle" is found to be a driver of social aggregation in nomadic foragers (Hancock et al., 2006). Navigational benefits are offset, however, by the intensified intra-specific competition to which group members are subjected. Understanding how these two competing effects impact foraging success of schooling animals might help to understand why the behavior has evolved so strongly in krill. For this purpose, I construct a quantitative model of resource acquisition by a social predator in a fluid environment; the framework can be used to address the success of schooling behavior as a foraging strategy.

The question of how and why collective behaviors have evolved is an old one, and still generates considerable interest; I am aware of several recent studies that use quantitative approaches to similar problems, including the works of Wood and Ackland (2007) and

Couzin (personal communication). Both simulate foraging in a spatially-intermittent resource field, with aggregation behavior based on the model of Couzin et al. (2002). The model used in this study assumes a different search strategy, and takes into account some aspects of the environmental variability. A physical-biological model is employed to simulate the patchiness of resources induced by the flow; upwelling resulting from turbulent motions provides a variable source of nutrients, which stimulate phytoplankton growth (Section 4.3). In this patchy environment, krill are represented as foraging individuals with social behavior; numerical simulations suggest that schooling can indeed improve the foraging success (Section 4.4). Simulated schools are compared to observed aggregations (Section 4.5). The next section describes the individual-based model.

4.2 Individual-based modeling approach

The motion of krill is simulated in a horizontal plane. To capture the dynamic features of schools, such as fusion and fission, I adopt an individual-based formulation [continuous models that simulate the distribution of biomass (cf. Chapters 2–3) can capture the formation and merging of groups but these groups do not exhibit spontaneous fission]. The attraction and alignment tendencies, which act on the individuals, result in large-scale self-organized patterns at the population level. Here a fixed number m of individuals is assumed; each organism is defined in terms of its position (x) and velocity (speed, v, and orientation, θ). Individuals move in a continuous two-dimensional space with doubly-periodic boundaries. A simple set of rules determines the motion of each individual.

4.2.1 Movement algorithm

At each time, individuals adjust their orientation according to the location and orientation of their neighbors (see schematic in Figure 4-1). The preferred direction results from a combination of alignment and attraction tendencies. The first is given by the weighted average velocity of all neighbors found within the perception radius; the weighting is max-

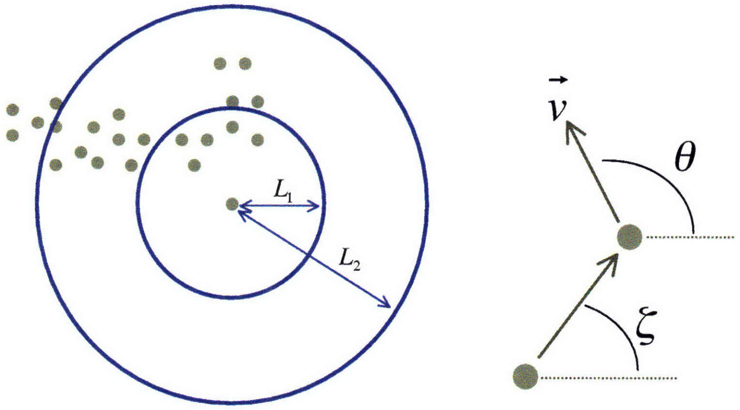

Figure 4-1: Individual-based model configuration; grey dots represent individuals. Left: concentric circles show areas of attraction (outer circle) and alignment (inner circle), L_1 and L_2 refer to the scaling used in Figure 4-2. Right: θ is the angle of the velocity vector; ζ is the angle of the distance vector between two individuals.

imum at the location of the individual, decaying to zero as the distance becomes large. The attraction tendency is in the direction of the weighted center of mass of neighbors within the perception radius, with negative weighting at short distances to account for repulsion when organisms are too close to one another. The weighting functions for attraction (W^{attrac}) and alignment (W^{align}) are functions of the distance between individuals; the choice of these functions affects the internal structure of self-organized groups (see Mirabet et al., 2007).

The expression for the preferred orientation (θ_{pref}) is

$$\theta_{\text{pref},i} = \alpha \sum_{j=1}^{m} W_{ij}^{\text{align}} \theta_j + (1-\alpha) \sum_{j=1}^{m} W_{ij}^{\text{attrac}} \zeta_{ij} \tag{4.1}$$

where α is weight on alignment and ζ is the angle of the distance vector between two individuals (Figure 4-1).

The alignment and attraction functions are shown in Figure 4-2; we consider gaussian functions with half-widths that reflect the perception length of an individual. A narrow

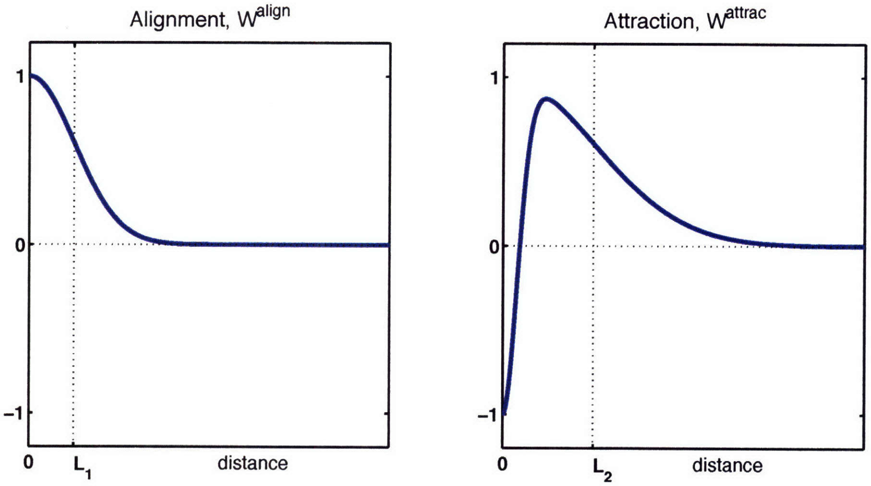

Figure 4-2: Weighting functions for attraction (left) and alignment (right) L_1 and L_2 are half-widths of gaussian functions. There is repulsion at short distances.

gaussian is subtracted from the attraction function to account for repulsion at short distances. To improve the biological realism we can impose a cut-off distance at which W vanishes, although in practice this has little impact on the simulated groups.

The motion of individual i is described by the following stochastic differential equations:

$$\frac{\partial \theta_i}{\partial t} = -\beta_\theta(\theta_i - \theta_{\text{pref},i}) + \mathcal{R}_\theta \tag{4.2}$$

$$\frac{\partial v_i}{\partial t} = -\beta_v(v_i - V) + \mathcal{R}_v \tag{4.3}$$

$$\frac{\partial \mathbf{x}_i}{\partial t} = [v_i \cos\theta_i \, , \; v_i \sin\theta_i] \tag{4.4}$$

where β is a relaxation constant, and V is the preferred swimming speed (cruising speed). $\mathcal{R}_\theta$ and $\mathcal{R}_v$ represent random turns and random accelerations, respectively. These equations are discretized with a finite-difference scheme and solved numerically. (4.2) and (4.3) can

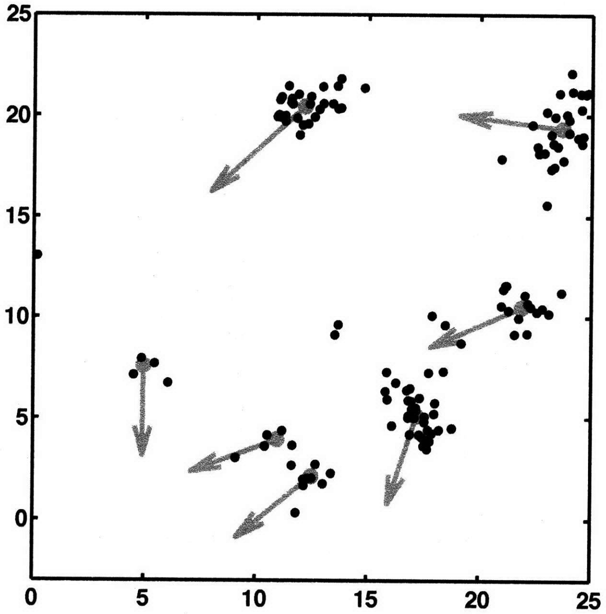

Figure 4-3: Schools in the horizontal plane. Black dots represent individuals; the center of mass of each school is indicated by a gray dot which coincides with the tail of a gray arrow, showing the mean velocity for that school. Parameters are $V = 3$, $\alpha = 0.6$, $\beta_\theta = 4$.

be expressed as

$$d\theta = F_\theta \, dt + d\mathcal{R}_\theta \tag{4.5}$$

$$dv = F_v \, dt + d\mathcal{R}_v \tag{4.6}$$

where the functions F_θ and F_v represent the deterministic terms in (4.2) and (4.3), dt is the time step, and the random increments come from a normal distribution with zero mean such that $< d\mathcal{R}_\theta >= 0$, $< d\mathcal{R}_\theta{}^2 >= \sigma_\theta{}^2 \, dt$, and $< d\mathcal{R}_v >= 0$, $< d\mathcal{R}_v{}^2 >= \sigma_v{}^2 \, dt$; the standard deviations (σ_θ and σ_v) are either constant, or a function of the environment (Section 4.4).

4.2.2 Simulated groups

The model captures the spontaneous formation of groups resulting from social forces. An initially random distribution becomes spatially intermittent as social aggregations form; in aquatic animal populations these groups are called swarms or schools, depending on whether the groups are disorganized (swarms) or whether group members tend to align their velocities (schools). The properties of the aggregations strongly depend on the values of the parameters describing the swimming behavior; the different types of groups are discussed in Section 4.5 (see also Wood and Ackland, 2007). Depending on the cruising speed and the ratio of attraction and alignment tendencies, the schools may be few, large, robust, and move slowly; or there may be a distribution of groups with different sizes, moving rapidly, and interacting with nearby schools in frequent merging and splitting events. Figure 4-3 shows an example of self-organized schools.

A typical trajectory for a single isolated school ($m = 16$) is shown in Figure 4-4. From an ensemble of simulated trajectories, we can estimate the mean squared displacement, which is shown in Figure 4-4 for different group sizes and compared to the mean squared displacement of non-schooling individuals ($m = 1$). We see easily that schools disperse faster than individuals, with dispersion rates that increase with the number of group members. This might provide an advantage for schooling organisms searching for resources if they can, on average, explore a larger area than random walkers.

The spatial distribution of organisms in statistical steady-state again depends on the parameters describing social behavior, in particular those affecting the probabilities of groups merging and splitting. When fission occurs less frequently than fusion, the distribution of organisms converges to a asymptotic state with a few dense groups (in a relatively small domain, it is common to get a single group). In contrast, when the system reaches a statistical equilibrium where groups interact with other groups by exchanging members, merging, and splitting, then we observe a continuous distribution of group sizes. In MATLAB, the "cluster" function can be used to identify groups, which we define as aggregations of individuals whose separation does not exceed the attraction radius (L_2 in Figure 4-2). The

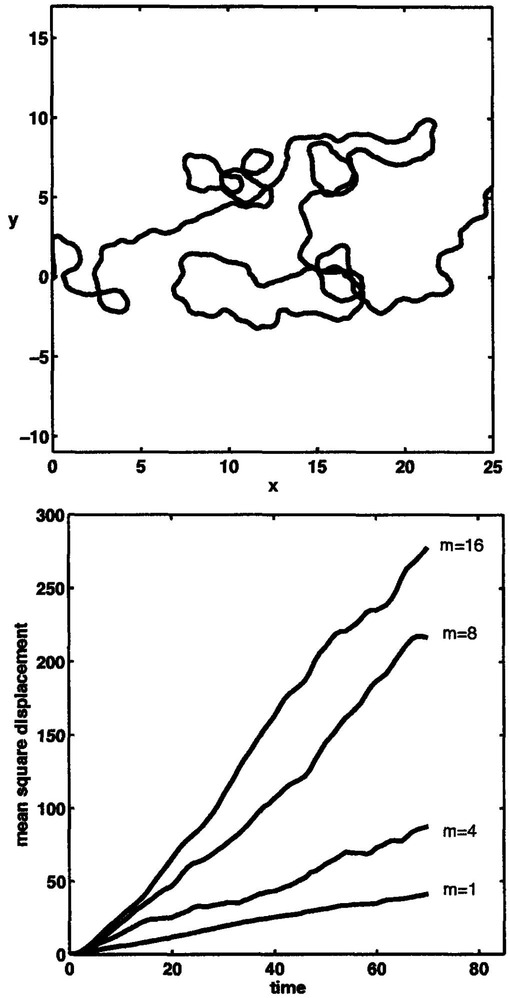

Figure 4-4: Left: Trajectory of a 16-member school initially located at $(0, 0)$. Right: mean squared displacement of versus time, for different group sizes; m is the number of individuals in a group. Schools disperse faster than random walkers (lower curve, $m = 1$).

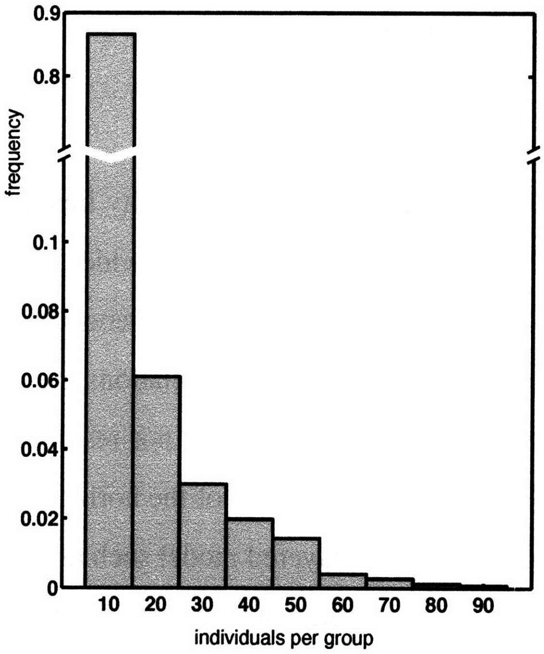

Figure 4-5: Histogram of group size distribution; parameters are $m = 128$, $D = 25$, $V = 4$, $\alpha = 0.9$.

groups size distribution is shown in Figure 4-5 for interacting schools with $m = 128$; we have averaged the instantaneous distribution over a sufficiently long period of time to obtain a smooth profile. There is a high probability of small groups of two or three individuals; these often "break off" from a larger group.

Using the information extracted from numerical simulations, one can think of parameterizing the mean velocity, acceleration, and turning rates of groups as a function of the number of individuals and of the environment. This would represent a considerable step towards the construction of a random flight model for schools. An individual-based approach in which particles are schools, as opposed to individual organisms, would enable us to increase the number of groups and the spatial scale in simulations (these are computationally expensive); however, this extension implies significant challenges – such as incorporating social interactions between groups and dealing with variable numbers of individuals – and will be the focus of future work.

4.3 Variability of the flow

I incorporate in the model some aspects of the variability inherent to fluid environments. An idealized representation of turbulent advection provides a time-dependent source of spatial heterogeneity. The horizontal flow transports biogeochemical tracers, here a nutrient field and a phytoplankton population. Vertical circulations are responsible for supplying nutrients to the euphotic zone, but since these are not resolved in the two-dimensional model, they must be parameterized as a function of the horizontal components of the flow. This is done by relying on the idea of a layered model such as the one illustrated in Figure 4-6, with the top layer representing the euphotic zone, where phytoplankton grow, and the bottom layer representing the nutrient-rich thermocline; interactions between the deep and shallow layers take place through upwelling associated with quasi-geostrophic dynamics.

The turbulent advection scheme considered here is a "lattice mixing algorithm" (Pierrehumbert, 2000). The horizontal space is discretized into a lattice, each site being a square of side Δx; lattice elements are displaced by alternating sinusoidal flows. The flow is assumed to a have a period T such that advection is in the x-direction during the first half period and in the y-direction during the second half; the sinusoidal spatial patterns have randomly-varying phases.

The horizontal components of the flow are expressed as:

$$\left.\begin{aligned} u(t) &= U \sin[ky - \phi_u(t)] \\ v(t) &= 0 \end{aligned}\right\} \quad \text{first half period} \tag{4.7}$$

$$\left.\begin{aligned} u(t) &= 0 \\ v(t) &= U \sin[kx - \phi_v(t)] \end{aligned}\right\} \quad \text{second half period} \tag{4.8}$$

where U is the maximum flow speed, $k = 2\pi/D$ is the wavenumber, and the phase evolves

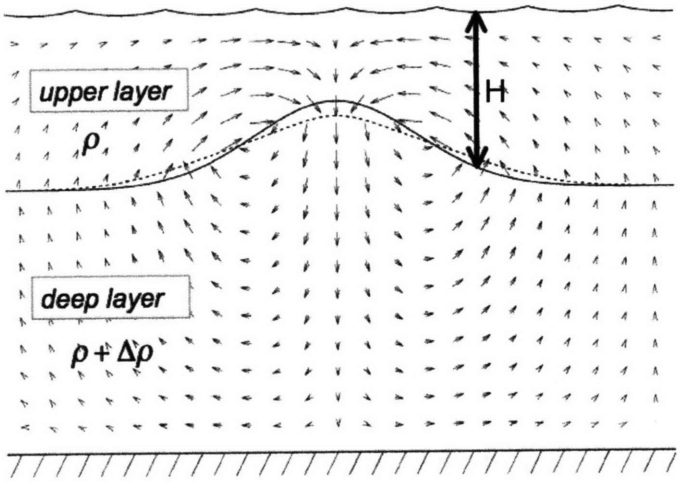

Figure 4-6: A two-layer model; h is the depth of the upper layer. Vectors show the circulation associated with deepening of the interface in the center of the feature. Adapted from Flierl and McGillicuddy, 2002.

according to a first-order autoregressive process,

$$\phi_u(t+T) = \phi_u(t) + \mathcal{R}_u(t) \tag{4.9}$$

$$\phi_v(t+T) = \phi_v(t) + \mathcal{R}_v(t) \tag{4.10}$$

where the random component $\mathcal{R}_{(u,v)}$ is obtained from a uniform distribution in the interval $[0\,,\,2\pi]$.

The position of fluid particles is iterated at discrete time intervals according to the map

$$x(t + \Delta t) = x(t) + \left[\frac{u(t)}{\Delta x}\Delta t\right] \Delta x \tag{4.11}$$

$$y(t + \Delta t) = y(t) + \left[\frac{v(t)}{\Delta x}\Delta t\right] \Delta x \tag{4.12}$$

The horizontal displacements are constrained to be multiples of the grid size Δx, which is achieved by rounding the terms inside square brackets to the nearest integer. By setting $\Delta t = T/2$, we simulate flows that change direction at each time step.

In the conceptual two-layer model (Figure 4-6), we assume that only the upper layer supports horizontal flows. The deep layer experiences indirect effects from the turbulent motions, which induce vertical displacements of the interface between the two layers. The depth of the top layer is allowed to vary in time and in space; we write $H = \bar{H} + h$, where the total depth is given by the sum of the average depth $\bar{H}$ and the perturbations h. Each layer has a uniform density: ρ in the top layer, $\rho + \Delta\rho$ in the heavier deep layer. Reduced gravity is defined as $a_g' = \frac{\Delta\rho}{\rho_0} a_g$, where a_g is gravitational acceleration. In the geostrophic equations, we replace pressure by $p = \rho a_g' h$ and obtain

$$fu = -a_g' \frac{\partial h}{\partial y} \tag{4.13}$$

$$-fv = -a_g' \frac{\partial h}{\partial x} \tag{4.14}$$

where f is the Coriolis parameter. We define the streamfunction Ψ such that $\mathbf{u} = \nabla \times \Psi$; substituting in (4.13-4.14) yields

$$h = \frac{f}{a_g'}\Psi \tag{4.15}$$

From (4.7-4.8) we infer

$$\Psi = \frac{-U}{k}\cos(kx - \phi_v) + \frac{U}{k}\cos(ky - \phi_u) \tag{4.16}$$

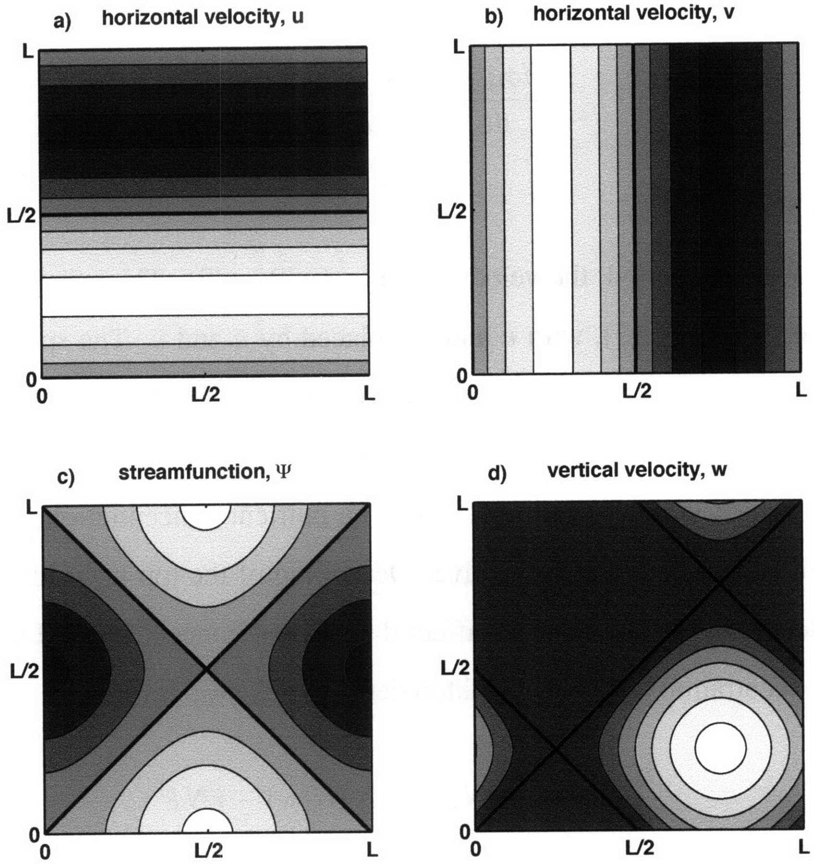

Figure 4-7: Circulation patterns in the turbulent map. a,b) Horizontal velocity. c) Streamfunction. d) Vertical velocity. In this specific example, the instantaneous phases vanish, $\phi_u = \phi_v = 0$, and are evolving at the same rate, $\frac{d\phi_u}{dt} = \frac{d\phi_v}{dt} > 0$. Values increase from black to white; thick black curves indicate the zero contour.

The vertical velocity is $\mathrm{w} \equiv -\frac{dh}{dt}$; we make use of (4.15) and (4.16) to get

$$\mathrm{w} = \frac{f}{a_g}\left[\frac{u}{k}\frac{d\phi_u}{dt} - \frac{v}{k}\frac{d\phi_v}{dt}\right] \tag{4.17}$$

where, from (4.9-4.10),

$$\frac{d\phi_{(u,v)}}{dt} = \frac{\mathcal{R}_{(u,v)}}{2} \tag{4.18}$$

since we have set $\Delta t = T/2$.

Averaged over one period, the velocity is $\bar{\mathrm{u}} = (u/2\,,\, v/2)$. The mean vertical motion is then calculated from (4.17), with u and v replaced by $\bar{u}$ and $\bar{v}$. The spatial structure is given by $\bar{u}(x,y) - \bar{v}(x,y)$; the time-varying component of the amplitude is determined by the random phase (Figure 4-7). Local shoaling of the top layer ($\frac{dh}{dt} < 0$) implies upwelling of deep water, which is rich in nutrients; thus the nutrient concentration in the top layer increases when vertical velocity is positive. Deepening of the top layer implies export of water to the deeper layer, but does not affect the nutrient concentration. Let N and P be the nutrient concentration and phytoplankton density in the top layer;

$$\frac{\partial N}{\partial t} = \frac{\mathrm{w}}{\bar{H}}(N_{deep} - N)\mathcal{H}(\mathrm{w}) - rNP \tag{4.19}$$

$$\frac{\partial P}{\partial t} = \epsilon rNP - dP \tag{4.20}$$

where N_{deep} is the concentration of nutrients in the deep layer (below the thermocline); $\mathcal{H}(\mathrm{w})$ is a Heaviside function equal to 1 when $\mathrm{w} > 0$ and 0 otherwise; ϵ is the assimilation efficiency, r is the growth rate, and d the mortality rate.

We consider nitrogen as the nutrient limiting growth and express phytoplankton density in terms of the amount of nitrogen in algal cells. The parameter values are chosen so that the mean nutrient and phytoplankton concentrations are within the range of observed values in the Southern Ocean (Serebrennikova and Fanning, 2004; Moore and Abbott, 2000). Snapshots of tracer fields are shown in Figure 4-8. The anti-correlation between nutrient

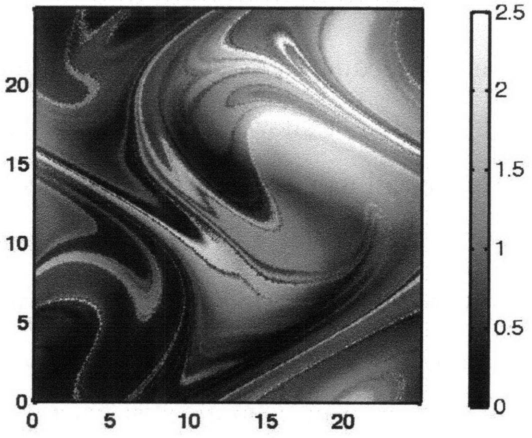

a) Nutrients (N)

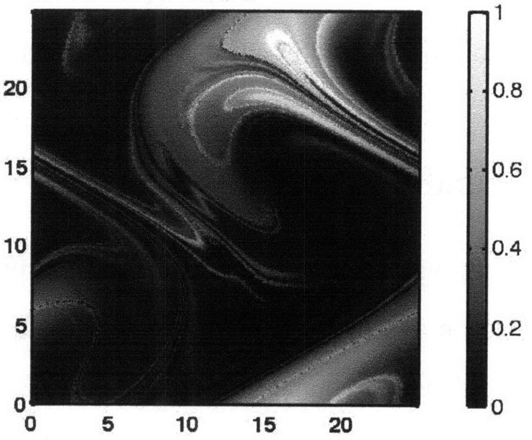

b) Phytoplankton (P)

Figure 4-8: Snapshots from simulations with turbulent advection. a) nutrient concentration; b) phytoplankton density. Lighter shades of gray indicate larger values. The two fields tend to be anti-correlated.

and phytoplankton densities reflects the rapid uptake rate of nutrients by the autotrophs.

4.4 Foraging on patchy resources

In a heterogeneous environment, feeding individuals respond to variations in food levels. It seems fair to assume that krill do not know a priori the location of prey patches or the local gradient in prey density, i.e. all individuals are uninformed. Instead, we assume that individuals have a "memory" of the grazing success they have had in the recent past, and movement rules are based on comparing the local prey density to the values remembered. Individuals tend to turn more often when the resource density is lower, and tend not to change their orientation when the density is higher. The behavior can be expressed as a biased random walk, and on average individuals tend to move up the gradient of resource density. An equivalent advection-diffusion equation can be written that captures the effect at the population level of individual search behavior (Grünbaum, 1999; 2002).

4.4.1 Hybrid model and foraging algorithm

Individual zooplankton are moving in a continuous space, and interacting with a resource whose density is discretized on a lattice. Predation is simulated as a deterministic process for which the local resource density (P) and predator density (Z) determine the rate of resource depletion. The predator density is given by the cumulative weight of all individuals inside a given site in the lattice, divided by the area of that site:

$$Z(\mathbf{x}) = \sum_i \frac{w_i}{(\Delta x)^2} \tag{4.21}$$

where w is the weight of a predator individual (to convert numbers of individuals into biomass); subscripts i denote the i^{th} individual, and the summation is taken over all individuals located inside the site considered. For simplicity, here we will assume that all individuals have the same weight.

A Holling Type II function of prey density is assumed: the predation rate is

$$G = g\frac{P}{P+P_h}Z \tag{4.22}$$

where g is the maximum grazing rate and P_h is the half-saturation prey density, so that the prey equation becomes

$$\frac{\partial P}{\partial t} = \epsilon r N P - dP - G \tag{4.23}$$

We incorporate foraging behavior in the movement algorithm of Section 4.2.1 by making the turning rate a function of the local resource density. For this purpose we introduce a variable monitoring the amount of internal resources (it can thought of as gut-fullness), ξ, defined as

$$\frac{\partial \xi_i}{\partial t} = \frac{P(\mathbf{x}_i)}{P(\mathbf{x}_i)+P_h} - \beta_\xi \xi_i \tag{4.24}$$

where β_ξ is the exponential decay rate.

The random term in the equation for the orientation 4.2 is multiplied by the probability of turning, which is small when local resources exceed the internal resources (individuals are moving up-gradient) and large otherwise:

$$\frac{\partial \theta_i}{\partial t} = -\beta_\theta(\theta_i - \theta_{\mathrm{pref},i}) + \left[1 + \tanh\left(\frac{\xi_i - P(x_i, y_i)}{c}\right)\right]\mathcal{R}_\theta \tag{4.25}$$

where c is a constant.

4.4.2 Optimal strategy

The success of a foraging population is investigated through numerical simulations, for different behaviors under different environmental conditions. For simplicity it is assumed that populations are homogeneous, i.e. in a given simulation all individuals have the same behavior. Simulations are then repeated several times to sample the range of all possible strategies, which are defined by the value of α (the ratio of alignment to attraction forces). Environmental conditions are varied by changing the amount of available resources as well as the strength of the turbulent flow.

Foraging success is measured by the total amount of resources ingested, averaged over a period of time. This value is normalized by the foraging success of a population without social behavior ($\beta_\theta = 0$); this is expressed as

$$\text{relative foraging success} = \frac{\sum < G >_{\text{schooling}}}{\sum < G >_{\text{random walk}}} \tag{4.26}$$

where G is given by (4.22) and brackets denote a time average.

Results shown in Figure 4-9 suggest that schooling individuals can perform better than random walkers; however the optimal strategy is strongly dependent on environmental conditions, as is the degree to which it is successful. Each panel in Figure 4-9 shows how well the schooling population does compared to an equivalent population of random walkers; schooling is a good strategy when the relative success exceeds 1. Each column represents a different level of resource abundance, which in the model is controlled by the ratio of grazing rate over resource growth rate, g/r. Panels a, d, and g correspond to very abundant resources, $g/r = 0$: resources grow so quickly that depletion due to predator grazing is negligible. Panels b, e, and h correspond to an intermediate level of resources, and panels c, f, and i to scarce resources. Each row represents a different timescale of resource variability, which is controlled by the characteristic period of the turbulent flow (T). In panels a, b, and c, there is no temporal variability $T^{-1} = 0$; the resource field is constant. Panels d, e, and f correspond to weak turbulent stirring; panels g, h, and i correspond to strong turbulent stirring.

Under fixed environmental conditions, there is an optimal strategy corresponding to the value of α that yields that highest foraging success. Intermediate values of the ratio parameter are typically optimal, implying that mixed strategies are more favorable than

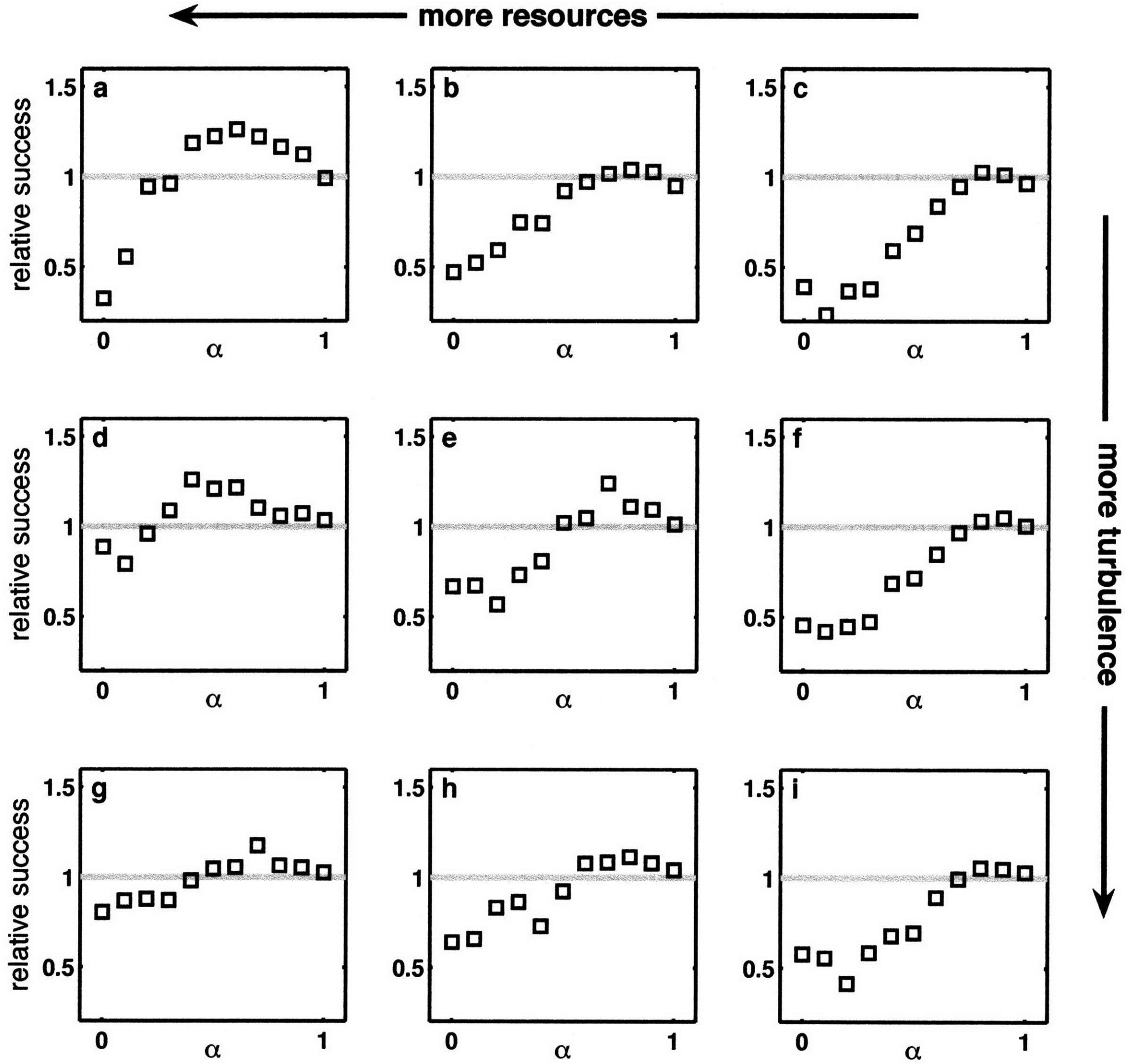

Figure 4-9: Foraging success of schooling organisms ($\beta_\theta = 3$), normalized by the success of random walkers under the same conditions. In each panel, the relative success (equation 4.26) is shown for different strategies (α, the ratio of alignment to attraction, varying between 0 and 1). Each column corresponds to a different level of resource availability; each row has different flow characteristics (see text).

pure attraction or pure alignment strategies. Attraction without alignment results in tightly packed groups that move very slowly, which means that competition between group members is high and that the group search for resources is inefficient; for these reasons small values of α are associated with low foraging success (worse than the success of random walkers). Alignment without attraction does not result in the formation of groups, hence it has little effect on foraging success.

When resources are plentiful, collective motion enhances foraging success by up to 25% (panel a), with the optimal strategy corresponding to $\alpha \approx 0.6$. The optimal ratio shifts to higher values ($\alpha \rightarrow 1$) as the abundance of resources decreases. In these simulations, schooling populations are clearly more successful when the resource level is high, because the cost of sharing resources with group members is lower. The effect of turbulence is less clear, but more stirring arguably reduces the relative success of schooling strategies.

4.5 Phase transitions in the density-distribution of Antarctic krill

Antarctic krill are observed to assemble in schools. The behavior has important consequences for the dynamics of the krill population (cf. Chapter 3) and broader impacts on the Southern Ocean food web, in which krill plays a central role. Higher-trophic level predators that feed on krill have developed search strategies to efficiently find aggregations.

Based on the results from numerical experiments described in earlier sections of this Chapter, it seems possible that the schooling behavior of krill would have evolved because of the benefits related to foraging success. In the model, following group members helps individuals finding resources when the environment is spatially patchy and variable in time. In the ocean, aggregations of schooling krill are observed at all times of day, although feeding is thought to occur primarily at night (references). During periods of sunlight krill tend to move deeper in the water column, where there are no resources; why then do they form aggregations? Interestingly, the characteristic of the schools are observed to vary as organisms migrate vertically (Section 4.5.1). Here I argue that changes in average school size and density can result from changes in swimming velocity in response to local resource availability. Accelerations cause transitions in the density-distribution of schooling organisms, even without modification of the schooling behavior. This is examined in an idealized model.

Individuals moving in a two-dimensional domain are considered as a dynamical system, in which attraction and alignment forces control interactions between individuals, leading to the spontaneous formation of groups. In the physics literature, these systems are referred to as *self-propelled particles* (SPP) – although the particles usually represent living organisms. The self-propulsion arises from short-range interactions between particles attempting to follow their neighbors (see the review by Toner et al., 2005); a simple SPP model was formulated by Viscek et al. (1995). Although intrinsically non-equilibrium, these systems exhibit distinct "phases", much like physical systems in thermodynamic equilibrium. It is Viscek (1995) who first drew the analogy between the phase transitions in SPP and those observed in ferromagnets: both systems can experience spontaneous large-scale alignment, of velocities and magnetic spins, respectively.

4.5.1 Observed patterns

Acoustic measurements show aggregations of Antarctic krill range in size from tens of meters to several kilometers (Lawson, 2006). The average density and depth of these aggregations vary throughout the diurnal cycle, suggesting that the behavior is an adaptive response to predatory pressure and resources availability: during the day time, krill tend to form dense aggregations deep in the water column, possibly to avoid being detected by predators; at night, they tend to form low-density aggregations at shallow depths, where food is abundant (Figure 4-10). This diel migration pattern is most evident in the measurements of Fall and Winter 2002.

These observations support the hypothesis that krill tend to form cohesive aggregations during the day and disperse at night (Everson, 1982). Other data from the same region sug-

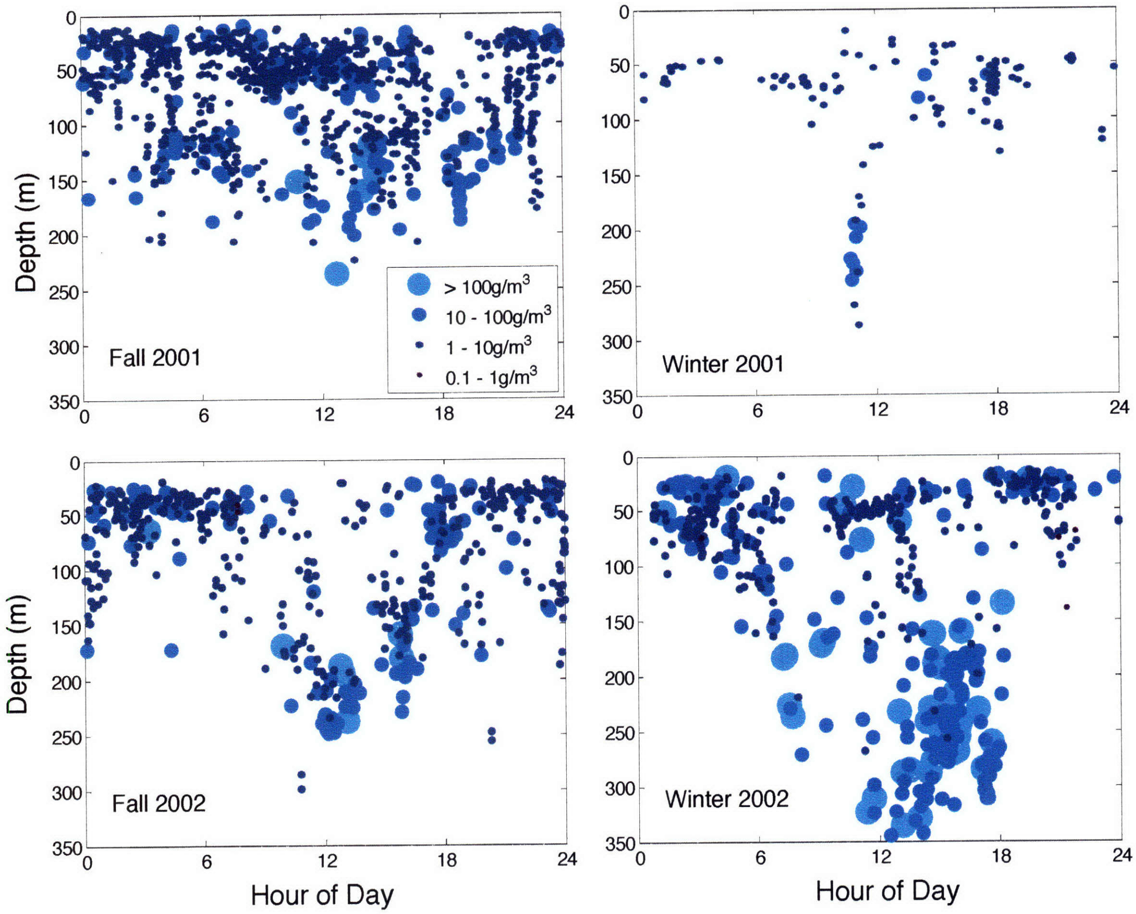

Figure 4-10: Observed aggregations of Antarctic krill from acoustic measurements. Each dot represents an aggregation, plotted as a function of the time of day when it was observed (x-axis) and its mean depth (y-axis). Size and color of dots indicate the mean density of aggregations (see legend). [Figure courtesy of Gareth Lawson; adapted from Lawson (2006).]

gest that day-time aggregations are more compact because there is less randomness in the swimming velocities than during the night, when individuals scatter to look for resources (Zhou and Dorland, 2004). There is also evidence that krill adjust their swimming velocity to the local conditions; in a laboratory experiment, Price (1989) found that krill in an environment where food is abundant swim twice as fast as when there is no food. It has been suggested that the same thing occurs in the ocean, and that euphausiids reduce their swimming velocity during the day when they presumably stop feeding (Zhou and Dorland, 2004).

4.5.2 Emergent properties of simulated schools

I examine the properties of schools simulated with the individual-based model described in Section 4.2, in the absence of turbulent stirring and other environmental variability. The model captures the self-organization of social aggregations. If the organisms are initially randomly distributed in space, groups will emerge spontaneously as a result of the social interactions, as long as the stochastic component of the turning rate and acceleration, $\mathcal{R}_{\theta,v}$ is small compared to the deterministic component, $\beta_{\theta,v}$. Depending on parameter values, the model can exhibit a variety of phases, from dispersed random walkers to disordered aggregations (swarms) to polarized aggregations (schools).

The swimming velocity and the relative weight of attraction and alignment forces are found to have a significant impact on the characteristics of self-organized groups. The polarization is a measure of the alignment within a group; it is calculated as in Couzin et al. (2002) and shown in Figure 4-11 as a function of the parameters controlling social behavior, for simulations in which 128 individuals are initially randomly distributed. Typical phases are also shown. I) a "mill": individuals move in circle (some clockwise, some counter-clockwise) around the group's center of mass; II) a swarm: individuals move randomly around the group's center of mass; III) large school: group's density is high, fission rate is low; IV) many interacting schools: groups interact with each other, density is low, fission and fusion rates are high; V) no well-defined groups: there is transient alignment between

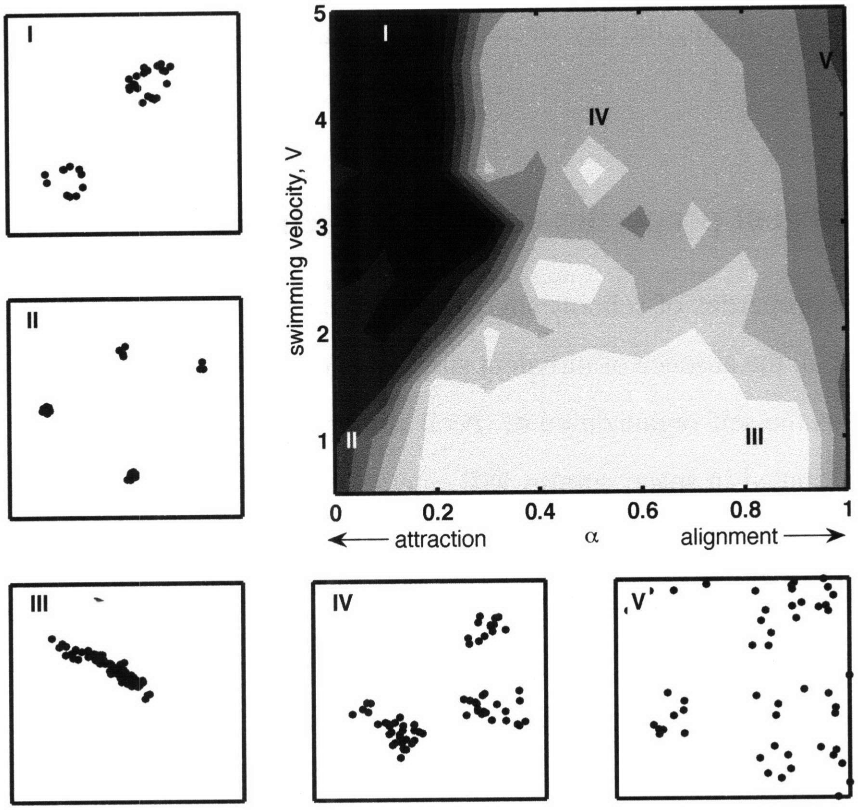

Figure 4-11: Gray shades: average polarization within groups, versus α and V. Polarization increases from dark to light gray. Labels I-V indicate distinct phases; typical distributions of individuals are shown is smaller windows. Parameters: $m = 128$, $\beta_\theta = 4$.

individuals.

Phases labeled I and II are characterized by groups that are quasi-stationary: the center of mass of each aggregation exhibits very slow random motion. In contrast, large schools (phase III) show a clear orientation; the position of the center of mass follows a random walk and although mean velocities are small, their decorrelation timescale is relatively long. Smaller schools (phase IV) move much faster than large ones, which is consistent with previous findings (Flierl et al., 1999). These simulations show that changes in the schooling strategy, as defined by the ratio of alignment to attraction (α) induce phase transitions, as do changes in the mean swimming velocity.

4.5.3 Behavior switching as a mechanism for observed phase transitions

The observed day/night differences in krill aggregations also reflect phase transitions, from fewer dense schools at depth during the day (similar to phase III in Figure 4-11) to many small schools (phase IV in Figure 4-11). One explanation for the transition would be that individual change their social behavior as they move up and down the water column; in the model this would translate in a change in α or a change in β_θ. Decreasing the response time (β_θ) weakens the tendency to aggregate. This would suggest that schooling behavior has evolved because it benefits organisms when they are hiding from predators, the behavior being relaxed at night when the predation risk is decreased.

An alternative explanation is that phase transitions occur because schooling individuals decrease their speed during the day when they are not feeding without changing their social tendencies; this would suggest that schooling behavior has evolved because of the benefits for organisms when they are foraging. That hypothesis is supported by the simulations of krill foraging on patchy resources (Section 4.4), and is discussed conceptually here. The model that we use simulates motion in a horizontal plane and therefore does not capture the diel vertical migration behavior; however, we can adjust the resource availability to mimic the conditions at different depths in the water column.

In the euphotic zone, where resources are abundant, schooling can represent a successful strategy (Figure 4-9). Below the euphotic zone, where there are no resources, all strategies are equivalent in terms of foraging success (not shown). We could add to the definition of foraging success (equation 4.26) a term that accounts for the losses due to respiration, which as a first approximation will be assumed to depend only on the swimming velocity. Let's write

$$\text{success} = \sum < G > - \sum (\delta Z) \tag{4.27}$$

where again $< \cdot >$ denotes a time average, G is given by (4.22), and δ is the respiration rate. A piecewise linear function of the velocity V is considered:

$$\delta = \begin{cases} \delta_0 & V < 0.5 \\ 2\delta_0 V & V \geq 0.5 \end{cases} \tag{4.28}$$

where δ_0 is a constant.

It is easy to see from (4.27-4.28) that if there are no resources ($P = 0$, hence $G = 0$) the best strategy is to swim slowly ($V < 0.5$) to minimize the costs. This is true regardless of the social behavior (or lack thereof). When there are resources, then there will be optimal values of V and α that maximize the success. It is expected that an intermediate velocity will be optimal, as moving slowly reduces costs but moving fast increases the uptake of resources.

In summary, the qualitative changes in aggregations of krill can be explained by changes in the swimming velocity as krill move from surface waters to greater depths and back each day. Individuals swim fast during the night when they are feeding, and align their velocities with their neighbors to forage more efficiently. They reduce the swimming activity during the day in order to lower metabolic costs; this might also reduce encounter rates with ambush predators (Jaffe, 1999). The deceleration causes aggregations to become denser and larger, as nearby groups tend to merge.

4.6 Conclusions

In simulations of krill swimming in a variable environment, following group members can help individuals find resources. This result that was anticipated by Grünbaum (1998) based on an idealized model, which assumes a fixed large-scale gradient in resources. The model that I have constructed takes into account some aspects of the variability inherent in aquatic environments, such as stirring by a turbulent flow and localized upwelling of resources (the upwelling is assumed to be an indirect effect of turbulent stirring). Krill are represented as individual particles moving in the two-dimensional space; a combination of attraction and alignment tendencies results in the formation of schools. In the spatially-intermittent and temporally-variable resource field, schools forage more efficiently than individuals, but they have to share resources with other group members. The success of schooling behavior is determined by the net balance of these positive and negative effects.

The parameters of the biological-physical model were chosen so that we get spatial and temporal variability in the phytoplankton field on scales that are relevant for the simulated schools. The dimensions of the physical space are not specified so those parameter values are somewhat arbitrary. Further investigation will be required to check whether the results presented here still hold in other regions of the parameter space. In particular, we will verify that the values correspond to realistic conditions of the Southern Ocean, as well as realistic characteristics for Antarctic krill's physiology, life cycle and behavior.

When schooling represents a successful strategy in numerical simulations, optimal attraction and alignment tendencies select for the formation of rapidly-moving, strongly interacting schools. The shallow, low-density aggregations observed in krill during the night are consistent with the optimal behavior predicted by the model. When food is not available, collective motion does not affect fitness, since there is no energy to be gained. In order to preserve the energy they have stored, individuals should decrease their cruising speed. If the attraction and tendencies are kept the same, the deceleration causes a phase transition; slowly-moving schools tend to merge and form large, dense groups. Observations of krill aggregations during day-time are again consistent with the model's prediction.

Chapter 5

Sensitivity analysis of reactive ecological dynamics

Adapted from the manuscript by A. Verdy and H. Caswell
Submitted to the *Bulletin of Mathematical Biology*

Abstract

Ecological systems with asymptotically stable equilibria may exhibit significant transient dynamics following perturbations. In some cases, these transient dynamics include the possibility of excursions away from the equilibrium before the eventual return; systems that exhibit such amplification of perturbations are called reactive. Reactivity is a common property of ecological systems, and the amplification can be large and long-lasting. The transient response of a reactive ecosystem depends on the parameters of the underlying model. To investigate this dependence, we develop sensitivity analyses for indices of transient dynamics (reactivity, the amplification envelope, and the optimal perturbation) in both continuous- and discrete-time models written in matrix form. The sensitivity calculations require expressions, some of them new, for the derivatives of equilibria, eigenvalues, singular values, and singular vectors, obtained using matrix calculus. Sensitivity analysis provides a quantitative framework for investigating the mechanisms leading to transient growth. We apply the methodology to a predator-prey model and a size-structured food web model. The results suggest top-down and bottom-up mechanisms for transient amplification resulting from multi-species interactions.

5.1 Introduction

Sufficiently small perturbations of an asymptotically stable equilibrium will eventually decay. The asymptotic rate of return to equilibrium has long been used as a measure of ecological stability (e.g. May, 1973; Pimm, 1984; Ives and Carpenter, 2007). However, this long-term return to the equilibrium does not determine the transient response to the perturbation, which may carry the trajectory farther away from the equilibrium before its eventual return. Equilibria with this property are called "reactive" (Neubert and Caswell, 1997). It is now known that reactivity is a common property of predator-prey models, food web models, ecosystem compartment models, and stage-classified matrix population models (Neubert and Caswell, 1997; Caswell, 2001; Chen and Cohen, 2001; Neubert et al., 2004; Marvier et al., 2004; Caswell and Neubert, 2005). It has been shown to be a necessary condition for pattern formation via Turing instability (Neubert et al., 2002).

The transient amplification of perturbations is important because ecological systems may not complete their response to a perturbation before the next one occurs. Instead, they are buffeted by a more-or-less continual series of perturbations and the appearance of transient responses in our observations of nature may be the norm rather than the exception (Hastings, 2004). Managers charged with ecosystem restoration, for example, are likely to be interested in both the short-term and long-term effects of their manipulations (cf. Caswell, 2007), particularly if the short-term effects can be large.

To understand transient dynamics, it is useful to know how their properties respond to the parameters in the underlying model. To this end, we present here the sensitivity analysis of several properties of reactive transient dynamics. The paper begins with a brief introduction of the indices used to describe transient growth, followed by a description of the sensitivity problem. Section 5.2 deals with the calculation of the sensitivity of equilibrium solutions and of linearized dynamics; these are used to calculate sensitivities of indices of transient dynamics in Section 5.3. The method is applied to two ecological problems in Section 5.4 and briefly discussed in Section 5.5.

5.1.1 Characterizing transient dynamics

The stability and asymptotic properties of an equilibrium are determined by the dominant and subdominant eigenvalues of the linearization of the model at that equilibrium. Simple analysis of these eigenvalues does not, however, capture the transient behavior of systems whose time evolution is described by non-normal matrices or operators (Trefethen and Embree, 2005). Mathematical developments in areas such as fluid dynamics (e.g. Farrell and Ioannou, 1996; Trefethen et al., 1993) and numerical analysis (e.g. Trefethen, 1992) have led to the formulation of indices that characterize the transient response of nonlinear ecological systems (Neubert and Caswell, 1997).

We focus on three such indices of transient dynamics. The *reactivity* of an asymptotically stable equilibrium is the maximum (over all perturbations) of the rate of departure of the trajectory (in the linearized system, or equivalently, for small enough perturbations) from the equilibrium immediately following the perturbation. It measures the maximum instantaneous amplification of perturbations of that equilibrium. At any time following a perturbation, there is a maximum (again, over all perturbations) possible deviation from the equilibrium. This maximum is the *amplification envelope* (Neubert and Caswell, 1997). It provides an upper bound on the extent of transient amplification as a function of time. Transient amplification depends on the direction of the initial perturbation. The perturbation that produces the maximum amplification at a specified time is the *optimal perturbation*, sometimes called "optimal excitation" (Farrell and Iaonnou, 1996). These indices are important descriptions of the behavior of ecosystems subject to random perturbations. They provide information about the timing and magnitude of the growth of perturbations, the potential for transient amplification, and the perturbations to which the system is most sensitive.

We consider both continuous and discrete models, written in matrix form:

$$\frac{d\mathbf{x}}{dt} = \mathbf{A}[\boldsymbol{\theta},\mathbf{x}]\mathbf{x} \qquad \text{continuous} \qquad (5.1)$$

$$\mathbf{x}(t+1) = \mathbf{A}[\boldsymbol{\theta},\mathbf{x}]\mathbf{x}(t) \qquad \text{discrete} \qquad (5.2)$$

where $\mathbf{x}$ is a vector ($s \times 1$) of state variables and the matrix $\mathbf{A}$ contains per-capita vital rates. The vital rates depend on the current system state $\mathbf{x}$ and on a vector $\boldsymbol{\theta}$ of parameters. Many ecological systems, including structured populations, interacting species, and food webs, can be written in this form. When it seems unlikely to cause confusion, we will suppress the explicit dependence of $\mathbf{A}$ on $\mathbf{x}$ and $\boldsymbol{\theta}$.

Let $\hat{\mathbf{x}}$ be an equilibrium. The linearization around $\hat{\mathbf{x}}$ is given by the Jacobian matrix $\mathbf{M} = \mathbf{M}[\boldsymbol{\theta}, \hat{\mathbf{x}}]$. Deviations from $\hat{\mathbf{x}}$, defined as $\mathbf{z}(t) = \mathbf{x}(t) - \hat{\mathbf{x}}$, follow

$$\frac{d\mathbf{z}}{dt} = \mathbf{M}[\boldsymbol{\theta}, \hat{\mathbf{x}}]\mathbf{z}(t) \qquad \text{continuous} \tag{5.3}$$

$$\mathbf{z}(t+1) = \mathbf{M}[\boldsymbol{\theta}, \hat{\mathbf{x}}]\mathbf{z}(t) \qquad \text{discrete} \tag{5.4}$$

We assume that $\hat{\mathbf{x}}$ is asymptotically stable, so that the dominant eigenvalue of $\mathbf{M}$ has negative real part (in continuous time) or is less than 1 in magnitude (in discrete time).

The transient dynamics of the perturbed system are described by the evolution of the magnitude of $\mathbf{z}$, as measured by the Euclidian norm $||\mathbf{z}|| = \sqrt{\mathbf{z}^{\mathsf{T}}\mathbf{z}}$. We consider the transient response following a perturbation $\mathbf{z}_0$ at $t = 0$.

The reactivity is the maximum, over all perturbations, of the growth rate of $||\mathbf{z}||$, as $t \longrightarrow 0$. In continuous time, the reactivity is

$$\nu_0 = \max_{||\mathbf{z}_0|| \neq 0} \frac{1}{||\mathbf{z}||} \frac{d||\mathbf{z}||}{dt} \bigg|_{t=0} \tag{5.5}$$

$$= \max_{||\mathbf{z}_0|| \neq 0} \frac{\mathbf{z}_0^{\mathsf{T}}\mathbf{H}(\mathbf{M})\mathbf{z}_0}{\mathbf{z}_0^{\mathsf{T}}\mathbf{z}_0} \tag{5.6}$$

$$= \lambda_1(\mathbf{H}) \tag{5.7}$$

where $\mathbf{H}(\mathbf{M}) = (\mathbf{M} + \mathbf{M}^{\mathsf{T}})/2$ is the Hermitian part of $\mathbf{M}$ and λ_1 denotes the eigenvalue with largest real part (Neubert and Caswell, 1997).

In discrete time, reactivity is defined as the average instantaneous rate of growth, from

$t = 0$ to $t = 1$, following the perturbation $\mathbf{z}_0$:

$$\nu_0 = \log\left(\max_{\|\mathbf{z}\|\neq 0} \frac{\|\mathbf{M}\mathbf{z}_0\|}{\|\mathbf{z}_0\|}\right) \tag{5.8}$$

$$= \log |||\mathbf{M}||| \tag{5.9}$$

$$= \log\left[\sigma_1(\mathbf{M})\right] \tag{5.10}$$

where $\log(\cdot)$ is the natural logarithm, and the matrix norm $|||\cdot|||$ induced by the Euclidian norm is the largest singular value, denoted by σ_1. In either continuous or discrete time, if $\nu_0 > 0$ there exists a perturbation that produces a trajectory departing from $\hat{\mathbf{x}}$ at the rate ν_0.

To obtain the amplification envelope, we solve (5.3) and (5.4) as $\mathbf{z}(t) = \mathbf{\Phi}(t)\mathbf{z}_0$, where $\mathbf{\Phi}(t)$ is the fundamental matrix[1] (Coddington and Levinson, 1955, p. 69), given by

$$\mathbf{\Phi}(t) \equiv \begin{cases} e^{\mathbf{M}t} & \text{continuous} \\ \mathbf{M}^t & \text{discrete} \end{cases} \tag{5.11}$$

and the matrix exponential is defined as $e^{\mathbf{M}t} = \sum_{i=0}^{\infty} \frac{(\mathbf{M}t)^i}{i!}$.

The amplification envelope at time t is the maximum, over all initial perturbations, of the relative size of $\mathbf{z}(t)$,

$$\rho(t) = \max_{\|\mathbf{z}_0\|\neq 0} \frac{\|\mathbf{z}(t)\|}{\|\mathbf{z}_0\|} \tag{5.12}$$

$$= |||\mathbf{\Phi}(t)||| \tag{5.13}$$

$$= \sigma_1\left(\mathbf{\Phi}(t)\right) \tag{5.14}$$

The optimal perturbation, normalized to length 1, is given by the right singular vector $\mathbf{v}(t)$ corresponding to the singular value $\sigma_1\left(\mathbf{\Phi}(t)\right)$.

---

[1] Also called the propagator (Farrell and Ionannou, 1996; 2000), or matricant (e.g. Gantmacher ,1959, p. 125).

The rate at which perturbations decay in the asymptotic limit $t \longrightarrow \infty$ is the *resilience* (ν_∞), as measured by the real part of the leading eigenvalue of the Jacobian M evaluated at equilibrium (Pimm and Lawton, 1977)

$$\nu_\infty = -\mathrm{Re}[\lambda_1(\mathbf{M})]$$

Resilience is a positive quantity since the real part of λ_1 is negative for stable equilibria; it is traditionally used to describe the response of ecosystems to perturbations, but it fails to address the property to amplify these perturbations. This paper does not address the sensitivity of resilience; instead, we focus on reactivity, the amplification envelope, and the optimal perturbations.

5.1.2 The sensitivity problem

We can define the sensitivity problem for these three indices of transient dynamics. Let r denote one of these indices; r is a function of the linearization M, which in turn depends on the parameters $\boldsymbol{\theta}$ and the equilibrium $\hat{\mathbf{x}}$: $r(\mathbf{M}) = r\left(\mathbf{M}\left[\boldsymbol{\theta}, \hat{\mathbf{x}}(\boldsymbol{\theta})\right]\right)$.

The sensitivity problem is addressed here using matrix calculus notation. Appendix 5.6 presents the same calculations using index notation. The resulting expressions are equivalent, but some readers might be more familiar to one notation than an other, so both are included in this chapter.

Our goal is to obtain the sensitivities

$$\frac{dr}{d\boldsymbol{\theta}^{\mathsf{T}}} \tag{5.15}$$

and the elasticities

$$\frac{1}{r}\frac{dr}{d\boldsymbol{\theta}^{\mathsf{T}}}\mathrm{diag}\left(\boldsymbol{\theta}\right) \tag{5.16}$$

in a way that accounts for both the direct effects of $\boldsymbol{\theta}$ on M and the indirect effects of $\boldsymbol{\theta}$ on

M through $\hat{\mathbf{x}}$. This sensitivity is

$$\frac{dr}{d\boldsymbol{\theta}^{\mathsf{T}}} = \frac{dr}{d\mathrm{vec}^{\mathsf{T}}\mathbf{M}} \frac{d\mathrm{vec}\,\mathbf{M}}{d\boldsymbol{\theta}^{\mathsf{T}}} \tag{5.17}$$

$$= \left(\frac{dr}{d\mathrm{vec}^{\mathsf{T}}\mathbf{M}}\right)\left(\frac{\partial\mathrm{vec}\,\mathbf{M}}{\partial\boldsymbol{\theta}^{\mathsf{T}}} + \frac{\partial\mathrm{vec}\,\mathbf{M}}{\partial\hat{\mathbf{x}}^{\mathsf{T}}}\frac{d\hat{\mathbf{x}}}{d\boldsymbol{\theta}^{\mathsf{T}}}\right) \tag{5.18}$$

The sensitivity of r in (5.18) requires four pieces: the linearization M at the equilibrium, the sensitivity of the equilibrium $\hat{\mathbf{x}}$ to the parameters, the sensitivity of the transient index r to the linearization, and the sensitivity of the linearization to the parameters (which involves derivatives of M with respect to x and $\boldsymbol{\theta}$).

These derivatives are written using the matrix calculus conventions of Magnus and Neudecker (1985, 1988) [see Nel (1980) for a review, and Caswell (2007) for an ecological introduction]. In this approach, the derivative of a $n \times 1$ vector y with respect to a $m \times 1$ vector x is the $n \times m$ Jacobian matrix

$$\frac{d\mathbf{y}}{d\mathbf{x}^{\mathsf{T}}} = \left(\frac{dy_i}{dx_j}\right) \tag{5.19}$$

Derivatives of, or with respect to, matrices are converted to vector derivatives using the vec operator, which stacks the columns of a matrix one above the other. Thus the derivative of the $m \times n$ matrix $\mathbf{Y}$ with respect to the $p \times q$ matrix $\mathbf{X}$ is the $mn \times pq$ matrix

$$\frac{d\mathrm{vec}\,\mathbf{Y}}{d\mathrm{vec}^{\mathsf{T}}\mathbf{X}} \tag{5.20}$$

where $\mathrm{vec}^{\mathsf{T}}\mathbf{X} = (\mathrm{vec}\,\mathbf{X})^{\mathsf{T}}$. We make frequent use of the result (Roth, 1934) that

$$\mathrm{vec}\,(\mathbf{ABC}) = (\mathbf{C}^{\mathsf{T}} \otimes \mathbf{A})\,\mathrm{vec}\,\mathbf{B} \tag{5.21}$$

5.2 Equilibria, linearizations, and their sensitivities

In this section, we present the analysis of the linearization and the equilibrium. In Section 5.3 we will combine these to obtain the sensitivity of reactivity, the amplification envelope, and the optimal perturbation.

5.2.1 The linearization

The matrix of the linearization at an equilibrium $\hat{\mathbf{x}}$ is

$$\mathbf{M} = \begin{cases} \left.\frac{\partial \dot{\mathbf{x}}}{\partial \mathbf{x}^{\mathsf{T}}}\right|_{\hat{\mathbf{x}}} & \text{continuous} \\ \\ \left.\frac{\partial \mathbf{x}(t+1)}{\partial \mathbf{x}^{\mathsf{T}}(t)}\right|_{\hat{\mathbf{x}}} & \text{discrete} \end{cases} \tag{5.22}$$

where $\dot{\mathbf{x}} = d\mathbf{x}/dt$ is given in (5.1) and $\mathbf{x}(t+1)$ is given in (5.2). The expression for $\mathbf{M}$ is the same for both models; here is the derivation for the continuous case.

Differentiating $\dot{\mathbf{x}}$ in (5.1) gives

$$d\dot{\mathbf{x}} = (d\mathbf{A})\,\mathbf{x} + \mathbf{A}\,(d\mathbf{x}) \tag{5.23}$$

Applying the vec operator to both sides gives

$$d\dot{\mathbf{x}} = \left(\mathbf{x}^{\mathsf{T}} \otimes \mathbf{I}_s\right) d\mathrm{vec}\,\mathbf{A} + \mathbf{A}d\mathbf{x} \tag{5.24}$$

from which

$$\mathbf{M} = \left(\mathbf{x}^{\mathsf{T}} \otimes \mathbf{I}_s\right) \frac{d\mathrm{vec}\,\mathbf{A}}{d\mathbf{x}^{\mathsf{T}}} + \mathbf{A} \tag{5.25}$$

where $\mathbf{I}_s$ is an identity matrix of order s. The linearization at the equilibrium is obtained by evaluating $\mathbf{M}$ at $\mathbf{x} = \hat{\mathbf{x}}$:

$$\mathbf{M}\left[\boldsymbol{\theta}, \hat{\mathbf{x}}\right] = \left(\hat{\mathbf{x}}^{\mathsf{T}} \otimes \mathbf{I}_s\right) \left.\frac{\partial\mathrm{vec}\,\mathbf{A}}{\partial \mathbf{x}^{\mathsf{T}}}\right|_{\hat{\mathbf{x}}} + \mathbf{A}\left[\boldsymbol{\theta}, \hat{\mathbf{x}}\right] \tag{5.26}$$

The last term in (5.26) vanishes if $\mathbf{A}[\boldsymbol{\theta}, \mathbf{x}]$ is diagonal and $\hat{\mathbf{x}}$ is non-zero. It is always possible to write $\mathbf{A}$ as a diagonal matrix; often, it simplifies the calculations of the derivatives of $\mathbf{M}$.

5.2.2 Sensitivity of equilibria

The equilibrium $\hat{\mathbf{x}}$ depends on the parameters through the entries in $\mathbf{A}[\boldsymbol{\theta}, \mathbf{x}]$. Its sensitivity is obtained by differentiating the equations defining the equilibrium (see Appendix 5.7 for the continuous case, and Caswell (in prep) for the discrete case). The sensitivity in the continuous case is

$$\frac{d\hat{\mathbf{x}}}{d\boldsymbol{\theta}^{\mathsf{T}}} = \left\{ -\mathbf{A} - \left(\hat{\mathbf{x}}^{\mathsf{T}} \otimes \mathbf{I}_s\right) \frac{\partial \mathrm{vec}\, \mathbf{A}}{\partial \mathbf{x}^{\mathsf{T}}} \right\}^{-1} \left(\hat{\mathbf{x}}^{\mathsf{T}} \otimes \mathbf{I}_s\right) \frac{\partial \mathrm{vec}\, \mathbf{A}}{\partial \boldsymbol{\theta}^{\mathsf{T}}}. \tag{5.27}$$

The sensitivity in the discrete case is

$$\frac{d\hat{\mathbf{x}}}{d\boldsymbol{\theta}^{\mathsf{T}}} = \left\{ \mathbf{I}_s - \mathbf{A} - \left(\hat{\mathbf{x}}^{\mathsf{T}} \otimes \mathbf{I}_s\right) \frac{\partial \mathrm{vec}\, \mathbf{A}}{\partial \mathbf{x}^{\mathsf{T}}} \right\}^{-1} \left(\hat{\mathbf{x}}^{\mathsf{T}} \otimes \mathbf{I}_s\right) \frac{\partial \mathrm{vec}\, \mathbf{A}}{\partial \boldsymbol{\theta}^{\mathsf{T}}}. \tag{5.28}$$

for discrete time. In both expressions, the matrix $\mathbf{A}$ and all its derivatives are evaluated at $\hat{\mathbf{x}}$.

5.2.3 Sensitivity of the linearization

To obtain the sensitivity of the linearization, we differentiate equation (5.26) for $\mathbf{M}[\boldsymbol{\theta}, \hat{\mathbf{x}}]$:

$$d\mathbf{M} = \left\{ d\left(\hat{\mathbf{x}}^{\mathsf{T}} \otimes \mathbf{I}_s\right) \right\} \frac{\partial \mathrm{vec}\, \mathbf{A}}{\partial \mathbf{x}^{\mathsf{T}}} + \left(\hat{\mathbf{x}}^{\mathsf{T}} \otimes \mathbf{I}_s\right) d\left(\frac{\partial \mathrm{vec}\, \mathbf{A}}{\partial \mathbf{x}^{\mathsf{T}}} \right) + d\mathbf{A} \tag{5.29}$$

Applying the vec operator to both sides gives

$$\begin{aligned} d\mathrm{vec}\, \mathbf{M} &= \left\{ \left(\frac{\partial \mathrm{vec}\, \mathbf{A}}{\partial \mathbf{x}^{\mathsf{T}}} \right)^{\mathsf{T}} \otimes \mathbf{I}_s \right\} d\mathrm{vec}\, \left(\hat{\mathbf{x}}^{\mathsf{T}} \otimes \mathbf{I}_s\right) \\ &\quad + \left\{ \mathbf{I}_s \otimes \left(\hat{\mathbf{x}}^{\mathsf{T}} \otimes \mathbf{I}_s\right) \right\} d\mathrm{vec}\, \left(\frac{\partial \mathrm{vec}\, \mathbf{A}}{\partial \mathbf{x}^{\mathsf{T}}} \right) + d\mathrm{vec}\, \mathbf{A} \end{aligned} \tag{5.30}$$

Theorem 11 of Magnus and Neudecker (1985), for the differential of a Kronecker product, implies that

$$d\left[\mathrm{vec}\left(\hat{\mathbf{x}}^{\mathsf{T}} \otimes \mathbf{I}_s\right)\right] = \left(\mathbf{I}_s \otimes \mathrm{vec}\,\mathbf{I}_s\right) d\hat{\mathbf{x}} \tag{5.31}$$

To differentiate $\partial \mathrm{vec}\,\mathbf{A}/\partial \mathbf{x}^{\mathsf{T}}$, define

$$\mathbf{B}[\boldsymbol{\theta}, \hat{\mathbf{x}}] \equiv \frac{d\mathrm{vec}\,\mathbf{A}}{d\mathbf{x}^{\mathsf{T}}}$$

Then

$$d\mathrm{vec}\,\mathbf{B} = \frac{\partial \mathrm{vec}\,\mathbf{B}}{\partial \boldsymbol{\theta}^{\mathsf{T}}} d\boldsymbol{\theta} + \frac{\partial \mathrm{vec}\,\mathbf{B}}{\partial \mathbf{x}^{\mathsf{T}}} \frac{d\hat{\mathbf{x}}}{d\boldsymbol{\theta}^{\mathsf{T}}} d\boldsymbol{\theta} \tag{5.32}$$

Similarly,

$$d\mathrm{vec}\,\mathbf{A} = \frac{\partial \mathrm{vec}\,\mathbf{A}}{\partial \boldsymbol{\theta}^{\mathsf{T}}} d\boldsymbol{\theta} + \frac{\partial \mathrm{vec}\,\mathbf{A}}{\partial \mathbf{x}^{\mathsf{T}}} \frac{d\hat{\mathbf{x}}}{d\boldsymbol{\theta}^{\mathsf{T}}} d\boldsymbol{\theta} \tag{5.33}$$

Substituting (5.31), (5.32), and (5.33) into (5.30) and collecting terms gives

$$\begin{aligned} \frac{d\mathrm{vec}\,\mathbf{M}}{d\boldsymbol{\theta}^{\mathsf{T}}} &= \left\{ \left(\frac{\partial \mathrm{vec}\,\mathbf{A}}{\partial \mathbf{x}^{\mathsf{T}}} \right)^{\mathsf{T}} \otimes \mathbf{I}_s \right\} \left(\mathbf{I}_s \otimes \mathrm{vec}\,\mathbf{I}_s\right) \frac{d\hat{\mathbf{x}}}{d\boldsymbol{\theta}^{\mathsf{T}}} + \left\{\mathbf{I}_s \otimes \left(\hat{\mathbf{x}}^{\mathsf{T}} \otimes \mathbf{I}_s\right)\right\} \\ &\quad \times \left(\frac{\partial \mathrm{vec}\,\mathbf{B}}{\partial \boldsymbol{\theta}^{\mathsf{T}}} + \frac{\partial \mathrm{vec}\,\mathbf{B}}{\partial \mathbf{x}^{\mathsf{T}}} \frac{d\hat{\mathbf{x}}}{d\boldsymbol{\theta}^{\mathsf{T}}} \right) + \frac{\partial \mathrm{vec}\,\mathbf{A}}{\partial \boldsymbol{\theta}^{\mathsf{T}}} + \frac{\partial \mathrm{vec}\,\mathbf{A}}{\partial \mathbf{x}^{\mathsf{T}}} \frac{d\hat{\mathbf{x}}}{d\boldsymbol{\theta}^{\mathsf{T}}} \end{aligned} \tag{5.34}$$

where all matrices and derivatives are evaluated at $\hat{\mathbf{x}}$, and where $d\hat{\mathbf{x}}/d\boldsymbol{\theta}^{\mathsf{T}}$ is given by (5.27) for continuous models and (5.28) for discrete models.

5.3 Sensitivity of transient indices

We turn now to the sensitivity of reactivity, the amplification envelope, and the optimal perturbation. To do so, we must find the sensitivity of each index to the linearization $\mathbf{M}[\boldsymbol{\theta}, \hat{\mathbf{x}}]$ and then, following (5.18), combine this with the sensitivity of $\mathbf{M}$ as given in (5.34).

5.3.1 Sensitivity of reactivity

In continuous systems, the reactivity ν_0 is the dominant eigenvalue of the matrix $\mathbf{H}(\mathbf{M}) = (\mathbf{M}+\mathbf{M}^{\mathsf{T}})/2$. Appendix 5.7.2 shows that differentiating ν_0 with respect to $\mathbf{M}$ gives

$$\frac{d\nu_0}{d\mathrm{vec}^{\mathsf{T}}\mathbf{M}} = \left(\mathbf{w}^{\mathsf{T}} \otimes \mathbf{w}^{\mathsf{T}}\right) \tag{5.35}$$

where $\mathbf{w}$ is the eigenvector of $\mathbf{H}(\mathbf{M})$ associated with the eigenvalue ν_0 (Magnus and Neudecker, 1988). This result is given in different notation in Neubert and Caswell (1997).

In discrete systems, the reactivity is the logarithm of the dominant singular value σ_1 of $\mathbf{M}$. Appendix 5.7.2 (cf. Stewart, 1991; Caswell and Neubert, 2005) shows that

$$\frac{d\nu_0}{d\mathrm{vec}^{\mathsf{T}}\mathbf{M}} = \frac{1}{|||\mathbf{M}|||}\left(\mathbf{v}^{\mathsf{T}} \otimes \mathbf{u}^{\mathsf{T}}\right) \tag{5.36}$$

where $\mathbf{u}$ is the left singular vector and $\mathbf{v}$ is the right singular vector of $\mathbf{M}$ corresponding to σ_1. Thus the sensitivity of reactivity is

$$\frac{d\nu_0}{d\boldsymbol{\theta}^{\mathsf{T}}} = \begin{cases} \left(\mathbf{w}^{\mathsf{T}} \otimes \mathbf{w}^{\mathsf{T}}\right)\dfrac{d\mathrm{vec}\,\mathbf{M}}{d\boldsymbol{\theta}^{\mathsf{T}}} & \text{continuous} \\[2ex] \dfrac{1}{|||\mathbf{M}|||}\left(\mathbf{v}^{\mathsf{T}} \otimes \mathbf{u}^{\mathsf{T}}\right)\dfrac{d\mathrm{vec}\,\mathbf{M}}{d\boldsymbol{\theta}^{\mathsf{T}}} & \text{discrete} \end{cases} \tag{5.37}$$

where $d\mathrm{vec}\,\mathbf{M}/d\boldsymbol{\theta}^{\mathsf{T}}$ is given by (5.34).

5.3.2 Sensitivity of the amplification envelope

The amplification envelope $\rho(t)$ is the largest singular value of $\mathbf{\Phi}(t)$. Its sensitivity is

$$\frac{d\rho(t)}{d\mathrm{vec}^{\mathsf{T}}\mathbf{M}} = \frac{d\rho(t)}{d\mathrm{vec}^{\mathsf{T}}\mathbf{\Phi}(t)}\frac{d\mathrm{vec}\,\mathbf{\Phi}(t)}{d\mathrm{vec}^{\mathsf{T}}\mathbf{M}} \tag{5.38}$$

As in (5.36), the derivative of the singular value is

$$\frac{d\rho(t)}{d\mathrm{vec}^{\mathsf{T}}\mathbf{\Phi}(t)} = \left(\mathbf{v}^{\mathsf{T}}(t) \otimes \mathbf{u}^{\mathsf{T}}(t)\right) \tag{5.39}$$

where $\mathbf{u}(t)$ and $\mathbf{v}(t)$ are the left and right singular vectors of $\mathbf{\Phi}(t)$ corresponding to σ_1.

In continuous time, the derivative of the fundamental matrix is (e.g. Chen and Zadrozny, 2001)

$$\begin{aligned} \frac{d\mathrm{vec}\,\mathbf{\Phi}(t)}{d\mathrm{vec}^{\mathsf{T}}\mathbf{M}} &= \frac{d\mathrm{vec}\,e^{\mathbf{M}t}}{d\mathrm{vec}^{\mathsf{T}}\mathbf{M}} \\ &= \sum_{i=0}^{\infty} \frac{t^i}{i!} \sum_{j=1}^{i} (\mathbf{M}^{\mathsf{T}})^{i-j} \otimes (\mathbf{M})^{j-1} \end{aligned} \tag{5.40}$$

The equivalent in discrete time is

$$\begin{aligned} \frac{d\mathrm{vec}\,\mathbf{\Phi}(t)}{d\mathrm{vec}^{\mathsf{T}}\mathbf{M}} &= \frac{d\mathrm{vec}\,\mathbf{M}^t}{d\mathrm{vec}^{\mathsf{T}}\mathbf{M}} \\ &= \sum_{j=1}^{t} (\mathbf{M}^{\mathsf{T}})^{t-j} \otimes \mathbf{M}^{j-1} \end{aligned} \tag{5.41}$$

Thus the sensitivity of the amplification envelope is

$$\frac{d\rho(t)}{d\boldsymbol{\theta}^{\mathsf{T}}} = \begin{cases} \left(\mathbf{v}^{\mathsf{T}}(t) \otimes \mathbf{u}^{\mathsf{T}}(t)\right) \left(t \displaystyle\sum_{i=0}^{\infty} \frac{1}{i!} \sum_{j=1}^{i} (\mathbf{M}^{\mathsf{T}}t)^{i-j} \otimes (\mathbf{M}t)^{j-1} \right) \dfrac{d\mathrm{vec}\,\mathbf{M}}{d\boldsymbol{\theta}^{\mathsf{T}}} & \text{continuous} \\ \left(\mathbf{v}^{\mathsf{T}}(t) \otimes \mathbf{u}^{\mathsf{T}}(t)\right) \left(\displaystyle\sum_{j=1}^{t} (\mathbf{M}^{\mathsf{T}})^{t-j} \otimes \mathbf{M}^{j-1} \right) \dfrac{d\mathrm{vec}\,\mathbf{M}}{d\boldsymbol{\theta}^{\mathsf{T}}} & \text{discrete} \end{cases} \tag{5.42}$$

where $d\mathrm{vec}\,\mathbf{M}/d\boldsymbol{\theta}^{\mathsf{T}}$ is given by (5.34).

5.3.3 Sensitivity of the optimal perturbation

The optimal perturbation is given by $\mathbf{v}(t)$, the leading right singular vector of $\mathbf{\Phi}(t)$. To calculate the sensitivity of $\mathbf{v}(t)$ we require the sensitivity of the singular vector to the matrix

$\boldsymbol{\Phi}$. This is given by

$$\begin{aligned}\frac{d\mathbf{v}}{d\mathrm{vec}^{\mathsf{T}}\boldsymbol{\Phi}} &= \left(\sigma^2\mathbf{I}_s - \boldsymbol{\Phi}^{\mathsf{T}}\boldsymbol{\Phi} + \frac{\sigma^2}{2}(\mathbf{v}^{\mathsf{T}}\otimes\mathbf{v}) + \frac{\sigma^2}{2}\mathbf{v}\mathbf{v}^{\mathsf{T}}\right)^{-1} \\ &\quad\times\left[(\mathbf{v}^{\mathsf{T}}\otimes\mathbf{I}_s) - (\mathbf{v}^{\mathsf{T}}\otimes\mathbf{v}\mathbf{v}^{\mathsf{T}})\right]\left[(\boldsymbol{\Phi}^{\mathsf{T}}\otimes\mathbf{I})\mathbf{P} + (\mathbf{I}\otimes\boldsymbol{\Phi}^{\mathsf{T}})\right] \qquad (5.43)\end{aligned}$$

where $\mathbf{P}$ is the vec permutation matrix (Henderson and Searle, 1981); see Appendix 5.7.2 for the derivation. The sensitivity of the optimal perturbation is then

$$\frac{d\mathbf{v}(t)}{d\boldsymbol{\theta}^{\mathsf{T}}} = \frac{d\mathbf{v}(t)}{d\mathrm{vec}\,\boldsymbol{\Phi}(t)}\,\frac{d\mathrm{vec}\,\boldsymbol{\Phi}(t)}{d\mathrm{vec}^{\mathsf{T}}\mathbf{M}}\,\frac{d\mathrm{vec}\,\mathbf{M}}{d\boldsymbol{\theta}^{\mathsf{T}}} \qquad (5.44)$$

where $d\mathrm{vec}\,\boldsymbol{\Phi}(t)/d\mathrm{vec}^{\mathsf{T}}\mathbf{M}$ is given by (5.40) for continuous systems and by (5.41) for discrete systems, and $d\mathrm{vec}\,\mathbf{M}/d\boldsymbol{\theta}^{\mathsf{T}}$ is given by (5.34).

5.3.4 Anisotropic measures of transient amplification

In Section 5.1.1 the reactivity, amplification envelope, and optimal perturbation are defined in terms of the Euclidean distance from the equilibrium $\hat{\mathbf{x}}$. In applications, some components of the perturbation may be of more interest than others. For example, one might want apply relative weights to the elements of the perturbation vector, to translate numbers of individuals into biomass or nutrient content. Or, one might want to focus on the response of a subset of species (e.g., one trophic level, or a pest species subject to biological control) out of an entire community. The transient dynamics of such anisotropic state vectors can be easily analyzed.

Weighting kernels

To apply weights to the elements of the perturbation, define a diagonal weighting kernel matrix $\mathbf{K}$, whose elements give the relative importance of each element of $\mathbf{z}$. Define the rescaled vector $\tilde{\mathbf{z}} = \mathbf{K}\mathbf{z}$, the norm of which is $\|\tilde{\mathbf{z}}\| = (\mathbf{z}^{\mathsf{T}}\mathbf{K}^2\mathbf{z})^{1/2}$. Solving the optimization problem for $||\tilde{\mathbf{z}}||$, we obtain a modified expression for the reactivity and the amplification envelope; these are the same as 5.7 and 5.14 but with the Jacobian and fundamental matrix replaced by

$$\tilde{\mathbf{M}} = \mathbf{K}\mathbf{M}\mathbf{K}^{-1} \tag{5.45}$$

$$\tilde{\mathbf{\Phi}} = \mathbf{K}\mathbf{\Phi}\mathbf{K}^{-1} \tag{5.46}$$

Differentiating these expressions gives

$$\frac{d\mathrm{vec}\,\tilde{\mathbf{M}}}{d\mathrm{vec}^{\mathsf{T}}\mathbf{M}} = \frac{d\mathrm{vec}\,\tilde{\mathbf{\Phi}}}{d\mathrm{vec}^{\mathsf{T}}\mathbf{\Phi}} = \left(\mathbf{K}^{-1} \otimes \mathbf{K}\right) \tag{5.47}$$

Then, for any transient index r, we can write

$$\frac{dr}{d\boldsymbol{\theta}^{\mathsf{T}}} = \frac{dr}{d\mathrm{vec}^{\mathsf{T}}\tilde{\mathbf{\Phi}}} \frac{d\tilde{\mathbf{\Phi}}}{d\mathrm{vec}^{\mathsf{T}}\mathbf{\Phi}} \frac{d\mathrm{vec}\,\mathbf{\Phi}}{d\mathrm{vec}^{\mathsf{T}}\tilde{\mathbf{M}}} \frac{d\mathrm{vec}\,\tilde{\mathbf{M}}}{d\mathrm{vec}^{\mathsf{T}}\mathbf{M}} \frac{d\mathrm{vec}\,\mathbf{M}}{d\boldsymbol{\theta}^{\mathsf{T}}} \tag{5.48}$$

The weighting kernel effectively "stretches" the space in which we measure deviations from equilibrium. The same result could be obtained by scaling the nonlinear model, and then analyzing the perturbations in the rescaled space. The advantage of the weighting kernel is that is allows for consideration of different norms without the need to repeat the calculations of sensitivity matrices.

Projection operators

To optimize the transient response along a subset of the total number of dimensions, we define a projection operator, $\mathbf{Q}$, whose entries are $Q_{ii} = 1$ if the i^{th} element of $\mathbf{z}$ is to be included in the optimization and 0 otherwise.

We want to maximize the norm of $\tilde{\mathbf{z}} = \mathbf{Q}\mathbf{z}$ in response to arbitrary perturbations $\mathbf{z}_0$, which are still measured by their Euclidian norm. Reactivity and the amplification envelope are calculated by replacing the jacobian and fundamental matrix by

$$\tilde{\mathbf{M}} = \mathbf{Q}\mathbf{M} \tag{5.49}$$

$$\tilde{\mathbf{\Phi}} = \mathbf{Q}\mathbf{\Phi} \tag{5.50}$$

Substituting in the optimization problems (5.6) and (5.12), we find that reactivity is given by the leading eigenvalue of the Hermitian part of $\tilde{\mathbf{M}}$ and the amplification envelope by the leading singular value of $\tilde{\mathbf{\Phi}}$.

It should be noted that these expressions for ν_0 and $\rho(t)$ can also be derived by generalizing the idea of weighted norms (above) but using different weighting kernels for the perturbations at time t and for initial perturbations (Farrell and Ionannou, 1996).

Differentiating these gives

$$\frac{d\mathrm{vec}\,\tilde{\mathbf{M}}}{d\mathrm{vec}^{\mathsf{T}}\mathbf{M}} = \frac{d\mathrm{vec}\,\tilde{\mathbf{\Phi}}}{d\mathrm{vec}^{\mathsf{T}}\mathbf{\Phi}} = (\mathbf{I} \otimes \mathbf{Q}) \tag{5.51}$$

which can be substituted in (5.48) to calculate the sensitivity of transient indices in the projection space.

5.4 Applications to consumer-resource dynamics

Consumer-resource models are often reactive, and reactivity tends to increase with the number of species (Chen and Cohen, 2001; Neubert et al., 2004). In this section, we apply sensitivity analysis to a predator-prey model and a multi-species food web model. The results provide insight into the mechanisms by which reactivity and transient amplification can be produced.

5.4.1 Predator-prey interactions

The Rosenzweig-MacArthur model (Rosenzweig and MacArthur, 1963) for a predator (Z) and prey (P) is

$$\frac{dP}{dt} = rP\left(1-\frac{P}{K}\right) - g\frac{P}{P+P_h}Z \tag{5.52}$$

$$\frac{dZ}{dt} = \epsilon g\frac{P}{P+P_h}Z - \delta Z \tag{5.53}$$

The prey grows logistically, with maximum growth rate r and carrying capacity K. The predator has a mortality rate δ and exhibits a Holling type II functional response; g is the maximum predation rate, P_h the half-saturation prey density, and ϵ the assimilation efficiency.

The system has a single coexistence equilibrium, given by

$$\hat{P} = \frac{P_h\delta}{\epsilon g-\delta} \tag{5.54}$$

$$\hat{Z} = r\left(1-\frac{\hat{P}}{K}\right)\frac{\hat{P}+P_h}{g} \tag{5.55}$$

The model (5.52-5.53) can be expressed in the formalism (5.1), with [2]

$$\mathbf{A} = \begin{bmatrix} r\left(1-\frac{P}{K}\right) - \frac{g}{P+P_h}Z & 0 \\ 0 & \epsilon\frac{gP}{P+P_h} - \delta \end{bmatrix} \tag{5.56}$$

We define a population vector $\mathbf{x} \equiv [P\,Z]^{\mathsf{T}}$ and a parameter vector $\boldsymbol{\theta} \equiv [\epsilon\, g\, \delta\, P_h\, r\, K]^{\mathsf{T}}$.

---

[2] It is not essential to write $\mathbf{A}$ as a diagonal matrix, but in some cases – like this one – it simplifies the calculation of derivatives.

The first derivatives of **A** are

$$\mathbf{B} \equiv \frac{\partial \operatorname{vec} \mathbf{A}}{\partial \mathbf{x}^{\mathsf{T}}} = \begin{bmatrix} \frac{-r}{K} + \frac{g}{(P+P_h)^2} Z & \frac{-g}{P+P_h} \\ 0 & 0 \\ 0 & 0 \\ \epsilon \frac{gP_h}{(P+P_h)^2} & 0 \end{bmatrix} \tag{5.57}$$

$$\frac{\partial \operatorname{vec} \mathbf{A}}{\partial \boldsymbol{\theta}^{\mathsf{T}}} = \begin{bmatrix} 0 & \frac{-Z}{P+P_h} & 0 & \frac{g}{(P+P_h)^2} Z & 1 - \frac{P}{K} & \frac{-rP}{K^2} \\ 0 & 0 & 0 & 0 & 0 & 0 \\ 0 & 0 & 0 & 0 & 0 & 0 \\ \frac{gP}{(P+P_h)} & \frac{\epsilon P}{(P+P_h)} & -1 & \frac{-\epsilon g P}{(P+P_h)^2} & 0 & 0 \end{bmatrix} \tag{5.58}$$

The second derivatives are

$$\frac{\partial \operatorname{vec} \mathbf{B}}{\partial \mathbf{x}^{\mathsf{T}}} = \begin{bmatrix} -2 \frac{g}{(P+P_h)^3} Z & \frac{g}{(P+P_h)^2} \\ 0 & 0 \\ 0 & 0 \\ -2\epsilon \frac{gP_h}{(P+P_h)^3} & 0 \\ \frac{g}{(P+P_h)^2} & 0 \\ 0 & 0 \\ 0 & 0 \\ 0 & 0 \end{bmatrix} \tag{5.59}$$

$$\frac{\partial \operatorname{vec} \mathbf{B}}{\partial \boldsymbol{\theta}^{\mathsf{T}}} = \begin{bmatrix} 0 & \frac{Z}{(P+P_h)^2} & 0 & -2 \frac{g}{(P+P_h)^3} Z & \frac{-1}{K} & \frac{r}{K^2} \\ 0 & 0 & 0 & 0 & 0 & 0 \\ 0 & 0 & 0 & 0 & 0 & 0 \\ \frac{gP}{(P+P_h)^2} & \frac{\epsilon P}{(P+P_h)^2} & 0 & \frac{\epsilon g (P-P_h)}{(P+P_h)^3} & 0 & 0 \\ 0 & \frac{-1}{(P+P_h)} & 0 & \frac{g}{(P+P_h)^2} & 0 & 0 \\ 0 & 0 & 0 & 0 & 0 & 0 \\ 0 & 0 & 0 & 0 & 0 & 0 \\ 0 & 0 & 0 & 0 & 0 & 0 \end{bmatrix} \tag{5.60}$$

Table 5.1: Parameters for the predator-prey model

symbol	definition	value		units
		Equilibrium A	Equilibrium B	
ϵ	assimilation efficiency	0.15	0.8	-
g	predation rate	2.3	0.8	d^{-1}
δ	mortality rate	0.1	0.1	d^{-1}
P_h	half-saturation prey density	1	1	μmol m^{-3}
r	prey growth rate	1	1	d^{-1}
K	carrying capacity	1.25	1.25	μmol m^{-3}
$\hat{P}$	equilibrium prey biomass	0.41	0.18	μmol m^{-3}
$\hat{Z}$	equilibrium predator biomass	0.41	1.26	μmol m^{-3}

We will examine two equilibria, with parameters given in Table 5.1; both are locally stable. We focus first on equilibrium A.

Transient growth following arbitrary perturbations

Figure 5-1 illustrates the transient growth of perturbations around equilibrium A. The predator-prey system, pushed away from equilibrium at $t = 0$, exhibits interesting transient dynamics before returning to its stable state. In the linear approximation, deviations from the equilibrium evolve according to (5.3). We consider initial conditions on the unit circle centered on the equilibrium, shown as gray dots in Figure 5-1; the transient responses corresponding to those initial conditions are shown as black dots.

States outside the unit circle at any time (e.g. Figure 5-1a) correspond to initial perturbations that are amplified. The amplification continues for some time, with the largest growth of perturbations occurring at $t = 5.7$; this is when the amplitude of the ellipse is greatest (Figure 5-1b). Perturbations then decay (Figure 5-1c) and the system eventually returns to equilibrium. The direction of the optimal perturbation at each time is shown by a gray arrow (positive and negative perturbations have the same effect due to symmetry of the

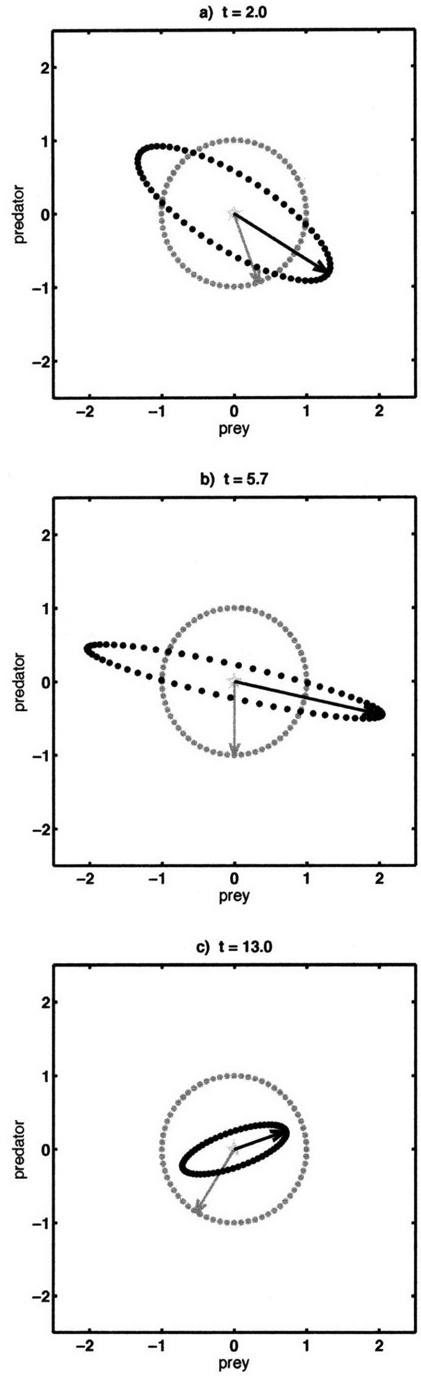

Figure 5-1: Transient amplification of perturbations in the predator-prey model (5.54–5.55) at $t = 2.0$ (showing growth of perturbations), $t = 5.7$ (maximum of the amplification envelope), and $t = 13$ (as perturbations decay). Initial conditions (with unit norm) are represented by gray dots; the response is shown by black dots. Parameters from Table 5.1, Equilibrium A.

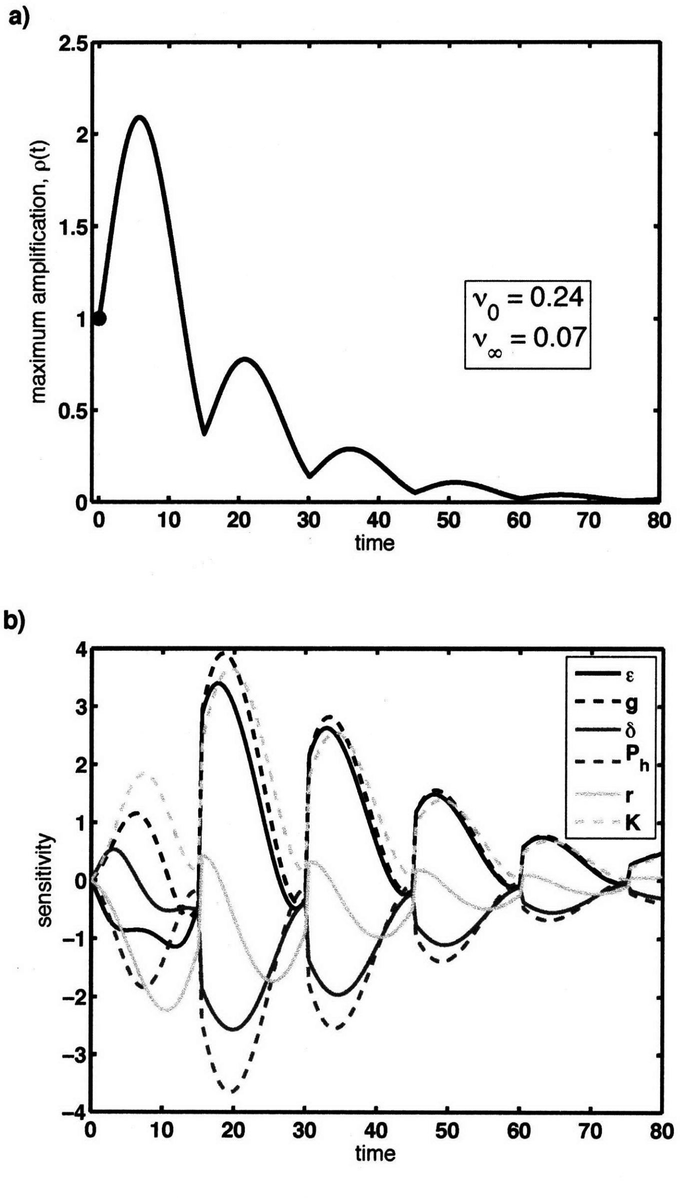

Figure 5-2: a) The amplification envelope $\rho(t)$ for Equilibrium A of the predator-prey model (5.54–5.55), showing the potential amplification of random perturbations. Maximum growth occurs at $t = 5.7$. b) The sensitivity of the amplification envelope to the log of each parameter, as a function of time.

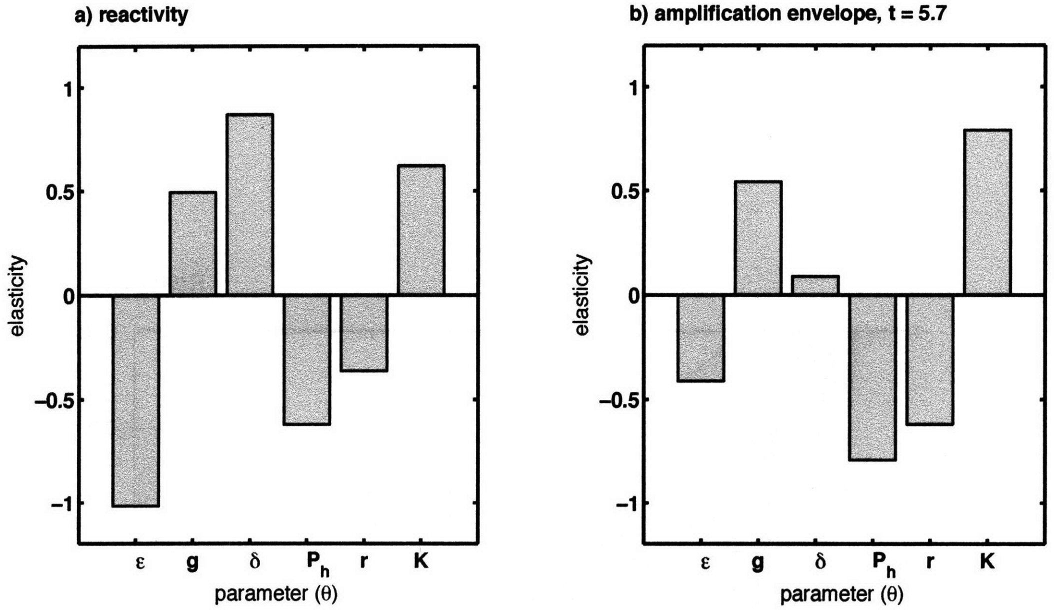

Figure 5-3: Perturbation analysis of transient dynamics for Equilibrium A of the predator-prey model (5.54–5.55). a) The elasticity of reactivity. b) The elasticity of the amplification envelope at the time of maximum amplification.

linearized system). The optimal perturbation rotates clockwise between $t = 2$ and $t = 5.7$. The largest growth at $t = 5.7$ results from a perturbation of the predator population only; this suggests a "top-down" control of reactive dynamics around this equilibrium.

The amplification envelope (Figure 5-2a) shows that maximum amplification occurs at $t = 5.7$. The initial rate of growth is the reactivity (ν_0); the rate at which perturbations decay in the asymptotic limit $t \to \infty$ is the resilience (ν_∞). Fluctuations in the amplification envelope reflect damped oscillations in the dynamics of the perturbed system.

Sensitivity of the amplification envelope, calculated from (5.42) is shown as a function of time in Figure 5-2b. The sensitivities exhibit synchronous fluctuations that appear to be modulated by the amplification itself. For some parameters, the sensitivity changes sign during the period of oscillation. There also appears to be a qualitative change in the effect

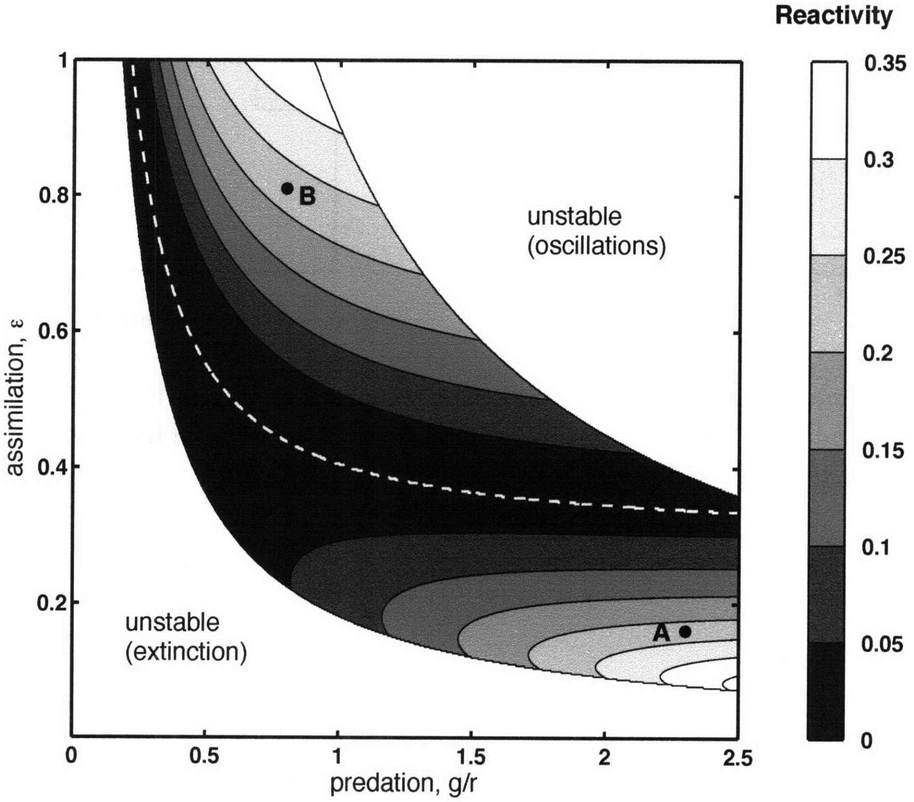

Figure 5-4: Reactivity ν_0 of the predator-prey model (5.54–5.55) in parameter space. Shades of gray give the value of ν_0 in region where the coexistence equilibrium is stable. The white dashed line indicates a ratio of $\hat{Z}/\hat{P} = 3$ (above the curve, ratio is higher). Equilibria A and B (see Table 5.1) have identical reactivities, but different mechanisms are responsible for transient growth.

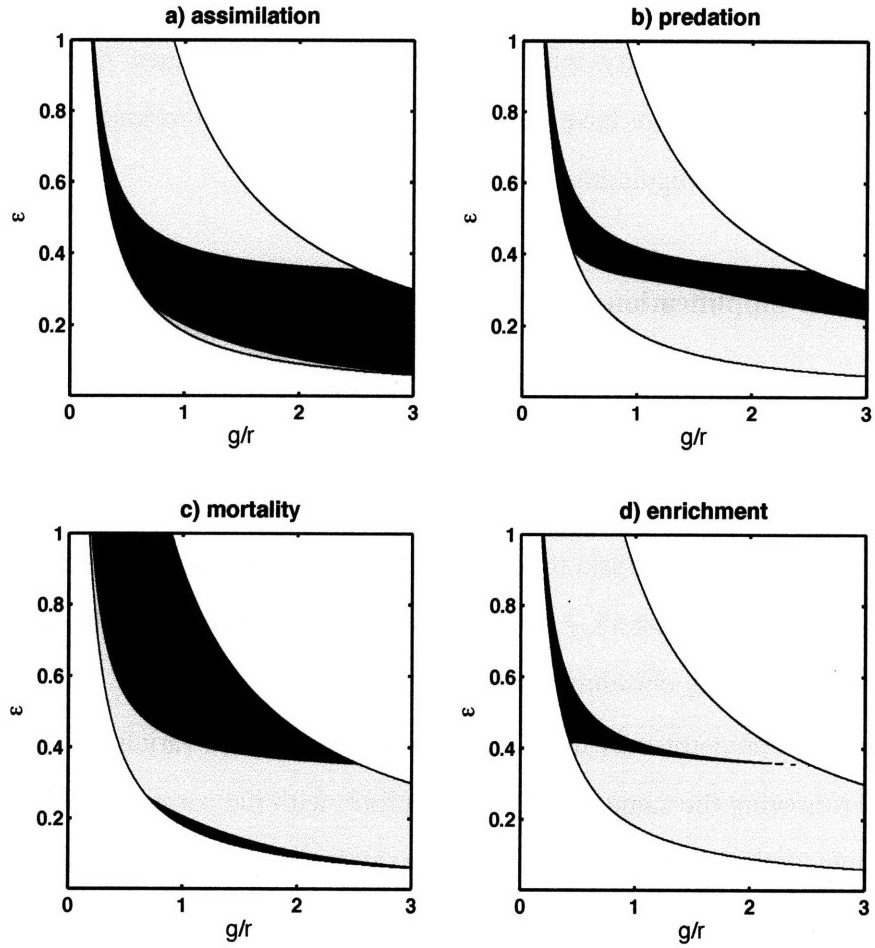

Figure 5-5: The sign of the sensitivity of reactivity of the predator-prey model (5.54–5.55) in the region of parameter space where the coexistence equilibrium is stable. Dark areas indicate negative sensitivity to the non-dimensional parameters, light gray areas indicate positive sensitivity. Sensitivity of ν_0 to a) assimilation (ϵ), b) predation (g/r), c) mortality (d/r), and d) enrichment (K/P_h).

of parameters after the first minimum of the amplification envelope, suggesting a change in dynamics between the initial growth and the period of decay.

The elasticities of reactivity and of the amplification envelope at the time of maximum growth are shown in Figure 5-3. Increases in the predation rate, mortality rate, or carrying capacity will increase reactivity, whereas the assimilation efficiency, half-saturation prey density, and prey growth rate have the opposite effect. This information can be used to explore the mechanisms regulating transient dynamics.

Mechanisms for amplification

Sensitivity analysis can identify the ecological processes responsible for transient amplification. In this model there appear to be two distinct mechanisms for leading to reactive dynamics; we describe them as "top-down" and "bottom-up" controls on transient amplification. We carry out this analysis in terms of the dimensionless parameters ϵ (the assimilation efficiency of the predator), g/r (the scaled predation rate), δ/r (the scaled mortality rate), and K/P_h (the prey enrichment ratio).

We rewrite the predator-prey model in terms of these scaled variables, and compute the sensitivities following the same procedure as before, with the parameter $\boldsymbol{\theta}$ now containing the four dimensionless parameters. First, we examine the effect of assimilation and predation. Reactivity is plotted in Figure 5-4 in the $(\epsilon,\, g/r)$-plane, in the region where the coexistence equilibrium is stable. (Below that wedge of stability, coexistence is not possible; above it, the asymptotic dynamics are oscillatory.) There are two distinct regions of high reactivity, corresponding to high assimilation efficiency but low predation rate, and vice versa. Intermediate values of ϵ and g/r lead to low reactivity. To describe the mechanisms driving transient growth, we will focus on the equilibrium points A and B (Table 5.1); these have the same reactivity, but differ in other properties.

Mapping the sign of the sensitivity of reactivity reveals some differences between the two reactive regions. The effect of each non-dimensional parameter is summarized in Figure 5-5, in terms of whether they increase (light gray areas) or decrease reactivity (dark gray areas). Predation and enrichment have positive effects on reactivity, except where reactivity is very small. Assimilation and mortality can have a positive or negative effect, depending on the parameter values.

Reactivity at equilibrium A is increased by reducing the assimilation efficiency and increasing the mortality rate. This implies that the mechanism for amplification relies on slow predator growth. At equilibrium, a relatively small predator population keeps the prey constant; consequently, a small reduction in the predator population translates into rapid multiplication of the prey. We call this *top-down* control. Eventually, the predator catches up and removes the excess prey; this explains the qualitative change in sensitivity of the amplification envelope for $t > 11$ (Figure 5-2b).

In contrast, at equilibrium B there is a *bottom-up* transient response. At equilibrium, a large predator population is sustained by the highly efficient, albeit slow, consumption of prey. The predators can take advantage of transient increases in the prey. Because amplification at equilibrium B relies on rapid predator growth, reactivity is enhanced by increasing assimilation efficiency and reducing mortality rate.

The transition between these two scenarios is accompanied by a change in the ratio of predator to prey biomass. The dashed white line in Figure 5-4 bounds the region of resource-depleted equilibria (above the curve), where the transient dynamics are controlled by the lower species in the food chain.

These mechanisms are also reflected in the directions of the optimal initial perturbations and the resulting responses, as shown in Figure 5-6 for a fixed time ($t = 4$) during the initial period of growth. Perturbations leading to maximal growth in the top-down scenario correspond to a decrease in predator biomass and increase in prey or, by symmetry, increase in predator and decrease in prey. The transient response also lies in the second and fourth quadrants (Figure 5-6a). In the bottom-up scenario, by contrast, optimal perturbations and their associated transient response are found in the first and third quadrants; they correspond to concurrent increase or reduction in the prey and predator biomass (Figure 5-6b).

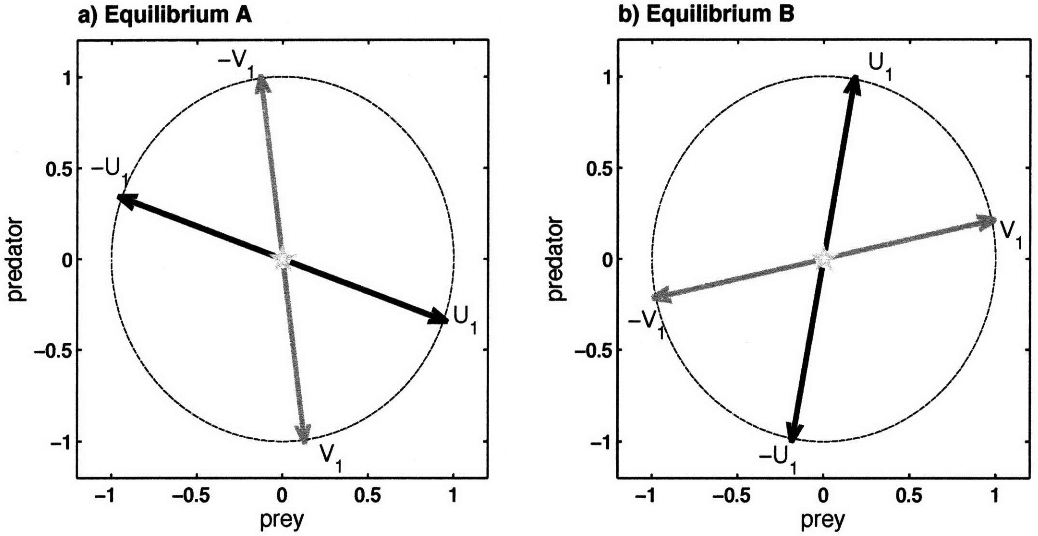

Figure 5-6: Optimal perturbations and transient reponses, for transient growth around a) equilibrium A and b) equilibrium B (labeled on Figure 5-4). Leading initial singular vectors (optimal perturbation), gray; leading final singular vectors (when multiplied by the leading singular value, gives the transient reponse), black, at $t = 4$.

Reactive dynamics with Allee effect

A modified version of the Rosenzweig-MacArthur model includes an Allee effect for the predator (Chapter 1); here we examine how adding this density-dependent term affects reactive dynamics. The matrix for the model with Allee effect is

$$\mathbf{A}' = \begin{bmatrix} r\left(1-\frac{P}{K}\right) - \frac{g}{P+P_h}\frac{Z^2}{Z+c} & 0 \\ 0 & \epsilon\frac{gP}{P+P_h}\frac{Z}{Z+c} - \delta \end{bmatrix} \tag{5.61}$$

where c is the Allee effect constant; $c = 0$ yields the standard model discussed above.

Sensitivities are calculated by differentiating $\mathbf{A}'$; for easy comparison with the standard model discussed above, we evaluate the derivatives at $c = 0$. As shown in Figure 5-7, adding an Allee effect can either increase or decrease the reactivity; the sensitivity pattern is qualitatively very similar to that of predator mortality (Figure 5-5d).

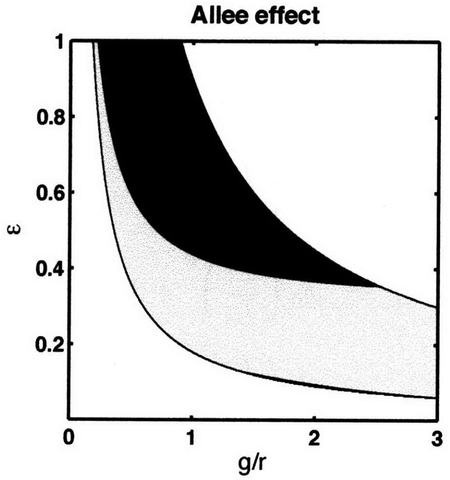

Figure 5-7: Sensitivity of reactivity to the Allee effect parameter c; light gray (dark gray) areas indicate positive (negative) sensitivity.

5.4.2 Multiple food chains

Armstrong (1994) introduced a model for a size-structured marine food web. The model includes size classes of phytoplankton ($P_1, P_2, \ldots$) and zooplankton ($Z_1, Z_2, \ldots$). We consider the case of connected food chains, where each zooplankton size class feeds on phytoplankton in the corresponding size class and on zooplankton in the size class below (Figure 5-8). Allometric relations are assumed for the size-dependence of biological activities.

In our model, we assume logistic growth of phytoplankton, with a carrying capacity chosen to produce the same equilibrium as in Armstrong (1994; his case $N_T = 5$) for the case $N_T = 5$. Using the parameters in Table 5.2 (the values are taken from Armstrong 1994), the model allows for coexistence of 3 phytoplankton classes and 5 zooplankton classes.

The equations are

$$\begin{aligned}\frac{dP_i}{dt} &= \left[r_i\left(1-\frac{\sum P}{K}\right)-\lambda-Z_i\frac{g_i}{P_s}\right]P_i &\quad (5.62)\\ \frac{dZ_i}{dt} &= \left[\epsilon\frac{g_i}{P_s}(P_i+Z_{i-1})-\delta_i-Z_{i+1}\frac{g_{i+1}}{P_s}\right]Z_i &\quad (5.63)\end{aligned}$$

with $i \in [0, 4]$.

The predation rate g_i, mortality rate δ_i, and prey growth rate r_i depend on the body length L_i according to the allometric relations:

$$\begin{aligned}g_i &= g_0\left(\frac{L_i}{L_0}\right)^\beta\\ \delta_i &= \delta_0\left(\frac{L_i}{L_0}\right)^\beta+\lambda\left(\frac{L_i}{L_0}\right)^\gamma\\ r_i &= r_0\left(\frac{L_i}{L_0}\right)^\beta\\ L_i &= 4^i\times L_0\end{aligned}$$

Values for β and γ are given in Table 5.2.

The unique coexistence equilibrium is shown in Figure 5-9. In this food web, the total

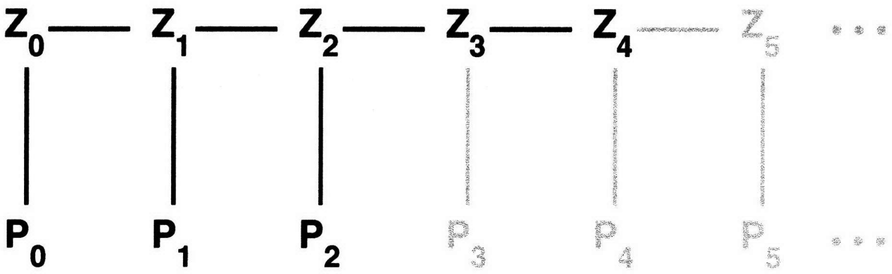

Figure 5-8: Size-structured multiple food chains model, inspired by Armstrong (1994). Each size class of zooplankton can feed on a single class of phytoplankton, as well as on the next smaller zooplankton class. For the parameters of Table 5.2, phytoplankton in size classes P_3 and P_4 become extinct (shown in gray), as do zooplankton in size classes Z_i for $i > 4$.

Table 5.2: Parameters for the multiple food chains model; values are from Armstrong (1994).

symbol	definition	value	units
L_0	length of organism in smallest size class	1	*(arbitrary)*
β	allometric constant	-0.75	-
γ	another allometric constant	-0.4	-
ϵ	assimilation efficiency	0.4	-
g_0	maximum predation rate of organism in smallest size class	1.4	d^{-1}
δ_0	mortality rate of predators in smallest size class	0.068	d^{-1}
r_0	maximum growth rate of prey in smallest size class	1.4	d^{-1}
P_s	full-saturation prey density	2	mmol m^{-3}
λ	mortality rate (size-independent component)	0.016	d^{-1}
K	carrying capacity	2.43	mmol m^{-3}

predator biomass exceeds the prey biomass because of the rapid turnover rate of phytoplankton.

For sensitivity analysis, we write the model in matrix form with a state vector, of length $m = 8$, $\mathbf{x} = [P_0\, P_1\, P_2\, Z_0\, Z_1\, Z_2\, Z_3\, Z_4]^\mathsf{T}$. The matrix $\mathbf{A}$ in (5.1) is diagonal, with elements

$$
\begin{aligned}
A_{11} &= r_0\left(1 - \frac{P_0 + P_1 + P_2}{K}\right) - \lambda - Z_0\frac{g_0}{P_s} \\
A_{22} &= r_0 4^\beta\left(1 - \frac{P_0 + P_1 + P_2}{K}\right) - \lambda - Z_1\frac{g_0 4^\beta}{P_s} \\
A_{33} &= r_0 4^{2\beta}\left(1 - \frac{P_0 + P_1 + P_2}{K}\right) - \lambda - Z_2\frac{g_0 4^{2\beta}}{P_s} \\
A_{44} &= \epsilon\frac{g_0}{P_s}P_1 - \delta_0 - \lambda - Z_1\frac{g_0 4^\beta}{P_s} \\
A_{55} &= \epsilon\frac{g_0 4^\beta}{P_s}\left[(P_1 + Z_0\right] - \delta_0 4^\beta - \lambda 4^\gamma - Z_2\frac{g_0 4^{2\beta}}{P_s} \\
A_{66} &= \epsilon\frac{g_0 4^{2\beta}}{P_s}\left[P_2 + Z_1\right] - \delta_0 4^{2\beta} - \lambda 4^{2\gamma} - Z_3\frac{g_0 4^{3\beta}}{P_s} \\
A_{77} &= \epsilon\frac{g_0 4^{3\beta}}{P_s}Z_2 - \delta_0 4^{3\beta} - \lambda 4^{3\gamma} - Z_4\frac{g_0 4^{4\beta}}{P_s} \\
A_{88} &= \epsilon\frac{g_0 4^{4\beta}}{P_s}Z_3 - \delta_0 4^{4\beta} - \lambda 4^{4\gamma}
\end{aligned}
$$

The matrices $d\text{vec}\,\mathbf{A}/d\mathbf{x}^\mathsf{T}$, $d\text{vec}\,\mathbf{A}/d\boldsymbol{\theta}^\mathsf{T}$, and $d\text{vec}\,\mathbf{B}/d\boldsymbol{\theta}^\mathsf{T}$ required for the sensitivity analysis are large, but because $\mathbf{A}$ is diagonal, most of their entries are zero (Appendix 5.7.3).

The equilibrium is reactive, with the maximum amplification occurring at $t = 37$ (Figure 5-10). Time is measured in days in this parameterization, so the largest effect of perturbing the equilibrium appears more than a month later. The amplification envelope remains above 1 for over 3 years ($t = 1185$ days). This is an example of a system in which transient amplification is likely to be more ecologically relevant than the asymptotic return to the equilibrium.

Even in the 2-species predator-prey model, the effects of the parameters were not always intuitive. In more complex models, sensitivity analysis is particularly useful for understanding what controls the transient dynamics and how a system responds to changes in

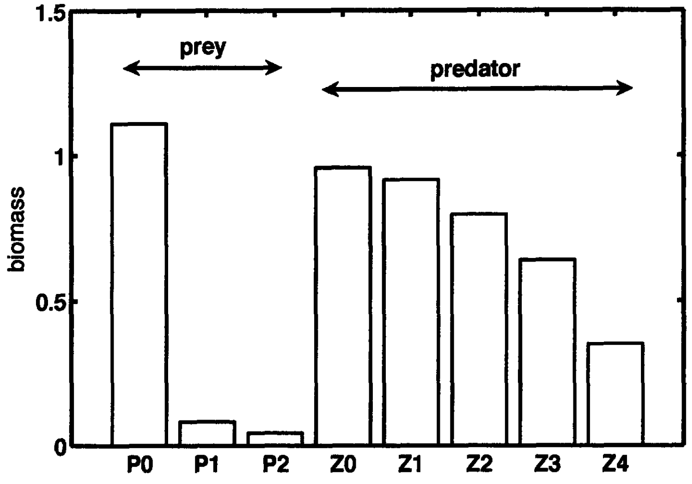

Figure 5-9: Equilibrium densities in the size-structured multiple food chains model (5.63), for the parameters given in Table 5.2.

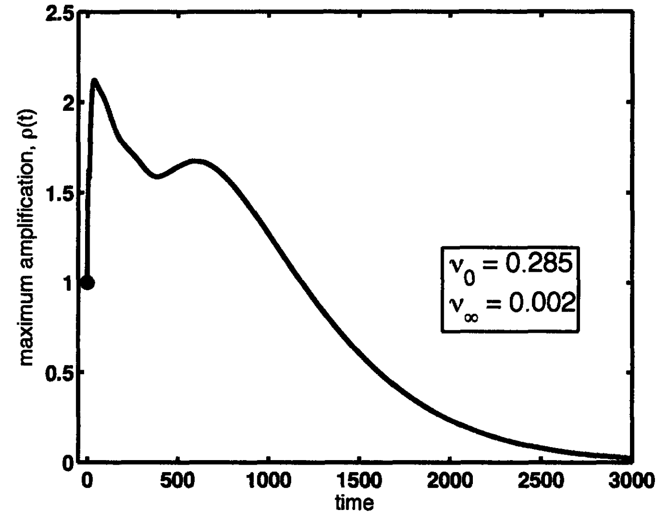

Figure 5-10: The amplification envelope for the size-structured multiple food chains model (5.63). Maximum transient growth occurs at $t = 37$.

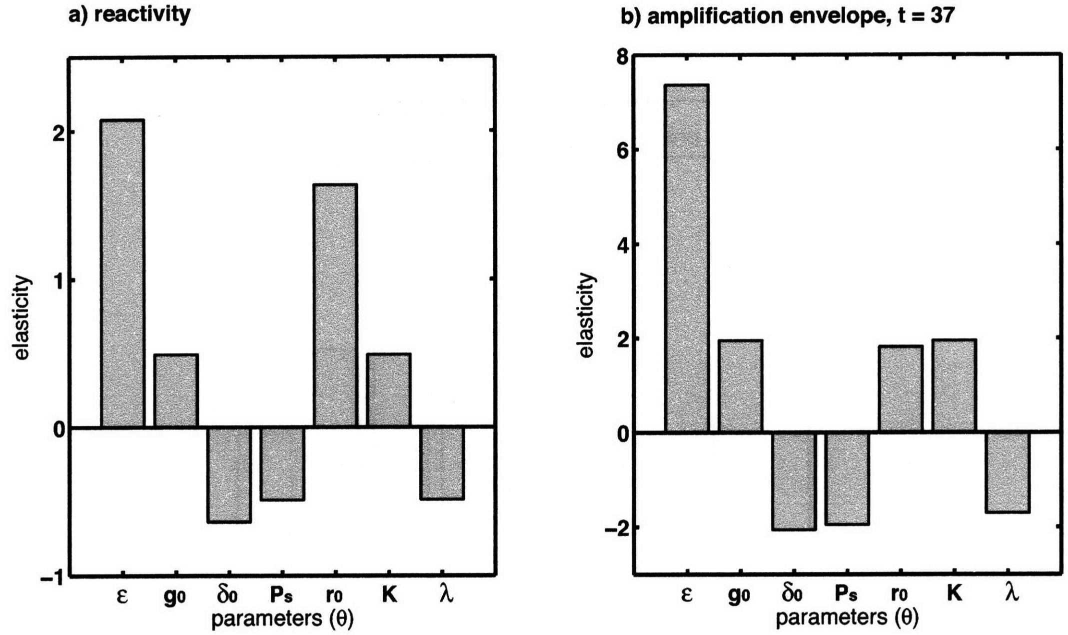

Figure 5-11: Perturbation analysis of transient dynamics for the size-structured multiple food chains model (5.63). a) The elasticity of reactivity. b) The elasticity of the amplification envelope at the time ($t = 37$) of maximum amplification.

the parameters. For this, sensitivity analysis is particularly useful. In this food web model, the assimilation efficiency, predation rate, prey growth rate and carrying capacity have positive impacts on reactivity, whereas mortality and saturation prey density have negative impacts (Figure 5-11a). Parameters that increase reactivity are found to increase the maximum amplification as well (Figure 5-11b), an indication that the same mechanism driving amplification at $t = 0$ causes the maximum growth at $t = 37$. The elasticity to assimilation efficiency is particularly large: a 10% increase in ϵ would increase reactivity by more than 20% and the maximum amplification by more than 70%.

Sensitivity analysis could be employed to investigate, for example, how the mechanisms of transient dynamics vary with food chains' lengths. In Armstrong's (1994) model, the number of trophic levels is controlled by the total nutrient availability. Although this question is not addressed here, it could be studied using the framework presented in this paper.

5.5 Discussion

Ecosystems perturbed from their equilibria exhibit transient dynamics; these can last for extended periods of time and have important ecological consequences. When the equilibrium is reactive, small fluctuations can be amplified. In nature, perturbations result from the stochasticity inherent to the environment and the biological processes themselves. Ecologists have long conceptualized ecological stability in terms of the asymptotic rate of return to equilibrium [see Ives and Carpenter (2007) for a recent example], but it is not yet widely appreciated how deficient this approach is. It bears repeating that the asymptotic rate of return does not determine the transient amplification. For example, it is easy to construct matrices with identical eigenvalues, and hence identical asymptotic rates of return, but with very different reactivities and amplification envelopes (e.g. Trefethen et al., 1993; Neubert and Caswell, 1997).

As more examples accumulate of reactive ecological models, it becomes of more interest to understand how the transient responses depend on the parameters of the underlying model. The sensitivity analyses we have presented here make it possible to do so. Sensitivity analysis, in this context, can serve two purposes. One is to reveal the biological mechanisms that produce it. Knowing, for example, that reactivity in the size-structured food web model is highly elastic to assimilation efficiency suggests that the amplification of perturbations is related to the efficiency of energy transfer between trophic levels. The second is predicting the effect of parameter changes, such as might occur due to pollution, nutrient input, climate change, or other events.

Sensitivity analysis is particularly useful for nonlinear systems involving a large number of variables, which translate into high-dimensional models and in which the transient dynamics may be complex. The framework could be applied to systems other than those examined here. Of particular interest would be analysis of infectious disease outbreaks and biological invasions, both of which are essentially transient phenomena.

5.6 Appendix A: The sensitivity problem in index notation

In this appendix, I formulate the sensitivity problem using index notation, and obtain expressions for the sensitivity of reactivity. I will focus on the continuous-time model

$$\frac{\partial x_i}{\partial t} = B_i(x, \theta) \tag{5.64}$$

with an equilibrium $\hat{x}$ such that

$$B_i(\hat{x}, \theta) = 0 \tag{5.65}$$

Here x_i is the i^{th} element of the vector x.

Notes on notation:

i) The summation convention, in which an index appearing two or more times in a single term implies summation over that index, is adopted. Hence B_i is related to the matrix A in (5.1) according to $B_i = A_{ij}x_j = \sum_j A_{ij}x_j$.

ii) Partial derivatives are expressed with the comma notation; roman letters indicate derivation with respect to x and greek letters indicate derivation with respect to θ.

Perturbations $z = x - \hat{x}$ satisfy

$$\frac{\partial z_i}{\partial t} = L_{ij}z_j \tag{5.66}$$

where $L_{ij} = B_{i,j}$ is the linearization of the model around $\hat{x}$. Sensitivity analysis requires the derivative of L_{ij}, which in turn requires the derivative of the equilibrium. Differentiating the equilibrium condition gives

$$B_{i,j}\delta x_j + B_{i,\alpha}\delta\theta_\alpha = 0 \tag{5.67}$$

therefore

$$\delta x_j = -L_{ij}^{-1} \frac{\partial B_i}{\partial \theta_\alpha} \delta\theta_\alpha \tag{5.68}$$

$$= -L_{ij}^{-1} B_{i,\alpha} \delta\theta_\alpha \tag{5.69}$$

Differentiating the linearization gives

$$\delta L_{ij} = L_{ij,\alpha} \delta\theta_\alpha + L_{ij,k} \delta x_k \tag{5.70}$$

$$= \left[L_{ij,\alpha} - L_{ij,k} L_{mk}^{-1} B_{m,\alpha}\right] \delta\theta_\alpha \tag{5.71}$$

This can be equivalently written as

$$\delta B_{i,j} = \left[B_{i,j\alpha} - B_{i,jk} B_{m,k}^{-1} B_{m,\alpha}\right] \delta\theta_\alpha \tag{5.72}$$

For the sensitivity of reactivity, the expression for the right eigenvector v of the Hermitian part of the linearization, $H_{ij} = \frac{L_{ij}}{2} + \frac{L_{ji}}{2}$,

$$H_{ij} v_j = \lambda_1 v_i \tag{5.73}$$

is differentiated, giving (after some manipulations)

$$v_i^{\dagger} \delta H_{ij} v_j = \delta\lambda_1 v_i^{\dagger} v_i \tag{5.74}$$

where $v_i^{\dagger}$ is the adjoint of v_i. If eigenvectors are normalized, this simplifies to

$$\delta\lambda_1 = v_i^{\dagger} \delta H_{ij} v_j \tag{5.75}$$

Substituting the expressions for H_{ij} and δL_{ij} gives

$$\delta\lambda_1 = \frac{1}{2} v_i^{\dagger} \left[L_{ij,\alpha} - L_{ij,k} L_{mk}^{-1} B_{m,\alpha} + L_{ji,\alpha} - L_{ji,k} L_{mk}^{-1} B_{m,\alpha}\right] v_j \, \delta\theta_\alpha \tag{5.76}$$

The derivative of reactivity is then

$$\nu_{0,\alpha} = \frac{1}{2} v_i{}^{\dagger} \left[L_{ij,\alpha} - L_{ij,k} L^{-1}_{mk} B_{m,\alpha} + L_{ji,\alpha} - L_{ji,k} L^{-1}_{mk} B_{m,\alpha} \right] v_j \tag{5.77}$$

This last equation can be solved numerically (for example with MATLAB) once the derivatives of M and L are known. Using a symbolic algebra solver such as Maxima can be helpful to obtain those derivatives.

Expressions for the sensitivities of the amplification envelope and optimal perturbations can be derived following similar procedures.

5.7 Appendix B: Derivatives of equilibria and indices of transient dynamics, with an example

5.7.1 Sensitivity of stable equilibria

The sensitivity of the equilibrium for the discrete model is derived in Caswell (in prep). Here we show the derivation for the continuous model (5.1). The equilibrium $\hat{\mathbf{x}}$ satisfies

$$0 = \mathbf{A} \left[\boldsymbol{\theta}, \hat{\mathbf{x}}(\boldsymbol{\theta}) \right] \hat{\mathbf{x}} \tag{5.78}$$

Taking the differential of both sides gives

$$0 = (d\mathbf{A})\, \hat{\mathbf{x}} + \mathbf{A}\, (d\hat{\mathbf{x}}) \tag{5.79}$$

Applying the vec operator to both sides, noting that $\mathrm{vec}\, \hat{\mathbf{x}} = \hat{\mathbf{x}}$, and using Roth's (1934) relation (5.21), gives

$$0 = (\hat{\mathbf{x}}^{\mathsf{T}} \otimes \mathbf{I}_s)\, d\mathrm{vec}\, \mathbf{A} + \mathbf{A} d\hat{\mathbf{x}} \tag{5.80}$$

But $\mathbf{A}$ depends on both $\boldsymbol{\theta}$ and $\hat{\mathbf{x}}$, so

$$0 = (\hat{\mathbf{x}}^{\mathsf{T}} \otimes \mathbf{I}_s) \left(\frac{\partial \operatorname{vec} \mathbf{A}}{\partial \boldsymbol{\theta}} d\boldsymbol{\theta} + \frac{\partial \mathbf{A}}{\partial \mathbf{x}^{\mathsf{T}}} d\hat{\mathbf{x}} \right) + \mathbf{A} d\hat{\mathbf{x}} \tag{5.81}$$

Collecting terms, solving for $d\hat{\mathbf{x}}$, and rearranging gives

$$d\hat{\mathbf{x}} = \left(-\mathbf{A} - (\hat{\mathbf{x}} \otimes \mathbf{I}_s) \frac{\partial \operatorname{vec} \mathbf{A}}{\partial \mathbf{x}^{\mathsf{T}}} \right)^{-1} (\hat{\mathbf{x}}^{\mathsf{T}} \otimes \mathbf{I}_s) \frac{\partial \mathbf{A}}{\partial \boldsymbol{\theta}^{\mathsf{T}}} d\boldsymbol{\theta} \tag{5.82}$$

The "first identification theorem" of Magnus and Neudecker (1985) says that the matrix multiplying $d\boldsymbol{\theta}$ is the derivative $d\hat{\mathbf{x}}/d\boldsymbol{\theta}^{\mathsf{T}}$, as shown in (5.27).

5.7.2 Sensitivities of eigenvalues, singular values, singular vectors

Sensitivity of eigenvalues

We consider an arbitrary matrix $\mathbf{X}$, and obtain an expression for the the derivative of its eigenvalues. This is followed by the proof that the derivative with respect to $\mathbf{X}$ is equivalent to the derivative with respect to the Hermitian part $\mathbf{H}(\mathbf{X})$.

Starting with the expression for the right eigenvector of $\mathbf{X}$

$$\mathbf{X}\mathbf{w}_i = \lambda_i \mathbf{w}_i \tag{5.83}$$

we take the differential of both sides

$$(d\mathbf{X})\,\mathbf{w}_i + \mathbf{X}\,d\mathbf{w}_i = d\lambda_i\,\mathbf{w}_i + \lambda_i\,d\mathbf{w}_i \tag{5.84}$$

and multiply on the left by the left eigenvector

$$\tilde{\mathbf{w}}_i\,(d\mathbf{X})\,\mathbf{w}_i = (\tilde{\mathbf{w}}_i \mathbf{w}_i)\,d\lambda_i \tag{5.85}$$

Taking the vec of both sides yields

$$\left(\mathbf{w}_i^{\mathsf{T}} \otimes \tilde{\mathbf{w}}_i\right) d\mathrm{vec}\,\mathbf{X} = \left(\tilde{\mathbf{w}}_i \mathbf{w}_i\right) d\lambda_i \tag{5.86}$$

so that the derivative is, when eigenvectors are normalized,

$$\frac{d\lambda_i}{d\mathrm{vec}\,\mathbf{X}} = \left(\mathbf{w}_i \otimes \tilde{\mathbf{w}}_i^{\mathsf{T}}\right) \tag{5.87}$$

and we note that $\tilde{\mathbf{w}}_i = \mathbf{w}_i^{\mathsf{T}}$ if the matrix is symmetric.

The sensitivity of reactivity in continuous systems requires the sensitivity of the largest eigenvalue of $\mathbf{H}(\mathbf{X}) = \left(\mathbf{X} + \mathbf{X}^{\mathsf{T}}\right)/2$. The sensitivity of λ_1 to $\mathbf{X}$ is

$$\frac{d\lambda_1}{d\mathrm{vec}^{\mathsf{T}}\mathbf{X}} = \frac{d\lambda_1}{d\mathrm{vec}^{\mathsf{T}}\mathbf{H}(\mathbf{X})} \frac{d\mathrm{vec}\,\mathbf{H}(\mathbf{X})}{d\mathrm{vec}^{\mathsf{T}}\mathbf{X}} \tag{5.88}$$

where the eigenvalue sensitivity is given by (5.87). The sensitivity of $\mathbf{H}$ to $\mathbf{M}$ is

$$\frac{d\mathrm{vec}\,\mathbf{H}}{d\mathrm{vec}^{\mathsf{T}}\mathbf{X}} = \frac{1}{2}\left(\mathbf{I}_{s^2} + \mathbf{P}\right) \tag{5.89}$$

where $\mathbf{P}$ is the vec-permutation matrix (Henderson and Searle, 1981). The effect of multiplying on the left by $\mathbf{P}$ is to rearrange the rows of a matrix such that $\mathbf{P}\mathrm{vec}\,\mathbf{A} = \mathrm{vec}\left(\mathbf{A}^{\mathsf{T}}\right)$; in the same way multiplying on the right by $\mathbf{P}$ permutes the column of that matrix. Because both $\mathbf{H}$ and $\mathbf{P}$ are symmetric in this case, it follows that

$$\frac{d\lambda_1}{d\mathrm{vec}^{\mathsf{T}}\mathbf{H}}\mathbf{P} = \frac{d\lambda_1}{d\mathrm{vec}^{\mathsf{T}}(\mathbf{H}^{\mathsf{T}})} = \frac{d\lambda_1}{d\mathrm{vec}^{\mathsf{T}}\mathbf{H}} \tag{5.90}$$

Thus

$$\frac{d\lambda_1}{d\mathrm{vec}^{\mathsf{T}}\mathbf{X}} = \mathbf{w}_1^{\mathsf{T}} \otimes \mathbf{w}_1^{\mathsf{T}} \tag{5.91}$$

Sensitivity of singular values

The singular value decomposition of a real $n \times n$ matrix $\mathbf{X}$ is

$$\mathbf{X} = \mathbf{U\Sigma V}^{\mathrm{T}} \tag{5.92}$$

where $\mathbf{U}$ and $\mathbf{V}$ are square matrices whose columns are the left and right singular vectors, respectively, and $\mathbf{\Sigma}$ is a diagonal matrix of the singular values. The matrix norm of $\mathbf{X}$ is given by $\sigma_1 \equiv \Sigma_{11}$.

Following Wright (1992), we differentiate both sides of (5.92),

$$d\mathbf{X} = (d\mathbf{U})\mathbf{\Sigma V}^{\mathrm{T}} + \mathbf{U}(d\mathbf{\Sigma})\mathbf{V}^{\mathrm{T}} + \mathbf{U\Sigma}(d\mathbf{V}^{\mathrm{T}}) \tag{5.93}$$

and multiply on the left by $\mathbf{U}^{\mathrm{T}}$ and on the right by $\mathbf{V}$

$$\mathbf{U}^{\mathrm{T}}(d\mathbf{X})\mathbf{V} \quad = \quad \mathbf{U}^{\mathrm{T}}(d\mathbf{U})\mathbf{\Sigma} + d\mathbf{\Sigma} + \mathbf{\Sigma}(d\mathbf{V}^{\mathrm{T}})\mathbf{V} \tag{5.94}$$

The first and last terms on the right hand side are anti-symmetric matrices, hence they have zeros on the diagonal (Wright, 1992). This is easily seen by differentiating the products of $\mathbf{U}$ and $\mathbf{V}$ and their respective transpose; since these matrices are unitary, it follows that

$$\mathbf{U}^{\mathrm{T}}\mathbf{U} = 1 \tag{5.95}$$

$$\mathbf{U}^{\mathrm{T}}(d\mathbf{U}) = -(d\mathbf{U}^{\mathrm{T}})\mathbf{U} \tag{5.96}$$

$$\mathbf{U}^{\mathrm{T}}(d\mathbf{U}) = -\mathbf{U}^{\mathrm{T}}(d\mathbf{U}) \tag{5.97}$$

and similarly for $\mathbf{V}$. This last expression can only be true if $\mathbf{U}^{\mathrm{T}}(d\mathbf{U})$ is anti-symmetric, a property that is preserved through multiplication by the diagonal matrix $\mathbf{\Sigma}$.

We select the diagonal elements of the matrices on both sides of (5.93),

$$\mathbf{I} \odot (\mathbf{U}^{\mathsf{T}} d\mathbf{X}\mathbf{V}) = d\boldsymbol{\Sigma} \tag{5.98}$$

then take the vec, and divide by $d\mathrm{vec}^{\mathsf{T}}\mathbf{X}$ to get

$$(\mathrm{vec}\,\mathbf{I}) \odot (\mathbf{V}^{\mathsf{T}} \otimes \mathbf{U}^{\mathsf{T}}) = \frac{d\mathrm{vec}\,\boldsymbol{\Sigma}}{d\mathrm{vec}^{\mathsf{T}}\mathbf{X}} \tag{5.99}$$

which gives an equation for the sensitivity of singular values ($\sigma_j = \Sigma_{jj}$):

$$\frac{d\sigma_j}{d\mathrm{vec}^{\mathsf{T}}\mathbf{X}} = \mathbf{v}_j^{\mathsf{T}} \otimes \mathbf{u}_j^{\mathsf{T}} \tag{5.100}$$

where $\mathbf{u}_j$ and $\mathbf{v}_j$ are left and right singular vectors associated with σ_j, given by the j^{th} columns of $\mathbf{U}$ and $\mathbf{V}$ respectively.

In theory, the sensitivity of eigenvectors can be inferred from (5.99) (e.g. Wright, 1992), although in practice the derivatives cannot always be obtained numerically. Here we present an alternative derivation of the sensitivity of singular vectors.

Sensitivity of singular vectors

We treat the right singular vector $\mathbf{v}$ of a matrix $\mathbf{X}$, corresponding to a singular value σ, as the eigenvector $\mathbf{v}$ of $\mathbf{X}^{\mathsf{T}}\mathbf{X}$ corresponding to the eigenvalue σ^2, normalized to unit length. We find the derivative of $\mathbf{v}$ using by adapting the approach used for eigenvectors of population projection matrices by Caswell (in prep.). Let $\mathbf{Y} = \mathbf{X}^{\mathsf{T}}\mathbf{X}$. Then $\mathbf{Y}\mathbf{v} = \sigma^2\mathbf{v}$ and $\mathbf{v}$ is also a fixed point of the system

$$\mathbf{u}(t+1) = \frac{\mathbf{Y}\mathbf{u}(t)}{\|\mathbf{Y}\mathbf{u}(t)\|} \tag{5.101}$$

Write this fixed point as

$$\mathbf{v} = \frac{\mathbf{Y}\mathbf{v}}{(\mathbf{v}^{\mathrm{T}}\mathbf{Y}^{\mathrm{T}}\mathbf{Y}\mathbf{v})^{1/2}} \tag{5.102}$$

and differentiate, obtaining

$$d\mathbf{v} = \frac{\mathbf{Y}(d\mathbf{v}) + (d\mathbf{Y})\mathbf{v}}{(\mathbf{v}^{\mathrm{T}}\mathbf{Y}^{\mathrm{T}}\mathbf{Y}\mathbf{v})^{1/2}} - \frac{\mathbf{Y}\mathbf{v}\, d(\mathbf{v}^{\mathrm{T}}\mathbf{Y}^{\mathrm{T}}\mathbf{Y}\mathbf{v})}{2\,(\mathbf{v}^{\mathrm{T}}\mathbf{Y}^{\mathrm{T}}\mathbf{Y}\mathbf{v})^{3/2}} \tag{5.103}$$

Expand the differential in the second term and then simplify, using the relations

$$\begin{aligned} \mathbf{Y}\mathbf{v} &= \mathbf{Y}^{\mathrm{T}}\mathbf{v} = \sigma^2\mathbf{v} \\ \mathbf{v}^{\mathrm{T}}\mathbf{Y}^{\mathrm{T}} &= \mathbf{v}^{\mathrm{T}}\mathbf{Y} = \sigma^2\mathbf{v}^{\mathrm{T}} \\ \mathbf{v}^{\mathrm{T}}\mathbf{v} &= 1 \\ \mathbf{v}^{\mathrm{T}}\mathbf{Y}^{\mathrm{T}}\mathbf{Y}\mathbf{v} &= \sigma^4 \end{aligned} \tag{5.104}$$

Applying the vec operator yields, after some rearrangement

$$\left(\sigma^2\mathbf{I}_s - \mathbf{Y} + \frac{\sigma^2}{2}(\mathbf{v}^{\mathrm{T}} \otimes \mathbf{v}) + \frac{\sigma^2}{2}\mathbf{v}\mathbf{v}^{\mathrm{T}}\right) d\mathbf{v} = [(\mathbf{v}^{\mathrm{T}} \otimes \mathbf{I}_s) - (\mathbf{v}^{\mathrm{T}} \otimes \mathbf{v}\mathbf{v}^{\mathrm{T}})]\, d\mathrm{vec}\,\mathbf{Y} \tag{5.105}$$

Since $\mathbf{Y} = \mathbf{X}^{\mathrm{T}}\mathbf{X}$, it follows that

$$d\mathrm{vec}\,\mathbf{Y} = [(\mathbf{X}^{\mathrm{T}} \otimes \mathbf{I})\mathbf{P} + (\mathbf{I} \otimes \mathbf{X}^{\mathrm{T}})]\, d\mathrm{vec}\,\mathbf{X} \tag{5.106}$$

where $\mathbf{P}$ is the vec-permutation matrix. Finally,

$$\begin{aligned} \frac{d\mathbf{v}}{d\mathrm{vec}^{\mathsf{T}}\mathbf{X}} &= \left(\sigma^2\mathbf{I}_s - \mathbf{X}^{\mathrm{T}}\mathbf{X} + \frac{\sigma^2}{2}(\mathbf{v}^{\mathrm{T}} \otimes \mathbf{v}) + \frac{\sigma^2}{2}\mathbf{v}\mathbf{v}^{\mathrm{T}}\right)^{-1} \\ &\quad \times \left[(\mathbf{v}^{\mathrm{T}} \otimes \mathbf{I}_s) - (\mathbf{v}^{\mathrm{T}} \otimes \mathbf{v}\mathbf{v}^{\mathrm{T}})\right] \left[(\mathbf{X}^{\mathrm{T}} \otimes \mathbf{I})\mathbf{P} + (\mathbf{I} \otimes \mathbf{X}^{\mathrm{T}})\right] \end{aligned} \tag{5.107}$$

5.7.3 Sensitivity matrices for multiple food chains model

We compute the first and second derivatives of the matrix $\mathbf{A}$ for the multiple food chains models (Section 5.4.2). Consider a vector of the population densities:

$$\mathbf{x} = [P_0\, P_1\, P_2\, Z_0\, Z_1\, Z_2\, Z_3\, Z_4]^{\mathsf{T}}$$

and a vector of selected model parameters:

$$\boldsymbol{\theta} = [\epsilon\, g_0\, \delta_0\, P_s\, r_0\, K\, \lambda]^{\mathsf{T}}$$

The derivative $\mathbf{B} = d\mathrm{vec}\,\mathbf{A}/d\mathbf{x}^{\mathsf{T}}$ is an $m^2 \times m$ matrix, where m is the length of $\mathbf{x}$. Most elements of $\mathbf{B}$ vanish as a consequence of $\mathbf{A}$ being diagonal. We adopt a MATLAB-like notation for writing the rows of that matrix, with $B(i,:)$ being the i^{th} row of $\mathbf{B}$. The non-zero rows are

$$\begin{array}{lclllllllll}
B(1,:) & = & [\frac{-r_0}{K} & \frac{-r_0}{K} & \frac{-r_0}{K} & \frac{-g_0}{P_s} & 0 & 0 & 0 & 0] \\
B(m+2,:) & = & [\frac{-r_0 4^{\beta}}{K} & \frac{-r_0 4^{\beta}}{K} & \frac{-r_0 4^{\beta}}{K} & 0 & \frac{-g_0 4^{\beta}}{P_s} & 0 & 0 & 0] \\
B(2m+3,:) & = & [\frac{-r_0 4^{2\beta}}{K} & \frac{-r_0 4^{2\beta}}{K} & \frac{-r_0 4^{2\beta}}{K} & 0 & 0 & \frac{-g_0 4^{2\beta}}{P_s} & 0 & 0] \\
B(3m+4,:) & = & [\epsilon\frac{g_0}{P_s} & 0 & 0 & 0 & \frac{-g_0 4^{\beta}}{P_s} & 0 & 0 & 0] \\
B(4m+5,:) & = & [0 & \epsilon\frac{g_0 4^{\beta}}{P_s} & 0 & \frac{\epsilon g_0 4^{\beta}}{P_s} & 0 & \frac{-g_0 4^{2\beta}}{P_s} & 0 & 0] \\
B(5m+6,:) & = & [0 & 0 & \epsilon\frac{g_0 4^{2\beta}}{P_s} & 0 & \epsilon\frac{g_0 4^{2\beta}}{P_s} & 0 & \frac{-g_0 4^{3\beta}}{P_s} & 0] \\
B(6m+7,:) & = & [0 & 0 & 0 & 0 & 0 & \epsilon\frac{g_0 4^{3\beta}}{P_s} & 0 & \frac{-g_0 4^{4\beta}}{P_s}] \\
B(m^2,:) & = & [0 & 0 & 0 & 0 & 0 & 0 & \epsilon\frac{g_0 4^{4\beta}}{P_s} & 0]
\end{array}$$

The derivative $\mathbf{C} = d\mathrm{vec}\,\mathbf{A}/d\boldsymbol{\theta}^{\mathsf{T}}$ is an $m^2 \times q$ matrix, where q is the length of $\boldsymbol{\theta}$. The non-zero rows of **C** are

$$
\begin{array}{lclcccccc}
C(1,:) & = & [0 & -Z_0\frac{1}{P_s} & 0 & Z_0\frac{g_0}{P_s^2} & S & r_0\frac{\sum P}{K^2} & -1] \\
C(m+2,:) & = & [0 & -Z_1\frac{4^\beta}{P_s} & 0 & Z_1\frac{g_0 4^\beta}{P_s^2} & 4^\beta S & r_0 4^\beta\frac{\sum P}{K^2} & -1] \\
C(2m+3,:) & = & [0 & -Z_2\frac{4^{2\beta}}{P_s} & 0 & Z_2\frac{g_0 4^{2\beta}}{P_s^2} & 4^{2\beta} S & r_0 4^{2\beta}\frac{\sum P}{K^2} & -1] \\
C(3m+4,:) & = & [\frac{g_0}{P_s}P_0 & \frac{1}{P_s}Q_{3m+4} & -1 & -\frac{g_0}{P_s^2}Q_{3m+4} & 0 & 0 & -1] \\
C(4m+5,:) & = & [\frac{g_0 4^\beta}{P_s}(P_1+Z_0) & \frac{1}{P_s}Q_{4m+5} & -4^\beta & -\frac{g_0}{P_s^2}Q_{4m+5} & 0 & 0 & -4] \\
C(5m+6,:) & = & [\frac{g_0 4^{2\beta}}{P_s}(P_2+Z_1) & \frac{1}{P_s}Q_{5m+6} & -4^{2\beta} & -\frac{g_0}{P_s^2}Q_{5m+6} & 0 & 0 & -4^{2\gamma}] \\
C(6m+7,:) & = & [\frac{g_0 4^{3\beta}}{P_s}Z_2 & \frac{1}{P_s}Q_{6m+7} & -4^{3\beta} & -\frac{g_0}{P_s^2}Q_{6m+7} & 0 & 0 & -4^{3\gamma}] \\
C(m^2,:) & = & [\frac{g_0 4^{4\beta}}{P_s}Z_3 & \frac{\epsilon 4^{4\beta}}{P_s}Z_3 & -4^{4\beta} & -\frac{\epsilon g_0 4^{4\beta}}{P_s^2}Z_3 & 0 & 0 & -4^{4\gamma}]
\end{array}
$$

where we have defined

$$
\begin{array}{rcl}
S & = & 1-\frac{\sum P}{K} \\
Q_{3m+4} & = & [\epsilon P_0 - 4^\beta Z_1] \\
Q_{4m+5} & = & [\epsilon 4^\beta(P_1+Z_0) - 4^{3\beta}Z_2] \\
Q_{5m+6} & = & [\epsilon 4^{2\beta}(P_2+Z_1) - 4^{4\beta}Z_3] \\
Q_{6m+7} & = & [\epsilon 4^{3\beta}Z_2 - L_5^\beta Z_4]
\end{array}
$$

The second derivative $\mathbf{D} = d\mathrm{vec}\,\mathbf{B}/d\boldsymbol{\theta}^{\mathrm{T}}$ is an $m^3 \times q$ matrix. The n^{th} column of **D** is given by the vec of the derivative of **B** with respect to the n^{th} element of $\boldsymbol{\theta}$, which we write

$\mathbf{B}_{\theta(n)}$. The derivatives of $\mathbf{B}$ are

$$\begin{array}{lcllllllll}
B_\epsilon(3m+4,:) & = & [\frac{g_0}{P_s} & 0 & 0 & 0 & 0 & 0 & 0 & 0] \\
B_\epsilon(4m+5,:) & = & [0 & \frac{g_0 4^\beta}{P_s} & 0 & \frac{g_0 4^\beta}{P_s} & 0 & 0 & 0 & 0] \\
B_\epsilon(5m+6,:) & = & [0 & 0 & \frac{g_0 4^{2\beta}}{P_s} & 0 & \frac{g_0 4^{2\beta}}{P_s} & 0 & 0 & 0] \\
B_\epsilon(6m+7,:) & = & [0 & 0 & 0 & 0 & 0 & \frac{g_0 4^{3\beta}}{P_s} & 0 & 0] \\
B_\epsilon(7m+8,:) & = & [0 & 0 & 0 & 0 & 0 & 0 & \frac{g_0 4^{4\beta}}{P_s} & 0]
\end{array}$$

$$\begin{array}{lcllllllll}
B_{g_0}(1,:) & = & [0 & 0 & 0 & \frac{-1}{P_s} & 0 & 0 & 0 & 0] \\
B_{g_0}(m+2,:) & = & [0 & 0 & 0 & 0 & \frac{-4^\beta}{P_s} & 0 & 0 & 0] \\
B_{g_0}(2m+3,:) & = & [0 & 0 & 0 & 0 & 0 & \frac{-4^{2\beta}}{P_s} & 0 & 0] \\
B_{g_0}(3m+4,:) & = & [\epsilon\frac{1}{P_s} & 0 & 0 & 0 & \frac{-4^\beta}{P_s} & 0 & 0 & 0] \\
B_{g_0}(4m+5,:) & = & [0 & \epsilon\frac{4^\beta}{P_s} & 0 & \epsilon\frac{4^\beta}{P_s} & 0 & \frac{-4^{2\beta}}{P_s} & 0 & 0] \\
B_{g_0}(5m+6,:) & = & [0 & 0 & \epsilon\frac{4^{2\beta}}{P_s} & 0 & \epsilon\frac{4^{2\beta}}{P_s} & 0 & \frac{-4^{3\beta}}{P_s} & 0] \\
B_{g_0}(6m+7,:) & = & [0 & 0 & 0 & 0 & 0 & \epsilon\frac{4^{3\beta}}{P_s} & 0 & \frac{-4^{4\beta}}{P_s}] \\
B_{g_0}(m^2,:) & = & [0 & 0 & 0 & 0 & 0 & 0 & \epsilon\frac{4^{4\beta}}{P_s} & 0]
\end{array}$$

$$\begin{array}{lclllllllll}
B_{P_s}(1,:) & = & [0 & 0 & 0 & \frac{g_0}{P_s^2} & 0 & 0 & 0 & 0] \\
B_{P_s}(m+2,:) & = & [0 & 0 & 0 & 0 & \frac{g_0 4^{\beta}}{P_s^2} & 0 & 0 & 0] \\
B_{P_s}(2m+3,:) & = & [0 & 0 & 0 & 0 & 0 & \frac{g_0 4^{2\beta}}{P_s^2} & 0 & 0] \\
B_{P_s}(3m+4,:) & = & [-\epsilon\frac{g_0}{P_s^2} & 0 & 0 & 0 & \frac{g_0 4^{\beta}}{P_s^2} & 0 & 0 & 0] \\
B_{P_s}(4m+5,:) & = & [0 & -\epsilon\frac{g_0 4^{\beta}}{P_s^2} & 0 & -\epsilon\frac{g_0 4^{\beta}}{P_s^2} & 0 & \frac{g_0 4^{2\beta}}{P_s^2} & 0 & 0] \\
B_{P_s}(5m+6,:) & = & [0 & 0 & -\epsilon\frac{g_0 4^{2\beta}}{P_s^2} & 0 & -\epsilon\frac{g_0 4^{2\beta}}{P_s^2} & 0 & \frac{g_0 4^{3\beta}}{P_s^2} & 0] \\
B_{P_s}(6m+7,:) & = & [0 & 0 & 0 & 0 & 0 & -\epsilon\frac{g_0 4^{4\beta}}{P_s^2} & 0 & \frac{g_0 4^{4\beta}}{P_s^2}] \\
B_{P_s}(m^2,:) & = & [0 & 0 & 0 & 0 & 0 & 0 & -\epsilon\frac{g_0 4^{4\beta}}{P_s^2} & 0]
\end{array}$$

$$\begin{array}{lclllllllll}
B_{r_0}(1,:) & = & [\frac{-1}{K} & \frac{-1}{K} & \frac{-1}{K} & 0 & 0 & 0 & 0 & 0] \\
B_{r_0}(m+2,:) & = & [\frac{-4^{\beta}}{K} & \frac{-4^{\beta}}{K} & \frac{-4^{\beta}}{K} & 0 & 0 & 0 & 0 & 0] \\
B_{r_0}(2m+3,:) & = & [\frac{-4^{2\beta}}{K} & \frac{-4^{2\beta}}{K} & \frac{-4^{2\beta}}{K} & 0 & 0 & 0 & 0 & 0]
\end{array}$$

$$\begin{array}{lclllllllll}
B_K(1,:) = & = & [\frac{r_0}{K^2} & \frac{r_0}{K^2} & \frac{r_0}{K^2} & 0 & 0 & 0 & 0 & 0] \\
B_K(m+2,:) = & = & [\frac{r_0 4^{\beta}}{K^2} & \frac{r_0 4^{\beta}}{K^2} & \frac{r_0 4^{\beta}}{K^2} & 0 & 0 & 0 & 0 & 0] \\
B_K(2m+3,:) = & = & [\frac{r_0 4^{2\beta}}{K^2} & \frac{r_0 4^{2\beta}}{K^2} & \frac{r_0 4^{2\beta}}{K^2} & 0 & 0 & 0 & 0 & 0]
\end{array}$$

and $\mathbf{B}_{\delta_0} = \mathbf{B}_{\lambda} = 0$.

The other second derivative, $d\text{vec}\,\mathbf{B}/d\mathbf{x}^{\mathrm{T}}$, vanishes for this model.

Chapter 6

Carbon dioxide and oxygen fluxes in the Southern Ocean: mechanisms of interannual variability

Adapted from A. Verdy, S. Dutkiewicz, M. Follows, J. Marshall, and A. Czaja (2007)
Published in *Global Biogeochemical Cycles*, 21, GB2020

Abstract

We analyze the variability of air-sea fluxes of carbon dioxide and oxygen in the Southern Ocean during the period 1993-2003, in a biogeochemical and physical simulation of the global ocean. Our results suggest that the non-seasonal variability is primarily driven by changes in entrainment of carbon-rich, oxygen-poor waters into the mixed layer during winter convection episodes. The Southern Annular Mode (SAM), known to impact the variability of air-sea fluxes of carbon dioxide, is also found to affect oxygen fluxes. We find that ENSO also plays an important role in generating interannual variability in air-sea fluxes of carbon and oxygen. Anomalies driven by SAM and ENSO constitute a significant fraction of the simulated variability; the two climate indices are associated with surface heat fluxes, which in turn control the modeled mixed-layer depth variability. We adopt a Lagrangian view of tracers advected along the Antarctic Circumpolar Current (ACC) to highlight the importance of convective mixing in inducing anomalous air-sea fluxes of carbon dioxide and oxygen. The idealized Lagrangian model captures the principal features of the variability simulated by the more complex model, suggesting that knowledge of entrainment, temperature, and mean geostrophic flow in the mixed layer is sufficient to obtain a first-order description of the large-scale variability in air-sea transfer of soluble gases. Distinct spatial and temporal patterns arise from the different equilibration timescales of the two gases.

6.1 Introduction

Deep waters in the Southern Ocean are rich in dissolved inorganic carbon (DIC) and depleted in oxygen. When circulation brings these waters into the mixed layer, the soluble gases are exchanged at the air-sea interface. The formation of deep mixed layers combined with high biological productivity makes the Southern Hemisphere extra-tropical oceans an important component of the global carbon cycle.

Variability of the circulation and biology of the Southern Ocean has been suggested to impact local air-sea exchange of carbon dioxide. LeQuéré et al. (2003) described how ocean pCO_2 responds to changes in stratification, through variations in supply of DIC and in the average light available to phytoplankton. Lovenduski and Gruber (2005) examined how the Southern Annular Mode (SAM), a dominant mode of local atmospheric variability, is related to observed variability in primary production; they speculate that the biological response to SAM would largely compensate the supply of DIC resulting from SAM-induced changes in ocean circulation. More recent modeling studies, however, suggest that SAM drives about a third of regional CO_2 air-sea flux variability on interannual timescale, primarily due to changes in the physical circulation (Lenton and Matear, 2007; Lovenduski et al., 2007). In the region of the Antarctic Circumpolar Current (ACC), the oceanic response to SAM during its positive phase consists of northward Ekman currents, upwelling near the coast of Antarctica, and intensification of the geostrophic zonal flow (Hall and Visbeck, 2002).

While these studies focused on SAM, there is also evidence for ENSO-related physical variability in the Southern Ocean. Both SAM and ENSO are important sources of sea surface temperature (SST) variability in the ACC (Verdy et al., 2006). Sea-ice variability in the Southern Ocean is thought to be strongly influenced by ENSO teleconnections (Yuan, 2004, and references therein). ENSO is also the main driver of CO_2 air-sea flux variability in the equatorial Pacific, where it modulates convective mixing and biological export production (Feely et al., 2002; McKinley et al., 2004).

In this study, we investigate the interannual variability of air-sea fluxes of CO_2 and O_2

in the Southern Ocean, addressing the respective roles of ENSO and SAM. Variations in these climatic indices reflect large-scale patterns in anomalous surface heat fluxes, convective mixing, and entrainment of DIC and oxygen into the mixed layer. Comparing the response of the two gases, which have different air-sea equilibration timescales, affords a more complete picture of the ocean-atmosphere interactions regulating the variability of air-sea fluxes in a global physical-biogeochemical model.

We then apply a Lagrangian theoretical framework to investigate the mechanisms responsible for air-sea fluxes of CO_2 and O_2. Using a highly simplified model of tracers propagating in the ocean mixed layer, we are able to idealize the physical and biogeochemical systems and focus on the key mechanisms. The idealized Lagrangian model captures the behavior of the complex 3-dimensional system, and clearly illustrates how changes in entrainment due to mixed layer depth variations are the primary driver of the large-scale variability in gas fluxes in the region of the ACC.

6.2 Air-sea fluxes of carbon and oxygen in a global ocean model

6.2.1 Model description

Air-sea fluxes of CO_2 and O_2 are simulated in a global numerical ocean model (hereafter referred to as GCM, global circulation model) for the period 1993-2003. Temperature, salinity and flow fields are obtained from the Estimating the Circulation and Climate of the Ocean (ECCO) state-estimation project (Wunsch and Heimbach, 2006), which uses available observations to constrain the MIT-general circulation model (Marshall et al., 1997). An iterative data-assimilation procedure serves to determine the initial conditions, surface fluxes, and model parameters that minimize the misfit between data and model; the data sets used are listed in the Appendix of Wunsch and Heimbach (2006), and include measurements of sea surface temperature and salinity, altimetry data, and float profiles.

The model has a horizontal resolution of 1°; there are 23 vertical levels whose thickness ranges from 10 m near the surface to 500 m at depth, with 13 levels in the top kilometer of the water column. We use the GM/Redi parameterization of geostrophic eddy fluxes (Gent and McWilliams, 1990; Redi, 1982) and the K-Profile Parameterization (KPP) vertical mixing scheme (Large et al., 1994) to account for sub-gridscale processes. The flow fields transport biogeochemical tracers of inorganic and organic forms of carbon, phosphorus, iron and oxgen, as well as alkalinity. We do not resolve the ocean ecosystem; instead, the biogeochemical model adopts a simple carbon export scheme with limitation by phosphate, iron and light availability. The net community production of organic matter is given by

$$\mu \frac{I}{I+\kappa_I} \min\left(\frac{PO_4}{PO_4+\kappa_{PO4}}, \frac{Fe}{Fe+\kappa_{Fe}}\right) \tag{6.1}$$

where μ is maximum community production, and κ_I, κ_{PO4}, κ_{Fe} are half-saturation coefficients. Two thirds of net production is assumed to enter the dissolved organic pool, the remaining fraction of organic production being exported to depth as sinking particles. Surface carbonate chemistry is explicitly solved (Follows et al., 2006) and air-sea transfer of CO_2 and O_2 is parameterized following Wanninkhof (1992). Aspects of this model are described in more detail by McKinley et al. (2003), Dutkiewicz et al. (2005) and Parekh et al. (2006). Modeled phosphate, oxygen, iron, DIC and alkalinity distributions capture the observed large scale horizontal and vertical gradients; the annual-mean DIC concentration at 100 m in the GCM agrees well with observations from the Global Ocean Data Analysis Project, GLODAP (Key et al., 2004).

Results used in this 11-year study were obtained after 120 years of spin-up of the biogeochemistry model with pre-industrial atmospheric CO_2. The analysis is performed on monthly-averaged fields, from which the long-term trend and mean seasonal cycle are removed. We focus on the region of the ACC, where the non-seasonal variability of air-sea fluxes is largest in our model. In order to examine the advection of anomalies by the mean flow, we analyze the variability along geostrophic streamlines, estimated from the mean sea surface height (Figure 6-1). This procedure will facilitate the comparison of GCM results

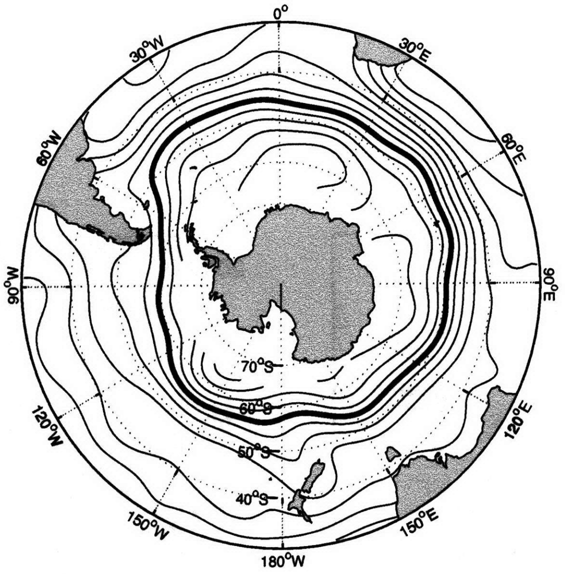

Figure 6-1: Geostrophic streamlines in the Southern Ocean; contour interval is 2×10^3 m^2/s. Bold curve indicates streamline along which the simulated variability is plotted in Figure 6-2 and Figure 6-3.

with results from the 1-dimensional Lagrangian model (Section 6.4). Here we show the variability along the circumpolar streamline indicated by the bold curve in Figure 6-1, with a mean latitude of 52°S.

6.2.2 Simulated variability

The variability of CO_2 and O_2 fluxes is presented in Figure 6-2. The time-longitude diagrams highlight three features of the simulated variability: first, there is eastward propagation of the anomalies; second, oxygen fluxes have a larger amplitude and are more localized in time and space than carbon fluxes; and third, O_2 and CO_2 fluxes tend to have opposite signs.

This anti-correlation in the large-scale patterns of carbon and oxygen fluxes suggests that the variability is primarily driven by entrainment (Gruber et al., 2002). Comparison with surface heat flux (not shown) reveals that heating of the ocean occur simultaneously

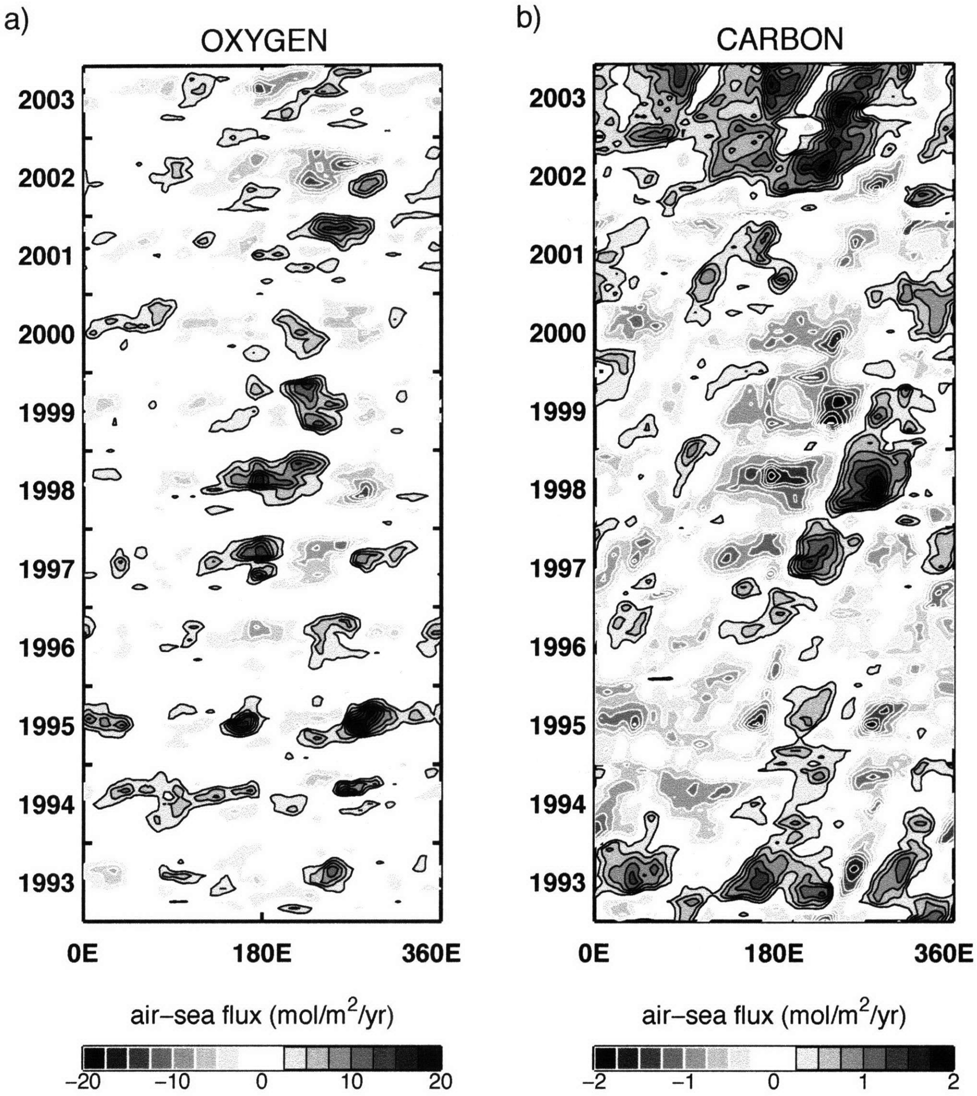

Figure 6-2: Air-sea flux variability of a) oxygen and b) carbon dioxide from the GCM simulation. The time-longitude diagrams show deviations from the mean seasonal cycle, for the period 1993-2003, along a geostrophic streamline. Positive values (black contours) correspond to fluxes into the ocean; white contours denote negative values.

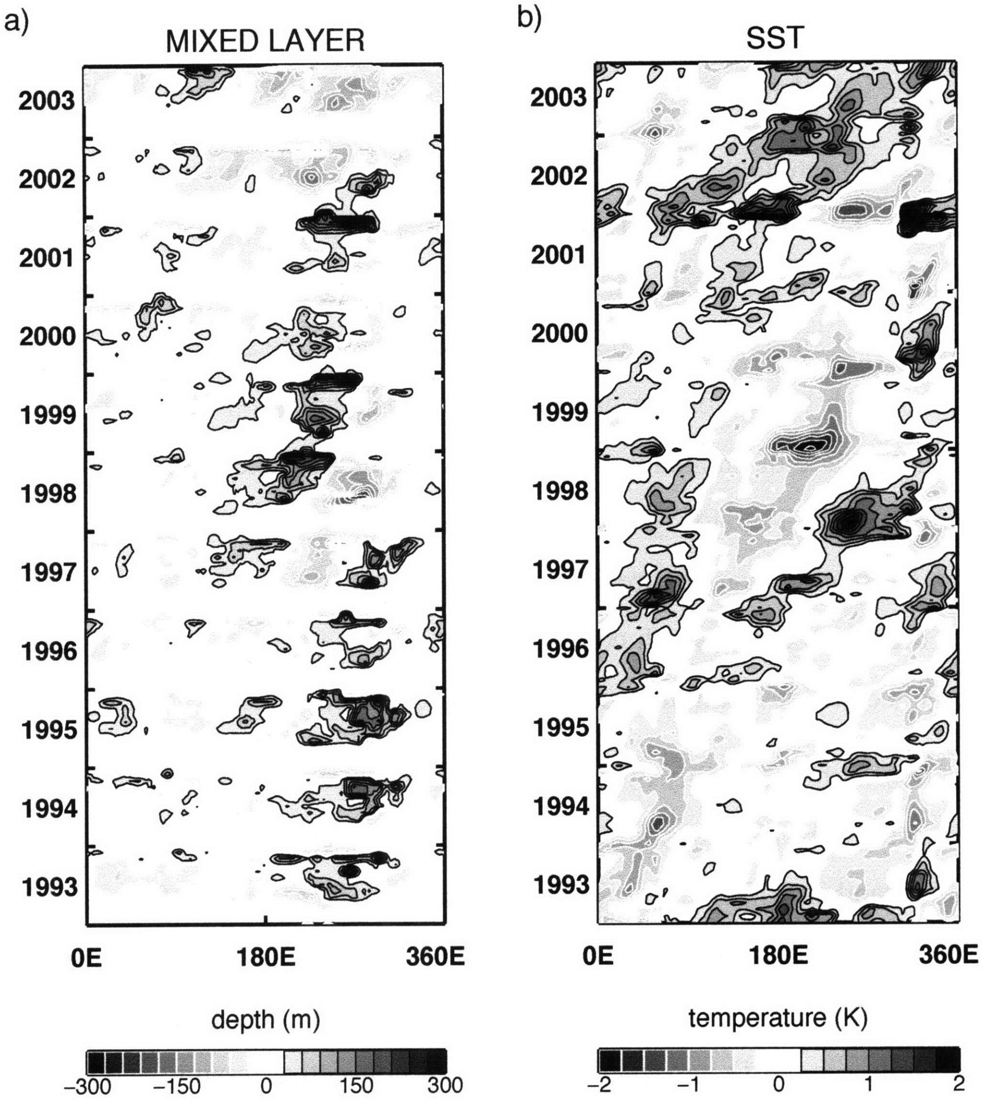

Figure 6-3: Time-longitude diagrams of anomalous a) mixed layer depth and b) sea surface temperature (SST), along a geostrophic streamline. Positive values (black contours) correspond to deep mixed layers and high temperatures; white contours denote negative values.

with outgassing of O_2 and intake of CO_2. If thermal solubility was the dominant cause of air-sea fluxes, warming would result in outgassing of both gases. The two fields exhibit more variance in the Pacific, during the austral winter and spring; this timing and location corresponds to that of mode water formation, associated with the deepest mixed layers, reinforcing the idea that entrainment is the dominant term driving anomalous fluxes.

Dissolved oxygen adjusts rapidly to the atmospheric concentration, the equilibration timescale being roughly 1 month. This causes large air-sea fluxes and results in rapid dissipation of the anomalies generated in winter-time, so the variability of O_2 appears localized in time and space. In contrast, carbonate chemistry causes the equilibration timescale for carbon to be much longer, on the order of 1 year (depending on the depth of the mixed layer); the amplitude of anomalous carbon fluxes is thus weaker and relatively constant throughout the year. The slowly decaying anomalies are then able to propagate with the mean flow. Estimation from Figure 6-2b suggests that model anomalies travel eastward at a speed of roughly 8 cm/s, which corresponds to the observed propagation speed of SST anomalies and coincides with the mean geostrophic flow in the ACC (Verdy et al., 2006).

In Figure 6-3, the variability of simulated mixed layer depth (MLD) and SST is shown along the same geostrophic streamline. We identify the MLD from the potential density (σ) profile as the depth at which σ exceeds the surface value by at least 0.15 kg/m^3. The similitude between anomalous MLD and anomalous O_2 fluxes (Figure 6-2a) is most apparent during winter months, when convection events cause the mixed layers to deepen. Interannual variability in MLD impacts the strength of convective mixing, and deeper mixed layers are associated with enhanced entrainment of oxygen-depleted water into the mixed layer. Anomalous CO_2 fluxes (Figure 6-2b) are also consistent with changes in MLD, but because of the longer equilibration time, they appear to be more similar to SST variability (Figure 6-3b); SST anomalies have a decay timescale of approximately 8 months for a 100m-thick mixed-layer. Unlike CO_2, SST exhibits more variability during the austral summer, when the mixed layer is shallow; this suggests that thermal effects are dominant over entrainment in inducing temperature changes, which is consistent with the results of

Verdy et al. (2006).

The propagation speed of SST anomalies matches that of CO_2 anomalies. Despite a decay timescale of a few months, in some instances anomalies are found to persist for several years; the interplay between mean oceanic advection and random heat flux forcing is thought to explain the long persistence (Verdy et al., 2006, and references therein). We also find a hint of propagation of MLD anomalies in the GCM (Figure 6-3a) that is likely to result from the same mechanism, since temperature and stratification are both affected by heat flux variability. In turn, propagation of the MLD signal explains the persistence of CO_2 and O_2 anomalies, which during some periods are found to last for up to 5 years (Figure 6-2). Successive years of anomalously large or weak entrainment seem to reinforce air-sea flux anomalies generated in the previous winter.

The large-scale patterns of variability along other streamlines in the region of the ACC, extending roughly from 55°S to 65°S, are very similar to the ones presented here. Further south, the simulated variability is more complex, and since near-shore processes are not well resolved in the model, is not discussed here; further north, air-sea flux anomalies are weak and do not propagate eastward.

6.3 Modes of air-sea flux variability, ENSO and SAM

The spatial patterns of variability are identified by the first 3 empirical orthogonal functions (EOF) of air-sea flux of CO_2 and O_2 south of 30°S. To focus on interannual variability, time series are filtered with a 12-month running mean. We then examine the influence of two modes of climate variability, ENSO and SAM. The spatial patterns are presented in Figure 6-4; the associated time series, shown in Figure 6-5, are compared to indices of ENSO and SAM variability. The Niño3 index is calculated from the SST averaged between 5°S and 5°N, from 150W° to 90°W (Cane et al., 1986). For the SAM-index, we use the time series of the NOAA Climate Prediction Center, constructed by projecting the 700 hPa height anomalies poleward of 20°S onto the leading EOF mode of mean 700 hPa height, consistent with Thompson and Wallace (2000).

The first three EOFs of oxygen fluxes are associated with 29%, 16%, and 14% of the variance, respectively. The first mode (Figure 6-4a) appears as a wide zone of ingassing over most of the South Pacific basin and a narrow band of outgassing centered on Drake Passage. It is associated with SAM, the time series having a correlation coefficient of $r = 0.75$ (no lag). The second EOF (Figure 6-4b) reflects the influence of ENSO. It shows outgassing in the eastern Pacific; the maximum correlation occurs for a 3-month lag, the correlation coefficient being $r = 0.75$. These values are significant at the 99% level[1]. The third EOF is not significantly correlated to either SAM or ENSO. In the top panels of Figure 6-5, the time series corresponding to the first and second EOFs are overlain on the SAM-index and Niño3 index, also smoothed with a 12-month running mean.[2]

The first three EOFs of carbon dioxide fluxes are associated with 31%, 22%, and 17% of the variance, respectively. The spatial patterns for the first and third modes of variability shown in Figure 6-4 (c,d) are similar to the patterns of O_2 variability described above. The second EOF, not shown, is not significantly correlated to SAM or ENSO. The first mode is once again linked to SAM; with a 3 month lag, the correlation coefficient r = 0.71 is significant at the 95% level. The third mode appears to indicate ENSO-related variability, the maximum correlation occurring for a 6-month lag; the correlation coefficient with Ninõ3 is $r = 0.80$, which is significant at the 99% level. The time series are shown in Figure 6-5, bottom panels, together with indices for SAM and ENSO.

Although the fraction of variance explained by the ENSO-related EOF is less than that explained by the SAM-related EOF, the magnitude of the induced fluxes is comparable. Both flux patterns have a dipole structure in the Pacific basin, a feature that is also seen in Figure 6-2. This reflects the spatial patterns of atmospheric forcing induced by SAM and ENSO: both are associated with anomalous winds over the Southern Ocean that cause

---

[1] For the number of degrees of freedom, we divide the length of the time series by the e-folding autocorrelation time.

[2] We obtain similar results without filtering the time series: for O_2 the first EOF is correlated with SAM ($r = 0.38$) and the third with niño3 ($r = 0.50$); for CO_2 the first EOF is correlated with SAM ($r = 0.29$) and the third with niño3 ($r = 0.77$). All correlations fall within the 95% confidence interval.

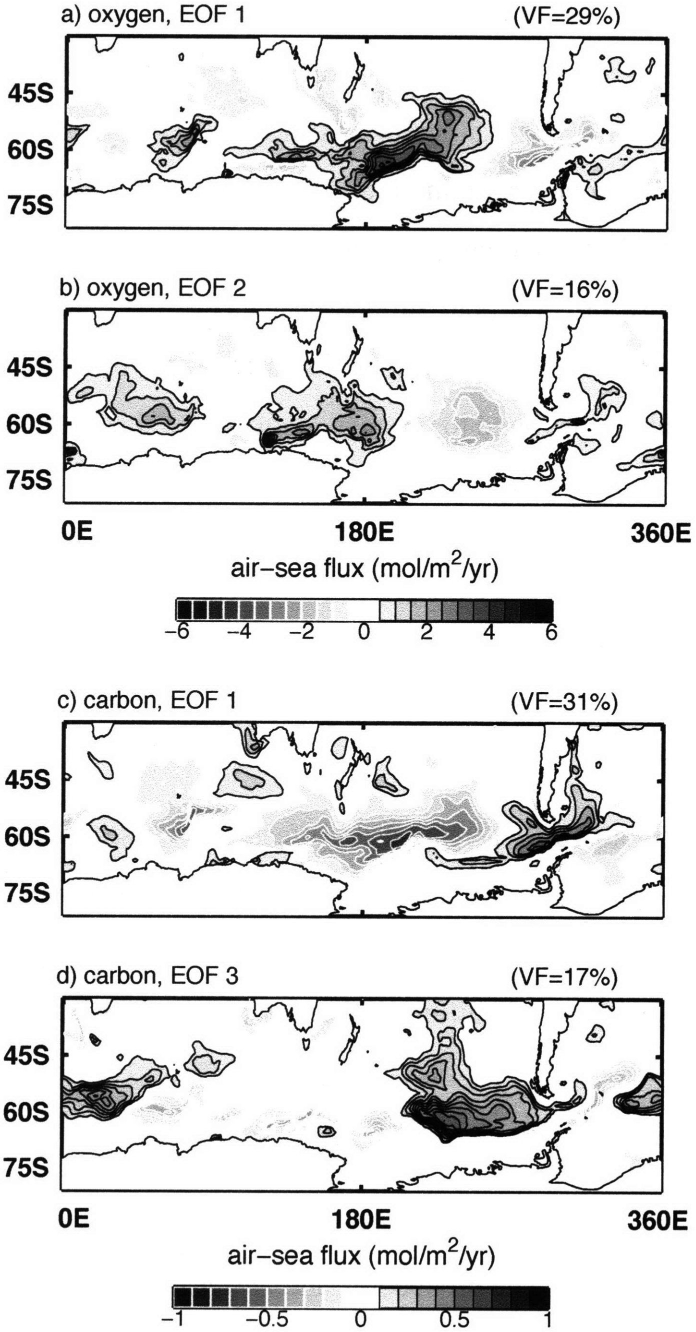

Figure 6-4: Spatial patterns of the leading empirical orthogonal functions, for air-sea flux variability of oxygen (a, b) and carbon dioxide (c, d), and fraction of the total variance (VF) associated with each mode. Black (white) contours denote positive (negative) fluxes into the ocean. SAM is associated with the first EOF of O_2 and CO_2 fluxes; ENSO is associated with the second EOF of O_2 fluxes and the third EOF of CO_2 fluxes. The second EOF of CO_2 fluxes, not shown, is not correlated with SAM or ENSO.

surface fluxes of sensible and latent heat. During the positive phase of the SAM, and during El Ninõ events, surface pressure over the South-Pacific is anomalously low; the resulting zonal pressure gradients drive meridional winds and thus heat fluxes which, in turn, induce changes in solubility and convective mixing. The ENSO and SAM heat flux patterns are shown in Verdy et al. (2006) and are discussed in relation to their role in generating SST anomalies. In the case of SST, both surface heat fluxes and oceanic Ekman advection of heat contribute to the observed variability; in contrast, the role of Ekman advection in driving gas flux variability is found to be small compared to that of surface heat fluxes (an explanation is given in Section 6.4.2).

6.4 Mechanisms

6.4.1 Diagnostic Framework

DIC and oxygen are biologically active tracers affected by air-sea fluxes, entrainment, biological production, advection, and dilution by evaporation and precipitation. Averaged over the depth of the mixed-layer, the time development of the tracer concentration, C, can be described by the following simple differential equation (see Williams and Follows, 1998):

$$\frac{DC}{Dt} = \frac{F}{h} + (C_{th} - C)\mathcal{H}\frac{1}{h}\frac{\partial h}{\partial t} + \frac{1}{h}(\mathrm{E} - \mathrm{P})C + \mathcal{B} \qquad (6.2)$$

where h is the mixed layer depth, F the air-sea flux, E and P the evaporation and precipitation, respectively, $\mathcal{B}$ the biological production, and $D/Dt \equiv \partial/\partial t + \mathbf{u}\cdot\nabla$ is the Lagrangian derivative. Here, the value of $\mathcal{B}$ is tracer-dependent, as biological production produces O_2 but uses DIC.

Equation 6.2 is an idealized description of the processes that change the concentration of dissolved gas, following a parcel of fluid. Each term on the right hand side expresses a mechanism through which an amount of tracer is added to or removed from the surface waters. The first term represents fluxes to the atmosphere. The second term represents the

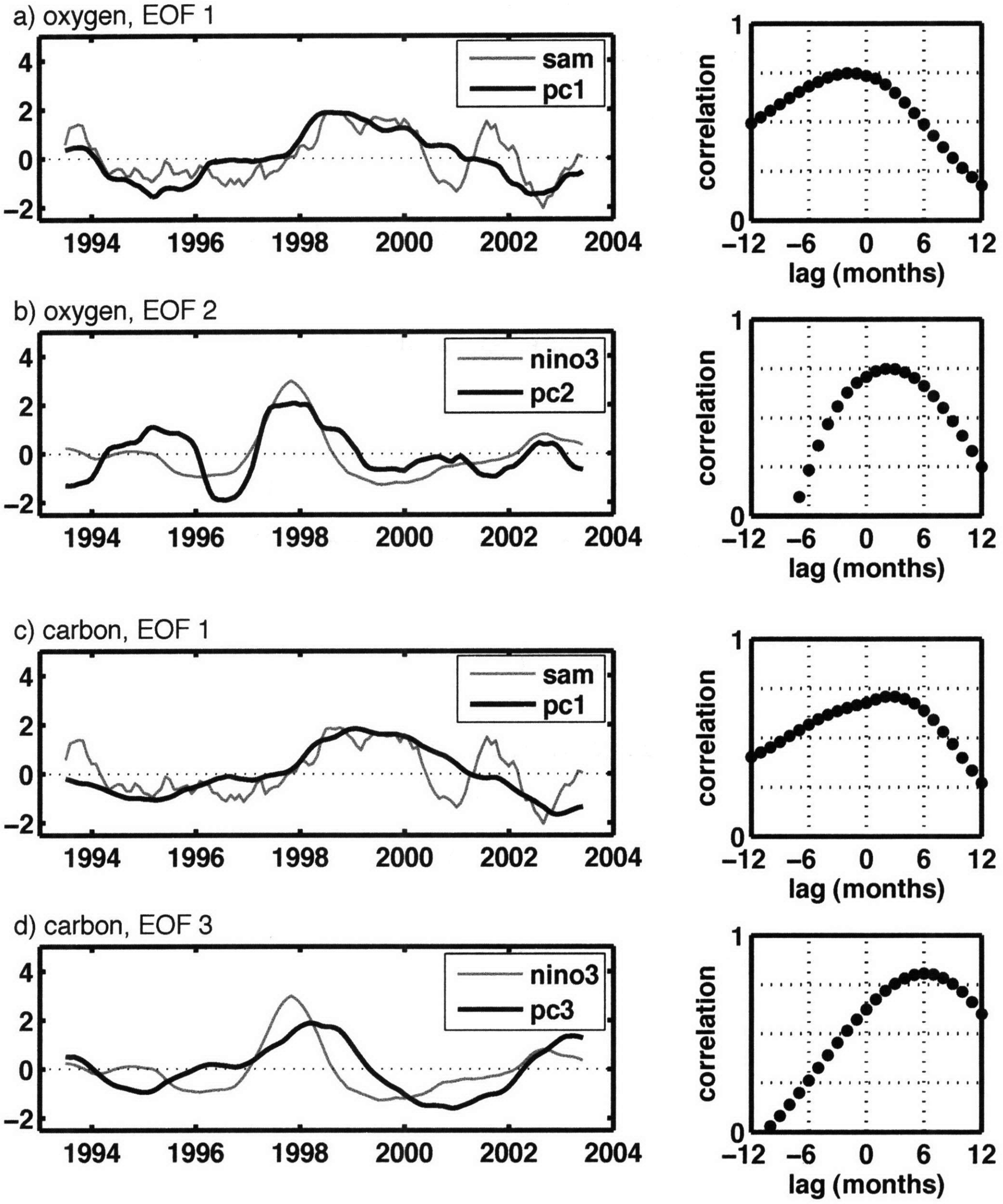

Figure 6-5: Principal components associated with the empirical orthogonal functions of Figure 6-3, along with a) and c) the SAM index; b) and d) the Niño3 index. All time series are filtered with a 12-month running-mean and normalized. Right panels show the lagged correlations between the time series in the left panels; for positive lags, the climate index leads.

entrainment from the thermocline when the mixed layer is deepening: C_{th} is the concentration in the thermocline, and $\mathcal{H}$ is a heaviside function; we set $\mathcal{H} = 1$ when $\partial h/\partial t > 0$, i.e. when the mixed layer is deepening, and 0 otherwise, because shoaling of the mixed layer does not affect C. (It is assumed that vertical velocities are small compared to the entrainment term; otherwise it would appear in that second term.) The rate of change of h can be related to the surface heat fluxes and wind stress (Kraus and Turner, 1967). The third term accounts for dilution of the tracer concentration by addition of freshwater; the fourth term represents uptake or release of tracer resulting from biological activities.

When the tracer in the mixed layer is at equilibrium with the atmosphere, its concentration is equal to the saturation concentration, C^{sat}. Departures from this equilibrium are defined as

$$\Delta C = C - C^{sat} \tag{6.3}$$

and drive the air-sea flux, which can be written as

$$F = -K_T \Delta C \tag{6.4}$$

where K_T is the gas transfer coefficient. F is defined as positive when the flux is into the ocean.

Assuming that the saturation concentration is a function of temperature only allows some simplifications to be made. This is a reasonable assumption in the case of oxygen, and, although alkalinity strongly affects the solubility of DIC, in the ACC region its effect appears to be small compared to the effect of temperature (Lovenduski et al., 2007). For the two tracers in Southern Ocean conditions, the dependence of solubility on temperature is close to linear. As in Takahashi et al. (1993), we write

$$\frac{DC^{sat}}{Dt} = \frac{\partial C^{sat}}{\partial T}\frac{DT}{Dt} \approx \alpha \frac{DT}{Dt} \tag{6.5}$$

and

$$\frac{DT}{Dt} = \frac{Q}{\rho c_p h} + (T_{th} - T)\mathcal{H}\frac{1}{h}\frac{\partial h}{\partial t} \tag{6.6}$$

where T is the sea surface temperature, T_{th} the temperature in the thermocline, α is a negative constant (resulting from a linear approximation of the reduction of solubility with increasing temperature) that is tracer-dependent, Q is the sum of sensible and latent surface heat fluxes, and ρ and c_p are the density and heat capacity of seawater, respectively.

Because we are interested in diagnosing the air-sea gas fluxes, it is convenient to derive an equation for ΔC, which is directly related to the flux according to (6.4). We substitute (6.3) into (6.2) and, making use of (6.5) and (6.6), obtain a prognostic equation for the disequilibrium concentration:

$$\frac{D\Delta C}{Dt} = \frac{F}{h} - (C^\dagger - \alpha T^\dagger)\mathcal{H}\frac{1}{h}\frac{\partial h}{\partial t} - \alpha\frac{Q}{\rho c_p h} + \frac{1}{h}(\mathrm{E} - \mathrm{P})C + \mathcal{B} \tag{6.7}$$

where we have defined $X^\dagger = X - X_{th}$, the anomaly relative to the thermocline value. In addition to the four mechanisms involved in changes to the tracer concentration that appeared in (6.2), changes in solubility resulting from heat fluxes and entrainment also affect the disequilibrium concentration.

6.4.2 Lagrangian model

We now address the relative importance of thermodynamics, entrainment, advection, dilution and biological production in generating the air-sea flux variability described in Section 6.2. We substitute (6.4) into (6.7) to obtain an equation for the air-sea flux, from which we remove the mean seasonal cycle. With a view to reducing the complexity of the model as much as possible, we assume a constant value for K_T. This yields:

$$\begin{aligned}\frac{\partial F'}{\partial t} + \overline{\mathbf{u}}\cdot\nabla F' &= -\frac{K_T}{h}F' + K_T\left[(C^\dagger - \alpha T^\dagger)\mathcal{H}\frac{1}{h}\frac{\partial h}{\partial t}\right]' \\ &\quad + K_T\alpha\frac{Q'}{\rho c_p h} - \frac{K_T}{h}[(\mathrm{E} - \mathrm{P})C]' - K_T\mathcal{B}' - \mathbf{u}'\cdot\nabla\overline{F}\end{aligned} \tag{6.8}$$

where primes denote deviations from the seasonal cycle, $\overline{\mathbf{u}}$ is the mean flow velocity, and $\nabla\overline{F}$ is the mean seasonal gradient of the flux. We have expanded the Lagrangian derivative and linearized the advection term, assuming that anomalies are small compared to the seasonal cycle. As a result, we are left with the local rate of change, mean advection, and anomalous advection terms. Of these, the first two are written on the left hand side in (6.8); they represent the rate of change of the flux into a parcel of fluid following the mean flow. The anomalous advection term is moved to the right hand side, as it acts as a forcing mechanism for particles following the mean flow, through advection of the mean disequilibrium tracer concentration by anomalous Ekman currents.

Monthly averaged anomaly fields from the GCM (e.g. heat fluxes, mixed layer depth, biological production) are used to estimate the forcing terms in (6.8), which is then solved numerically for F'. We consider the variability of fluxes following a particle traveling around Antarctica, along the geostrophic streamline shown in Figure 6-1. For the mean advection velocity, we take the value of the mean geostrophic flow speed in the ACC, $\overline{\mathbf{u}} =$ 8 cm/s (Verdy et al., 2006). The timescale for equilibration of dissolved gases is a function of the gas transfer coefficient, mixed-layer depth and, for carbon, seawater chemistry. For a mixed layer depth of 75 m and a gas transfer coefficient of $K_T = 3 \times 10^{-5}$ m/s, the e-folding timescale for oxygen equilibration is about one month. Carbonate chemistry causes the equilibration timescale for carbon to be about an order of magnitude greater and so here we impose a timescale of 1 year by setting $K_T = 2.5 \times 10^{-6}$ m/s.

The fluxes estimated from (6.8) are compared with the fluxes calculated from the GCM. Figure 6-6 shows the non-seasonal air-sea gas fluxes following a particle that was located at 0^o longitude in January 1993 and travels along the ACC (as depicted by the dashed line) until December 2003, at which time it is situated at 36^oE. In the two lower panels, solid black lines show results from the idealized model (6.8), which will be referred to as the Lagrangian model; the solid grey line show results from the GCM. The magnitude and broad patterns of the variability are captured well, given the simplicity of the model and the assumptions made. The agreement is particularly good for the oxygen fluxes, which

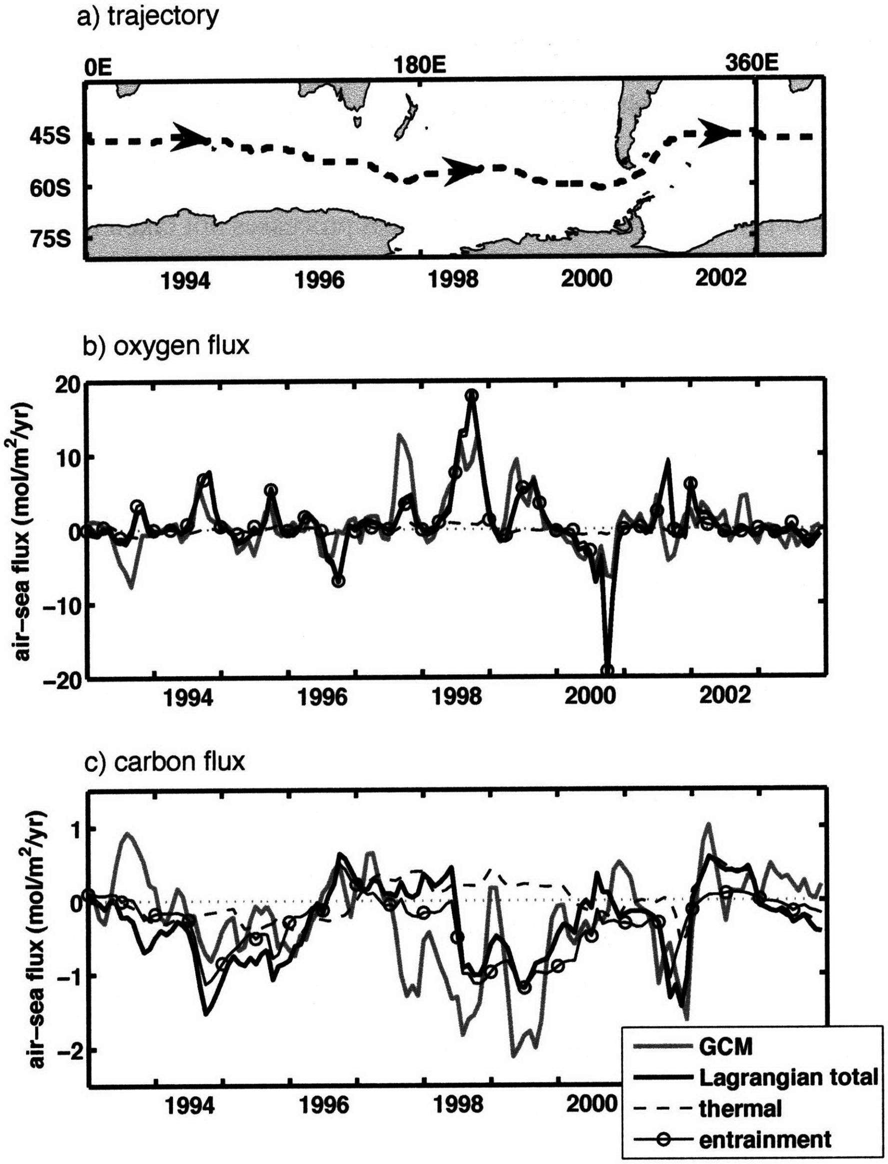

Figure 6-6: Variability of air-sea fluxes following a particle along a geostrophic streamline. a) trajectory of the particle, starting at $0^o E$ in January 1993 and propagating eastward; years indicate time of passage at the corresponding longitude; note that longitudes 0^o – $36^o E$ are repeated, with vertical line indicating $0^o E$. b) O_2 fluxes and c) CO_2 fluxes obtained using GCM (solid gray line) and obtained using Eq. 6.8 (solid black). Contribution due to thermal fluxes (dashed) and entrainment fluxes (circles) from Eq. 6.8. Fluxes resulting from dilution (E – P), biological production and from Ekman advection are small and are not shown. Time axes are aligned in all 3 panels such that spatial location of the air-sea fluxes can be inferred from (a).

exhibit mostly high-frequency variability, in concert with heat flux anomalies. Carbon fluxes simulated with the Lagrangian model capture the low-frequency variability of the GCM field; fluctuations on shorter timescales are filtered out by the Lagrangian model, as a result of the parameterized slow equilibration time of the tracer. The fast variability found in the GCM probably results from dynamical processes not taken into account in our simple Lagrangian model: for instance the mixed layer is assumed to be actively mixing at all times, and advection is only crudely represented.

By solving (6.8) for other initial longitudes, we recreate the time-longitude diagrams of Figure 6-2 with reasonable agreement (not shown). Following a single particle allows us to compare the magnitude of the fluxes induced by the different mechanisms. Figure 6-6 shows the thermal (dashed line) and entrainment (circles) components of the flux. Clearly, entrainment is the dominant forcing for both CO_2 and O_2. Thermodynamic effects are small in comparison, and other forcing terms in (6.8) have a negligible impact on the fluxes simulated with the Lagrangian model. Ekman advection of tracer is, to leading order, balanced by the advection of temperature, such that $\mathbf{u}' \cdot \overline{C} \approx \mathbf{u}' \cdot \overline{C^{sat}}$; thus the anomalous advection of disequilibrium tracer concentration, the last term in (6.8), is small. Indirectly, gas fluxes also result from meridional Ekman currents as they exchange heat with the atmosphere, but this is included in the thermal solubility term. Evaporation and precipitation effects are highly variable in time and in space; consequently they are mostly filtered out by the simple model. Finally, we find that the Southern Ocean region of our GCM simulation exhibits very little interannual variability in biological productivity, and the diagnosed $\mathcal{B}'$ is negligible. Other studies also find that the effects of biology on interannual variability in ocean pCO_2 and air-sea fluxes of CO_2 are small (LeQuéré et al., 2003; Lovenduski et al., 2007; Lenton and Matear, 2007).

6.4.3 Further simplifications to the diagnostic framework

These results suggest that the large-scale patterns of oxygen and carbon dioxide fluxes variability can be accounted for by entrainment of deep water into the mixed layer. Convective mixing brings to the surface water that is rich in carbon, and depleted in oxygen; interannual variability in the strength of this mixing causes anomalous air-sea gas fluxes. In light of these findings, we consider the equation for the disequilibrium tracer concentration (6.7) in the absence of dilution and biological production. We then have:

$$\frac{D\Delta C}{Dt} = -\frac{1}{\tau_{eq}}\Delta C - \alpha\frac{DT}{Dt} + (C_{th} - C)\,\mathcal{H}\frac{1}{h}\frac{\partial h}{\partial t} \tag{6.9}$$

where we have defined an equilibration timescale $\tau_{eq} = h/K_T$: this is the time taken for the decay of disequilibrium concentrations through air-sea fluxes. There are two limit cases:

- $\tau_{eq} \to 0$: the tracer equilibrates rapidly, thus $\Delta C \to 0$ and the rate of change of ΔC can be neglected. The balance is primarily between the air-sea flux and the forcing: $\Delta C \sim \{DT/Dt,\ \partial h/\partial t\}$. The timescale of tracer flux variability approaches that of heat flux variability, as heat fluxes are responsible for changes in SST and MLD. This is what we find for oxygen.

- $\tau_{eq} \to \infty$: the tracer equilibrates slowly, thus air-sea fluxes can be neglected. The balance is then between $D\Delta C/Dt$ and the forcing terms: $\Delta C \sim \{T,\ h\}$. For carbon dioxide, we find an intermediate response, in-between these two limit cases. Although carbon dioxide has a finite equilibration timescale, it responds slowly compared to the timescale of SST and MLD variability; this explains the similitude of CO_2 fluxes with SST and, to a certain extent MLD, as discussed in Section 6.2.

6.5 Conclusions

We have used results from a physical-biogeochemical model to examine the variability of carbon dioxide and oxygen air-sea fluxes in the Southern Ocean. As with earlier studies (Lenton and Matear, 2007; Lovenduski et al., 2007) we find a strong link between carbon dioxide flux variability and the Southern Annular Mode (SAM). However, not emphasized in previous studies, we also find a strong correlation with ENSO. This suggests that both

SAM and ENSO should be taken into account when addressing the ocean's response to atmospheric forcing; an analogous conclusion was reached from analyzing the Southern Ocean SST variability.

In the region of the ACC, we find that ocean circulation strongly impacts the non-seasonal variability of CO_2 and O_2 air-sea fluxes in the GCM. This highlights the importance of capturing the physical processes accurately in models of the ocean biogeochemistry. By incorporating observations from many different sources, the ECCO state-estimation aims at obtaining simulated dynamical fields that are close to the true ocean state.

On the other hand, the time series available are relatively short, and our analysis relies on only 11 years of simulated fields. It is possible that the spatial patterns of ENSO and SAM variability would be different for other time periods. We do, however, find our results to be consistent with the SAM and ENSO patterns of CO_2 variability in the model of McKinley et al. (2003) which uses the MIT-gcm flow fields and a biogeochemical model similar to ours in a simulation that extends to the period 1980-1998. The same Pacific-intensified patterns with a dipolar structure appear in both models.

We have also used a simple Lagrangian representation of CO_2 and O_2 flux variability. It captures the main features of the variability simulated with a higher-complexity GCM; this is quite remarkable given the simplicity of the framework. Many assumptions have been made in deriving the Lagrangian model; we would not argue that it captures the true variability of tracer concentrations in the mixed layer. It does, however, serve the point of giving an estimated order of magnitude for the air-sea fluxes induced by different forcing mechanisms. The Lagrangian model allows us to examine the leading order causes of the large-scale variability and suggests that, at least in this simulation, biological effects are small compared to the entrainment of deep water into the mixed layer. Thermal effects have a small but not negligible effect on the variability, especially for CO_2 with its longer equilibriation timescale. Other processes are found to have a negligible impact on the large-scale patterns of variability. Our analysis being restricted to the ACC region, we acknowledge that the mechanisms in other parts of the Southern Ocean might be quite different, in particular in coastal regions.

If entrainment and thermal solubility are the main drivers as suggested in this study, one can derive an elegant expression for disequilibrium gas concentrations in the surface waters (Eq. 6.9) involving air-sea heat fluxes and the mean geostrophic flow. These may be deduced from satellite data and, along with mixed-layer depth variability estimated from a mixed-layer model forced with remotely observed heat fluxes and winds, could provide a means to estimate some aspects of the variability of air-sea CO_2 and O_2 fluxes from space.

Chapter 7

Concluding remarks

The work presented in this thesis is highly interdisciplinary, and includes contributions to the fields of theoretical ecology, oceanography, and ocean biogeochemistry. This follows from the complex nature of marine ecosystems, which are influenced by the structure of their physical and biogeochemical environment, as well as the biological processes they carry out. The dynamics of idealized ecosystems can be captured by simple mathematical models (such as the one presented in Chapter 1). The main focus of this thesis is on the formation of spatial patterns in the distribution of zooplankton arising from social interactions between individuals (Chapters 2, 3 and 4). I have also considered two sources of temporal variability for marine ecosystems: the first is transient amplification of small perturbations to stable equilibrium solutions (Chapter 5); the second is climatic variability affecting the local biogeochemical environment (Chapter 6). The main results of each chapter are summarized below.

Chapter 1 In this first chapter, I formulate and analyze a predator-prey model with density-dependent mating success for the predator. An Allee effect results from the positive correlation between population size and mating probability, with implications for the population dynamics: as in standard predator-prey models, stable coexistence and sustained oscillations are possible asymptotic states; however, as a consequence of the Allee effect, extinction of the predator is always a stable solution. This result holds when both discrete-stage and continuous-weight models are used to describe the predator's life cycle; under simple assumptions, the two formulations simplify to an equivalent unstructured consumer-resource model. Because it modulates the rate at which offspring are produced, the mating probability appears in the equation for the resource as well as the equation for the predator.

The main consequence of the Allee effect in predator-prey models is to alter the intensity of inter-specific interactions: Specifically, the rate at which biomass is moved from one trophic level to the next. High densities accelerate the predator growth, which is also associated with faster depletion of resources. In addition to changing the bifurcation structure of the predator-prey model, inclusion of the Allee effect makes the model sensitive to initial conditions and to external perturbations, as there can be multiple stable asymptotic states. Most relevant to the study of social behavior in zooplankton, it can significantly alter the impacts of patchiness on the average per capita growth rate (a measure of individual fitness). To this end, the predator-prey model with Allee effect is incorporated into a spatially-explicit framework in the following chapter.

Chapter 2 addresses the evolution of social behavior in a population of krill, when the benefits related to the abundance of mates are offset by the enhanced competition for resources between group members. The predator-prey model with Allee effect (Chapter 1) is combined with the continuous-field model of Flierl et al. (1999) for the formation of social aggregations. Linear instability of the coupled system leads to self-organized patchiness in the density-distribution of krill, despite the stabilizing effect of predator-prey interactions. Chaotic advection, representing turbulence at the scale of the aggregations and larger, plays a significant role in the development of aggregations. I employ the model to simulate the evolutionary dynamics of social behavior, which I assume to be induced by a recessive allele. Although the framework is highly idealized and ignores many aspects of group dynamics, it provides a new and quantitative approach for investigating what determines the success of the aggregation strategy.

Social behavior can evolve in the model when the benefit resulting from the local abundance of mates overcomes the cost associated with having to share resources with other group members. This can happen when reproduction increases with density in part of the range, and mixing of prey into patches is rapid enough to offset the depletion. Stirring and mixing by turbulent flows control the availability of resources for the krill and therefore influence the success of the social population; factors controlling the swimming behavior (cruising speed, sensing radius, and diffusivity) play a less significant role. There are three possible scenarios following the introduction of the social allele in the populations. (i) aggregations cannot form because the turbulent flow is too strong or the swimming behavior is too weak; neutral evolution then brings the ratio of genotypes to equilibrium: 25% social, 75% asocial. (ii) aggregations form but the turbulent flow is not strong enough to supply resources to the clustered zooplankton; social organisms remain at low density – less than 25%. (iii) aggregations form and the social population outcompetes other types, driving them to extinction; this scenario, corresponding to the evolution of social behavior in the model, takes place when turbulent mixing is rapid enough to supply resources and the swimming behavior is sufficiently strong for aggregations to resist the dispersive effects of that turbulent flow.

Chapter 3 This chapter extends the analysis of the mathematical model introduced in Chapter 2. An approximate solution for the steady-state spatial distribution of predator and prey densities, derived from weakly nonlinear stability analysis, captures well the spatial patterns obtained from the full numerical model. The combination of social behavior and population dynamics can lead to non-steady asymptotic dynamics; in the one-dimensional spatial domain, these include chaotic behavior and traveling waves. When movements are fast compared to population dynamics, however, aggregation tends to stabilize the density-distribution.

Chapter 4 addresses the foraging success of zooplankton schooling in a variable environment. I develop a coupled physical-biological model that simulates the horizontal variability of phytoplankton density induced by turbulent circulation patterns. The simplistic formulation offers an economical way of simulating the temporal and spatial variability of the resource field that is nevertheless grounded on principles of geophysical fluid dynamics. Foraging zooplankton are represented as individuals moving in this patchy resource field. In addition to the attraction rule producing aggregations, the individual-based model accounts for the tendency of krill to align their velocity with that of their neighbors; such behavior can lead to the spontaneous formation of polarized groups called schools.

Results suggest that schooling can improve the foraging success. In the model, the optimal strategy (as defined by the ratio of attraction and alignment tendencies) yields the formation of many schools that are not very dense, which is consistent with the observed night-time aggregations of Antarctic krill. I suggest that a reduction of the swimming speed of krill during day-time, when they are not feeding, could explain the observed change in the mean density of aggregations.

Chapter 5 introduces a new mathematical framework for analyzing the transient dynamics in ecosystem models. The transient behavior of an ecosystem perturbed away from equilibrium can be described in terms of the “reactivity” and “amplification envelope” associated with that equilibrium. Expressions for the sensitivity of reactive dynamics to the parameters of the nonlinear ecological model are derived. Sensitivity analysis is used to reveal the ecological mechanisms producing the transient dynamics in a predator-prey model, and to predict how changing the parameters of the model affects the transient response.

In the predator-prey model with Allee effect (cf. Chapter 1), perturbations can be amplified in two different ways. Either the predation rate is slow but the energy transfer is highly efficient, in which case the predator can take advantage of transient increases of prey (bottom-up mechanism); or the prey is removed quickly but poorly assimilated by the predator, in which case the prey can grow opportunistically when the predator biomass is below equilibrium (top-down mechanism). Increasing the density-dependence of the mating success has a negative effect on the bottom-up mechanism but a positive effect on the top-down mechanism. Increasing the maximum predation rate, however, always positively affects the potential for transient amplification, an indication that modulation of the predation rate by the mating probability is not dynamically equivalent to reducing the density-independent component of the predation term.

Chapter 6 In this chapter, I examine the variability of the biogeochemical environment in the Southern Ocean, using results from a numerical simulation of the global ocean. In an earlier paper (Verdy et al., 2006), it was found that ENSO and the Southern Annular Mode affect the observed sea surface temperature, which in turn influences the solubility of carbon dioxide and oxygen. This solubility effect is, however, small compared to the effect of convective mixing in driving interannual variability of air-sea fluxes of CO_2 and O_2 in the model.

The dominant modes of variability, identified from statistical analysis, are associated with forcing by ENSO and the Southern Annular Mode (SAM). These have different spatial patterns, but both exhibit a dipolar structure over the South Pacific, where the variaibility of air-sea fluxes is largest. ENSO- and SAM-induced surface winds carry cold air from the pole and cause northward transport of cold water resulting from Ekman currents; by cooling the surface, these processes enhance convective mixing taking place in the winter. The resulting entrainment of carbon-rich, oxygen-depleted deep waters into the mixed layer is what drives the anomalous fluxes of soluble gases. Lateral advection also contributes to the variability, especially for carbon dioxide which has a longer equilibration timescale (roughly one year) than oxygen (about one month). Changes in the carbon and oxygen cycles are likely to affect the dynamics of plankton communities in the Southern Ocean.

Future work

The natural extension of the work presented in Chapters 2 to 4 would entail comparisons of the simulated zooplankton aggregations with observations of Antarctic krill. As a result of the Southern Ocean GLOBal ECosystems dynamics (SO GLOBEC) program, large amounts of data are becoming available for analysis (e.g. Ashjian et al, 2008; Costa et al., 2008; Marrari et al., 2008; Lawson et al., 2008). The spectral properties of simulated phytoplankton and zooplankton density (from the coupled physical-biological simulations of Chapter 4) should be compared with these observations. It is expected that, as a result of turbulent stirring combined with diffusion, the variance of phytoplankton increases with the spatial scale; the variance of zooplankton is expected to be more uniform due to the small-scale variability resulting from social aggregations.

Also relevant to the formation of spatial patterns in the density-distribution of zooplankton, and missing in the models presented in this thesis, are the processes causing aggregation of schools. Social groups may form at relatively small spatial scales controlled by the swimming behavior of individuals, but in the ocean they are observed to assemble into large-scale patterns, possibly with fractal structure (Lawson, 2006). Variability of the flow may contribute to the formation of these "super-swarms", but the mechanisms are not well known. Incorporating such interactions between schools in models will contribute to a better understanding of the overall population dynamics of schooling organisms.

Bibliography

[1] Abraham, E.R. (1998), The generation of plankton patchiness by turbulent stirring. *Nature* **391**, 577–580.

[2] Abrams, P.A. (2007), Habitat choice in predator-prey systems: Spatial instability due to interacting adaptive movements. *Am. Nat.* **169**, 581–594.

[3] Alonzo, S.H., P.V. Switzer, and M. Mangel (2003). Ecological games in space and time: the distribution and abundance of Antarctic krill and penguins. *Ecology* **84**, 1598–1607.

[4] Armstrong, R.A. (1994), Grazing limitation and nutrient limitation in marine ecosystems: Steady-state solutions of an ecosystem model with multiple food chains. *Limnol. Oceanogr.* **39**, 597–608.

[5] Ashjian, C.J., C.S. Davis, S.M. Gallager, P.H. Wiebe, and G.L. Lawson (2008), Distribution of larval krill and zooplankton in association with hydrography in Marguerite Bay, Antarctic Peninsula, in austral fall and winter 2001 described using the Video Plankton Recorder. *Deep-Sea Res., accepted.*

[6] Bazykin, A.D. (1998), *Nonlinear dynamics of interacting populations.* World Scientific, River Edge, NJ.

[7] Bednekoff, P.A., and S.L. Lima (1998), Re-examining safety in numbers: interactions between risk dilution and collective detection depend upon predator targeting behavior. *Proc. R. Soc. Lond. B* **265**, 2021–2026.

[8] Benczik, I.J. (2005), Discrete time model for chemical and biological decay in chaotic flows: Reentrance phase transitions. *Phys. Rev. E* **71**, doi:10.1103/PhysRevE.71.066205.

[9] Blackburn, M. (1980), Observations on the distribution of Nyctiphanes australis Sars (Crustacea, Euphausiidae) in Australian waters. *Report CSIRO Division of Fisheries and Oceanography* **119**, 1–10.

[10] Boukal, D.S., and L. Berec (2002), Single-species models of the Allee effect: extinction boundaries, sex ratios and mate encounters. *J. Theor. Biol.* **218**, 375–394.

[11] Boyd, C.M., M. Heyraud, and C.N. Boyd (1984), Feeding of Antarctic krill Euphausia superba. *J. Crust. Biol.* **4**, 123–141.

[12] Bracco, A., A. Provenzale, and I. Scheuring (2000), Mesoscale vortices and the paradox of the plankton. *Proc. Royal Soc. Lond. B* **267**, 1795–1800.

[13] Brentnall, S.J., K.J. Richards, J. Brindley, and Murphy (2003), Plankton patchiness and its effect on larger-scale productivity. *J. Plankton Res.* **25**, 121–140.

[14] Cane, M., S. Zebiak, and S. Dolan (1986), Experimental forecasts of El-Niño. *Nature* **321**, 827–832.

[15] Caswell, H. (2001), *Matrix population models: Construction, Analysis, and Interpretation*, 2nd edn. Sinauer Associates, Sunderland, MA.

[16] Caswell, H., and M.G. Neubert (2005), Reactivity and transient dynamics of discrete-time ecological systems. *J. Diff. Eq. and Appl.* **2**, 295–310.

[17] Caswell, H. (2007), Sensitivity analysis of transient population dynamics. *Ecol. Lett.* **10**, 1–15.

[18] Caswell, H. (2007), Perturbation analysis of nonlinear matrix population models. In preparation.

[19] Chen, X., and J.E. Cohen (2001), Transient dynamics and food-web complexity in the Lotka-Volterra cascade model. *Proc. R. Soc. Lond. B* **268**, 1–10.

[20] Chen, B.L., and P.A. Zadrozny (2001), Analytic derivatives of the matrix exponential for estimation of linear continuous-time models. *J. Econ. Dyn. Control* **25**, 1867-1879.

[21] Clark, C.W., and M. Mangel (1986), The evolutionary advantages of group foraging. *Theor. Pop. Biol.* **30**, 45–75.

[22] Coddington, E.A., and N. Levinson (1955), *Theory of ordinary differential equations*, McGraw-Hill, New York, NY.

[23] Connell, S.D. (2000), Is there safety-in-numbers for prey? *Oikos* **88**, 527–532.

[24] Cotté, C., and Y. Simard (2005), Formation of dense krill patches under tidal forcing at whale feeding hot spots in the St. Lawrence Estuary. *Mar. Ecol. Prog. Ser.* **288**, 199–210.

[25] Courchamp, F., T. Clutton-Brock, and B. Grenfell (1999), Inverse density dependence and the Allee effect. *Trends Ecol. Evol.* **14**, 405–410.

[26] Couzin, I.D., J. Krause, R. James, G.D. Ruxton, and N.R. Franks (2002), Collective memory and spatial sorting in animal groups. *J. Theor. Biol.* **218**, 1–11.

[27] Couzin, I.D., J. Krause, N.R. Franks, and S.A. Levin (2005), Effective leadership and decision-making in animal groups on the move. *Nature* **433**, 513–516.

[28] Costa, D.P., J.M. Klinck, E.E. Hofmann, M.S. Dinniman, and J.M. Burns (2008), Upper ocean variability in West Antarctic Peninsula continental shelf waters as measured using instrumented seals. *Deep-Sea Res., accepted.*

[29] de Lafontaine, Y., S. Demers, and J. Runge (1991), Pelagic food web interactions and productivity in the Gulf of St. Lawrence: a perspective. *Can. Spec. Publ. Fish. Aquat. Sci.* **11**, 99–123.

[30] De Roos, A.M., L. Persson, and E. McCauley (2003), The influence of size-dependent life-history traits on the structure and dynamics of populations and communities. *Ecol. Lett.* **6**, 473–487.

[31] Dennis, B. (1989), Allee effects: population growth, critical density, and the chance of extinction. *Nat. Res. Model.* **3**, 481–538.

[32] Dutkiewicz, S., A. Sokolov, J. Scott, and P. Stone (2005), A Three-dimensional ocean-seaice-carbon cycle model and its coupling to a two-dimensional atmospheric model: Uses in climate change studies. *Report 122, Joint Program of the Science and Policy of Global Change*, MIT, Cambridge, MA.

[33] Epstein, A.W., and R.C. Beardsley (2001), Flow-induced aggregation of plankton at a front: a 2-D Eulerian model study. *Deep-Sea Res. II* **48**, 395–418.

[34] Everson, I. (1982), Diurnal variations in mean volume backscattering strength of an Antarctic krill Euphausia superba patch. *J. Plankt. Res.* **4**, 155–162.

[35] Farrell, B.F., and P.J. Ioannou (1996), Generalized stability theory. Part I: Autonomous operators. *J. Atmos. Sci.* **53**, 2025–2040.

[36] Feely, R.A., and co-authors (2002), Seasonal and interannual variability of CO_2 in the equatorial Pacific. *Deep Sea Res. II* **49**, 2443–2469.

[37] Flierl, G., D. Grünbaum, S.A. Levin, and D. Olson (1999), From individuals to aggregations: the interplay between behavior and physics. *J. Theor. Biol.* **196**, 397–454.

[38] Flierl, G., and D.G. McGillicuddy (2002), Mesoscale and submesoscale physical-biological interactions. In: *The Sea* **12**, 113–185.

[39] Foster, W.A., and J.E. Treherne (1981), Evidence for the dilution effect in the selfish herd from fish predation on a marine insect. *Nature* **293**, 466–467.

[40] Franks, P.J.S. (1992), Sink or swim - accumulation of biomass at fronts. *Mar. Ecol. Prog. Ser.* **82**, 1–12.

[41] Follows, M.J., S. Dutkiewicz, and T. Ito (2006), On the solution of the carbonate system in ocean biogeochemistry models. *Ocean Modelling* **12**, 290–301.

[42] Folt, C.L., and C.W. Burns (1999), Biological drivers of zooplankton patchiness. *Trends Ecol. Evol.* **14**, 300–305.

[43] Gantmacher, F.R. (1959), *The Theory of Matrices Vol. 1*, Chelsea, NY.

[44] Genin, A., J.S. Jaffe, R. Reef, C. Richter, and P.J.S. Franks (2005), Swimming against the flow: a mechanism of zooplankton aggregation. *Science* **308**, 860–862.

[45] Gent, P.R., and J.C. McWilliams (1990), Isopycnal mixing in ocean general circulation models. J. Phys. Oceanogr. **20**, 150–155.

[46] Gilpin, M.E. (1972), Enriched predator-prey systems: theoretical stability. *Science* **177**, 902–904.

[47] Gómez-Gutiérrez, J., W.T. Peterson, A. De Robertis, and R.D. Brodeur (2003), Mass mortality of krill caused by parasitoid ciliates. *Science* **301**, 339.

[48] Gruber, N., C.D. Keeling, and N.R. Bates (2002), Interannual variability in the North Atlantic Ocean carbon sink. *Science* **298**, 2374–2378.

[49] Grünbaum, D. (1994), Translating stochastic density-dependent individual behavior to a continuum model of animal swarming. *J. Math. Biol.* **33**, 139–161.

[50] Grünbaum, D. (1998), Schooling as a strategy for taxis in a noisy environment. *Evolutionary Ecol.* **12**, 503–522.

[51] Grünbaum, D. (1999), Advection-diffusion equations for generalized tactic searching behaviors. *J. Math. Biol.* **38**, 169–194.

[52] Grünbaum, D. (2002), Predicting availability to consumers of spatially and temporally variable resources. *Hydrobiologia* **480**, 175–191.

[53] Gurney, W.S.C., and R.M. Nisbet (1998), *Ecological Dynamics*. Oxford University Press, New York, NY.

[54] Hall, A., and M. Visbeck, (2002), Synchronous variability in the Southern Hemisphere atmosphere, sea ice, and ocean resulting from the annular mode. *J. Climate* **15,** 3043–3057.

[55] Hamilton, W.D. (1971), Geometry for the selfish herd. *J. Theor. Biol.* **31**, 295–311.

[56] Hamner, W.M., P.P. Hamner, S.W. Strand, and R.W. Gilmer (1983). Behavior of Antarctic krill, Euphausia superba – Chemoreception, feeding, schooling, and molting. *Science* **220**, 433-435.

[57] Hamner, W.M. (1983), Aspects of schooling in Euphausia superba. *J. Crust. Biol.* **4**, 67–74.

[58] Hamner, W.M., and P.P. Hamner (2000), Behaviour of Antarctic krill (Euphausia superba): Schooling, foraging, and antipredatory behaviour. *Can. J. Fish. Aquat. Sci.* **57** (suppl. S3), 192–202.

[59] Hancock, P.A., E.J. Milner-Gulland, and M.J. Keeling (2006), Modelling the many-wrongs principle: the navigational advantages of aggregation in nomadic foragers. *J. Theor. Biol.* **240**, 302–310.

[60] Hastings, A. (2004), Transients: the key to long-term ecological understanding? *Trends Ecol. Evol.* **19**, 39–45.

[61] Henderson, H.V., and S.R. Searle (1981), The vec-permutation matrix, the vec operator and Kronecker products: a review. *Linear and Multilinear Algebra* **9**, 271–288.

[62] Hewitt, R.P., and D.A. Demer (1993), Dispersion and abundance of Antarctic krill in the vicinity of Elephant Island in the 1992 austral summer. *Mar. Ecol. Prog. Ser.* **99**, 29–39.

[63] Hobson, L.A. (1989), Paradox of the plankton – an overview. *Biological Oceanography* **6**, 493–504.

[64] Hofmann, E.E., and E.J. Murphy (2004), Advection, krill, and Antarctic marine ecosystems. *Antarctic Science* **16**, 487–499.

[65] Hofmann, E.E., A.G.E. Haskell, J.M. Klinck, and C.M. Lascara (2004). Lagrangian modeling studies of Antarctic krill (*Euphausia superba*) swarm formation. *ICES J. Mar. Sci.* **61**, 617–631.

[66] Ives, A.R., and S.R. Carpenter (2007), Stability and diversity of ecosystems. *Science* **317**, 58–62.

[67] Jaffe J.S., M.D. Ohman, and A. De Robertis (1999), Sonar estimates of daytime activity levels of Euphausia pacifica in Saanich Inlet. *Can. J. Fish. Aquat. Sci.* **56**, 2000–2010.

[68] Kalinowski, J., and Z. Witek (1985), Scheme for classifying aggregations of Antarctic krill. BIOMASS handbook No 27.

[69] Kårolyi, G., Z. Neufeld, and I. Scheuring (2005), Rock-scissors-paper game in a chaotic flow: The effect of dispersion on the cyclic competition of microorganisms. *J. Theor. Biol.* **236**, 12–20.

[70] Kent, A., C.P. Doncaster, and T.Sluckin, (2003), Consequences for predators of rescue and allee effects on prey. *Ecol. Modelling* **162,** 233–245.

[71] Key, R.M., and co-authors (2004), A global ocean carbon climatology: Results from GLODAP. *Global Biogeochem. Cycles* **18**, GB4031.

[72] Kils, U. (1982), Swimming behavior, swimming performance and energy balance of Antarctic krill *Euphausia superba*. BIOMASS Sci. Ser. No 3.

[73] Kingsley, M.C.S., and R.R. Reeves (1998), Aerial surveys of cetaceans in the Gulf of St. Lawrence in 1995 and 1996. *Can. J. Zool.* **76**, 1529–1550.

[74] Kot, M. (2001), *Elements of mathematical ecology*. Cambridge University Press, Cambridge, UK.

[75] Kraus, E.B., and J.S. Turner (1967), A one dimensional model of the seasonal thermocline. Part II. *Tellus* **19**, 98–105.

[76] Large, W.G., J.C. McWilliams, and S.C. Doney (1994), Oceanic vertical mixing: A review and a model with a nonlocal boundary layer parameterization. *Rev. Geophys.* **32**, 363–403.

[77] Lawson, G.L. (2006), *Distribution, patchiness, and behavior of antarctic zooplankton, assessed using multi-frequency acoustic techniques.* PhD Thesis, MIT-WHOI.

[78] Lawson, G.L., P.H. Wiebe, C.J. Ashjian, and T.K. Stanton (2008), Euphausiid distribution along the Western Antarctic Peninsula - (B) Distribution of euphausiid aggregations and biomass, and associations with environmental features. *Deep-Sea Res., accepted.*

[79] LeQuéré, C., O. Aumont, P. Monfray, and J. Orr, (2003), Propagation of climatic events on ocean stratification, and CO_2: Case studies over the 1979-1999 period. *J. Geophys. Res.* **108**, 3375, doi:10.1029/2001JC000920.

[80] Lenton, A., and R. Matear (2007), Interannual variability: the SAM and CO_2 uptake. *Global Biogeochem. Cycles* **21**, GB2016, doi:10.1029/2006GB002714.

[81] Levin, S.A. (1992), The Problem of Pattern and Scale in Ecology: The Robert H. MacArthur Award Lecture. *Ecology* **73**, 1943–1967.

[82] Levin, S.A. (1994), Patchiness in marine and terrestrial systems: from individuals to populations. *Phil. Trans. Royal Soc. Lond. B* **343**, 99–103.

[83] Lewis, M.A., and P. Kareiva, (1997), Allee dynamics and the spread of invading organisms. *J. Theor. Biol.* **43**, 141–158.

[84] Lovenduski, N.S., and N. Gruber (2005), Impact of the Southern Annular Mode on Southern Ocean circulation and biology. *Geophys. Res. Lett.* **32**, L11603, doi:10.1029/2005GL022727.

[85] Lovenduski, N.S., N. Gruber, S.C. Doney, and I.D. Lima (2007), Enhanced CO_2 outgassing in the Southern Ocean from a positive phase of the Southern Annular Mode. *Global Biogeochem. Cycles* **21**, GB2026, doi:10.1029/2006GB002900.

[86] Mackas, D., and C. Boyd (1979), Spectral analysis of zooplankton spatial heterogeneity. *Science* **204**, 62–64.

[87] Magnus, J.R., and H. Neudecker (1985), Matrix differential calculus with applications to simple, Hadamard, and Kronecker products. *J. Math. Psychol.* **29**, 474–492.

[88] Magnus, J.R., and H. Neudecker (1988), *Matrix Differential Calculus with Applications in Statistics and Econometrics*. John Wiley & Sons, New York, NY.

[89] Marrari, M., K.L. Daly, and C. Hu (2008), Spatial and temporal variability of SeaWiFS chlorophyll-a distributions west of the Antarctic Peninsula: Implications for krill production. *Deep-Sea Res., accepted.*

[90] Marshall, J., A. Adcroft, C. Hill, L. Perelman, and C. Heisey (1997), A Finite-volume, incompressible Navier Stokes model for studies of the ocean on parallel computers. *J. Geophys. Res.* **102**, 5753–5766.

[91] Martin, A.P., and M.A. Srokosz (2002), Plankton distribution spectra: inter-size class variability and the relative slopes for phytoplankton and zooplankton. *Geophys. Res. Lett.* **29**, 2213, 10.1029/2002GL015117.

[92] Martin, A.P. (2003), Phytoplankton patchiness: the role of lateral stirring and mixing. *Progr. Oceanogr.* **57**, 125–174.

[93] Marvier, M., P. Kareiva, and M.G. Neubert (2004), Habitat destruction, fragmentation, and disturbance promote invasion by habitat generalists in a multispecies metapopulation. *Risk Analysis* **24**, 869–878.

[94] Mauchline, J. (1980), The biology of rnysiids and euphausiids. *Adv. Mar. Biol.* **18**, 1–681.

[95] May, R.M. (1972), Limit cycles in predator-prey communities. *Science* **177**, 900–902.

[96] May, R.M. (1973), *Stability and complexity in model ecosystems*. Princeton University Press, Princeton, NJ.

[97] McCarthy, M.A. (1997), The Allee effect, finding mates and theoretical models. *Ecol. Modelling* **103**, 99–102.

[98] McKinley, G.A., M.J. Follows, and J. Marshall (2004), Mechanisms of air-sea CO_2 flux variability in the equatorial Pacific and the North Atlantic. *Global Biogeochem. Cycles* **18**, GB2011, doi:10.1029/2003GB002179.

[99] McKinley, G., M.J. Follows, J.C. Marshall, and S.-M. Fan (2003), Interannual variability of air-sea O_2 fluxes and the determination of CO_2 sinks using atmospheric O_2/N_2. *Geophys. Res. Lett.* **30**, 1101, 10.1029/2002GL016044.

[100] Miller, D.G.M., and I. Hampton (1989), Biology and ecology of the Antarctic krill (*Euphausia superba* Dana): A review. BIOMASS Sci. Ser. No 9.

[101] Mirabet, V., P. Auger, and C. Lett (2007), Spatial structures in simulations of animal grouping. *Ecol. Modelling* **201**, 468–476.

[102] Moore, J.K., and M.R. Abbott (2000), Phytoplankton chlorophyll distributions and primary production in the Southern Ocean. *J. Geophys. Res.* **105**, 28,709–28,722.

[103] Myerscough, M.R., M.J. Darwen, and W.L. Hogart (1996), Stability, persistence and structural stability in a classical predator-prey model. *Ecol. Modelling* **89**, 31–42.

[104] Nel, D.G. (1980), On matrix differentiation in statistics. *S. Afr. Stat. J.* **14**, 137–193.

[105] Neubert, M.G., and H. Caswell (1997), Alternatives to resilience for measuring the responses of ecological systems to perturbations. *Ecology* **78**, 653–665.

[106] Neubert, M.G., H. Caswell, and J.D. Murray (2002), Transient dynamics and pattern formation: reactivity is necessary for Turing instabilities. *Math. Biosci.* **175**, 1–11.

[107] Neubert, M.G., T. Klanjscek, and H. Caswell (2004), Reactivity and transient dynamics of predator-prey and food web models. *Ecol. Modelling* **179**, 29–38.

[108] Nicol, S., and R.K. O'Dor (1985), Predatory behavior of squid (Illex-Illecebrosus) feeding on surface swarms of Euphausiids. *Can. J. Zool.* **63**, 15–17.

[109] O'Brien, D.P. (1987), Description of escape responses of krill (Curstacea, Euphausiacea), with particular reference to swarming behavior and the size and proximity of the predator. *J. Crust. Biol.* **7**, 449-457.

[110] O'Brien, D.P. (1988), Surface schooling behaviour of the coastal krill Nyctiphanes australis (Curstacea: Euphausiacea) off Tasmania, Australia. *Mar. Ecol. Prog. Ser.* **42**, 219–233.

[111] Okubo, A. (1986), Dynamical aspects of animal grouping: swarms, schools, flocks, and herds. *Adv. Biophys.* **22**, 1–94.

[112] Parekh, P., M. Follows, S. Dutkiewicz, and T. Ito (2006), Physical and biological regulation of the soft tissue carbon pump, *Paleoceanography* **21**, PA3001, doi:10.1029/2005PA001258.

[113] Parrish, J.K., and L. Edelstein-Keshet (1999), Complexity, pattern, and evolutionary trade-offs in animal aggregation, *Science* **284**, 99–101.

[114] Pasquero, C. (2005), Differential eddy diffusion of biogeochemical tracers. *Geophys. Res. Lett.* **32**, L17603, doi:10.1029/2005GL023662.

[115] Persson, L., K. Leonardsson, A.M. de Roos, and M. Gyllenberg, (1998), Ontogenetic scaling of foraging rates and the dynamics of a size-structured consumer-resource model. *Theor. Pop. Biol.***54**, 270–293.

[116] Pierrehumbert, R.T. (2000), Lattice models of advection-diffusion. *Chaos* **10** 61–74.

[117] Pimm, S.L. (1984), The complexity and stability of ecosystems. *Nature* **307**, 321–326.

[118] Pimm, S.L., and J.H. Lawton (1977), Number of trophic levels in ecological communities. *Nature* **268**, 329–331.

[119] Price, H.J. (1989), Swimming Behavior of Krill in Response to Algal Patches: A Mesocosm Study. *Limnol. Oceanogr.* **34**, 649–659.

[120] Pulliam, H.R. (1973), On the advantages of flocking. *J. Theor. Biol.* **38**, 419–422.

[121] Redi, M.H. (1982), Oceanic isopycnal mixing by coordinate rotation. *J. Phys. Oceanogr.* **12**, 1154–1158.

[122] Ritz, D.A. (1994), Social aggregation in pelagic invertebrates. *Adv. Mar. Biol.* **30**, 156–216.

[123] Ritz, D.A. (2000), Is social aggregation in aquatic crustaceans a strategy to conserve energy? *Can. J. Fish. Aquat. Sci.* **57**, 59–67.

[124] Rosenzweig, M.L., and R.H. MacArthur (1963), Graphical representation and stability conditions of predator-prey interactions. *Am. Nat.* **97**, 209–223.

[125] Roth, W.E. (1934), On direct product matrices. *Bull. Am. Math. Soc.* **40**, 461–468.

[126] Scheffer, M., and R.J. de Boer (1995), Implications of spatial heterogeneity for the paradox of enrichment. *Ecology* **76**, 2270–2277.

[127] Scheuring, M.N. (1999), Allee effect increases the dynamical stability of populations. *J. Theor. Biol.* **199**, 407–414

[128] Schreiber, S.J. (2003), Allee effects, extinctions, and chaotic transients in simple population models. *Theor. Pop. Biol.***64**, 201–209.

[129] Serebrennikova, Y.M., and K.A. Fanning (2004), Nutrients in the Southern Ocean GLOBEC region: variations, water circulation, and cycling. *Deep-Sea Res. II* **51**, 1981–2002.

[130] Simard Y., and D. Lavoie (1999), The rich krill aggregation of the Saguenay-St. Lawrence Marine Park: hydroacoustic and geostatistical biomass estimates, structure, variability and significance for whales. *Can. J. Fish. Aquat. Sci.* **56**, 1182–1197.

[131] Simons, A.M. (2004), Many wrongs: the advantage of group navigation. *Trends Ecol. Evol.* **19**, 453–455.

[132] Sourisseau, M., Y. Simard, and F.J. Saucier (2006), Krill aggregation in the St. Lawrence system, and supply of krill to the whale feeding grounds in the estuary from the gulf. *Mar. Ecol. Progr. Ser.* **314**, 257–270.

[133] Steele, J.H. (1974), Spatial heterogeneity and population stability. *Nature* **248**, 83.

[134] Stephens, P.A., and W.J. Sutherland (1999), Consequences of the Allee effect for behaviour, ecology and conservation. *Trends Ecol. Evol.* **14**, 401–405.

[135] Stewart, G.W. (1991), Perturbation theory for the singular value decomposition. In: R.J. Vaccaro (Ed.) *SVD and Signal Processing II: Algorithms, Analysis, and Implementation.* Elsevier, Amsterdam, pp. 99–109.

[136] Strand, S.W., and W.M. Hamner (1990), Schooling behavior of Antarctic krill (*Euphausia superba*) in laboratory aquaria: reactions to chemical and visual stimuli. *Mar. Biol.* **106,** 355–359.

[137] Takahashi, T., J. Olafsson, J. Goddard, D.W. Chipman, and S.C. Sutherland (1993), Seasonal variation of CO_2 and nutrients in the high-latitude surface oceans: A comparative study. *Global Biogeochem. Cycles* **7**, 843–878.

[138] Taylor, C.M., and A. Hastings (2005), Allee effects in biological invasions. *Ecol. Lett.* **8**, 895–908.

[139] Thompson, D., and J. Wallace (2000), Annular modes in the extra-tropical circulation. Part I: Month-to-month variability. *J. Climate* **13**, 1000–1016.

[140] Toner, J., Y. Tu, and S. Ramaswamy (2005), Hydrodynamics and phases of flocks. *Annals of Physics*, **318**, 170–244.

[141] Trefethen, L.N. (1992), Pseudospectra of matrices. In: D. F. Griffiths and G. A. Watson (Ed.), *Numerical Analysis 1991, Proc. 14th Dundee Conf.*, Longman Scientific and Technical, Essex, UK, pp. 234–266.

[142] Trefethen, L.N., and M. Embree (2005), *Spectra and Pseudospectra: The Behavior of nonnormal matrices and operators*. Princeton University Press, Princeton, NJ.

[143] Trefethen, L.N., A.E. Trefethen, S.C. Reddy, and T.A. Driscoll (1993), Hydrodynamic stability without eigenvalues. *Science* **261**, 577–583.

[144] Verdy, A., J. Marshall, and A. Czaja (2006), Sea surface temperature variability along the path of the Antarctic circumpolar current. *J. Phys. Oceanogr.* **36**, 1317–1331.

[145] Verdy, A., S. Dutkiewicz, M.J. Follows, J. Marshall, and A. Czaja (2007), Carbon dioxide and oxygen fluxes in the Southern Ocean: Mechanisms of interannual variability. *Global Biogeochem. Cycles* **21**, GB2020:doi:2006GB002916.

[146] Verdy, A., and G.R. Flierl (2007), Evolution and social behavior in krill. *Accepted for publication in Deep-Sea Res. II.*

[147] Vicsek, T., A. Czirok, E. Benjacob, I. Cohen, and O. Shochet (1995), Novel type of phase-transition in a system of self-driven particles. *Phys. Rev. Lett.* **75**, 1226–1229.

[148] Wang, W. and L. Chen (1997), A predator-prey system with stage-structure for predator. *Computers Math. Applic.* **33**, 83–91.

[149] Wanninkhof, R. (1992), Relationship between wind speed and gas exchange over the ocean. *J. Geophys. Res.* **97**, 7373–7382.

[150] Webb, C. (2003), A complete classification of Darwinian extinction in ecological interactions. *Am. Nat.* **161**, 181–205.

[151] Weber, L., El-Sayed, S., and I. Hampton (1986), The variance spectra of phytoplankton, krill and water temperature in the Antarctic Ocean south of Africa. *Deep-Sea Res.* **33**, 1327–1343.

[152] Williams, R.G., and M.J. Follows (1998), The Ekman transfer of nutrients and maintenance of new production over the North Atlantic. *Deep-Sea Res. I* **45**, 461–489.

[153] Wood, A.J., and G.J. Ackland (2007), Evolving the selfish herd: emergence of distinct aggregating strategies in an individual-based model. *Proc. R. Soc. B* doi:10.1098/rspb.2007.0306.

[154] Wright, K. (1992), Differential-equations for the analytic singular value decomposition of a matrix. *Numer. Math.* **63**, 283–295.

[155] Wunsch, C., and P. Heimbach (2006), Decadal changes in the North Atlantic meridional overturning and heat flux. *J. Phys. Oceanogr.* **36**, 2012–2024.

[156] Young, W., A. Roberts, and G. Stuhne (2001), Reproductive pair correlations and the clustering of organisms. *Nature* **412**, 326–331.

[157] Yuan, X. (2004), ENSO-related impacts on Antarctic sea ice: a synthesis of phenomenon and mechanisms. *Antarctic Sci.* **16**, 415–425.

[158] Zhou, M., and R.D. Dorland (2004), Aggregation and vertical migration behavior of *Euphausia superba*. *Deep-Sea Res. II* **51**, 2119–2137.

[159] Zhou, S.-R., Y.-F. Liu, and G. Wang (2005), The stability of predator-prey systems subject to the Allee effect. *Theor. Pop. Biol.***76**, 23–31.